

HYPERSPECTRAL-ASSISTED SCANNING ELECTROCHEMICAL MICROSCOPY FOR  
SINGLE CELL ANALYSIS

Sondrica Goines

A dissertation submitted to the faculty at the University of North Carolina at Chapel Hill in partial fulfillment of the requirements for the degree of Doctor of Philosophy in the Department of Chemistry in the College of Arts and Sciences.

Chapel Hill  
2022

Approved by:

Jeffrey E. Dick

Matthew R. Lockett

Mark H. Schoenfisch

Koji Sode

Jillian L. Dempsey

© 2022  
Sondrica Goines  
ALL RIGHTS RESERVED

## ABSTRACT

Sondrica Goines: Hyperspectral-Assisted Scanning Electrochemical Microscopy for Single Cell Analysis  
(Under the direction of Jeffrey E. Dick)

As the scope of our knowledge surrounding cell response to stimuli widens, the value in an unambiguous understanding of cell-to-cell heterogeneity increases. The advancement of biological imaging relies on studying the smallest unit of life – a single, living cell. Scanning electrochemical microscopy (SECM) has served as a non-destructive method for imaging single cells with most biological platforms being equipped with correlated optical and fluorescence microscopy. While fluorescence microscopy has served as a minimally destructive method for analysis, it may also be compromised by low signal-to-noise and phototoxic effects. To overcome these barriers in live-cell microscopy, we combine a typical biological SECM platform with a variable fluorescence bandpass source for obtaining electrochemical, optical, and spectral data, simultaneously. Our novel imaging platform widens the scope of biological imaging by allowing one to capture spectral data with 1 nm resolution to probe dynamic extra- and intra-cellular interactions *via* hyperspectral-assisted SECM. To demonstrate the robust capabilities and versatility of our imaging platform, we use hyperspectral-assisted SECM to examine a two-dimensional co-culture system and to investigate two relevant public health concerns: the mechanism of human cytomegalovirus propagation and the mechanism of perfluorooctane sulfonate cytotoxicity within two-dimensional tissue cultures.

To my husband and best friend, Rafael.

Thank you for navigating the hills and valleys with me.

## ACKNOWLEDGEMENTS

I would like to acknowledge my advisor, Professor Jeffrey Dick, for his guidance and support throughout the completion of this work. From day one, he challenged me to master new skills in the pursuit of new knowledge. He is the most passionate scientist I have ever met, and I am extremely grateful for his motivation because he pushed me outside of my comfort zone and into a space where science is driven by pure curiosity. Not only did he influence my growth as a scientist, he influenced my growth as a person. He reminded me when to give myself grace and when to keep pushing towards results. He protected my voice as a student and my goals as a scientist. It has been an honor to be his second graduate student. Thank you, Jeffrey, for taking a chance on me.

I would also like to acknowledge my committee members, Professor Matthew Lockett, Professor Mark Schoenfisch, Professor Koji Sode, and Professor Jillian Dempsey, for taking the time to serve on my committee. I am extremely grateful for their helpful feedback and motivating questions. In addition, I am thankful for their continual support in all my academic endeavors; it is with their letters of support that I have been able to accomplish so much during my time at the University of North Carolina at Chapel Hill.

During my time at the University, I gained a special lab family – Matthew Glasscott, Rezvan (Rose) Kazemi, Silvia Voci, Koun (Kasha) Lim, Christophe Renault, Rebecca Clark, Joshua Reyes Morales, Nicole Tarolla, Kathryn Vannoy, Nicole Walker, Thomas Clarke, Guillermo Colón, Philip Kauffmann, Vanshika Gupta, Lynn Krushinski, Anthony Bishop,

Mingchu (Jasmine) Deng, Andy Hoang, Hadley McCormick, Andrew Pendergast, Lettie (Alli) Smith, and Ben Vanderkwaak. I am extremely thankful that each of them took a chance on a new laboratory. Together, we created a motivating and inclusive lab culture. I would especially like to thank my undergraduate mentees – Hadley, Ben, Jasmine, and Alli – for their commitment to bioanalytical research and support throughout this work.

I would also like to acknowledge Ross Warrington (Leica Microsystems), Chris Murphy (Leica Microsystems), and Chris Ballard (Sutter Instrument Company) for their assistance in the construction of the hyperspectral-assisted electrochemical imaging platform as well as Matthew Verber and Moinul Choudhury for helpful discussions.

In addition, I would like to thank the National Science Foundation Graduate Research Fellowship for giving me the freedom to pursue science at the graduate level for the past two years.

I would like to extend a special thanks to my family for the love, support, and prayers that carried me through this journey. To my husband, Rafael, thank you for your patience, love, and support. To my sister, Sarah, thank you for your words of comfort and motivation. To my grandfather, thank you for your prayers. Finally, I would like to thank my mom. Thank you, Mom, for putting your all into my education. From the beginning, you sacrificed and paved my way towards this degree. I would not be the scholar, or woman, I am today without you. This degree is more than a piece of paper, it is a symbol of how far we have come. I could say thank you a million times, and it would never be enough.

## TABLE OF CONTENTS

|  |      |
|--|------|
| LIST OF FIGURES .....  | xi   |
| LIST OF TABLES.....  | xvi  |
| LIST OF ABBREVIATIONS & SYMBOLS.....   | xvii |
| Chapter 1 Introduction to Scanning Electrochemical Microscopy.....   | 1    |
| 1.1 Historic Background of Scanning Probe Microscopy.....  | 1    |
| 1.2 Scanning Electrochemical Microscopy.....   | 3    |
| 1.2.1 Instrumentation.....   | 3    |
| 1.2.2 Operational Modes & Variables to Consider.....   | 5    |
| 1.3 Examining Two-Dimensional Tissue Culture Systems via Scanning Electrochemical<br>Microscopy .....          | 16   |
| 1.3.1 Practical Approaches to Scanning Electrochemical Microscopy of Two-<br>Dimensional Tissue Cultures ..... | 16   |
| 1.3.2 Mechanistic Insight.....   | 19   |
| REFERENCES .....   | 21   |
| Chapter 2 Methods.....   | 23   |
| 2.1 Electrochemical Characterization of Small Molecules .....  | 23   |
| 2.1.1 Effect of Electrode Material.....  | 23   |
| 2.1.2 Effect of pH.....  | 34   |
| 2.1.3 Determination of Diffusion Coefficient.....  | 34   |
| 2.1.4 Determination of Electrons Transferred .....   | 40   |
| 2.1.5 Mechanistic Insight through Electrolysis.....  | 44   |
| 2.2 Two-dimensional Tissue Culture .....   | 46   |

|           |   |     |
|-----------|---|-----|
| 2.2.1     | Standard Operating Procedures.....  | 46  |
| 2.2.2     | Reagents and Materials.....   | 48  |
| 2.2.3     | Adenocarcinoma (HeLa) Cells.....  | 50  |
| 2.2.4     | Hepatocarcinoma (Hep G2) Cells.....   | 52  |
| 2.2.5     | Normal Lung (MRC-5) Cells.....  | 55  |
| 2.2.6     | Pancreatic (HPAC, HPNE dt, HPNE-myo free, and HPNE-KRAS) Cells.....                                 | 58  |
| 2.2.7     | Osteosarcoma (U-2 OS) Cells.....  | 61  |
| 2.2.8     | Media Renewal.....  | 63  |
| 2.2.9     | Cell Counting & Viability.....  | 63  |
| 2.2.10    | Cryopreservation & Thawing.....   | 64  |
| 2.3       | General Fluorescence Staining & Loading.....  | 65  |
| 2.3.1     | Hoechst Staining.....   | 65  |
| 2.3.2     | CellROX™ Orange Staining.....   | 68  |
| 2.3.3     | 2',7'-Dichlorofluorescein Diacetate Loading.....  | 70  |
| 2.4       | Scanning Probe Microscopy of Living Cells.....  | 73  |
|           | REFERENCES.....   | 86  |
| Chapter 3 | Practical Use of Biologically Relevant Small Molecules as Redox Mediators.....                      | 88  |
| 3.1       | Electrochemical Characterization of Nicotinamide Riboside.....                                      | 89  |
| 3.1.1     | Effect of Electrode Material.....   | 93  |
| 3.1.2     | Effect of pH.....   | 97  |
| 3.1.3     | Determination of Diffusion Coefficient.....   | 99  |
| 3.1.4     | Determination of Electrons Transferred.....   | 104 |
| 3.1.5     | Mechanistic Insight through Electrolysis.....   | 107 |
| 3.2       | Scanning Electrochemical Microscopy of Living Cells <i>via</i> Nicotinamide Riboside Reduction..... | 117 |
| 3.3       | Concluding Remarks & Future Perspectives.....   | 121 |



|   |     |
|---|-----|
| REFERENCES .....  | 123 |
| Chapter 4    Hyperspectral-Assisted Scanning Electrochemical Microscopy .....   | 126 |
| 4.1    Correlated Scanning Electrochemical Microscopy .....   | 126 |
| 4.2    Hyperspectral Imaging .....  | 130 |
| 4.3    Variable Fluorescence Bandpass Hyperspectral-Assisted Scanning Electrochemical<br>Microscopy .....   | 133 |
| 4.3.1    Instrumentation .....  | 135 |
| 4.3.2    Data Acquisition & Analysis .....  | 139 |
| 4.3.3    Hyperspectral Imaging of Invitrogen FluoSpheres™ .....   | 148 |
| 4.3.4    Hyperspectral-Assisted Scanning Electrochemical Microscopy of<br>Hep G2 Cells .....  | 152 |
| REFERENCES .....  | 161 |
| Chapter 5    Applications of Hyperspectral-Assisted Scanning<br>Electrochemical Microscopy .....  | 164 |
| 5.1    Probing Dynamic Co-culture Systems .....   | 164 |
| 5.1.1    Methods to Distinguish Between Cell Boundaries .....   | 165 |
| 5.1.2    Assessing Redox Activity – Spectral Analysis of Glutathione.....   | 170 |
| 5.1.3    Concluding Remarks & Future Perspectives .....   | 173 |
| 5.2    Investigating the Propagation of Human Cytomegalovirus .....   | 173 |
| 5.2.1    Methods to Examine Viral Propagation.....  | 174 |
| 5.2.2    Concluding Remarks & Future Perspectives .....   | 178 |
| 5.3    Examining Perfluorooctane Sulfonate Exposure Effects on Living Cells .....   | 178 |
| 5.3.1    Cell Viability Following Exposure .....  | 181 |
| 5.3.2    Hyperspectral-Assisted Scanning Electrochemical Microscopy of Hep G2<br>Following PFOS Exposure: Reactive Oxygen Species Content Analysis..... | 185 |
| 5.3.3    Scanning Electrochemical Microscopy of Hep G2 Following PFOS Exposure:<br>Variation in Cellular Reactivity Over Time.....                      | 190 |

|           |   |     |
|-----------|---|-----|
| 5.3.4     | Ferrocenium Methanol Reduction <i>via</i> Glutathione.....  | 193 |
| 5.3.5     | Hyperspectral Imaging of Hep G2 Following PFOS Exposure: Glutathione Contribution Analysis .....  | 199 |
| 5.3.6     | Hyperspectral-Assisted Scanning Electrochemical Microscopy of Hep G2 Following PFOS Exposure: Superoxide Dismutase 1 Contribution Analysis..... | 203 |
| 5.3.7     | Concluding Remarks & Future Perspectives .....  | 207 |
|           | REFERENCES .....  | 209 |
| Chapter 6 | Nanoelectrode Fabrication for Single Cell Analysis .....  | 213 |
| 6.1       | Nanoelectrode Fabrication .....   | 214 |
| 6.1.1     | Materials & Methods .....   | 217 |
| 6.1.2     | The Seal Process .....  | 221 |
| 6.1.3     | The Pull Process.....   | 233 |
| 6.1.4     | How to Interpret Failure.....   | 239 |
| 6.1.5     | Making Connections & Maintenance .....  | 242 |
| 6.1.6     | Concluding Remarks.....   | 249 |
| 6.2       | Correlated Scanning Electrochemical Microscopy of Singe Living Cells.....   | 249 |
| 6.2.1     | Concluding Remarks & Future Perspectives .....  | 253 |
|           | REFERENCES .....  | 254 |
|           | APPENDIX A.....   | 257 |

## LIST OF FIGURES

|   |    |
|---|----|
| Figure 1.1. Generation/Collection Mode .....  | 7  |
| Figure 1.2. Tip-Substrate Distance in Feedback Mode.....  | 10 |
| Figure 1.3. Positive versus Negative Feedback SECM .....  | 13 |
| Figure 1.4. SECM Feedback Mechanisms for Living Cells .....   | 20 |
| Figure 2.1. Inner-sphere vs. Outer-sphere Electrode Reactions .....                                   | 25 |
| Figure 2.2. Example Cyclic Voltammetry Settings .....   | 28 |
| Figure 2.3. Standard Three-Electrode System .....   | 30 |
| Figure 2.4. Lateral vs. Radial Diffusion .....  | 33 |
| Figure 2.5. Example Chronoamperogram Settings.....  | 39 |
| Figure 2.6. Example Square Wave Voltammogram Settings .....   | 43 |
| Figure 2.7. Electrolysis Cell.....  | 45 |
| Figure 2.8. Hep G2 Morphology.....  | 53 |
| Figure 2.9. Hep G2 Morphology following Trypsinization.....   | 54 |
| Figure 2.10. MRC-5 Morphology.....  | 57 |
| Figure 2.11. HPNE Morphology.....   | 59 |
| Figure 2.12. HPAC Morphology .....  | 60 |
| Figure 2.13. U-2 OS Morphology.....   | 62 |
| Figure 2.14. Hoechst Nuclear Stain .....  | 67 |
| Figure 2.15. CellROX™ Orange Stain.....   | 69 |
| Figure 2.16. Mechanism of ROS Detection via 2',7'-Dichlorofluorescein Diacetate <sup>21</sup> .....   | 71 |
| Figure 2.17. Dichlorofluorescein Emission following 2',7'-Dichlorofluorescein Diacetate Loading ..... | 72 |
| Figure 2.18. Approach Curve Parameters.....   | 75 |

|   |     |
|---|-----|
| Figure 2.19. Negative Feedback Response .....   | 76  |
| Figure 2.20. Normalized Negative Feedback Response .....  | 77  |
| Figure 2.21. Negative Feedback Theoretical Fit.....   | 79  |
| Figure 2.22. Scanning Electrochemical Microscope Parameters.....  | 81  |
| Figure 2.23. Electrochemical Image following Tilt Correction.....   | 82  |
| Figure 2.24. Negative Feedback Approach to Cells .....  | 84  |
| Figure 2.25. Scanning Electrochemical Microscopy Image of Hep G2 Cells .....                                    | 85  |
| Figure 3.1. Nicotinamide Riboside .....   | 92  |
| Figure 3.2. Cyclic Voltammogram of Nicotinamide Riboside .....  | 95  |
| Figure 3.3. Effect of Electrode Material on Nicotinamide Riboside Cyclic Voltammetry .....                      | 96  |
| Figure 3.4. Effect of pH on Nicotinamide Riboside Cyclic Voltammetry .....                                      | 98  |
| Figure 3.5. Cyclic Voltammetry of Diffusion-Controlled Nicotinamide Riboside .....                              | 100 |
| Figure 3.6. Chronoamperometry of Nicotinamide Riboside .....  | 103 |
| Figure 3.7. Square Wave Voltammetry of Nicotinamide Riboside .....  | 106 |
| Figure 3.8. Schematic of Nicotinamide Riboside EC <sub>dim</sub> Mechanism .....                                | 108 |
| Figure 3.9. Bulk Electrolysis of Nicotinamide Riboside .....  | 110 |
| Figure 3.10. Mass Spectrum of Reduced Nicotinamide Riboside .....   | 113 |
| Figure 3.11. Cyclic Voltammogram of Nicotinamide Riboside in Whole Cell Lysate .....                            | 116 |
| Figure 3.12. Correlated Optical and Electrochemical Images of HPNE-KRAS<br>Cells in Nicotinamide Riboside ..... | 118 |
| Figure 3.13. Nicotinamide Riboside Redox Mechanism above HPNE-KRAS Cells.....                                   | 120 |
| Figure 4.1. Hyperspectral-Assisted Scanning Electrochemical Microscope Schematic .....                          | 138 |
| Figure 4.2. Lambda 10-3 Home Screen .....   | 140 |
| Figure 4.3. Lambda 10-3 Error After Wavelength Input .....  | 143 |

|   |     |
|---|-----|
| Figure 4.4. Lambda <i>SmartShutter</i> <sup>TM</sup> .....  | 143 |
| Figure 4.5. Open Lambda 10-3 Xenon Arc Lamp Shutter .....   | 143 |
| Figure 4.6. Lambda 10-3 TTL Shutter Settings Menu.....  | 145 |
| Figure 4.7. Lambda 10-3 TTL Shutter Settings Menu #2.....   | 145 |
| Figure 4.8. Hyperspectral Image of Invitrogen FluoSpheres <sup>TM</sup> .....   | 151 |
| Figure 4.9. Cyclic Voltammetry of Ferrocenemethanol Above Cells .....   | 154 |
| Figure 4.10. Approach Result with Pt Microelectrode SECM Tip.....   | 156 |
| Figure 4.11. Correlated Electrochemical and Fluorescence Imaging of<br>Hoechst Stained Hep G2 Cells.....  | 157 |
| Figure 4.12. Hyperspectral-Assisted Scanning Electrochemical Microscopy<br>of Hoechst Stained Hep G2 Cells .....  | 160 |
| Figure 5.1. Correlated Optical, Fluorescence, and Scanning Electrochemical<br>Microscopy of a Two-dimensional Co-culture .....                                  | 167 |
| Figure 5.2. Hyperspectral-Assisted Scanning Electrochemical Microscopy of<br>a Two-dimensional Co-culture .....   | 169 |
| Figure 5.3. Hyperspectral-Assisted Scanning Electrochemical Microscopy of<br>Hep G2 Cells and Monochlorobimane-Glutathione .....                                | 172 |
| Figure 5.4. AD169-GFP Human Cytomegalovirus Infected MRC-5 Cells.....   | 175 |
| Figure 5.5. Hyperspectral-Assisted Scanning Electrochemical Microscopy of<br>AD169-GFP Human Cytomegalovirus Infected MRC-5 Cells .....                         | 177 |
| Figure 5.6. Cell Viability Following PFOS Exposure .....  | 184 |
| Figure 5.7. Approach Curve to Hep G2 Cells.....   | 187 |
| Figure 5.8. Hyperspectral-Assisted Scanning Electrochemical Microscopy of<br>Hep G2 Following PFOS Exposure & 2',7'-Dichlorofluorescein Diacetate Loading ..... | 189 |
| Figure 5.9. Time Lapse Scanning Electrochemical Microscopy of Hep G2<br>Following PFOS Exposure .....   | 192 |
| Figure 5.10. Schematic Representation of PFOS Cytotoxic Mechanism .....   | 194 |
| Figure 5.11. Ferrocenium Methanol Reduction <i>via</i> Glutathione Voltammetric Controls .....  | 196 |

|  |     |
|--|-----|
| Figure 5.12. $E_rC_i'$ Mechanism Following Ferrocenemethanol Oxidation in Glutathione..... | 198 |
| Figure 5.13. Hyperspectral Imaging of Glutathione Following PFOS Exposure .....            | 201 |
| Figure 5.14. Glutathione Contribution Analysis Following PFOS Exposure.....                | 202 |
| Figure 5.15. Superoxide Dismutase 1 Contribution Analysis Following PFOS Exposure .....    | 206 |
| Figure 6.1. Schematic Representation of Laser Pulling Pt Nanoelectrodes .....              | 216 |
| Figure 6.2. P-2000 Laser Puller Modification .....   | 218 |
| Figure 6.3. Laser Puller Set Up During Seal .....  | 220 |
| Figure 6.4. Incomplete vs. Complete Seal .....   | 222 |
| Figure 6.5. Effect of Vacuum on the Seal Process .....                                     | 224 |
| Figure 6.6. Loss of Pt Wire Integrity Upon Complete Seal.....                              | 225 |
| Figure 6.7. Effect of Heat on the Sealing Process .....                                    | 227 |
| Figure 6.8. Variation in Heat Distribution Length Based on Filament.....                   | 229 |
| Figure 6.9. Interdependent Relationship Between Heat and Filament .....                    | 230 |
| Figure 6.10. Effect of Filament on the Seal Process.....                                   | 232 |
| Figure 6.11. Variation in Outer Diameter of Tip Based on Filament.....                     | 234 |
| Figure 6.12. Pinched Pt Wire Result.....   | 235 |
| Figure 6.13. Cyclic Voltammetry of Nanoelectrode Fabricated with a Delay of 100 .....      | 237 |
| Figure 6.14. Cyclic Voltammetry of Electrode Fabricated with a Delay < 128 .....           | 238 |
| Figure 6.15. Nanoelectrode Fabrication Failures.....                                       | 241 |
| Figure 6.16. Nanoelectrode Characterization by Cyclic Voltammetry.....                     | 243 |
| Figure 6.17. Cyclic Voltammogram of Electrode Without Exposed Platinum Tip.....            | 246 |
| Figure 6.18. Electrode Surface Following Subsequent Beveling .....                         | 247 |
| Figure 6.19. Scanning Electrochemical Microscopy of Single Living Cells.....               | 250 |

Figure 6.20. Intracellular Measurement with a Laser Pulled Pt Nanoelectrode ..... 252

## LIST OF TABLES

|  |     |
|--|-----|
| Table 1.1. Parameter Values for Equation 1.3 <sup>16</sup> .....         | 14  |
| Table 1.2. Parameter Values for Equation 1.4 <sup>16</sup> .....         | 14  |
| Table 2.1. Effect of Pulse Amplitude on Peak Height <sup>11</sup> .....  | 41  |
| Table 2.2. Working Volumes for Tissue Culture Vessels .....              | 50  |
| Table 4.1. Available VersaChrome <sup>®</sup> Tunable Filters .....      | 136 |
| Table A1. Operational Modes of Scanning Electrochemical Microscopy ..... | 257 |



## LIST OF ABBREVIATIONS & SYMBOLS

|                  |   |
|------------------|---|
| STM              | Scanning tunneling microscopy                                   |
| SECM             | Scanning electrochemical microscopy                             |
| $a, r, r_{elec}$ | Radius of the electrode   |
| $a_s, r_s$       | Radius of the substrate   |
| $i_T$            | Tip current   |
| $i_s$            | Substrate current   |
| $d$              | Tip-to-substrate distance                                       |
| $i_{T,\infty}$   | Steady state current or limiting current                        |
| $n$              | Number of electrons transferred                                 |
| $F$              | Faraday's constant (96,485 C mol <sup>-1</sup> )                |
| $D$              | Diffusion coefficient (cm <sup>2</sup> s <sup>-1</sup> )        |
| $C^*$            | Concentration of redox species (mol cm <sup>-3</sup> )          |
| $\beta$          | Geometric coefficient of the electrode tip                      |
| $L$              | Normalized tip-to-substrate distance ( $d/a$ )                  |
| $v$              | Scan rate (V s <sup>-1</sup> )                                  |
| $i_p$            | Peak current (A)  |
| $A$              | Area of the electrode (cm <sup>2</sup> )                        |
| $R$              | Ideal gas constant (8.314 J mol <sup>-1</sup> K <sup>-1</sup> ) |
| $T$              | Temperature (K)   |
| HeLa             | Adenocarcinoma cells  |
| Hep G2           | Hepatocarcinoma cells   |

|                      |                                      |
|----------------------|--------------------------------------|
| MRC-5                | Normal lung cells                    |
| U-2 OS               | Osteosarcoma cells                   |
| HPAC                 | Cancerous pancreatic cells           |
| HPNE dt              | Immortalized normal pancreatic cells |
| HPNE myo free        | Immortalized normal pancreatic cells |
| GFP                  | Green fluorescent protein            |
| RFP                  | Red fluorescent protein              |
| ROS                  | Reactive oxygen species              |
| RNS                  | Reactive nitrogen species            |
| DMEM                 | Dulbecco's Modified Eagle's Medium   |
| EMEM                 | Essential Modified Eagle's Medium    |
| FBS                  | Fetal bovine serum                   |
| DPBS                 | Dulbecco's phosphate buffered saline |
| DCF-DA               | 2',7'-dichlorofluorescein diacetate  |
| DMSO                 | Dimethyl sulfoxide                   |
| DCF                  | 2',7'-dichlorofluorescein            |
| MBCl                 | Monochlorobimane                     |
| GSH                  | Glutathione                          |
| FcCH <sub>2</sub> OH | Ferrocenemethanol                    |
| SOD 1                | Superoxide dismutase 1               |
| ECL                  | Electrochemiluminescence             |

## Chapter 1 Introduction to Scanning Electrochemical Microscopy

### 1.1 Historic Background of Scanning Probe Microscopy

For three decades, scanning probe microscopy has been at the forefront of nanoscience by allowing investigators to perform experiments down to the ultimate limit of detection (*i.e.*, down to a single molecule or atom). The innovation of scanning tunneling microscopy (STM) in 1982<sup>1</sup>, by Gerd Binnig and Heinrich Rohrer, not only earned the Nobel Prize in physics in 1986 but also served as a precedent for scanning probe microscopy techniques to come. STM exhibits the most fundamental aspects of all scanning probe microscopy techniques. Within STM, the probe is positioned above a substrate, then configured to scan an area of interest in the  $xyz$  plane. This allows local interactions within the probe-substrate gap to be measured as a function of the lateral position. In STM, a voltage is held at a metallic tip probe positioned  $< 1$  nm above the surface of a conducting substrate by an electronic controller, referred to as a piezoelectric actuator, allowing quantum mechanical current (*i.e.*, tunneling current) to flow between a single atom at the apex of the tip and a single atom of the conductor.<sup>2</sup> This form of microscopy consists of two operational modes: 1) constant current mode, where a tunneling current is held constant as the change in tip height is recorded as a function of lateral position, and 2) constant height mode, where a tunneling current is recorded as a function of lateral position. These operational modes provide investigators with atomic resolution when imaging the structures of crystalline, conducting surfaces. In other words, point and structural defects are resolved down to single atoms. A fundamental element of STM is the flow of non-faradaic current (*i.e.*, current flow that is not due to a chemical change<sup>3</sup>) between the tip and the sample, whether in vacuum or through

a thin insulator; this element limits the scanning probe technique to imaging conductive surfaces.<sup>2</sup>

In 1986, the Bard group at the University of Texas Austin used this methodology to measure electrochemical and tunneling current by immersing the probe and substrate in solution rather than conducting experiments under vacuum.<sup>4</sup> In addition, a large, ultramicroelectrode tip was used as the probe instead of a sharp metallic tip. The use of a conductive solvent permitted current exchange through faradaic reactions within the tip-substrate gap, which allowed users to position the electrode tip further from the substrate when imaging samples with large aspect ratios.<sup>4</sup> The Bard group continued to use this variation of STM to study conductive substrates and externally polarized electrodes into the late 1980s.<sup>5</sup> In 1988, Bard began to coin the platform used in his laboratory to electrochemically characterize, deposit, and etch substrates a scanning electrochemical microscope.<sup>6</sup> A year later, the group outlined the principles of the new analytical technique in the literature.<sup>3</sup> The group had designed a novel scanning probe microscope technique in which they combined the use of ultramicroelectrodes, piezoelectric positioners, and faradaic current to develop scanning electrochemical microscopy (SECM). By placing their ultramicroelectrode tip (diameter  $\leq 10 \mu\text{m}$ ) into an electroactive solution (*i.e.*, a solution containing a redox mediator) above a substrate, scanning probe microscopy was no longer limited to the study of conductive substrates. Instead, communication between the ultramicroelectrode tip and the substrate would be facilitated by the redox mediator in solution; additionally, measurements can be made within larger tip-substrate gaps, ranging from the nanometer to micrometer scale depending on the electrode size, since current is controlled by electron transfer kinetics and mass transfer processes in solution.<sup>3</sup> Moreover, SECM enabled the study of samples on the micrometer scale and below (*e.g.*, a single biological macromolecule<sup>7</sup> or

cell<sup>8</sup>) with the use of micro- and nano-electrode tips, while STM is limited to lateral regions on the nanometer scale with the use of sharp metallic tips (diameter  $\leq 900 \text{ nm}^2$ ).<sup>3</sup>

SECM widened the scope of scanning probe microscopy with the fundamental addition of electrolysis current. Similar to STM, investigators have combined SECM with other techniques such as quartz crystal microbalance, electrogenerated chemiluminescence, atomic force microscopy, and photoelectrochemical microscopy to extend its usefulness and applications in fields beyond physical chemistry.<sup>2</sup> This introductory chapter serves as a fundamental review of SECM and its development towards biological applications to familiarize readers with the technique before introducing a novel advancement: variable fluorescence bandpass hyperspectral-assisted SECM.

## **1.2 Scanning Electrochemical Microscopy**

The concept for SECM originated from an investigation by Engstrom and co-workers in 1986, when a microelectrode was used to amperometrically detect an electroactive species produced at a secondary electrode.<sup>9, 10</sup> Following the introduction of generation/collection mode, Bard and co-workers introduced various operational modes of SECM, expanding the applications of the technique. Regardless of the operational mode, a scanning electrochemical microscope is composed of four major parts: 1) a bipotentiostat, 2) a positioner, 3) a probe electrode, and 4) a computer.

### **1.2.1 Instrumentation**

As a scanning probe technique, SECM is similar to STM in design. For example, a positioner and a probe electrode are two key components of both microscope systems. Generally, positioners on recent scanning electrochemical microscope systems are equipped with stepper and piezoelectric motors for coarse and fine movement, respectively, allowing users to collect

images on the micrometer and nanometer scales. Specifically, the piezoelectric motor allows for three-dimensional fine movement for nanometer spatial resolution. The positioner on each system is equipped with a probe electrode holder for ease-of-use. In the case of SECM, the probe is a metallic tip surrounded by an insulator (*i.e.*, an ultramicroelectrode or a nanoelectrode with a diameter  $\leq 10 \mu\text{m}$ ).<sup>3</sup>

To quantify electroactivity within the tip-substrate gap as a function of the lateral position of the electrode tip (*i.e.*, to collect scanning electrochemical microscope images), the electrochemical signal measured at the electrode tip and the placement of the electrode tip must be synchronized using a bipotentiostat controlled by a computer; in addition, the computer is used for data acquisition. The bipotentiostat provides users with the precision and accuracy necessary to measure current at the electrode tip and control the voltage of the tip and substrate electrodes. Today, users can pick from a wide range of manufacturers such as CH Instruments, BioLogic, Heka Elektronik, Sensolytics, and Uniscan Instruments for a commercial bipotentiostat system.<sup>11</sup> Commercially available bipotentiostats for SECM are typically characterized as low current ( $\leq \text{pA}$  or  $10^{-12} \text{ A}$ ) instruments<sup>11</sup>, making the use of nanoelectrode tips feasible.

While the temporal resolution of a scanning electrochemical microscope system is dependent on the scan rate limitations of the positioner (*i.e.*, the increment time limitations), the spatial resolution is dependent on the spatial resolution of the positioner (*i.e.*, the increment distance limitations) as well as the tip dimensions. Moreover, to prevent oversampling, the spatial resolution of a scanning electrochemical microscope image is limited by the diameter of the metallic electrode tip. High spatial resolution is achievable if a nanoelectrode tip ( $r \leq 500 \text{ nm}$ , where  $r$  is the radius of the electrode) is used as the electrode tip. Nanoelectrodes are not

commercially available, but the demand for high resolution has produced many in-house nanoelectrode fabrication techniques, which will be the subject of **Chapter 6** section **6.1**.<sup>11-13</sup> Additionally, the spatial resolution is also limited by the smallest increment distance achievable by the positioner in use (*e.g.*, the CH Instruments 920D piezoelectric positioner is capable of 8 nm increment distances). High temporal and spatial resolution are key components to real-time electrochemical imaging and are often necessary to study physiological processes of single-living cells<sup>13</sup>, which is the overarching goal of this dissertation. Imaging of single-living cells using fabricated nanoelectrodes will be discussed in **Chapter 6**.

### **1.2.2 Operational Modes & Variables to Consider**

SECM has earned the reputation of being extremely versatile based on its various operational modes. As previously stated, generation/collection mode was introduced in 1986 by the Engstrom group prior to the Bard group coining the name “scanning electrochemical microscopy” later in 1989.<sup>10</sup> In addition to generation/collection mode, the Bard group introduced feedback mode in the late 1980s, making the two modes the first of their kind.<sup>3, 10, 11</sup> Generation/collection and feedback modes are primarily used in biological applications of SECM, and will be the focus of this section. Readers should consider that as new applications of SECM surfaced, new modes of operation were developed. A brief overview of current operational modes of SECM is provided in **Table A1** in **Appendix A**.

Now, imagine a scanning electrochemical microscope system where a bipotentiostat is used to control a positioner holding an electrode tip directly above a substrate immersed in a solution containing redox mediator species, *R*. Now, consider the reversible oxidation of species *R* to species *O* through the loss of *n* electrons at the electrode surface, assuming *R* and *O* are freely-diffusing species:



**Equation 1.1**

Below, various experimental designs will be generally outlined to describe generation/collection and feedback modes of SECM using the redox mechanism described above. In addition, we will make note of experimental components to consider when outlining a new experiment.

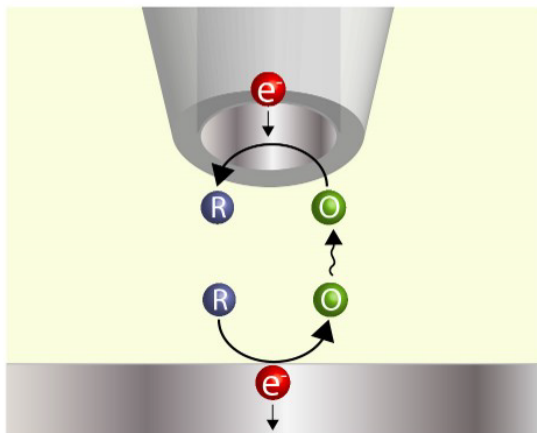
### **1.2.2.1 Generation/Collection Mode**

Within generation/collection mode, there are two experimental designs: 1) substrate generation/tip collection (SG/TC) and 2) tip generation/substrate collection (TG/SC). The design depends on the origin of the redox reaction; for example, in reference to **Equation 1.1**, if  $R$  is oxidized at the substrate and  $O$  is reduced at the electrode tip (*i.e.*,  $O$  is generated at the substrate, then collected at the electrode tip) as depicted in **Figure 1.1** then a SG/TC experiment is being performed.

This experimental design assumes that only  $R$  is present in solution prior to biasing the working electrodes at potentials sufficient to oxidize and reduce the redox mediator species; additionally, it is assumed that there is no measurable current prior to biasing the electrodes. While biasing both working electrodes, electrolysis (or faradaic) current is simultaneously measured at both electrodes. Here, the radius of the electrode tip is substantially less than the radius of the substrate ( $a_s/a \gg 1$ , where  $a_s$  is the radius of the substrate and  $a$  is the radius of the tip) such that the diffusion layer of the substrate ( $2a$ ) is substantially larger than that of the electrode tip. Moreover, collection efficiency is typically low due to the small size of the electrode tip.<sup>11</sup>



**Substrate Generation/Tip Collection**



**Tip Generation/Substrate Collection**

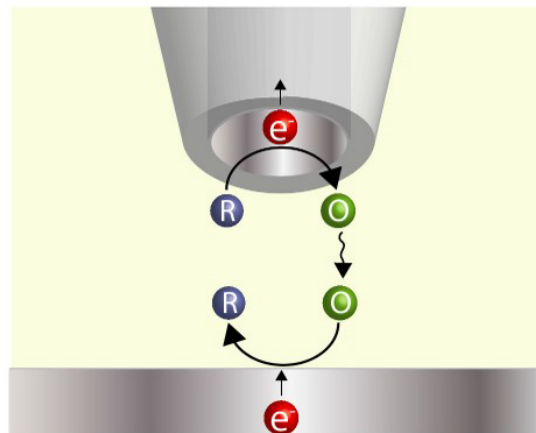


**Figure 1.1. Generation/Collection Mode**

Schematic representations of the redox mechanisms characteristic of substrate generation/tip collection and tip generation/substrate collection operational modes.

Collection efficiency in these experiments is described as  $i_T/i_S$ , where  $i_T$  is the tip current and  $i_S$  is the substrate current. This generation/collection mode is generally used to map concentration profiles or the flux of a redox species from a substrate.<sup>11</sup>

For tip generation/substrate collection (TG/SC) mode, visualize the reverse of the example previously provided, where  $R$  is oxidized at the electrode tip and  $O$  is reduced at the substrate (*i.e.*,  $O$  is generated at the electrode tip, then collected at the substrate). For a schematic representation refer to **Figure 1.1**. Once more, it should be assumed that only  $R$  is initially present in solution. Due to the size of the electrode tip versus the substrate,  $i_S$  is essentially zero as  $R$  is initially oxidized at the electrode tip. As time passes, the oxidation product,  $O$ , is given time to diffuse to the substrate surface allowing  $i_S$  to increase until the difference between  $i_S$  and  $i_T$  is insignificant. In contrast to SG/TC, high collection efficiency ( $i_S/i_T > 0.99$ ) is feasible in TG/SC experiments when the distance ( $d$ ) within the tip-substrate gap is small ( $L \leq 2$ , where  $L = d/a$ ).<sup>11</sup> TG/SC experiments are generally used to measure kinetics and modify the surface of the substrate electrode.<sup>11</sup>

When preparing to do SECM using a generation/collection mode experimental design, the redox mediator of choice may be more dynamic compared to those used in other operational modes. In general, a redox mediator should be stable in the solvent system of choice and inert in the presence of the electrode tip, substrate, counter, and reference electrodes.<sup>11</sup> Since specific reaction pathways may be investigated in generation/collection mode experiments by biasing the tip and substrate electrodes, various reaction mechanisms can be characterized in this operational mode. This specificity enables the investigation of homogeneous reaction mechanisms in solution and heterogeneous reaction mechanisms at both electrodes; additionally, this mode of operation allows an investigator to study redox mechanisms involving chemical transfers of two

or more electrons. More specifically, this mode of operation enabled single molecule detection; by placing a 15 nm-diameter electrode tip approximately 10 nm from a conductive substrate, Fan and Bard observed a single molecule of [(trimethylammonio)methyl] ferrocene enter and exit the tip-substrate gap.<sup>14</sup>

### 1.2.2.2 Feedback Mode

Similar to generation/collection mode, there are two experimental designs in feedback mode: 1) negative feedback and 2) positive feedback. Conceptualize the electrode tip submerged in a solution of species  $R$  above an insulating substrate with the tip biased sufficiently to oxidize species  $R$  to species  $O$  as described by **Equation 1.1**. When the electrode tip is at a tip-to-substrate distance ( $d$ ) greater than  $10a$  (where  $a$  is the radius of the metallic electrode tip) as shown in **Figure 1.2A**, the current measured at the tip is equivalent to the steady-state current ( $i_{T,\infty}$ ). **Equation 1.2** defines the steady-state current, where  $n$  is the number of electrons transferred,  $F$  is Faraday's constant ( $96,485 \text{ C mol}^{-1}$ ),  $D$  is the diffusion coefficient of species  $R$  ( $\text{cm}^2 \text{ s}^{-1}$ ),  $C^*$  is the concentration of species  $R$  ( $\text{mol cm}^{-3}$ ),  $a$  is the radius of the electrode tip (cm), and  $\beta$  is the geometric coefficient of the electrode tip.<sup>11</sup> This equation assumes that a microdisk electrode tip is in use.

$$i_{T,\infty} = 4nFDC^*a\beta \quad \text{Equation 1.2}$$

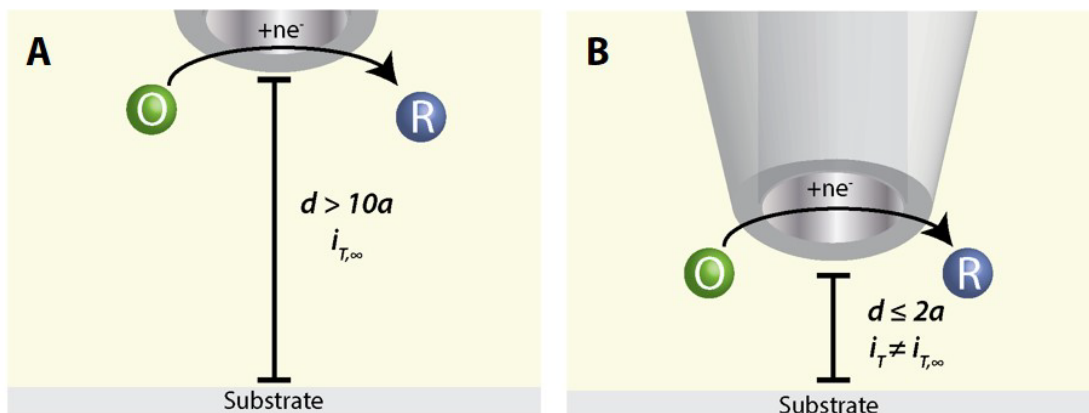


**Figure 1.2. Tip-Substrate Distance in Feedback Mode**

(A) Schematic representation of when the tip-to-substrate distance ( $d$ ) is greater than ten times the radius ( $a$ ) of the electrode tip indicating that the current measured is steady-state current. (B) Schematic representation of when the tip-to-substrate distance is less than or equal to two times the radius of the electrode tip indicating that the current measured is no longer equivalent to the steady state current, but dependent on characteristics of the substrate.

In **Equation 1.2**, the geometric coefficient  $\beta$  depends on the  $R_g$  of the electrode tip (defined as the ratio of the radius of the insulating sheath to the radius of the microdisk metallic tip); given an electrode tip with an  $R_g \geq 50$ , the geometric coefficient is equal to 1. If the  $R_g$  is sufficiently small ( $R_g \leq 1$ , where  $\beta \geq 1.43$ ), enhancement of the diffusion limiting current ( $i_{T, \infty}$ ) is feasible and  $\beta$  should be considered.<sup>15</sup> If the electrode tip is brought down towards the insulating substrate using the positioner controlled by the bipotentiostat, diffusion of species  $R$  to the electrode tip is hindered as  $d$  approaches  $2a$ . When  $d \leq 2a$  (**Figure 1.2B**), the current measured at the electrode tip decreases ( $i_T < i_{T, \infty}$ , where  $i_T$  is the current measured at the electrode surface). As the bipotentiostat measures  $i_T$  vs.  $d$ ,  $i_T$  becomes less than  $i_{T, \infty}$ . This describes negative feedback.

Suppose the substrate was no longer an insulator, but a conductor sufficiently biased by the bipotentiostat to reduce the oxidation product in **Equation 1.1** (*i.e.*, species  $O$ ). As the electrode tip approaches the conductive substrate, concurrently biased to oxidize  $R$ , the local flux of  $R$  to the electrode surface increases.<sup>13</sup> In this experimental design, as the bipotentiostat measures  $i_T$  vs.  $d$ ,  $i_T$  becomes greater than  $i_{T, \infty}$ . This describes positive feedback.

Similar to generation/collection mode, the redox mediator of choice must be stable in solution and chemically inert in the presence of the electrodes in use. Generally, we assume that the mediator will not adsorb to the surface of the tip and substrate electrodes. Moreover, the reaction mechanisms under investigation by feedback mode are typically less complex than those examined by generation/collection mode (*e.g.*, feedback mode is often used to examine one electron transfer chemical processes). Additionally, the redox pathway must be reversible or quasi-reversible with relatively fast heterogeneous kinetics at the substrate. This component is crucial to a decent experimental design as feedback mode is often used to determine the

electrochemical activity of the substrate and the topography of the substrate based on fluctuations in faradaic current at the electrode tip with high temporal resolution.<sup>11</sup>

Schematic representations of negative and positive feedback mode experimental designs are depicted in **Figure 1.3**. When previously describing each mode, a characteristic  $i_T$  vs.  $d$  current trace was mentioned; this  $i_T$  vs.  $d$  current trace is an approach curve. An approach curve provides information concerning the tip-to-substrate distance and the apparent kinetics of the redox reaction under investigation (again, highlighting the need for a redox mediator with fast heterogeneous kinetics).<sup>11</sup> A negative feedback approach curve for  $R_g$  values between 1.1 and 10 is modeled using **Equation 1.3**.<sup>16</sup>

$$I_T^{ins}(L) = \frac{1}{\left[A + \frac{B}{L} + Ce^{\left(\frac{D}{L}\right)}\right]} + \frac{E \times L}{(F+L)} \quad \text{Equation 1.3}$$

A positive feedback approach curve for  $R_g$  values between 1.1 and 10 is modeled using **Equation 1.4**.<sup>16</sup>

$$I_T^c(L) = A + \frac{B}{L} + Ce^{D/L} \quad \text{Equation 1.4}$$

Where  $L$  is the tip-to-substrate distance ( $d$ ) normalized by the radius of the electrode tip ( $a$ ) (*i.e.*,  $L=d/a$ ) and parameter values  $A$  through  $F$  are based on the  $R_g$  of the electrode tip. Parameter values for negative feedback fits are shown in **Table 1.1**, while parameter values for positive feedback fits are shown in **Table 1.2**.

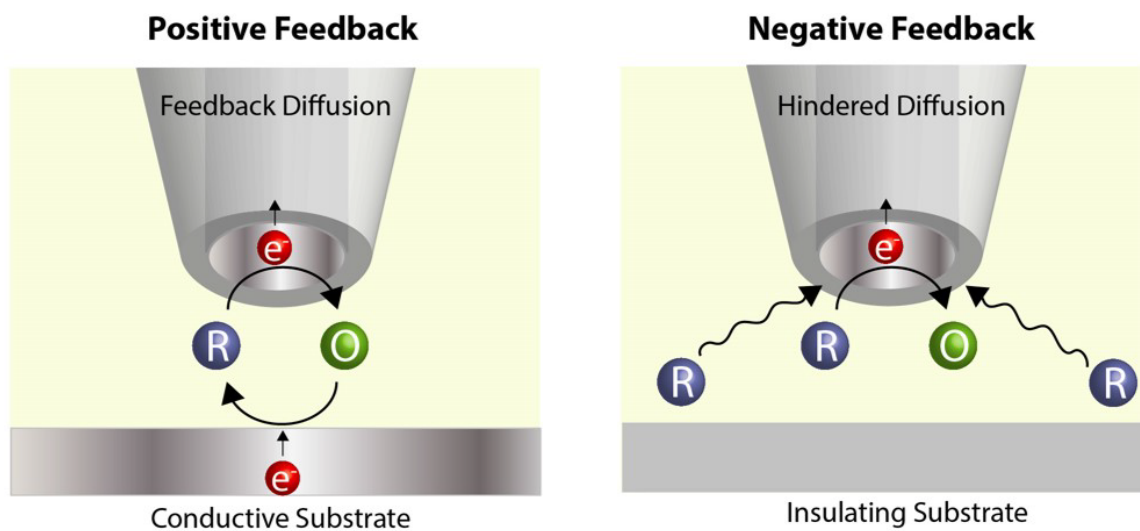


**Figure 1.3. Positive versus Negative Feedback SECM**

Schematic representations of positive and negative feedback SECM redox mechanisms, respectively.

**Table 1.1. Parameter Values for Equation 1.3<sup>16</sup>**

| $R_g$ | A         | B         | C         | D         | E         | F         |
|-------|-----------|-----------|-----------|-----------|-----------|-----------|
| 1.1   | 1.1675164 | 1.0309985 | 0.3800855 | -1.701797 | 0.3463761 | 0.0367416 |
| 1.5   | 1.0035959 | 0.9294275 | 0.4022603 | -1.788572 | 0.2832628 | 0.1401598 |
| 2.0   | 0.7838573 | 0.877792  | 0.4248416 | -1.743799 | 0.1638432 | 0.1993907 |
| 10    | 0.4571825 | 1.4604238 | 0.4312735 | -2.350667 | -0.145437 | 5.5768952 |

**Table 1.2. Parameter Values for Equation 1.4<sup>16</sup>**

| $R_g$ | A         | B         | C         | D         |
|-------|-----------|-----------|-----------|-----------|
| 1.1   | 0.5882629 | 0.6007009 | 0.3872741 | -0.869822 |
| 1.5   | 0.6368360 | 0.6677381 | 0.3581836 | -1.496865 |
| 2.0   | 0.6686604 | 0.6973984 | 0.3218171 | -1.744691 |
| 5.1   | 0.72035   | 0.75128   | 0.26651   | -1.62091  |
| 10    | 0.7449932 | 0.7582943 | 0.2353042 | -1.683087 |

By modeling experimental feedback approach curves, the apparent kinetics of dynamic redox mechanisms such as diffusion-controlled, irreversible heterogeneous, and quasi-reversible mechanisms can be determined using solutions outlined in *Scanning Electrochemical Microscopy*.<sup>16</sup>

### 1.2.2.3 Variables to Consider

In the aforementioned experimental designs, four key components were briefly described: 1) the redox mediator, 2) the probe electrode, 3) the substrate, and 4) the solvent system. Preferred characteristics of the redox mediator of choice for generation-collection and feedback modes were briefly described, but initially one must consider if it would be beneficial to use an indirect redox mediator (*i.e.*, an electroactive molecule or atom intrinsic to the sample) or a direct redox mediator (*i.e.*, an electroactive molecule or atom that must be added to the sample). Ensure that the chosen mediator is chemically stable and inert in the chosen solvent system as well as in the presence of the chosen electrode material. While the same redox mediator may be used for multiple modes of SECM, particular mediators may be more or less ideal for particular modes



(*e.g.*, an indirect, reversible, one-electron redox mediator is most commonly used within feedback operational mode). General characteristics to consider are: solubility, hydrophilicity, lipophilicity, pH dependence, standard reduction potential, charge, photostability, thermal stability, and toxicity to the sample.<sup>11</sup> Many of these characteristics are liable to change depending on the chosen solvent system (*i.e.*, the choice of electrolyte and solvent). The electrolyte of choice and concentration of the electrolyte should decrease solution resistance, moreover the concentration of the electrolyte should be at least 100× that of the redox mediator in solution to decrease mass transfer effects. Furthermore, changes in electrolyte concentration must be considered when comparing acquired data. Additionally, the chosen solvent system dictates the potential window (*i.e.*, the voltage range versus a particular reference electrode in which no faradaic current is measured) feasible for an experiment.

Since SECM branched from STM in the late 1980s with the addition of ultramicroelectrodes, the probe and substrate electrodes should also be addressed. For the purpose of this dissertation, an ultramicroelectrode will be defined as a microdisk electrode with a diameter between 1 and 10 micrometers (*i.e.*,  $1\ \mu\text{m} < d \leq 10\ \mu\text{m}$ ). Microelectrodes were fabricated by Fleischmann and Wightman, independently, in the early 1980s as a means to measure current on the orders of  $10^{-17}$  A, decrease  $iR$  drop across an electrode surface, decrease capacitive charging currents, and increase the rate of mass transport to quickly obtain steady-state currents<sup>17</sup>; additionally, microelectrodes were essential to physiological measurements such as measurements made in a mammalian brain.<sup>18</sup> While current measured at an ultramicroelectrode is typically independent of  $R_g$ , the ultramicroelectrodes used in scanning electrochemical microscope experiments are beveled to a tip to increase radial diffusion to the electrode surface and maintain ease-of-use while scanning a substrate. Additionally,

ultramicroelectrodes are ideal for scanning probe microscopy as they are immune to convective effects since the flux of the redox mediator described by  $\sim DC^*/a$  is large.<sup>16</sup> Here, ultramicroelectrodes are disk-shaped electrodes, but other electrode geometries may be used such as hemispherical geometries. Additionally, geometric features such as recession or off-centered insulation may be used to achieve a desired signal.<sup>11</sup> Recently, the fabrication of nanoelectrodes ( $d \leq 1 \mu\text{m}$ ) has advanced our ability to reach the ultimate limit of detection in measurement science, the limit of detection of single entities.<sup>12, 19</sup> Lastly, the substrate of choice is typically determined based on the need for an insulating or conductive substrate or based on the sample of interest; for example, for the purpose of this dissertation the substrate is often a two-dimensional cell culture.

### **1.3 Examining Two-Dimensional Tissue Culture Systems via Scanning Electrochemical Microscopy**

The biological applications of SECM were apparent from the initial construction of the technique as it was non-invasive, non-destructive, and easily coupled with other analytical techniques for *in vitro* analysis of live-cells.<sup>11, 13, 20</sup> While SECM may be used to map the topography and redox activity of living cells, a nanoelectrode tip may be used to obtain intracellular measurements with minimal perturbation to cellular homeostasis.

#### **1.3.1 Practical Approaches to Scanning Electrochemical Microscopy of Two-Dimensional Tissue Cultures**

Live-cell imaging using SECM prompted the electrochemical study of physiological processes such as the detection of extra- and intra-cellular reactive oxygen species (ROS) and reactive nitrogen species (RNS).<sup>13</sup> Specifically, SECM serves as a non-invasive means to study cellular redox activity by determining the apparent rate of redox mediator regeneration by a living-cell substrate.<sup>11</sup> These experiments permit the study of biologically relevant redox

reactions that are necessary for cellular respiration, metabolism, and protein synthesis.<sup>11</sup> This is particularly important as changes in the external environment or disease state of a living-cell can prompt changes in the cellular redox state (*e.g.*, exposure to micropollutants such as perfluorooctane sulfonate induces the production of ROS<sup>21</sup>).

The first application of SECM to study living cells within a two-dimensional cell culture was accomplished by the Mirkin group in 2000, where the authors measured differences between normal and metastatic human breast cells.<sup>22</sup> Current-distance traces were used to determine the apparent rate of charge transfer across the cell membrane of individual cells on time scales less than one minute with the use of ultramicroelectrodes; moreover, fitting of experimental and theoretical approach curves can provide heterogeneous rate constants at the cell surface using previously established SECM theory.<sup>22, 23</sup> Imaging of two-dimensional cell cultures came shortly after with the electrochemical imaging of pH dependence<sup>24</sup> as well as normal and metastatic cells<sup>25</sup>. Typically, two-dimensional cell cultures are imaged electrochemically after the electrode tip is used to approach the cell surface. Based on the approach, cell height may be approximated when the approach is compared to a similar approach to the cell substrate following theoretical modeling; an example of this is provided in **Chapter 2**. In generation-collection mode, the flux of a species from the local cell surface can be quantified in real time, subsequently providing the concentration profile of the species near the cell surface. In feedback mode, the topography or electrochemical redox activity of the cell can be mapped based on the electrolysis current measured. Additionally, an image can be recorded at a constant separation distance from the cell dish surface (*i.e.*, constant-height imaging) or at a constant distance from the cell surface (*i.e.*, constant-distance imaging) as the probe scans in the lateral position. Constant-height imaging provides visualization of the topography and the redox activity of cells, and was demonstrated by

Feng and co-workers in 2003 when they imaged normal and metastatic human breast cells.<sup>25</sup> The challenges associated with constant-height imaging are variations in the electrochemical response of high-density areas of cells versus low-density (or well separated) areas of cells of the same type, changes in cell height (*i.e.*, topography), as well as the choice of an adequate tip-to-dish distance. Constant-height imaging is most useful when cells are all relatively the same height. Constant-distance imaging allows a user to deconvolute changes in electrochemical activity from changes in topography. Constant-distance imaging necessitates the use of constant-current or constant-impedance for precise control of the tip-to-cell distance.<sup>26</sup> Constant-current mode is typically only used in biological imaging when a sample has a large number of high and low features because it requires that only one detectable electroactive species be present in solution for precise control of the tip-to-cell distance, which is often difficult to maintain when imaging living samples.<sup>26</sup> While constant-current may provide higher contrast within resulting electrochemical images, constant-impedance allows the user to image topography and redox reactivity.<sup>26</sup>

Initially, amperometric imaging with an ultramicroelectrode was typical and used for a variety of applications such as detection of cellular activity, chemical release, drug efflux, and paracrine interactions.<sup>27</sup> When an ultramicroelectrode is used to electrochemically image a two-dimensional cell culture, a population of cells is analyzed simultaneously and the characteristics of a single cell are based on the average response of the group.<sup>13</sup> While this approach may elucidate heterogeneities among populations of cells, diffusional broadening would convolute the signal of adjacent single-cells as the diffusion profiles of the each individual cell and the electrode probe would be on the order of tens of micrometers. Nonetheless, investigators have determined ingenious ways to characterize single-cells using SECM; for example, by printing

cell adhesive protein on the surface of glass substrates, Matsue and co-workers were able to map oxygen profiles above patterned HeLa cells.<sup>28</sup> Today, nanoelectrode fabrication has provided investigators with the tools necessary to image single-cells with higher spatio-temporal resolution than provided by ultramicroelectrodes. Moreover, the fabrication of nanoelectrodes enabled intracellular studies with minimal perturbation to cellular homeostasis.<sup>12</sup> Various nanoelectrode fabrication procedures will be discussed in **Chapter 6**.

### 1.3.2 Mechanistic Insight

The goals of analysis by SECM are characterization of the topography of a sample and the redox activity of a sample. When designing an experiment, one must consider the objective of the experiment and select the key components (*i.e.*, the redox mediator, the solvent system, the electrode tip, and the substrate) based on the question under investigation. For example, when investigating oxygen consumption, one may choose to use a platinum electrode rather than a carbon electrode since oxygen reduction is easier on platinum (*i.e.*, reduction occurs at a less negative potential). Additionally, the outcome of electrochemical imaging will be heavily reliant on the possible redox pathways of the mediator of choice. Four general mechanisms within feedback operational mode are provided in **Figure 1.4**; each panel accounts for a situation in which characteristics of the redox mediator (such as charge, hydrophilicity, and permeability) must be considered when determining the mechanism responsible for the feedback provided. For example, in panel (A) of **Figure 1.4**, a hydrophilic mediator is present and cannot penetrate the cell membrane barrier; this scenario would elucidate a negative feedback result. Furthermore, mechanistic insight from a scanning electrochemical microscope experiment is provided when the characteristics of each experimental component are considered.

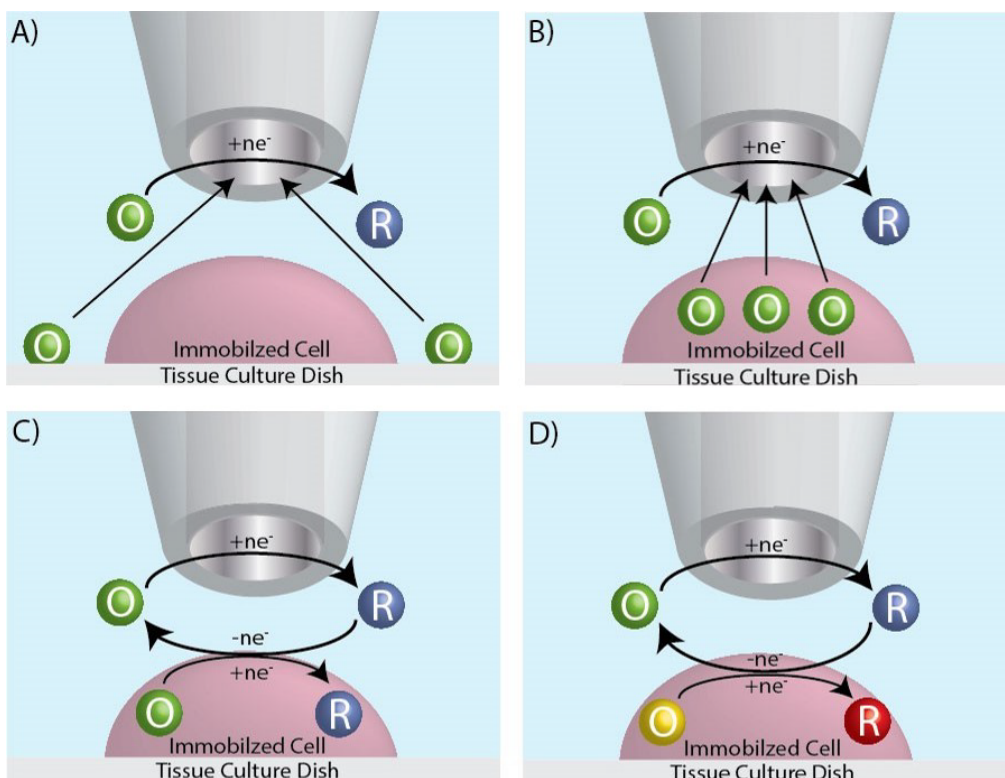


**Figure 1.4. SECM Feedback Mechanisms for Living Cells**

Schematic representations of the redox mechanisms for various mediators above living cells in feedback mode. (A) Representation of a hydrophilic mediator that cannot penetrate the cell membrane, resulting in negative feedback. (B) Representation of the redox pathway of a mediator readily available in the cell being expelled as it is reduced at the electrode surface, resulting in positive feedback. (C) Representation of electron transfer facilitated by a hydrophobic mediator, resulting in positive feedback. (D) Representation of bimolecular electron transfer facilitated by an intracellular electroactive species, resulting in positive feedback.

## REFERENCES

1. G. Binnig, H. Rohrer, C. Gerber and E. Weibel, *Physical Review Letters*, 1982, **49**, 57-61.
2. E. Meyer, H. J. Hug and R. Bennewitz, in *Scanning Probe Microscopy: The Lab on a Tip*, eds. E. Meyer, H. J. Hug and R. Bennewitz, Springer Berlin Heidelberg, Berlin, Heidelberg, 2004, pp. 1-13.
3. A. J. Bard, F. R. F. Fan, J. Kwak and O. Lev, *Analytical Chemistry*, 1989, **61**, 132-138.
4. H. Y. Liu, F. R. F. Fan, C. W. Lin and A. J. Bard, *Journal of the American Chemical Society*, 1986, **108**, 3838-3839.
5. O. Lev, F. R. Fan and A. J. Bard, *Journal of The Electrochemical Society*, 1988, **135**, 783-784.
6. O. E. Hüsser, D. H. Craston and A. J. Bard, *Journal of Vacuum Science & Technology B: Microelectronics Processing and Phenomena*, 1988, **6**, 1873-1876.
7. F. Fan Fu-Ren and J. Bard Allen, *Proceedings of the National Academy of Sciences*, 1999, **96**, 14222-14227.
8. A. J. Bard, X. Li and W. Zhan, *Biosensors & Bioelectronics*, 2006, **22**, 461-472.
9. R. C. Engstrom, M. Weber, D. J. Wunder, R. Burgess and S. Winkquist, *Analytical Chemistry*, 1986, **58**, 844-848.
10. R. C. Engstrom and C. M. Pharr, *Analytical Chemistry*, 1989, **61**, 1099A-1104A.
11. D. Polcari, P. Dauphin-Ducharme and J. Mauzeroll, *Chemical Reviews*, 2016, **116**, 13234-13278.
12. H. K. McCormick and J. E. Dick, *Analytical and Bioanalytical Chemistry*, 2021, **413**, 17-24.
13. H. J. Gwon, D. Lim and H. S. Ahn, *Bulletin of the Korean Chemical Society*, 2021, **42**, 1400-1410.
14. F. Fan Fu-Ren and J. Bard Allen, *Science*, 1995, **267**, 871-874.
15. C. Lefrou and R. Cornut, *Chemphyschem*, 2010, **11**, 547-556.
16. A. J. Bard and M. V. Mirkin, in *Scanning Electrochemical Microscopy*, eds. A. J. Bard and M. V. Mirkin, Taylor & Francis Group, LLC, Boca Raton, FL, 2 edn., 2012, ch. Theory, pp. 76-95.
17. M. Fleischmann and S. Pons, *Analytical Chemistry*, 1987, **59**, 1391A-1399A.

18. R. M. Wightman, *Analytical Chemistry*, 1981, **53**, 1125A-1134A.
19. S. Goines and J. E. Dick, *Journal of the Electrochemical Society*, 2019, **167**.
20. H. Shiku, T. Shiraishi, H. Ohya, T. Matsue, H. Abe, H. Hoshi and M. Kobayashi, *Analytical Chemistry*, 2001, **73**, 3751-3758.
21. X. Z. Hu and D. C. Hu, *Archives of Toxicology*, 2009, **83**, 851-861.
22. B. Liu, S. A. Rotenberg and M. V. Mirkin, *Proceedings of the National Academy of Sciences of the United States of America*, 2000, **97**, 9855-9860.
23. C. Wei, A. J. Bard and M. V. Mirkin, *The Journal of Physical Chemistry*, 1995, **99**, 16033-16042.
24. B. Liu, W. Cheng, S. A. Rotenberg and M. V. Mirkin, *Journal of Electroanalytical Chemistry*, 2001, **500**, 590-597.
25. W. Feng, S. A. Rotenberg and M. V. Mirkin, *Analytical Chemistry*, 2003, **75**, 4148-4154.
26. R. T. Kurulugama, D. O. Wipf, S. A. Takacs, S. Pongmayteegul, P. A. Garris and J. E. Baur, *Analytical Chemistry*, 2005, **77**, 1111-1117.
27. S. A. Rotenberg and M. V. Mirkin, *Journal of Mammary Gland Biology and Neoplasia*, 2004, **9**, 375-382.
28. M. Nishizawa, K. Takoh and T. Matsue, *Langmuir*, 2002, **18**, 3645-3649.



## Chapter 2 Methods

General methods, as well as troubleshooting suggestions, are specified in this chapter to assist researchers as they approach investigations similar to those featured in this dissertation. In later chapters, experimental methods specific to the featured results and discussions are provided for clarity.

### 2.1 Electrochemical Characterization of Small Molecules

When analyzing SECM results, preliminary mechanistic insight is derived from a rudimentary understanding of redox mediator characteristics.<sup>1</sup> For example, a researcher must consider the charge of the species and the species' potential to be oxidized or reduced. Electrochemical characterization of a redox active small molecule in bulk solution through voltammetry, amperometry, and electrolysis may reveal chemical and physical properties relevant to the mechanism under investigation.<sup>2</sup> General methods for the electrochemical characterization of small molecules as well as important considerations are detailed below. These methods are used in **Chapter 3** to characterize the redox mechanism of nicotinamide riboside.<sup>2</sup>

#### 2.1.1 Effect of Electrode Material

Heterogeneous redox mechanisms are characterized as inner-sphere or outer-sphere electrode reactions based on their interactions with the electrode surface within the Helmholtz layer (*i.e.*, the point of intersection between the electrode surface and the electrolyte where charge accumulates prior to electron transfer). Inner-sphere describes an electron-transfer reaction within the inner Helmholtz plane (IHP) that is facilitated by a strong interaction with the

electrode surface.<sup>3</sup> Specifically, within an inner-sphere electrode reaction, the reactant, intermediate, or product of the reaction adsorbs (or covalently bonds) to the electrode surface prior to electron-transfer (**Figure 2.1**); examples of inner-sphere electrode reactions are oxygen reduction in water and hydrogen oxidation at platinum working electrodes.<sup>4</sup> In many cases, these reactions involve the electron-transfer of multiple electrons, but this is not a requirement to classify a reaction as inner-sphere. Outer-sphere describes an electron-transfer reaction that is largely independent of the electrode material, and is instead dependent on electron tunneling.<sup>3</sup> In outer-sphere electrode reactions, electron-transfer occurs within the outer Helmholtz plane (OHP) at a distance equivalent to a single solvent layer from the electrode surface (**Figure 2.1**).<sup>3</sup> Here, it is important to note that an outer-sphere electrode reaction may depend on parameters dictated by the electrode material such as double-layer effects, material effects on the Helmholtz layer, or the distribution of electronic states at the electrode surface.<sup>4</sup> Nevertheless, outer-sphere electrode reactions are less reliant on electrode material; thus, to characterize inner-sphere versus outer-sphere electrode reactions, the working electrode material is exchanged between subsequent electrochemical measurements while other variables remain constant.

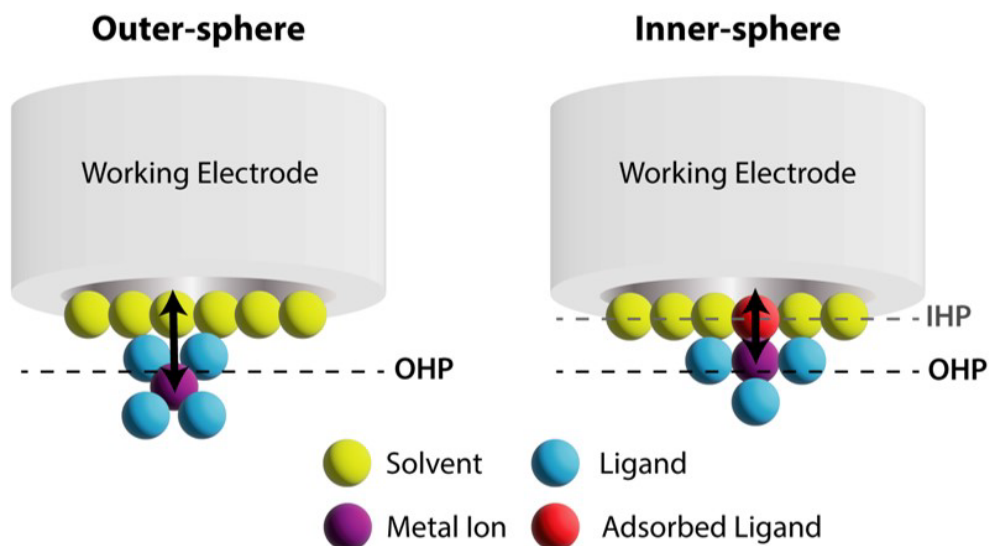


**Figure 2.1. Inner-sphere vs. Outer-sphere Electrode Reactions**

Illustration of heterogeneous mechanisms involving a solvated metal ion-ligand complex. In the outer-sphere reaction, electrons tunnel through a solvent layer within the outer Helmholtz plane (OHP) (solid line) for electron transfer. In the inner-sphere reaction, electrons are transferred (solid line) by interacting (*e.g.*, red adsorbed ligand) with the electrode surface within the inner Helmholtz plane (IHP).

To discern if a reaction is inner-sphere versus outer-sphere, we observed the effect of electrode material on cyclic voltammetry at macroelectrodes. When preparing the sample solution, we generally prepared the mediator in 1 mM quantities with  $\geq 250$  mM electrolyte. Generally, our electrolyte concentration is at least 100 $\times$  greater than the concentration of our analyte to reduce solution resistance and minimize mass transfer effects. Typically, 250 mM KCl was used as our aqueous electrolyte. If the concentration of the mediator was unknown, we adjusted the electrolyte concentration until an electrochemical signal was observed. Prior to collecting voltammograms, the sample solution was purged of oxygen for 10 to 15 minutes with an inert gas (*e.g.*, argon or nitrogen) to prevent competing reactions with dissolved oxygen in solution.

Cyclic voltammograms were collected using CH Instruments (Austin, TX) potentiostat models: 601E, 660D, and 920D. To reduce electronic noise, the potentiostat in use was grounded to a nearby ground of a wall outlet using a banana cable. Additionally, our electrochemical cells are often placed inside a grounded Faraday cage (*i.e.*, a container made of conductive material) to reduce electronic noise due to electromagnetic radiation emitted by nearby electronic devices and outlets. This cage is typically not necessary when using large macroelectrodes due to decreased sensitivity, but may be used out of an abundance of caution or if the measurement is particularly sensitive.

Voltammogram settings were specified in CH Instruments software, specific to the potentiostat in use, while purging the solution. The specified potential window (*i.e.*, High E to Low E) was based on the window of the working and reference electrodes in the electrolyte of choice. Typically, we determined this window based on the non-faradaic region of a cyclic voltammogram obtained in the solvent solution. The initial and final potentials were set to 0

Volts (V), while the scan polarity was set based on the expected redox activity of the sample (*i.e.*, negative if the mediator should be reduced or positive if the mediator should be oxidized in polarographic convention). If the redox activity was unknown, the scan polarity remained in the default setting (*i.e.*, negative in CH Instruments software). Later, based on the initial voltammetric response, the scan polarity was adjusted for accurate reproducibility. Additionally, the number of sweep segments was specified based on the number of scans necessary to obtain at least three complete voltammograms based on the potential window, initial and final potentials, and the scan polarity. The scan rate and sensitivity were specified based on the electrode size. For macroelectrodes, the scan rate and sensitivity were set between 0.1 to 0.3 Volts/seconds (V/s) and 1E-3 to 1E-6 Amperes/Volt (A/V), respectively. Lastly, the quiet time was set to 10 seconds. An example of the voltammogram settings used to characterize the small molecule, nicotinamide riboside, featured in **Chapter 3** are shown in **Figure 2.2**.

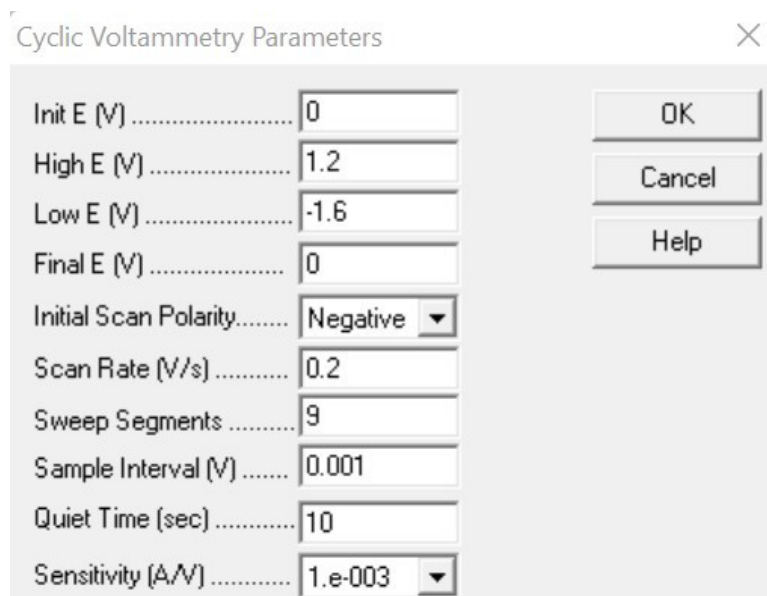


**Figure 2.2. Example Cyclic Voltammetry Settings**

Cyclic voltammetry settings used to obtain a voltammogram of nicotinamide riboside in KCl at a glassy carbon macroelectrode ( $r = 0.0015$  m) vs. Ag/AgCl.

Cyclic voltammetry was carried out using a three-electrode system (**Figure 2.3**) consisting of a macroelectrode, a Ag/AgCl (1 M KCl) reference electrode, and a counter electrode. Macroelectrodes and reference electrodes were purchased from CH Instruments (Austin, TX). Platinum foil and glassy carbon rods (Alfa Aesar) were generally used as counter electrodes. To characterize the effect of electrode material, glassy carbon ( $r = 0.0015$  m), gold ( $r = 0.001$  m), and platinum ( $r = 0.001$  m) macroelectrodes were used to collect voltammograms while blanketing the sample with inert gas.

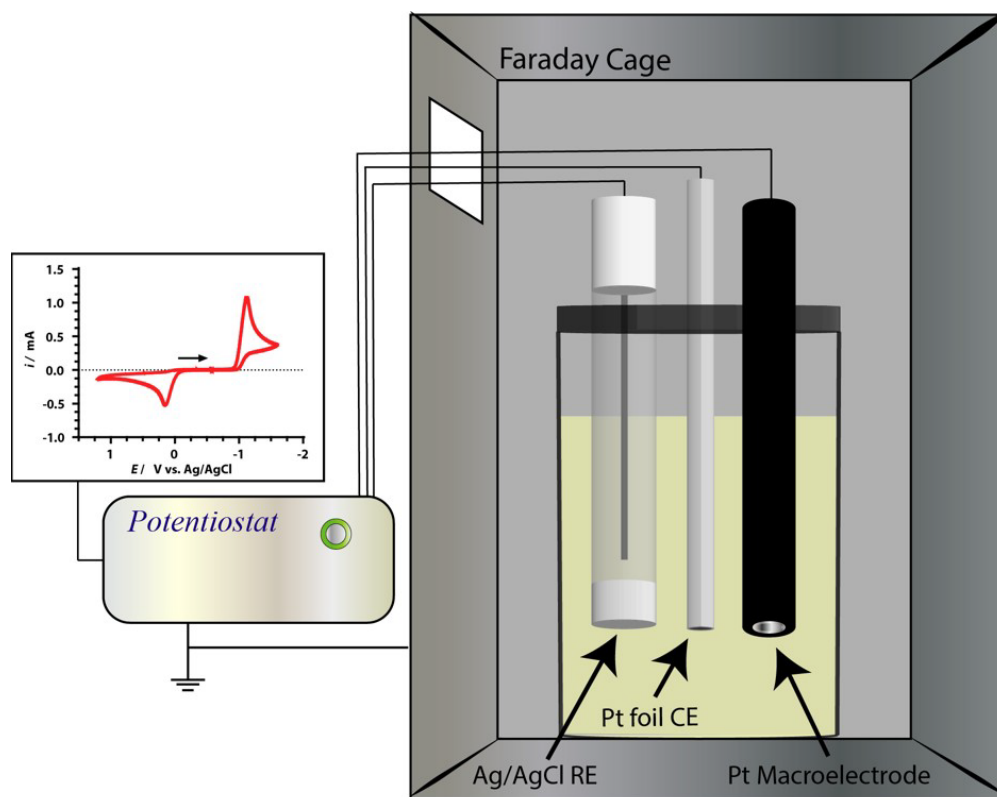


**Figure 2.3. Standard Three-Electrode System**

Schematic representation of the three-electrode system consisting of a macroelectrode, counter electrode (CE), and Ag/AgCl reference electrode (RE) in a redox mediator solution. This electrochemical cell is housed in a Faraday cage.



Voltammograms displaying significant shifts in redox potentials or variations in peak abundance (*i.e.*, the number of peaks) due to varying electrode material imply material facilitated electron-transfer (*i.e.*, an inner-sphere electrode reaction). Variations in peak height and shape were not immediately contributed to an inner-sphere electrode reaction since changing the electrode material may cause differences in the double-layer, the Helmholtz layer, or electronic states.<sup>4</sup> Additionally, peak height may vary based on electrode size; this is evident in the mathematical solution for voltammetry at macroelectrodes, the Randles–Ševčík equation (**Equation 2.1**), where peak current ( $i_p$ ) is directly proportional to the area of the electrode ( $A$ ).

$$i_p = 268,600 n^3 A D^{1/2} C v^{1/2} \quad \text{Equation 2.1}$$

In this equation,  $i_p$  is the peak current (A),  $n$  is the number of electrons transferred,  $A$  is the area of the electrode ( $\text{cm}^2$ ),  $D$  is the diffusion coefficient ( $\text{cm}^2 \text{s}^{-1}$ ),  $C$  is the concentration of the mediator ( $\text{mol cm}^{-3}$ ), and  $v$  is the scan rate (V/s) of the voltammogram. It is also important to note that the constant 268,600 ( $\text{C V}^{-1/2} \text{mol}^{-1}$ ) is the product of  $0.4463 \left(\frac{F^3}{RT}\right)^{1/2}$ , where  $R$  is the ideal gas constant  $8.314 \text{ (J mol}^{-1}\text{K}^{-1})$  and  $T$  is standard temperature at 298 K. Here, we preferred the use of macroelectrodes to observe obvious variations in peak potential, peak height, and peak abundance, but the use of microelectrodes may also elucidate subtle variations due to the electrode material. **Equation 2.2** is used to describe the limiting current in a cyclic voltammogram on a micro- or nano-electrode, where radial diffusion dominates opposed to lateral diffusion at a macroelectrode (**Figure 2.4**).

$$i_l = 4nFD C^* r \quad \text{Equation 2.2}$$

In **Equation 2.2**,  $i_l$  is the limiting current (A),  $n$  is the number of electrons transferred,  $F$  is Faraday's constant ( $96,485 \text{ C mol}^{-1}$ ),  $D$  is the diffusion coefficient of the redox couple ( $\text{cm}^2 \text{ s}^{-1}$ ),  $C^*$  is the concentration of the mediator ( $\text{mol cm}^{-3}$ ), and  $r$  is the radius of the electrode (cm). Note that a scan rate of  $0.05 \text{ V/s}$  and a sensitivity of  $1\text{E-}9 \text{ A/V}$  were typically used at micro- or nano-electrodes since a  $1 \text{ mM}$  solution yields a current of about  $1 \text{ nA}$ .

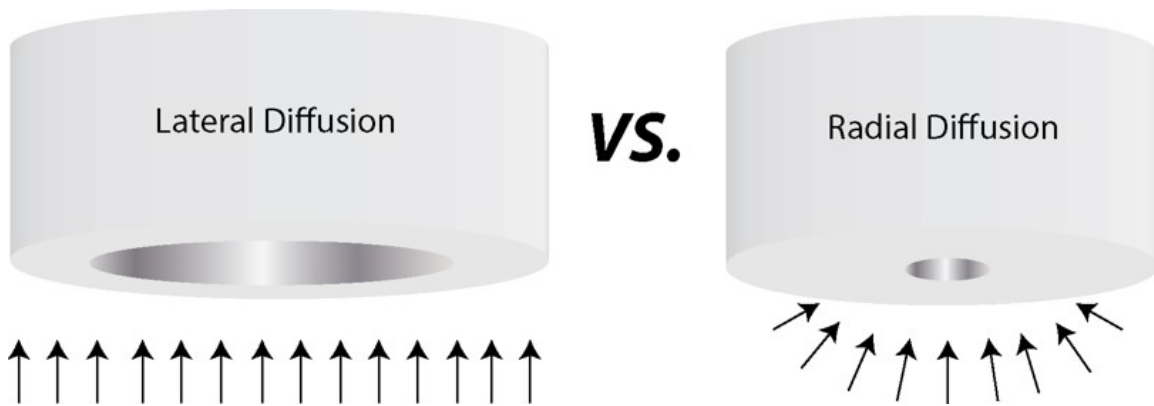


**Figure 2.4. Lateral vs. Radial Diffusion**

Schematic representation of lateral diffusion to a macroelectrode versus radial diffusion to a microelectrode.

### 2.1.2 Effect of pH

When electrochemically characterizing a small molecule, it is also important to make note of changes in pH. To investigate the effect of pH on the electrochemical response of a mediator, we prepared multiple sample solutions containing the same concentration of the mediator and the electrolyte, then varied the pH of the sample solutions using 1 M NaOH and 20% v/v HCl solutions. Cyclic voltammograms of each sample solution were obtained using a macro-disk working electrode, a glassy carbon rod counter electrode, and a Ag/AgCl (1 M KCl) reference electrode. Variations in peak height and peak abundance on resulting voltammograms suggested proton-coupled electron-transfer was feasible. To avoid changes in pH, we used a buffered electrolyte solution to prevent interfacial pH changes very near the electrode surface when applicable.

### 2.1.3 Determination of Diffusion Coefficient

Previously, inner-sphere versus outer-sphere electrode reactions were mentioned, with inner-sphere reactions being dependent on an interaction with the electrode surface and outer-sphere reactions being dependent on electron tunneling. Even in a quiescent solution, both inner-sphere and outer-sphere reactions may experience electrophoretic migration if the molecule of interest is charged and very little supporting electrolyte is used during voltammetry. The distinction between migration-controlled and diffusion-controlled reactions is often made by the procedure described in section **2.1.1 Effect of Electrode Material**, keeping in mind that variations in peak height and shape may be due to differences in the double layer, Helmholtz layer, or the distribution of electronic states between materials. Moreover, simply changing electrode material may not be sufficient if variations in redox potentials or peak abundance are not significant. An additional method of validation through cyclic voltammetry is collecting

voltammograms at various scan rates on one type of electrode material to determine if peak height scales linearly with respect to the square root of the scan rate ( $v^{\frac{1}{2}}$ ) based on the Randles–Ševčík equation (**Equation 2.1**); this relationship would confirm if a redox mechanism was a diffusion-controlled process (*i.e.*, an outer-sphere electrode reaction).<sup>5</sup>

Cyclic voltammograms were obtained at scan rates above and below 0.2 V/s. After obtaining voltammograms, peak current ( $i_p$ ) was graphed versus scan rate ( $v$ ) as well as versus  $v^{\frac{1}{2}}$ ; if the graph of  $i_p$  vs.  $v^{\frac{1}{2}}$  has greater linearity than the graph of  $i_p$  vs.  $v$ , then the redox mechanism is diffusion-controlled.

The diffusion coefficient of a redox couple is a physical parameter describing diffusion of a mediator towards the electrode surface. Specifically, the diffusion coefficient describes a gradient in the electrochemical potential of the mediator near the surface of the working electrode. Generally, this coefficient can be obtained by voltammetry using **Equation 2.1** for macroelectrodes (or **Equation 2.2** for micro- or nano-electrodes due to radial diffusion at smaller electrode surfaces), if the number of electrons transferred, mediator concentration, and electrode size are known. Unfortunately, when characterizing an unknown or an uncommon mediator, these characteristics are not common knowledge.

In 1991, Denuault and coworkers reported an electrochemical method using chronoamperometry for determining the diffusion coefficient when only the electrode radius is known.<sup>6</sup> It is important to note that this method is specific to the use of disk-shaped microelectrodes since the analytical solution for chronoamperometry at a microdisk microelectrode (**Equation 2.3**) dictates that the faradaic response is proportional to  $nAD^{\frac{1}{2}}C^*$  at short times and  $nADC^*$  at long times.

$$i_d(t) = \pi^{1/2} n F D^{1/2} C^* a^2 t^{-1/2} + 4 n F D C^* a \quad \text{Equation 2.3}$$

In **Equation 2.3**,  $n$  is the number of electrons transferred,  $F$  is Faraday's constant (96,485 C mol<sup>-1</sup>),  $D$  is the diffusion coefficient (cm<sup>2</sup> s<sup>-1</sup>),  $C^*$  is the concentration of the mediator (mol cm<sup>-3</sup>),  $a$  is the radius of the electrode (cm), and  $t$  is time (s). After normalizing **Equation 2.3** by the steady state current ( $i_{d,ss}$ ), **Equation 2.4** provides the normalized current as a function of  $\frac{1}{\sqrt{t}}$  allowing for direct determination of the diffusion coefficient by plotting  $\frac{i_d(t)}{i_{d,ss}}$  vs.  $\frac{1}{\sqrt{t}}$  with a y-intercept of 1; the slope of this function,  $S$ , may be used to determine the diffusion coefficient based on **Equation 2.5** if the electrode radius ( $a$ ) is known.<sup>6</sup> Due to the normalization, this practice yields diffusion coefficients without prior knowledge of number of electrons transferred or concentration.

$$\frac{i_d(t)}{i_{d,ss}} = (\pi^{1/2}/4) a (D t)^{-1/2} + 1 \quad \text{Equation 2.4}$$

$$D = \pi a^2 / 16 S^2 \quad \text{Equation 2.5}$$

The intercept of the plot may vary based on the time domain required for an accurate measurement. This is because at short times (*i.e.*, when the sample interval is  $\leq 100 \mu\text{s}$ ) semi-infinite linear diffusion dominates the diffusion of the redox couple to and from the microelectrode; this follows the Cottrell equation (**Equation 2.6**).

$$i(t) = i_d(t) = \frac{n F A D^{1/2} C^*}{\pi^{1/2} t^{1/2}} \quad \text{Equation 2.6}$$

At long times (*i.e.*, when the sample interval is  $\geq 10$  ms) hemispherical diffusion provides the steady-state current (*i.e.*, the last term in **Equation 2.3**). Moreover, diffusion coefficient determination through chronoamperometry is more accurate when using very short or long time intervals.<sup>6</sup> We found that at short times, the intercept was generally between 0.7 and 0.8, while at long times, the intercept was generally between 0.9 and 1.

Experimentally, the sample solution was made similar to that of section **2.1.1 Effect of Electrode Material**, where electrolyte is in excess to minimize mass transfer effects. Amperograms were collected with CH Instruments model 601E and 660D potentiostats, as well as with a three-electrode system consisting of a microelectrode in exchange for the macroelectrode featured in **Figure 2.3**. Additionally, the use of a microelectrode necessitated the use of a grounded Faraday cage to reduce electronic noise. This cage was grounded to the potentiostat in use, which was grounded to the ground of a nearby wall outlet.

Amperogram settings were input into CH Instruments software while purging the sample solution with inert gas for at least 5 minutes. The potential window (*i.e.*, the low potential to high potential) was based on the potential window of the redox mechanism under investigation (*e.g.*, for ferrocenemethanol,  $\text{FcCH}_2\text{OH}$ , oxidation the potential window would be set to +0.2 V to +0.5 V vs. Ag/AgCl). The initial potential and scan polarity were based on the potential window and the redox mechanism under investigation (*e.g.*, for  $\text{FcCH}_2\text{OH}$  oxidation the initial potential would be +0.2 V vs. Ag/AgCl and the initial scan polarity would be set to positive for oxidation). Generally, at least three to six steps were completed with a pulse width of 10 seconds. The sample interval was varied based on the desired time interval (*i.e.*, short, intermediate, or long time intervals). We generally collected chronoamperograms at 1 ms and 10 ms time intervals (*i.e.*, at intermediate to long time intervals). Lastly, the quiet time and sensitivity were generally

set to 10 seconds and  $1\text{E-}6$  A/V, respectively. An example of the chronoamperogram settings used to characterize the small molecule, nicotinamide riboside, featured in **Chapter 3** are shown in **Figure 2.5**.



Chronoamperometry Parameters ×

|                            |                                   |   |
|----------------------------|-----------------------------------|---|
| Init E (V) .....           | <input type="text" value="0"/>    | <input type="button" value="OK"/><br><input type="button" value="Cancel"/><br><input type="button" value="Help"/> |
| High E (V) .....           | <input type="text" value="0"/>    |   |
| Low E (V) .....            | <input type="text" value="-1.3"/> |   |
| Initial Step Polarity..... | Negative ▾                        |   |
| Number of Steps .....      | <input type="text" value="3"/>    |   |
| Pulse Width (sec) .....    | <input type="text" value="10"/>   |   |
| Sample Interval (sec) .... | <input type="text" value="0.01"/> |   |
| Quiet Time (sec) .....     | <input type="text" value="10"/>   |   |
| Sensitivity (A/V) .....    | 1.e-006 ▾                         |   |

Electrode 2

|                         |                                |                               |
|-------------------------|--------------------------------|-------------------------------|
| Potential (V) .....     | <input type="text" value="0"/> | <input type="checkbox"/> On   |
| Sensitivity (A/V) ..... | 1.e-006 ▾                      | <input type="checkbox"/> Step |

Auxiliary Signal Recording When Sample Interval >= 0.005 s

**Figure 2.5. Example Chronoamperogram Settings**

Chronoamperometry parameters used to obtain a chronoamperogram of nicotinamide riboside in KCl at a gold microelectrode ( $r = 6.25 \mu\text{m}$ ) vs. Ag/AgCl.

It is important to note that this method may also be used to determine the number of electrons transferred within single electron-transfer and multielectron-transfer mechanisms. Denuault and co-workers determined the number of electrons transferred for the multielectron-transfer oxidation of borohydride in water using **Equation 2.2** after determining the diffusion coefficient by chronoamperometry.<sup>6</sup>

#### **2.1.4 Determination of Electrons Transferred**

While the method described in section **2.1.3 Determination of Diffusion Coefficient** may be used to determine the number of electrons transferred if the concentration of the mediator is known, we made use of an alternate electrochemical method – square wave voltammetry – to determine the number of electrons transferred when characterizing an unknown or an uncommon mediator. Square wave voltammetry is a pulse voltammetry technique capable of background suppression and high sensitivity.<sup>7, 8</sup> Moreover, the technique is valued for its ability to characterize unknowns within complex matrices by isolating a single redox mechanism.<sup>9, 10</sup>

In this section, we used square wave voltammetry to approximate the number of electrons transferred without knowledge of the mediators' diffusion coefficient or concentration using the full width at half max (FWHM) based on the pulse amplitude. **Table 2.1** depicts the effect of pulse amplitude (*i.e.*,  $\Delta E$ ) on peak height, where  $(1 - \sigma) / (1 + \sigma)$  is the ratio of the peak height to the limiting value (*i.e.*, where  $\Delta E$  approaches zero).<sup>11</sup>

**Table 2.1. Effect of Pulse Amplitude on Peak Height<sup>11</sup>**

| $\Delta E$ , mV | $(1 - \sigma)/(1 + \sigma)$ |         |         |
|-----------------|-----------------------------|---------|---------|
|                 | $n = 1$                     | $n = 2$ | $n = 3$ |
| -10             | 0.0971                      | 0.193   | 0.285   |
| -50             | 0.453                       | 0.750   | 0.899   |
| -100            | 0.750                       | 0.960   | 0.995   |
| -150            | 0.899                       | 0.995   | —       |
| -200            | 0.960                       | —       | —       |

Additionally, **Equation 2.7** describes the FWHM ( $W_{1/2}$ ) as a function of  $\Delta E$ . When  $\Delta E$  approaches zero at 25 °C, the FWHM for  $n = 1, 2,$  and  $3$  is 90.4, 45.2, and 30.1 mV, respectively.<sup>11</sup>

$$W_{1/2} = \frac{3.52RT}{nF} \quad \text{Equation 2.7}$$

In **Equation 2.7**,  $R$  is the gas constant  $8.314 \text{ J K}^{-1} \text{ mol}^{-1}$ ,  $T$  is the temperature (K),  $n$  is the number of electrons transferred, and  $F$  is Faraday's constant ( $96,485 \text{ C mol}^{-1}$ ).

To determine the number of electrons transferred by square wave voltammetry, we dissolved the uncharacterized mediator in a solution of 1 mM FcCH<sub>2</sub>OH in 250 mM KCl. In its oxidized form, FcCH<sub>2</sub>OH is a blue-green color. Because this color was not observed, we surmised that no electron transfer reaction occurred between FcCH<sub>2</sub>OH and our molecule of interest. Here, FcCH<sub>2</sub>OH, a commonly used one-electron redox mediator, is used as a control. After purging the solution for at least 5 minutes with an inert gas, a voltammogram was obtained using a CH Instruments model 920D potentiostat and a three-electrode system containing a macroelectrode, a Ag/AgCl (1 M KCl) reference electrode, and a counter electrode. While purging the solution of oxygen, voltammogram settings were input into CH Instruments software. The initial and final potentials were selected based on the potential windows of the

mediators. Prior to this step, we always characterized the unknown mediator by cyclic voltammetry to determine the potential window of the redox mechanism with the three-electrode system and electrolyte in use. Generally, the increment potential was set to 1 mV, the amplitude was set to 1 mV, the frequency was set to 1 Hz, the quiet time was set to 10 seconds, and the sensitivity was set to 1E-5 A/V. An example of the voltammogram settings used to characterize the small molecule, nicotinamide riboside, featured in **Chapter 3** are shown in **Figure 2.6**.

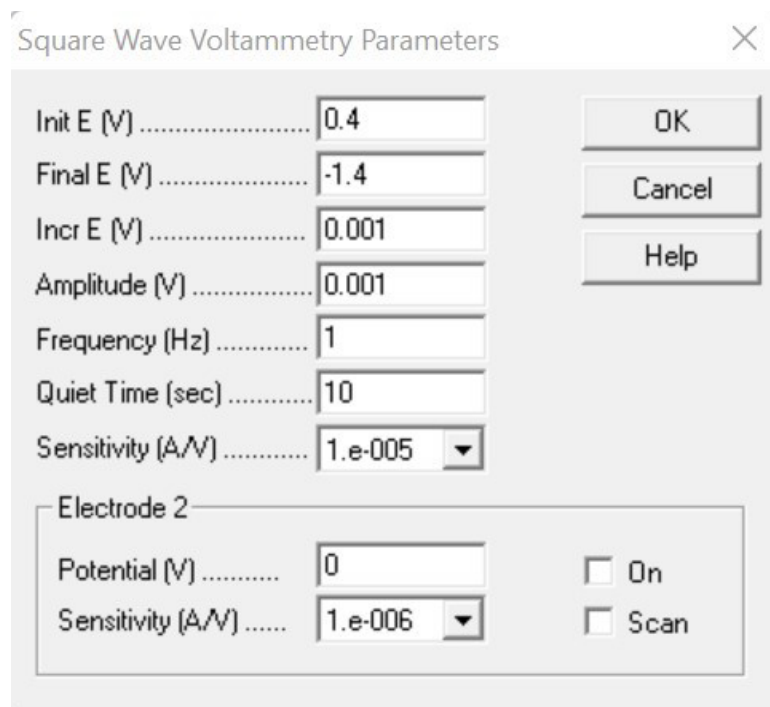


**Figure 2.6. Example Square Wave Voltammogram Settings**

Square wave voltammetry settings used to obtain a voltammogram of nicotinamide riboside and FcCH<sub>2</sub>OH in KCl at a glassy carbon macroelectrode ( $r = 0.0015$  m) vs. Ag/AgCl.

After obtaining the square wave voltammogram, the FWHM was used to approximate the number of electrons transferred. We compared the FWHM of FcCH<sub>2</sub>OH to the FWHM of the unknown. If the unknown was suspected to be a one-electron transfer redox species, the FWHM values were compared using a *t*-test.

### 2.1.5 Mechanistic Insight through Electrolysis

Lastly, additional mechanistic insight may be obtained following bulk electrolysis. This is necessary when two or more peaks are observed following reduction or oxidation of the mediator under investigation (*i.e.*, when two or more products are formed following the initial reduction or oxidation). Generally, we performed bulk electrolysis using a three-electrode system where the counter electrode is significantly larger than the working electrode (*e.g.*, the working electrode was typically a glassy carbon rod and the counter electrode was a platinum coil with much higher surface area). In addition to a large counter electrode, the electrodes were separated by a frit or a salt bridge to maintain charge balance. At the working electrode, the mediator was reduced or oxidized, while bubbling with an inert gas and stirring to facilitate mass transfer to the working electrode, using the potential of the initial redox peak determined through initial cyclic voltammetry. Normally, bulk electrolysis was performed in an electrolysis cell (**Figure 2.7**) until the current reached < 30% of the initial current. Next, cyclic voltammetry was used to reveal products of the homogeneous reaction that may have been formed during electrolysis. Cyclic voltammetry is a valuable diagnostic tool for elucidating redox mechanisms of heterogeneous reactions followed by homogeneous reactions in solution.<sup>12</sup> Finally, mass spectrometry analysis was used to determine the chemical structure of the products formed.



**Figure 2.7. Electrolysis Cell**

Custom glassware used to perform bulk electrolysis experiments.

## 2.2 Two-dimensional Tissue Culture

The experimental methods outlined in section 2.1 were used to characterize nicotinamide riboside<sup>2</sup>, which will be used later to analyze two-dimensional tissue cultures *via* SECM. Two-dimensional tissue culture was completed in-lab using the materials and methods detailed below.

### 2.2.1 Standard Operating Procedures

The following standard operating procedures were adapted from procedures provided by the Lineberger Tissue Culture Facility at the University of North Carolina at Chapel Hill in 2003.

The following tasks should be performed daily:

- Maintain incubator temperature and % CO<sub>2</sub> settings. The incubator was set to 37 °C and 5% CO<sub>2</sub>. If oxygen levels were maintained with nitrogen gas, oxygen was maintained at 10% O<sub>2</sub>. If abnormal fluctuations were observed in CO<sub>2</sub> levels, the CO<sub>2</sub> sensor should be calibrated using procedures outlined in the incubator manual and a Bluetooth CO<sub>2</sub> sensor. We used a Vernier Go Direct® CO<sub>2</sub> Gas Sensor.
- Disinfect work areas with 70% v/v ethanol before and after each use. Work areas include: surfaces inside hoods, hood sashes, pipetting devices, cabinet and drawer handles, door handles, the outside of centrifuges, and aspirator assemblies.
- Disinfect the interior of hoods with UV light for at least 1 hour following each use.
- Cover and/or close biohazardous waste after each use.
- Bleach aspirated biohazardous waste until colorless before discarding down the drain.

The following tasks should be performed weekly:

- Drain water baths and disinfect with 70% v/v ethanol before refilling with distilled water.
- Clean and disinfect interiors of centrifuges and rotators with 70% v/v ethanol.



- Autoclave biohazardous waste and replace waste bags in receptacles.

The following tasks should be performed monthly:

- Disinfect beneath hood work surfaces with 70% v/v ethanol. Specifically, disinfect the surface beneath the removeable interior hood surface.
- Mop laboratory floors. The Lineberger Tissue Culture Center at the University of North Carolina at Chapel Hill recommends using dilute hypochlorite (dilute bleach 1:500).
- Disinfect incubator interior and shelves with 70% v/v ethanol. Remove water in humidification pan. Disinfect pan with 70% v/v ethanol, then refill with autoclaved distilled water. The Lineberger Tissue Culture Center at the University of North Carolina at Chapel Hill recommends adding benzalkonium chloride (diluted to a 1% v/v working solution, 1:50 or 1: 100). Typically, we did not make any additions to autoclaved distilled water placed in the copper humidification pan of our incubator during this work. The metallic copper surface served well as an antimicrobial surface<sup>13</sup>; moreover, we recommend making the appropriate additions when using a stainless-steel lined incubator.

The following tasks should be performed annually:

- Hood recertification by an outside party.
- Replace CO<sub>2</sub> and N<sub>2</sub> gas lines to the incubator.

Additionally, hood users should refrain from storing items in the hood. Only items such as sterile micropipettes, pipette tips, and pipette racks for cell culture use may be stored in the hood, as well as a small supply of sterile cell culture vessels and centrifuge tubes. These items should not cover ventilation openings towards the back of the hood. We also suggest the use of

sterile, disposable, individually wrapped serological pipettes as well as sterile micropipette tips equipped with aerosol filters within hoods. These tasks and materials allowed us to maintain a clean working environment for tissue culture.

### **2.2.2 Reagents and Materials**

Initial cell line stock solutions were obtained from various sources. Adenocarcinoma (HeLa) cells were obtained from the Lineberger Tissue Culture Center at the University of North Carolina at Chapel Hill. Hepatocarcinoma (Hep G2) cells were obtained from the lab of Dr. Matthew Lockett at the University of North Carolina at Chapel Hill. Normal lung (MRC-5) cells and GFP-tagged human cytomegalovirus were obtained from the lab of Dr. Nathaniel Moorman at the University of North Carolina at Chapel Hill. Pancreatic (HPAC, HPNE dt, HPNE-myo free, and HPNE-KRAS) cells were obtained from the lab of Dr. Channing Der at the University of North Carolina at Chapel Hill. Lastly, osteosarcoma (U-2 OS) cells transfected with RFP-LC8 and GFP-H2A were obtained from the lab of Dr. Justin Leung at the University of Arkansas.

Frozen cells were kept at -80 °C in an ultra-low temperature freezer U725 Innova purchased from Eppendorf until needed. Additional materials were stored in a regular refrigerator and a -20 °C freezer. Cryovials and reagents were warmed using a Precision GP 150 water bath purchased from Thermo Fisher Scientific. Subculturing was performed in 1300 Series A2 Bio-safety hoods purchased from Thermo Fisher Scientific. Centrifugation was performed using a 5804 R centrifuge purchased from Eppendorf. Cells were initially inspected using a DMi1 inverted microscope purchased from Leica Microscope Systems. Cells were maintained within a HERAcell VIOS 160i CO<sub>2</sub> Incubator purchased from Thermo Fisher Scientific.

Cell media generally consisted of Dulbecco's Modified Eagle's Medium (DMEM) – high glucose (with 4500 mg L<sup>-1</sup> glucose, L-glutamine, sodium pyruvate, and sodium bicarbonate)

purchased from Sigma-Aldrich and Eagle's Minimum Essential Medium (EMEM) purchased from VWR International, LLC. Media supplements were purchased from a variety of vendors. Premium grade 100% fetal bovine serum (FBS) was purchased from VWR International, LLC. We purchased FBS in bulk based on the lot number to ensure reproducibility between cell cultures. 1 M HEPES buffer (sterile, pH 7.3) and penicillin-streptomycin were purchased from Sigma-Aldrich. Gibco™ Dulbecco's phosphate buffered saline (DPBS, 1X, no calcium, no magnesium, pH 7.4) and Gibco™ TrypLE Express were purchased from Thermo Fisher Scientific. Trypsin reagents were purchased from VWR International, LLC and Sigma-Aldrich. Cells were cultured in 15 cm-diameter, 10 cm-diameter, and 3.5 cm-diameter treated tissue culture dishes purchased from VWR International, LLC. These dishes were treated for optimal cell attachment with polymers such as poly-L-lysine. Occasionally, 6-well plates treated for optimal attachment were used in replace of 3.5 cm-diameter dishes. These plates were also purchased from VWR International, LLC and Sigma-Aldrich. Sterile, disposable, individually-wrapped serological pipettes (5 mL, 10 mL, 25 mL, and 50 mL) were purchased from Sigma-Aldrich as well as sterile Corning 15 mL and 50 mL centrifuge tubes. Cryovials were purchased from VWR International, LLC. When cell culture reagents and materials were needed immediately, they were purchased from the Lineberger Tissue Culture Facility at the University of North Carolina at Chapel Hill.

For fluorescence imaging, 2',7'-dichlorofluorescein diacetate (DCF-DA,  $\geq 97\%$ ) and monochlorobimane (MBCl,  $\geq 70\%$ ) were purchased from Sigma-Aldrich. CellROX™ Orange Reagent was purchased from Thermo Fisher Scientific. Glutathione (GSH) and superoxide dismutase 1 inhibitor (SOD1 inhibitor, LCS-1) were purchased from Sigma-Aldrich. Dimethyl sulfoxide (DMSO) was purchased from VWR International, LLC. Hoechst was purchased as a

powder, bisbenzimidazole H 33258, from Sigma-Aldrich. All reagents were used without further purification.

The following subculturing procedures were adapted from the American Type Culture Collection. The volumes used in these procedures are specific to the use of 10 cm-diameter tissue culture dishes. Please refer to **Table 2.2** to adjust volumes if an alternative culture vessel is being used.

**Table 2.2. Working Volumes for Tissue Culture Vessels**

| Culture Vessel       | Volume of Media (mL) | Volume of Trypsin (mL) | Effective Growth Area (cm <sup>2</sup> ) |
|----------------------|----------------------|------------------------|--|
| 3.5 cm-diameter dish | 2.5-3.0              | 0.5-1.5                | 9.6                                      |
| 10 cm-diameter dish  | 16.0-17.5            | 3.0-6.0                | 78.5                                     |
| 15 cm-diameter dish  | 45.0-50.0            | 6.0-10                 | 176.6                                    |
| 6-well plate         | 2.5-3.0              | 0.5-1.5                | 9.6                                      |
| T-25 flask           | 8.0-9.0              | 0.5-1.5                | 25                                       |
| T-75 flask           | 20-30                | 3.0-6.0                | 75                                       |

\*Total volume of Trypsin or TrypLE solution based on the culture vessel. Trypsin or TrypLE Express dilutions may vary based on cell type.

In addition, the cell lines examined throughout this dissertation are adherent lines (*i.e.*, these lines attach to surfaces). This characteristic is ideal for scanning probe microscopy.

Cell culture media and 1 M HEPES buffer were stored in the refrigerator. Penicillin-streptomycin, trypsin, and FBS were stored in the -20 °C freezer. These reagents were warmed in a 37 °C water bath prior to use.

### 2.2.3 Adenocarcinoma (HeLa) Cells

HeLa cells are human epithelial cells that once lined the uterus and cervix. They are characterized by the disease state adenocarcinoma, which is a form of cancer that develops within tissue lining organs. These cells are classified as bio-safety level 2, which means they are moderately hazardous. Moreover, any procedures that may cause exposure through aerosols or splashes should be performed in a hood.

HeLa cells were maintained using EMEM supplemented with 10% v/v FBS and 1% v/v penicillin-streptomycin (*i.e.*, full growth media). Prior to handling cells, cells were inspected using an inverted microscope. Full growth media was replaced every 2 to 3 days using the procedure outlined below in section **2.2.8 Media Renewal**.

Once cells reached medium to high density (65% to 85% confluence), cells were passaged (or split). For subculturing, spent media (*i.e.*, media currently being used by the cells) was aspirated from the dish. The cells were rinsed with 3 mL 0.05% w/v Trypsin-0.53 mM EDTA. After aspirating the rinse, 3 mL 0.05% w/v Trypsin-0.53 mM EDTA was added to the dish and the dish was placed in the incubator for 5 to 10 minutes. This incubation facilitated the suspension of the cells through trypsinization. We limited exposure to Trypsin to up to 10 minutes; longer incubations may contribute to changes in cell morphology and viability. Generally, the incubation was monitored using an inverted microscope until the cell layer was dispersed or cells were spherical in shape. Next, 9 mL full growth media was added to the dish to halt trypsinization (*i.e.*, FBS in full growth media inactivates Trypsin); we typically added media up to 3× the volume of added trypsin to stop trypsinization. If cells were not visibly dispersed, full growth media was pipetted directly above the dish to detach cells. To passage cells, the suspension was divided among new tissue culture vessels. If the total volume of the suspension was placed in one new vessel, we referred to this as a 1:1 split. If the total volume was divided equally between two new vessels, we referred to this as a 1:2 split, and so on. Next, the new tissue culture vessels were filled to their total working volumes using full growth media. The new vessels were labeled: HeLa, P# (*i.e.*, an updated passage number based on the previous plate; for example, P14 is updated to P15), the date, and the scientist's initials. Finally, the new tissue culture vessels were placed in the incubator.

#### 2.2.4 Hepatocarcinoma (Hep G2) Cells

Hep G2 cells (**Figure 2.8**) are human epithelial cells that once lined the human liver. Specifically, these cells are characterized by carcinoma, a common form of cancer that develops in the tissue of skin or internal organs. Hep G2 cells are classified as bio-safety level 1, which means they are minimally hazardous and do not generally cause disease in healthy adults. In other words, these cells can be handled on an open lab bench.

Hep G2 cells were maintained using DMEM – high glucose supplemented with 10% v/v FBS, 2.5% v/v 1 M HEPES buffer, and 1% v/v penicillin-streptomycin (*i.e.*, full growth media). Prior to handling cells, cells were inspected using an inverted microscope. Full growth media was replaced every 3 days using the procedure outlined below in section **2.2.8 Media Renewal**.

Once cells reached medium density (50% to 65% confluence), cells were passaged (or split). We avoided allowing Hep G2 cells to grow over 85% confluence because at high density, we observed changes in cell morphology that had the potential to propagate to new vessels after passaging. For subculturing, spent media was aspirated from the dish. The cells were rinsed with 5 mL DPBS. Next, a 2:1 mixture of DPBS to TrypLE Express was added to the dish; generally, 4 mL DPBS to 2 mL TrypLE Express was added to a 10 cm-diameter culture dish. The dish was placed in the incubator for 5 to 10 minutes to facilitate trypsinization. We limited exposure to dilute TrypLE Express to 5 to 6 minutes to avoid changes in cell morphology and viability. Trypsinization was monitored using an inverted microscope until cells became spherical in morphology (**Figure 2.9**) or suspended.

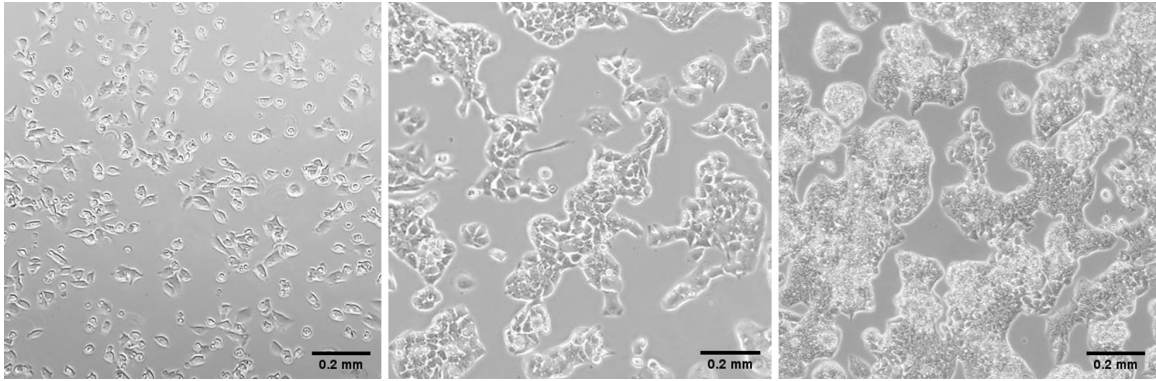


**Figure 2.8. Hep G2 Morphology**

Hep G2 P18 cells at 25% confluence (low density), Hep G2 P16 cells at 65% confluence (medium density), and Hep G2 cells at 80% confluence (high density).

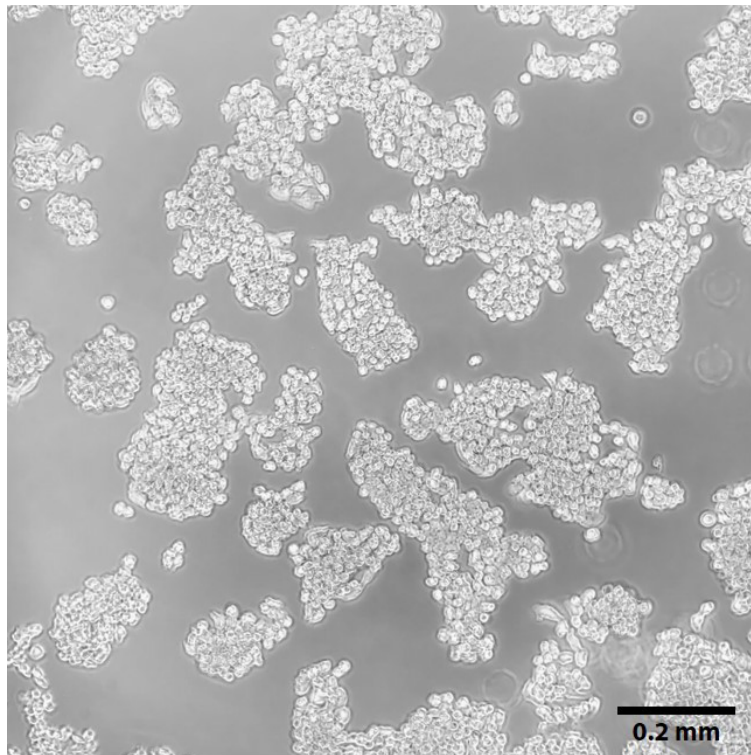


**Figure 2.9. Hep G2 Morphology following Trypsinization**

Hep G2 P21 spherical cell morphology following 5-minute exposure to 2:1 DPBS to TrypLE Express.



Cells that appeared adherent, but spherical in shape, were dislodged from the dish by tapping the side and/or bottom of the dish (or by washing the dish surface during the next step). Next, 9 mL full growth media was added to the dish to halt trypsinization. The resulting cell suspension was centrifuged at 1000 rpm for 5 minutes at room temperature, then cells were resuspended in 1 mL full growth media. To passage cells, this suspension is divided among new, labeled tissue culture vessels to be placed in the incubator.

### **2.2.5 Normal Lung (MRC-5) Cells**

MRC-5 cells (**Figure 2.10**) are normal human lung cells. These cells have a fibroblast morphology (*i.e.*, they are stringy and elongated in shape). Additionally, they are classified as bio-safety level 1. It is also important to note that the growth of this particular cell line is contact inhibited. Moreover, these cells should be passed (*i.e.*, subcultured or split) at high density (*i.e.*,  $\geq 85\%$  confluence).

MRC-5 cells were maintained using DMEM – high glucose supplemented with 10% v/v FBS and 1% v/v penicillin-streptomycin (*i.e.*, full growth media). Prior to handling cells, cells were inspected using an inverted microscope. Full growth media was replaced every 3 to 4 days using the procedure outlined below in section **2.2.8 Media Renewal**.

For subculturing, spent media was aspirated from the dish. The cells were rinsed with 5 mL DPBS. Next, 3 to 5 mL 0.05% Trypsin-EDTA (1X) was added to the dish. The dish was placed in the incubator for 5 minutes to facilitate trypsinization. Again, incubations longer than 10 minutes may contribute to changes in cell morphology and viability. Trypsinization was monitored using an inverted microscope until cells became suspended. At high density, cells suspended in solution should be visible with the eyes due to cell size. Next, 7 to 9 mL full growth media was added to the dish. To passage cells, this suspension was divided among new

tissue culture vessels and these vessels were labeled accordingly. This step is essential when subculturing normal cell lines with a limited number of passages prior to changes in morphology or viability due to age. Lastly, the new tissue culture vessels were placed in the incubator.

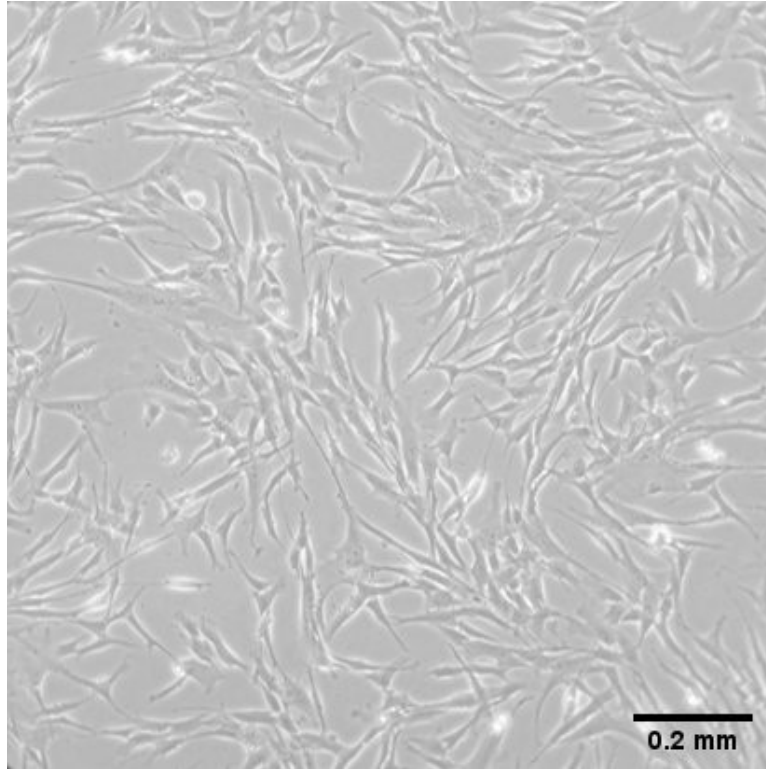


**Figure 2.10. MRC-5 Morphology**

MRC-5 P16 cells at 50% confluence.

### 2.2.6 Pancreatic (HPAC, HPNE dt, HPNE-myo free, and HPNE-KRAS) Cells

HPNE dt and HPNE-myo free are immortalized, normal, human epithelial cells that once lined the pancreas, while HPNE-KRAS cells are HPNE cells that have been modified to express the KRAS mutation specific to pre-cancerous pancreatic cells. These two lines are classified as bio-safety level 2 due to these modifications. Additionally, HPNE cells share similar morphology and are not identifiable based on cell shape (**Figure 2.11**). HPAC cells (**Figure 2.12**) are adenocarcinoma, human epithelial cells that once lined the pancreas. HPAC cells are classified as bio-safety level 1.

All pancreatic cell lines were maintained using DMEM – high glucose supplemented with 10% v/v FBS and 1% v/v penicillin-streptomycin (*i.e.*, full growth media). Prior to handling cells, cells were inspected using an inverted microscope. Full growth media was replaced every 3 to 4 days using the procedure outlined below in section **2.2.8 Media Renewal**. Additionally, the following subculturing procedure was followed for each pancreatic cell line.

For subculturing, spent media was aspirated from the dish and the cells were rinsed with 0.25% Trypsin-2.21 mM EDTA to remove traces of FBS that may inhibit trypsinization. Next, 3 to 5 mL 0.25% Trypsin-2.21 mM EDTA was added to the dish before placing the dish in the incubator for 5 to 10 minutes to facilitate trypsinization. Trypsinization was monitored using an inverted microscope until cells became spherical in morphology or suspended. To inhibit trypsinization, 7 to 9 mL full growth media was added to the dish. This suspension was centrifuged at 1000 rpm for 5 minutes at room temperature. Following centrifugation, the supernatant was aspirated and cells were resuspended in 1 mL full growth media. To passage cells, this suspension was divided among new tissue culture vessels and these vessels were labeled accordingly before being placed in the incubator.

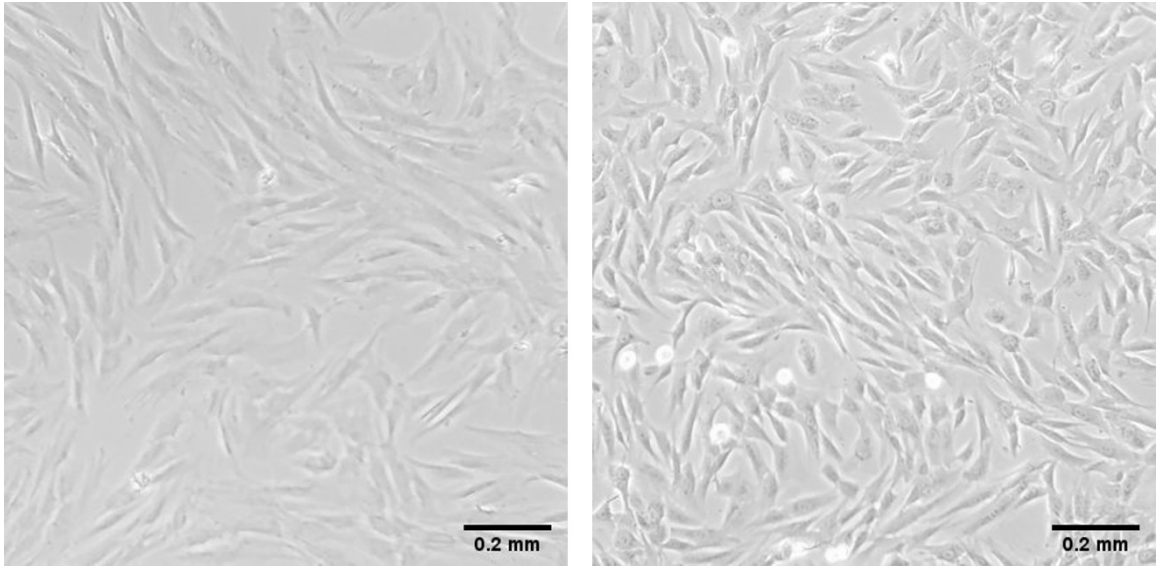


**Figure 2.11. HPNE Morphology**

HPNE dt cells at 70% confluence (medium to high density) and HPNE-KRAS cells at 95% confluence (high density).

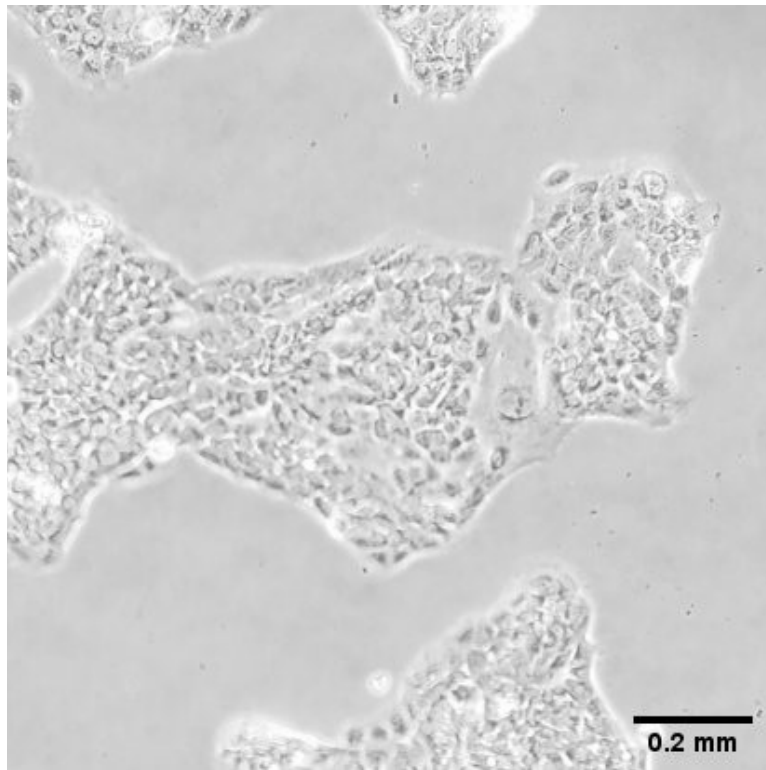


**Figure 2.12. HPAC Morphology**

HPAC cells at 50% confluence (medium density).

### 2.2.7 Osteosarcoma (U-2 OS) Cells

U-2 OS cells (**Figure 2.13**) are human epithelial cells from the bone. These are specifically osteosarcoma cells (*i.e.*, cancerous cells that were once osteoblasts, which are cells that form bone tissue). U-2 OS cells are classified as bio-safety level 1. Additionally, these cells were previously transfected to express GFP-H2A and RFP-LC8; fluorescence intensity decreased after frequent subculturing and freezing cycles.

U-2 OS cells were maintained using DMEM – high glucose supplemented with 10% v/v FBS and 1% v/v penicillin-streptomycin (*i.e.*, full growth media). Prior to handling cells, cells were inspected using an inverted microscope. Full growth media was replaced every 2 to 3 days using the procedure outlined below in section **2.2.8 Media Renewal**.

For subculturing, spent media was aspirated from the dish and the cells were rinsed with 0.25% Trypsin-2.21 mM EDTA to remove traces of FBS that may inhibit trypsinization. Next, 3 to 5 mL 0.25% Trypsin-2.21 mM EDTA was added to the dish before placing the dish in the incubator for 5 to 10 minutes to facilitate trypsinization. Trypsinization was monitored using an inverted microscope until cells became spherical in morphology or suspended. To inhibit trypsinization, 7 to 9 mL full growth media was added to the dish. To passage cells, this suspension was divided among new tissue culture vessels and these vessels were labeled accordingly. Lastly, the new tissue culture vessels were placed in the incubator.

While centrifugation (at 1000 rpm at room temperature for 5 minutes) following trypsinization is not recommended in each subculturing procedure above, we commonly used this step to remove trypsin following suspension of cells if variations in cell morphology or viability were frequently observed between passages.

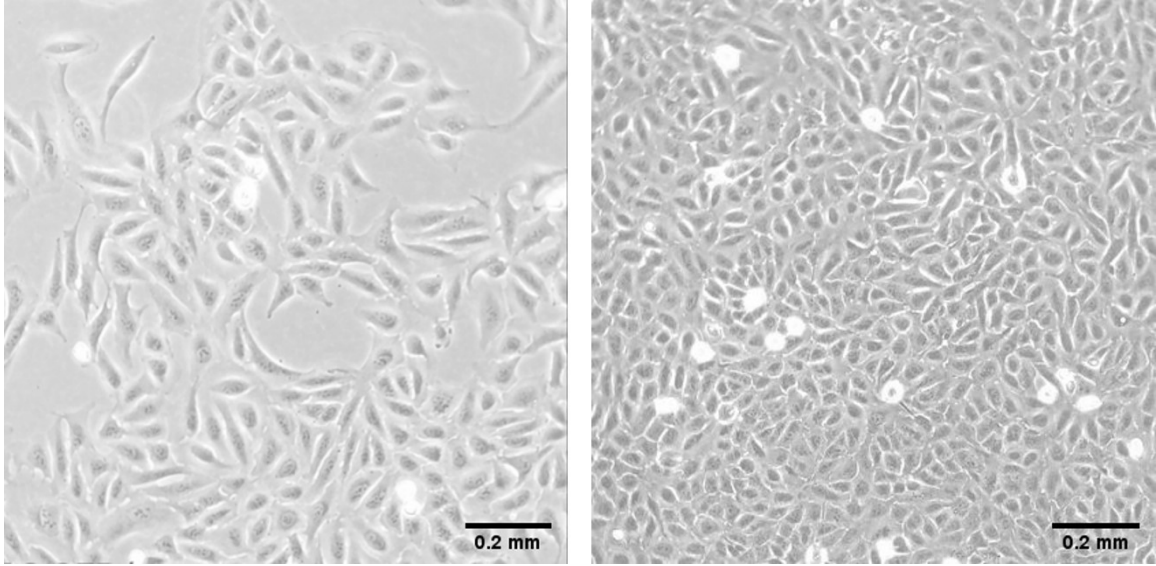


**Figure 2.13. U-2 OS Morphology**

U-2 OS cells at 70% confluence (high density) and 100% confluence (high density). These cells were previously transfected with RFP-LC8 and GFP-H2A.



### **2.2.8 Media Renewal**

Prior to handling cells, cells were inspected using an inverted microscope. If cells were too low density for use, full growth media was replaced as needed based on the subculturing procedures above. To renew media, spent media was aspirated from the dish, before rinsing cells with 5 mL DPBS once. An additional rinse was done if a large portion of cells were suspended during the initial inspection. After aspirating the rinse solution, 16 mL full growth media was added to the dish before placing it in the incubator.

### **2.2.9 Cell Counting & Viability**

Cells may be counted prior to being split amongst new culture vessels. We did this often when preparing samples of a specific density prior to experimentation. Prior to counting cells, we centrifuged suspended cells at 1000 rpm at room temperature for 5 minutes after inhibiting trypsinization. Next, the cell pellet was resuspended in 1 mL full growth media. Cells were counted using an automated Corning Cell Counter purchased from CytoSMART Technologies, LLC (Skillman, NJ). After resuspending the cells, 10  $\mu$ L of the cell suspension was loaded onto a counting chamber provided with the counter by holding a cover slip on the top side of the counting chamber (*i.e.*, the side with loading wells) while loading the suspension with a micropipette. Once the Corning Cell Counter is connected to a desktop or laptop through a USB 3.0 port, the CytoSMART application is opened and a project and experiment name are created. Next, the counting chamber is placed onto the counter and an average cell concentration (*i.e.*, results are provided in units of cells  $\text{mL}^{-1}$ ) is calculated by the software by collecting at least three images with the counter.

The counter may also provide viability information if the 1 mL cell suspension is mixed with 1 mL Trypan Blue (*i.e.*, a viability stain able to penetrate the damaged cell membranes of

dead cells). Cell viability assessments were completed with Trypan Blue purchased from VWR International, LLC. We performed viability assessments immediately following Trypan Blue additions to avoid variations to viability due to exposure.<sup>14, 15</sup>

### **2.2.10 Cryopreservation & Thawing**

Cryopreservation is the preservation of biological entities such as organelles, cells, and tissues by gradually cooling samples to low or freezing temperatures for later use.<sup>16</sup> For cryopreservation of adherent cells, cells were detached from the cell culture vessel using Trypsin or TrypLE Express as directed in the subculturing procedures above and counted as described in section **2.2.9 Cell Counting & Viability**. After counting the cells, the 1 mL suspension is centrifuged at 1000 rpm at room temperature for 5 minutes once more. Here, it is important to note that cells should be frozen at a concentration of  $1 \times 10^6$  to  $1 \times 10^7$  cells mL<sup>-1</sup>. Based on the cell concentration, the cell pellet is resuspended in the appropriate concentration of freezing media (*i.e.*, 95% v/v full growth media to 5% v/v DMSO) prior to delivering 1 mL aliquots to individual cryovials. If the concentration of cells was  $< 1 \times 10^6$  cells mL<sup>-1</sup>, we centrifuged the suspension at 1000 rpm at room temperature for 5 minutes before resuspending the cells in full growth media to place them in a new cell culture vessel to continue cell proliferation. To progressively freeze the cells, the cryovials were placed in a 4 °C refrigerator for 5 to 15 minutes, then placed in a Styrofoam box within a -80 °C freezer. After 24 hours, the cryovials were removed from the Styrofoam box and placed directly in the -80 °C freezer.

To thaw cells following cryopreservation, we initially warmed the water bath to 37 °C. After removing a cryovial from the -80 °C freezer, we gently swirled the vial in the water bath to thaw the frozen cells. Next, the vial was disinfected with 70% v/v ethanol before placing it in the bio-safety hood. The cells were poured directly in a 10 cm-diameter cell culture dish and 15 mL

full growth media, specific to the cell line, was added to the dish. The dish was labeled with the cell line, passage number, date, and the scientist's initials. The dish was placed in the incubator and the cells were incubated an appropriate amount of time for adherence to the dish. Cells were given at least 4 hours to adhere, but typically we allowed 24 hours for trypsinized cells to recover surface proteins and adhere.<sup>17</sup> After allowing cells to adhere to the dish, the cells were inspected using an inverted microscope. If the cells were < 50% confluent, media was replaced according to the procedure in section **2.2.8 Media Renewal**. If the cells were > 65 to 75% confluent, the cells were passaged based on the subculturing procedures in sections **2.2.3** through **2.2.7**.

## **2.3 General Fluorescence Staining & Loading**

### **2.3.1 Hoechst Staining**

Hoechst is a cell-permeant, nucleic acid stain that may pass through the plasma membrane of living and fixed cells to bind to double stranded-DNA within nuclei to fluoresce blue ( $\lambda_{ex}/\lambda_{em}$  340/510 nm).<sup>18</sup> This stain has the ability to propagate through a cell culture during growth and subculturing.

Hoechst was purchased as a powder; the powder was used to prepare a 1 mg mL<sup>-1</sup> stock solution in ultrapure water. This stock solution was separated into 100  $\mu$ L aliquots. These aliquots were covered using foil and maintained in the -20 °C freezer. Prior to use, we diluted the 1 mg mL<sup>-1</sup> aliquots to a 10 mL solution of 10  $\mu$ g mL<sup>-1</sup> in DPBS.

To stain cells, we initially aspirated spent full growth media and rinsed cells with DPBS once. After aspirating the rinse, the cell culture vessel was charged with enough Hoechst stain solution to coat the bottom of the vessel. Here, we used the highest suggested volume of trypsin from **Table 2.2**. Next, we covered the cell culture vessel with foil and placed the vessel on a rotator plate generally set to 10 to 15 rpm. The cells were allowed to incubate in the stain on the

plate at room temperature for at least 10 minutes. Following the incubation, the staining solution was aspirated from the vessel and the cells were rinsed with DPBS. After aspirating the rinse, full growth media was added to the vessel based on the suggested volume of media in **Table 2.2** and the cells were placed in the incubator for later use. Cells stained with Hoechst nuclear stain may be imaged using a standard DAPI (*i.e.*, 4',6-diamidino-2-phenylindole) filter cube. The filter cube is named for a fluorescent stain used to image nuclear DNA in living and fixed cells.<sup>19</sup> **Figure 2.14** is a bright field/fluorescence image overlay of Hep G2 P13 cells stained with Hoechst nuclear stain captured using a Leica DMI8 inverted microscope, a standard DAPI filter cube, and a digital CMOS camera.

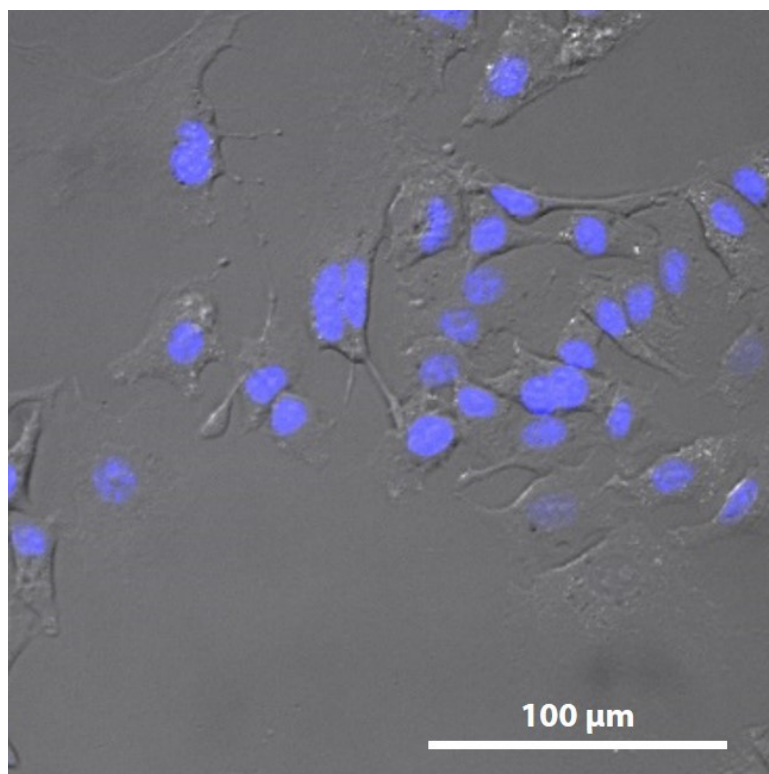


**Figure 2.14. Hoechst Nuclear Stain**

Bright field/fluorescence image overlay of Hep G2 P13 cells stained with  $10 \mu\text{g mL}^{-1}$  Hoechst nuclear stain in DPBS for 10 minutes at room temperature at 15 rpm. Image false colored for visual representation.

### 2.3.2 CellROX™ Orange Staining

CellROX™ Orange Reagent is a cell-permeant, fluorogenic probe for gauging oxidative stress within living cells. Upon oxidation by reactive oxygen species (ROS) in the cell, the reagent fluoresces orange ( $\lambda_{ex}/\lambda_{em}$  545/565 nm). The reagent was packaged in vials as a ready-to-use DMSO solution. These vials were maintained in a desiccator protected from light in the -20 °C freezer.

To stain cells, the 2.5 mM ready-to-use DMSO solution was diluted to 5  $\mu$ M with DPBS by combining 12  $\mu$ L of the stock solution with 5.9 mL DPBS. Next, spent full growth media was removed from the cells and the cells were rinsed with DPBS. After aspirating the rinse, the cell culture vessel was charged with enough 5  $\mu$ M CellROX™ Orange in DPBS solution to coat the bottom of the vessel. Here, we used the highest suggested volume of trypsin from **Table 2.2**. The vessel was placed in the incubator to incubate cells for 30 minutes. Following incubation, the reagent was removed from the vessel and the cells were rinsed with DPBS three times. After aspirating the rinse, full growth media was added to the vessel based on the suggested volume of media in **Table 2.2** and the cells were placed in the incubator for later use. Cells stained with CellROX™ Orange Reagent may be imaged using a standard TXR (*i.e.*, Texas Red) filter cube. **Figure 2.15** is a fluorescence image of Hep G2 P18 cells stained with CellROX™ Orange Reagent captured using a Leica DMI8 inverted microscope, a standard TXR filter cube, and a digital CMOS camera.

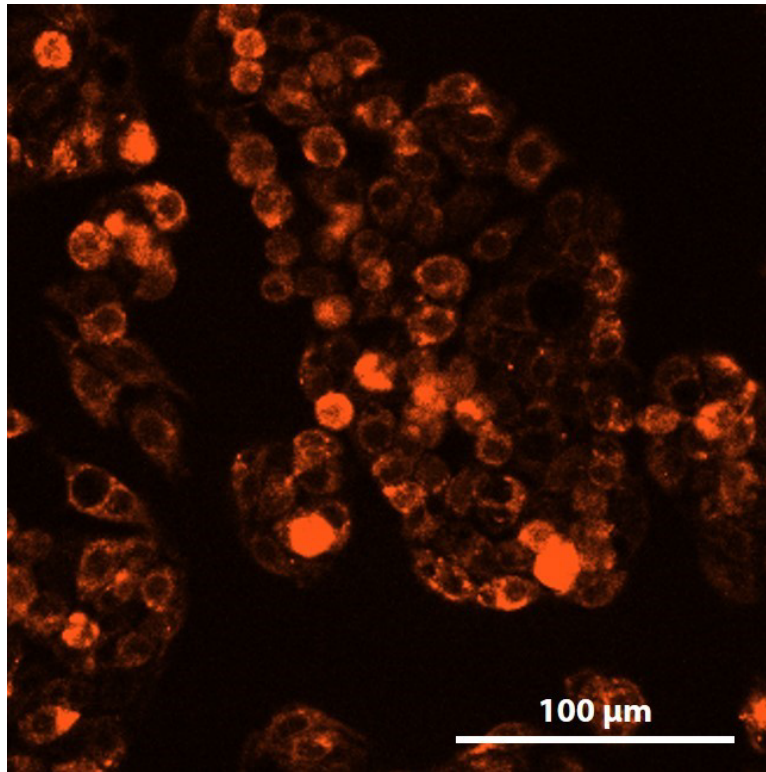


**Figure 2.15. CellROX™ Orange Stain**

Fluorescence image of Hep G2 P18 cells stained with 5  $\mu\text{M}$  CellROX™ Orange Reagent in DPBS for 30 minutes at 37 °C. Image false colored for visual representation.

### 2.3.3 2',7'-Dichlorofluorescein Diacetate Loading

DCF-DA is an additional cell permeant, non-fluorescent reagent for ROS detection. DCF-DA is generally used to measure hydrogen peroxide ( $\text{H}_2\text{O}_2$ ) and superoxide anion radical ( $\text{O}_2^{\bullet-}$ ) content in living cells.<sup>20</sup> Upon entering the cell, DCF-DA is deacetylated and oxidized by ROS in the cell to fluoresce green as dichlorofluorescein (DCF) (**Figure 2.16**).<sup>21</sup>

To load cells with DCF-DA, initially we prepared a  $\geq 1$  mM stock solution with DMSO in a black microcentrifuge tube to protect the photosensitive reagent. The stock solution was diluted to a 10 mL solution of 10  $\mu\text{M}$  DCF-DA using DPBS in a scintillation vial. The vial was covered with foil to avoid photodegradation. After removing spent full growth media from cells, the cells were rinsed with DPBS once. Next, the rinse was removed and enough 10  $\mu\text{M}$  DCF-DA in DPBS was added to coat the bottom of the cell culture vessel. The vessel was covered with foil and cells were allowed to incubate at room temperature for 10 to 20 minutes. Occasionally, the covered vessel was placed on a rotator plate set to 10 rpm to facilitate DCF-DA loading, but this was not a necessity. Following the incubation, the DCF-DA solution was removed from the vessel and the cells were rinsed with DPBS once before imaging. In addition, we typically completed DCF-DA loading in a dark room to avoid photodegradation.

Cells loaded with DCF-DA may be imaged using a standard GFP (*i.e.*, a standard green fluorescent protein) filter cube. Generally, cells stained with DCF-DA were imaged with our hyperspectral system outlined in **Chapter 4**. **Figure 2.17** is a fluorescence image of Hep G2 P24 cells loaded with 10  $\mu\text{M}$  DCF-DA in DPBS captured using a Leica DMI8 inverted microscope, the variable fluorescence bandpass hyperspectral imaging system, and a Leica DFC7000 GT digital camera.



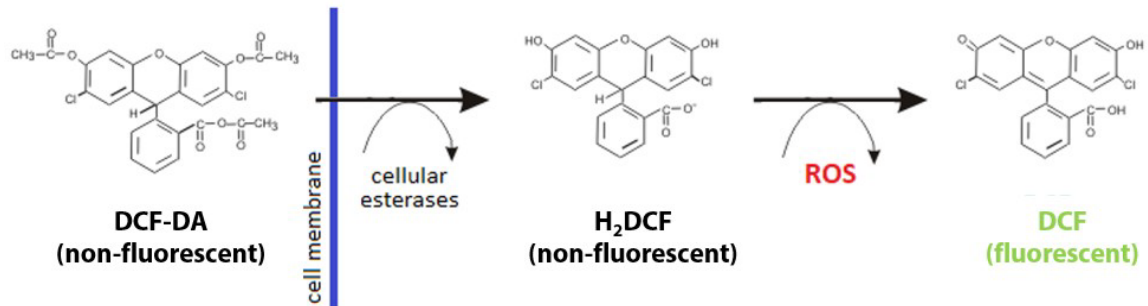


**Figure 2.16. Mechanism of ROS Detection via 2',7'-Dichlorofluorescein Diacetate<sup>21</sup>**

Mechanism of deacetylation of 2',7'-dichlorofluorescein diacetate (DCF-DA) by cellular esterases followed by oxidation by ROS to produce fluorescent 2',7'-dichlorofluorescein (DCF).

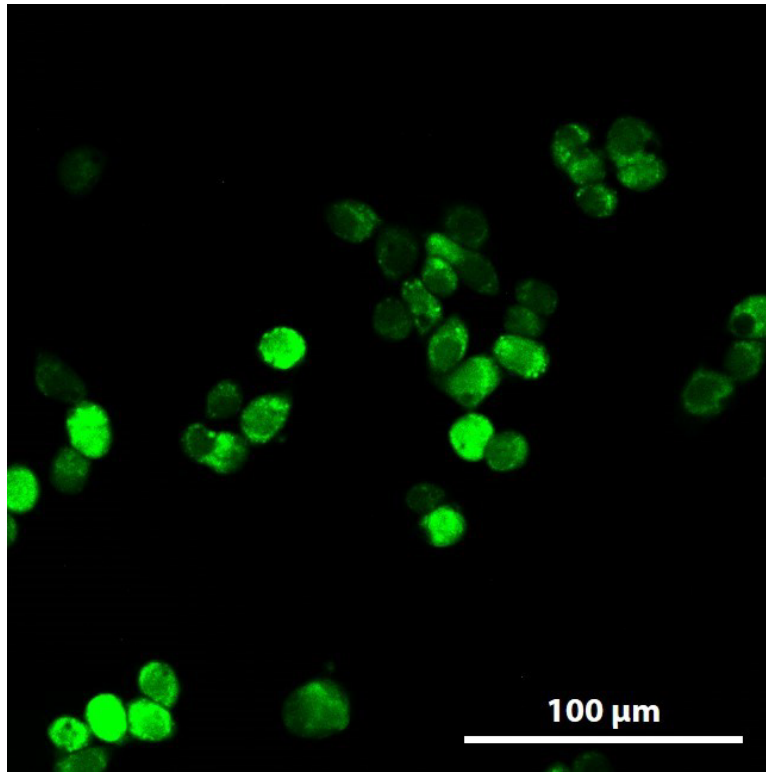


**Figure 2.17. Dichlorofluorescein Emission following 2',7'-Dichlorofluorescein Diacetate Loading**

DCF fluorescence image of Hep G2 P24 cells loaded with 10  $\mu$ M DCF-DA in DPBS for 20 minutes at room temperature. Image false colored for visual representation.

## 2.4 Scanning Probe Microscopy of Living Cells

Generally, biological scanning electrochemical microscope platforms consist of an inverted, fluorescence microscope equipped with a piezoelectric positioner for electrochemical imaging.<sup>22</sup> Our platform is composed of a standard Leica DMI8 inverted, fluorescence microscope with a CH Instruments 920D stepper and piezoelectric positioner in replace of the standard bright field light source and condenser. The stepper and piezoelectric positioner are operated using a 920D bipotentiostat. The Leica DMI8 is operated using Leica LAS X software, while the 920D bipotentiostat is operated using standard CH Instruments 920D software. The Leica DMI8 microscope is equipped with a hyperspectral imaging system (discussed in detail in **Chapter 4**), standard fluorescence cubes (*e.g.*, GFP, TXR, and DAPI cubes), a Leica DFC7000 GT digital camera, and a digital CMOS camera.

Typically, SECM of living cells throughout this work is performed using constant-height feedback mode with  $\text{FcCH}_2\text{OH}$ .<sup>23, 24</sup>  $\text{FcCH}_2\text{OH}$  is generally used as a simple, one-electron transfer, cell permeable redox mediator to examine the cellular redox state.<sup>1, 25-27</sup> Prior to collecting images of living cells, tilt correction of the Leica DMI8 stage was performed to minimize tip-to-substrate crashes during constant-height imaging (*i.e.*, when the  $z$  position of the electrode tip remains constant). For tilt correction, a 1 mM  $\text{FcCH}_2\text{OH}$  stock solution was diluted to a 2 mL solution of 0.5 mM  $\text{FcCH}_2\text{OH}$  in DPBS in an empty 3.5 cm-diameter tissue culture dish. The dish was placed on the microscope stage, then a three-electrode system featuring a salt bridge to an external  $\text{Ag}/\text{AgCl}$  (1 M  $\text{KCl}$ ) reference electrode in DPBS, a glassy carbon rod counter electrode ( $r = 1.5$  mm), and a Pt microelectrode SECM tip ( $r = 5$   $\mu\text{m}$ ) were placed in solution using a 3D printed holder attached to the piezoelectric positioner. After connecting each electrode to the proper electrode leads of the bipotentiostat, the “Probe Scan Curve” technique was selected from the techniques panel of the CH Instruments 920D bipotentiostat software.

Within “Probe Electrode,” the probe electrode was set to +0.5 V vs. Ag/AgCl (*i.e.*, sufficiently positive to oxidize FcCH<sub>2</sub>OH) with a sensitivity of 1E-9 A/V. “Amperometry” was selected from the list of modes, “Auto” was selected from the list of motor selections, and “Z” was selected from the list of scan directions. Next, the travel distance was set to 800 μm, a distance high enough to guarantee feedback within the acquisition window. The travel distance must also be a positive value for the tip to travel downward in the *z* direction. Lastly, the increment distance was set to 0.25 μm, the increment time was set to 0.05 seconds, and the quiet time was set to 10 seconds. **Figure 2.18** shows these settings within the parameters window of the software. The approach to the insulating dish resulted in the negative feedback response (*i.e.*, when  $i_T$  approaches zero as the distance,  $d$ , between the tip and substrate approaches zero<sup>28</sup>) shown in **Figure 2.19**. Generally, this experimental approach curve is represented as normalized current (*i.e.*,  $i_T/i_{T, \infty}$ ) versus normalized distance (*i.e.*,  $L = d/a$ , where  $d$  is the tip-to-substrate distance and  $a$  is the radius of the electrode) as shown in **Figure 2.20**.

Probe Scan Curve Parameters

Probe Electrode  
 Probe E (V) ..... 0.5  
 Sensitivity (A/V) ..... 1.e-009

Probe E Pulse before Sampling  
 Pulse E (V) ..... 0  
 Pulse Duration (s) ... 0  
 Pulse 2 E (V) ..... 0  
 Pulse 2 Duration (s). 0  
 Delay time (s) ..... 0.1  
 E1 Pulse On

Substrate Electrode  
 Substrate E (V) ..... 0  
 Sensitivity (A/V) ..... 1.e-006  
 E2 On     i2 On

Mode  
 Amperometry  
 Potentiometry  
 Constant Current  
 Impedance  
 Constant Impedance

Constant Current Mode  
 Constant Current (A) ..... 1e-009  
 Tolerance (%) ..... 1  
 Max Z Incr (um) ..... 1

Probe Stop at Current Level  
 No  
 Absolute (A) < 0  
    > 0.01

Impedance mode  
 Frequency (Hz) ... 100000  
 Amplitude (V) ..... 0.005  
 Impedance (ohm) .. 100000  
 Bias DC Current  
 AutoSens

Motor Selection  
 Auto     Stepper     Piezo

Scan Direction  
 X     Y     Z

Travel Distance (um) ..... 800  
 Incr. Dist. (um) ..... 0.25  
 Incr Time (s) ..... 0.05  
 Quiet Time (s) ..... 10

X Tilt Ratio: 0  
 Y Tilt Ratio: 0

OK  
 Cancel  
 Help

**Figure 2.18. Approach Curve Parameters**

Probe scan curve parameters for an approach to an insulating dish containing FcCH<sub>2</sub>OH.

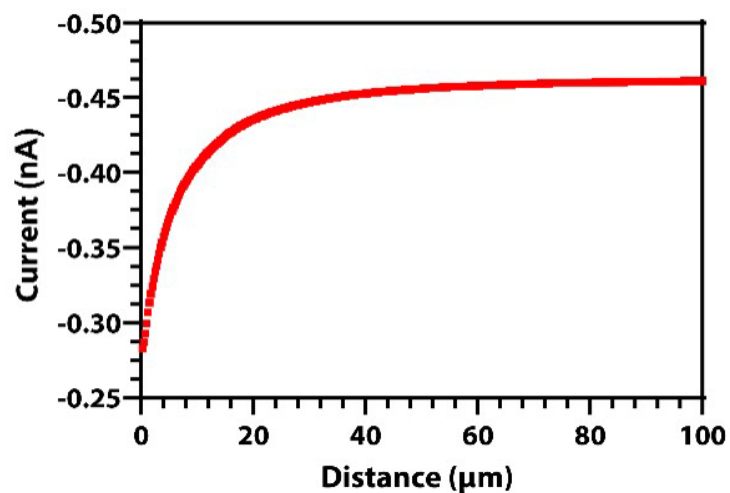


**Figure 2.19. Negative Feedback Response**

Experimental approach curve obtained using parameters in **Figure 2.18** and a Pt microelectrode tip ( $r = 5 \mu\text{m}$ ) biased at +0.5 V vs. Ag/AgCl (1 M KCl) within 0.5 mM FcCH<sub>2</sub>OH in DPBS in a 3.5 cm-diameter cell culture dish. A glassy carbon rod counter electrode ( $r = 1.5 \text{ mm}$ ) was used.

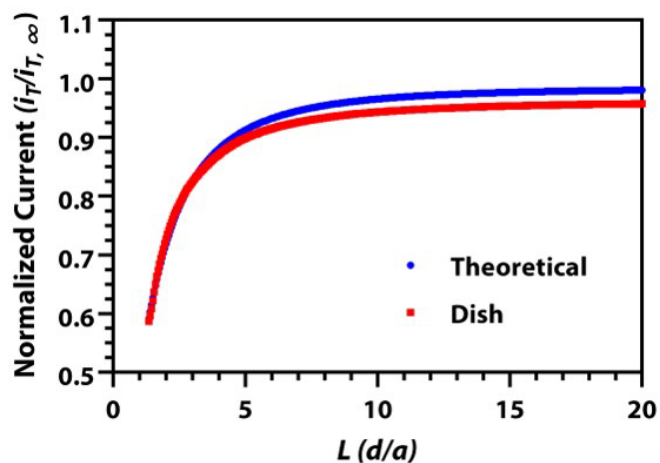


**Figure 2.20. Normalized Negative Feedback Response**

Normalized approach curve to a 3.5 cm-diameter tissue culture dish containing 0.5 mM FcCH<sub>2</sub>OH in DPBS. Approach was obtained using parameters in **Figure 2.18** and a Pt microelectrode tip ( $r = 5 \mu\text{m}$ ) vs. Ag/AgCl (1 M KCl). A glassy carbon rod was used as the counter electrode ( $r = 1.5 \text{ mm}$ ). The normalized approach curve is shown with its associated theoretical fit.

This normalized, negative feedback approach was theoretically fit based on **Equation 1.3** and **Table 1.1** (reprinted below) to determine the final tip-to-substrate distance of 6.75  $\mu\text{m}$ .<sup>29</sup> Moreover, the tip-to-substrate distance was sufficient to observe an electrochemical response based on properties of the substrate (*i.e.*,  $d \leq 2a$ , where  $d$  is the tip-to-substrate distance and  $a$  is the radius of the working electrode).

$$i_T^{ins}(L) = \frac{1}{\left[A + \frac{B}{L} + C\left(\frac{D}{L}\right)\right]} + \frac{E \times L}{(F+L)} \quad \text{Equation 1.3}$$

**Table 1.1. Parameter Values for Equations 1.3<sup>29</sup>**

| <b>RG</b> | <b>A</b>  | <b>B</b>  | <b>C</b>  | <b>D</b>  | <b>E</b> | <b>F</b>  |
|-----------|-----------|-----------|-----------|-----------|----------|-----------|
| 1.1       | 1.675164  | 1.0309985 | 0.3800855 | -1.701797 | -0.34638 | 0.0367416 |
| 1.5       | 1.003595  | 0.9294275 | 0.4022603 | -1.788572 | 0.283263 | 0.1401598 |
| 2         | 0.7838573 | 0.877792  | 0.4248416 | -1.743799 | 0.163843 | 0.1993907 |
| 10        | 0.4571825 | 1.4604238 | 0.4312735 | -2.350667 | -0.14537 | 5.5768952 |

Here, it is important to note that increasing the quiet time prior to obtaining an approach will improve the accuracy of the theoretical fit. This allows the dissipation of capacitive current due to relay switching within the potentiostat. This procedure was repeated with a quiet time of 300 seconds to provide the theoretical fit shown in **Figure 2.21**.



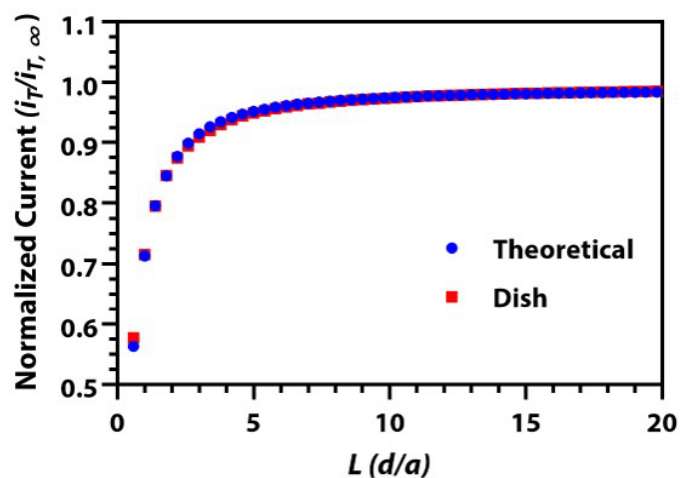


**Figure 2.21. Negative Feedback Theoretical Fit**

Normalized approach curve to a 3.5 cm-diameter tissue culture dish containing 0.5 mM FcCH<sub>2</sub>OH in DPBS. Approach was obtained using adjusted parameters from Figure 2.18 (*i.e.*, an adjusted quiet time of 300 seconds) and a Pt microelectrode tip ( $r = 5 \mu\text{m}$ ) vs. Ag/AgCl (1 M KCl). A glassy carbon rod was used as the counter electrode ( $r = 1.5 \text{ mm}$ ). The normalized approach curve is shown with its associated theoretical fit.

After obtaining the negative feedback response, we focused on the Pt microelectrode tip with the 20× objective and placed the tip in the upper left corner of the imaging region. Next, the “Scanning Electrochemical Microscope” technique was selected. In the parameter window, the probe potential was set to +0.5 V vs. Ag/AgCl, the quiet time was set to 180 seconds, and the sensitivity was set to 1E-9 A/V. “Amperometry” was selected from the list of modes, “Auto” was selected from the list of motor selections, and “X Axis as Long Distance” was selected from two long travel distance options. Movement of the working electrode was specified within “Probe Travel”; the *x* distance was set to 620 μm and the *y* distance was set to 470 μm (based on the acquisition area of the objective in use), while the increment distance was set to 10 μm (based on the diameter of the working electrode to avoid oversampling) and the increment time was set to 0.2 seconds. Lastly, “Return to Origin after Run” was selected. These parameters are shown in **Figure 2.22** and were used for subsequent electrochemical imaging. To image the magnitude of the tilt of the microscope stage, the Pt microelectrode tip was used to scan the dish surface in the *xy* plane at +0.5 V vs. Ag/AgCl (**Figure 2.23**).

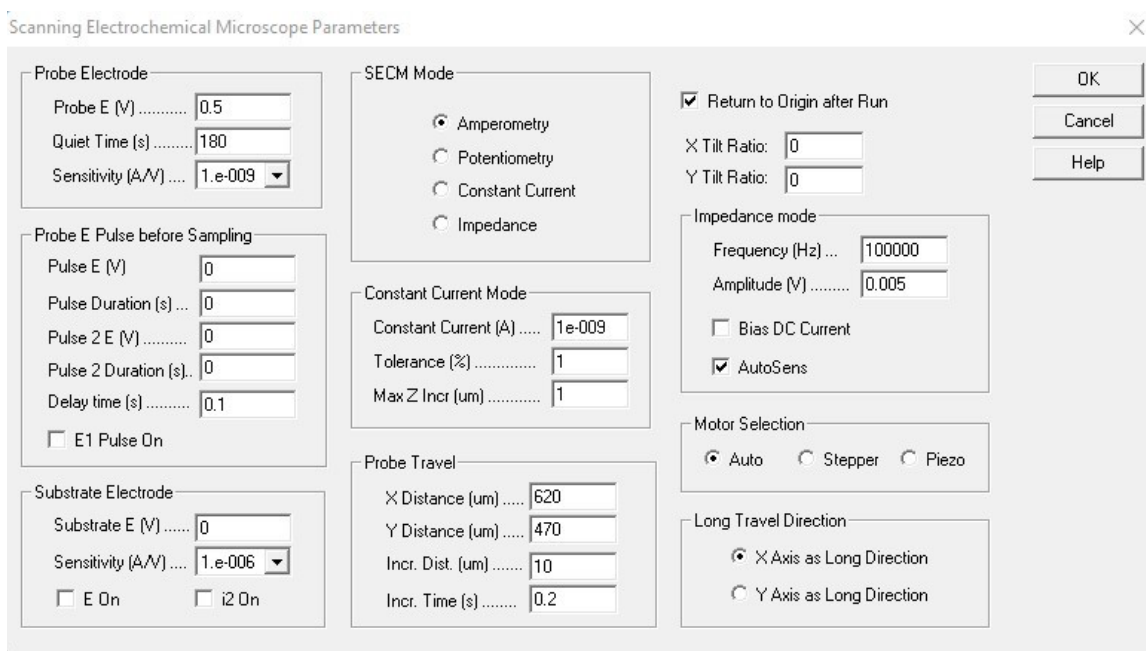


**Figure 2.22. Scanning Electrochemical Microscope Parameters**

Electrochemical imaging parameters for tilt correction and imaging of living cells in  $\text{FcCH}_2\text{OH}$ .

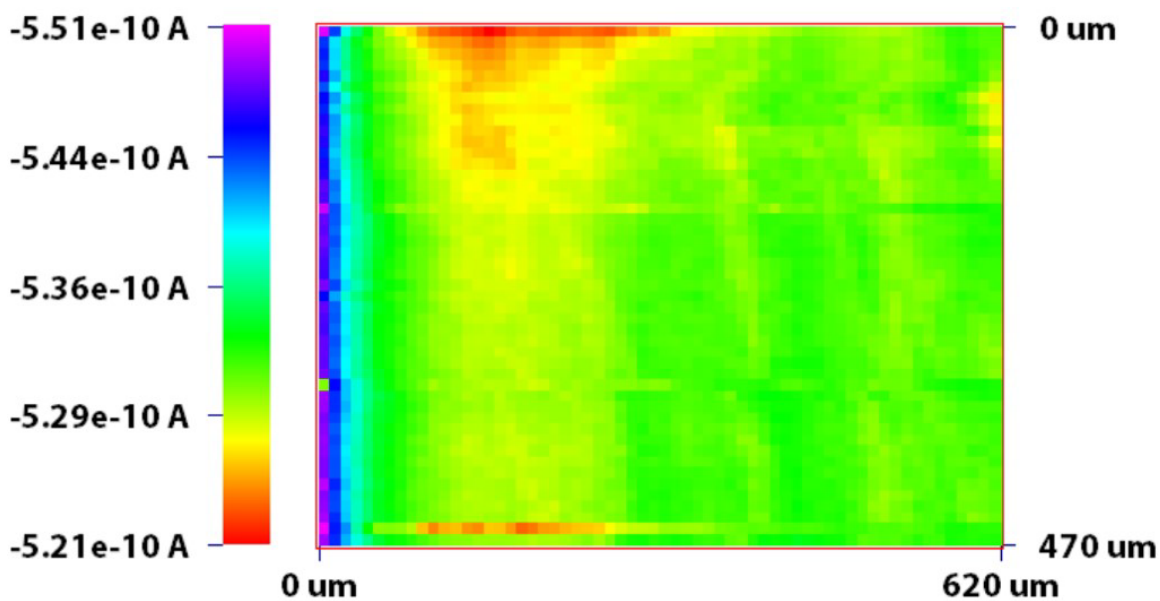


**Figure 2.23. Electrochemical Image following Tilt Correction**

Polarographic electrochemical image of a 3.5 cm-diameter tissue culture dish containing 0.5 mM FcCH<sub>2</sub>OH in DPBS. Image obtained with a Pt microelectrode tip ( $r = 5 \mu\text{m}$ ) at +0.5 V vs. Ag/AgCl (1 M KCl) and a glassy carbon rod counter electrode ( $r = 1.5 \text{ mm}$ ).

After confirming insignificant tilt (*i.e.*,  $\Delta i \leq 30$  pA), Hep G2 P20 cells subcultured into a 3.5 cm-diameter cell culture dish were imaged. To image the Hep G2 P20 cells, spent media was removed from the sample and the cells were rinsed two times with approximately 1 mL DPBS before the 1 mM FcCH<sub>2</sub>OH stock solution was diluted to 0.5 mM FcCH<sub>2</sub>OH with DPBS directly in the sample dish. Next, the dish was placed on the microscope stage, and the three-electrode system previously used to image the tilt was placed in solution. Cells were brought into focus in bright field using a 20× objective lens. After connecting electrodes and the 920D bipotentiostat electrode leads, the cells were approached with the Pt microelectrode tip at +0.5 V vs. Ag/AgCl until feedback (**Figure 2.24**) and cell movement were observed.

It is important to note that it is not uncommon to observe negative feedback with cell movement, rather than positive feedback, if cells are pushed away from the electrode tip as the tip approaches the insulating dish. After obtaining a feedback response and observing cell movement, the Pt microelectrode tip was moved upward 10 μm until no cell movement was observed. This is essential because a working distance  $\leq 10$  μm is necessary for feedback mode scanning electrochemical microscopy (*i.e.*,  $d \leq 2a$ ), while also avoiding tip-to-sample crashes that may be observed when imaging large aspect ratio samples; this technique has been used previously when imaging cell samples<sup>30</sup>. Next, the Pt microelectrode tip was placed in the upper left of the imaging region for electrochemical imaging. The electrochemical image was obtained with the parameters previously shown in **Figure 2.22** approximately one hour after adding the redox mediator solution to the cell culture dish. This incubation period allowed passive diffusion of FcCH<sub>2</sub>OH into the cells.<sup>26</sup> Following electrochemical imaging, a correlated bright field image was obtained using the Leica digital camera. **Figure 2.25** displays the resulting electrochemical image and the correlated optical image.

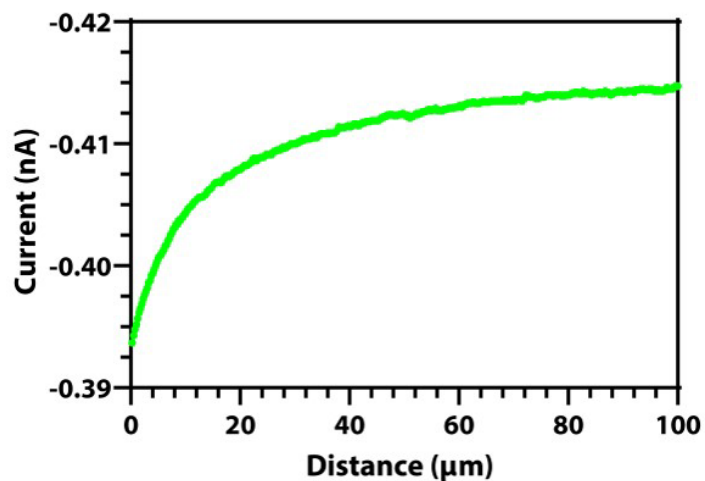


**Figure 2.24. Negative Feedback Approach to Cells**

Experimental approach curve obtained using a Pt microelectrode tip ( $r = 5 \mu\text{m}$ ) biased at +0.5 V vs. Ag/AgCl (1 M KCl) within 0.5 mM FcCH<sub>2</sub>OH in DPBS to approach Hep G2 P20 cells in a 3.5 cm-diameter cell culture dish. A glassy carbon rod counter electrode ( $r = 1.5 \text{ mm}$ ) was used.

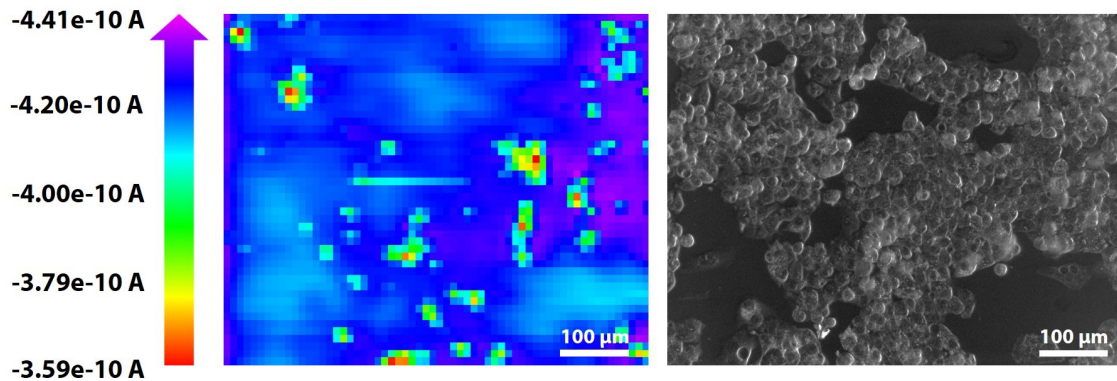


**Figure 2.25. Scanning Electrochemical Microscopy Image of Hep G2 Cells**

Correlated electrochemical and optical images of Hep G2 P20 cells. Images obtained in 0.5 mM  $\text{FcCH}_2\text{OH}$  in DPBS. Electrochemical image obtained using a Pt microelectrode tip ( $r = 5 \mu\text{m}$ ) at +0.5 V vs. Ag/AgCl (1 M KCl) and a glassy carbon rod counter electrode ( $r = 1.5 \text{ mm}$ ).

## REFERENCES

1. D. Polcari, P. Dauphin-Ducharme and J. Mauzeroll, *Chemical Reviews*, 2016, **116**, 13234-13278.
2. S. Goines and J. Dick, *ChemElectroChem*, 2019, **6**, 5264-5272.
3. S. Tanimoto and A. Ichimura, *Journal of Chemical Education*, 2013, **90**, 778-781.
4. A. J. Bard and L. R. Faulkner, in *Electrochemical Methods: Fundamentals and Applications*, eds. D. Harris, E. Swain, C. Rodney and E. Aiello, John Wiley & Sons, Inc., New York, NY, 2nd edn., 2001, ch. Kinetics of Electrode Reactions, pp. 115-132.
5. J. J. Van Benschoten, J. Y. Lewis, W. R. Heineman, D. A. Roston and P. T. Kissinger, *Journal of Chemical Education*, 1983, **60**, 772.
6. G. Denuault, M. V. Mirkin and A. J. Bard, *Journal of Electroanalytical Chemistry*, 1991, **308**, 27-38.
7. J. G. Osteryoung and R. A. Osteryoung, *Analytical chemistry*, 1985, **57**, 101-110.
8. L. Ramaley and M. S. Krause, *Analytical Chemistry*, 1969, **41**, 1362-1365.
9. R. G. Fuller, D. Rappleye, T. Williams and M. Schvaneveldt, *ECS Meeting Abstracts*, 2021, **MA2021-02**, 1921-1921.
10. V. Mirceski and R. Gulaboski, *Macedonian Journal of Chemistry and Chemical Engineering*, 2014, **33**, 1-12.
11. A. J. Bard and L. R. Faulkner, in *Electrochemical Methods: Fundamentals and Applications*, eds. D. Harris, E. Swain, C. Rodney and E. Aiello, John Wiley & Sons, Inc., New York, NY, 2 edn., 2001, ch. Polarography and Pulse Voltammetry, pp. 275-301.
12. P. T. Kissinger and W. R. Heineman, *Journal of Chemical Education*, 1983, **60**, 702.
13. G. Grass, C. Rensing and M. Solioz, *Applied and environmental microbiology*, 2011, **77**, 1541-1547.
14. K. T. Tsaousis, N. Kopsachilis, I. T. Tsinopoulos, S. A. Dimitrakos, F. E. Kruse and U. Welge-Luessen, *Clin Exp Ophthalmol*, 2013, **41**, 484-490.
15. A. K. Kwok, C. K. Yeung, T. Y. Lai, K. P. Chan and C. P. Pang, *Br J Ophthalmol*, 2004, **88**, 1590-1594.
16. T. H. Jang, S. C. Park, J. H. Yang, J. Y. Kim, J. H. Seok, U. S. Park, C. W. Choi, S. R. Lee and J. Han, *Integrative medicine research*, 2017, **6**, 12-18.



17. Y. Kurashina, C. Imashiro, M. Hirano, T. Kuribara, K. Totani, K. Ohnuma, J. Friend and K. Takemura, *Communications Biology*, 2019, **2**, 393.
18. J. Bucevičius, G. Lukinavičius and R. Gerasimaitė, *Chemosensors*, 2018, **6**, 18.
19. B. I. Tarnowski, F. G. Spinale and J. H. Nicholson, *Biotech Histochem*, 1991, **66**, 297-302.
20. H. Kim and X. Xue, *JoVE (Journal of Visualized Experiments)*, 2020, e60682.
21. Z. Nova, H. Skovierova, J. Strnadel, E. Halasova and A. Calkovska, *International Journal of Molecular Sciences*, 2020, **21**, 1148.
22. S. Amemiya, J. Guo, H. Xiong and D. A. Gross, *Analytical and Bioanalytical Chemistry*, 2006, **386**, 458-471.
23. S. Goines, M. Deng, M. W. Glasscott, J. Leung and J. E. Dick, *Analyst*, 2022.
24. S. Goines and J. E. Dick, *Analyst*, 2022.
25. A. J. Bard, X. Li and W. Zhan, *Biosensors & Bioelectronics*, 2006, **22**, 461-472.
26. S. Kuss, D. Polcari, M. Geissler, D. Brassard and J. Mauzeroll, *Proceedings of the National Academy of Sciences*, 2013, **110**, 9249.
27. S. Kuss, R. Cornut, I. Beaulieu, M. A. Mezour, B. Annabi and J. Mauzeroll, *Bioelectrochemistry*, 2011, **82**, 29-37.
28. A. J. Bard and M. V. Mirkin, in *Scanning Electrochemical Microscopy*, eds. A. J. Bard and M. V. Mirkin, Taylor & Francis Group, LLC, Boca Raton, FL, 2 edn., 2012, ch. Introductions and Principles, pp. 2-6.
29. A. J. Bard and M. V. Mirkin, in *Scanning Electrochemical Microscopy*, eds. A. J. Bard and M. V. Mirkin, Taylor & Francis Group, LLC, Boca Raton, FL, 2 edn., 2012, ch. Theory, pp. 76-95.
30. I. Beaulieu, S. Kuss, J. Mauzeroll and M. Geissler, *Analytical Chemistry*, 2011, **83**, 1485-1492.

### Chapter 3 Practical Use of Biologically Relevant Small Molecules as Redox Mediators

Selecting a redox mediator for scanning electrochemical microscopy (SECM) investigations typically depends on the operational mode in use. In this work, we rely on feedback mode to elucidate variations in the cellular redox state. Mediators used within feedback mode SECM should follow fast, reversible, one-electron transfer redox mechanisms to examine substrate reactivity in real time.<sup>1</sup> The use of cell permeant mediators provides an indirect method for investigating cell metabolism and redox activity based on the mediator's intracellular interactions; these reactions are generally facilitated by bimolecular electron transfer mechanisms involving intracellular redox species or centers.<sup>1, 2</sup> Ferrocenemethanol (FcCH<sub>2</sub>OH), menadione, and 1,2-naphthoquinone are commonly used one-electron transfer, cell permeant redox mediators used in SECM investigations to indirectly investigate intracellular redox activity; specifically, they have been used to monitor cell reactivity<sup>3, 4</sup>, oxidative stress<sup>5</sup>, and cell membrane transport<sup>6-8</sup> by feedback and generation-collection mode SECM. Unfortunately, these redox mediators may induce oxidative stress (apparent *via* upregulation of glutathione<sup>6-8</sup>) or become cytotoxic at high concentrations over long periods exposure<sup>9</sup>. The use of biologically relevant electroactive species as redox mediators in SECM investigations would mitigate these deleterious effects while providing answers to pertinent biological questions. In the following sections, we will electrochemically characterize nicotinamide riboside (NR), a precursor to nicotinamide adenine dinucleotide (NAD<sup>+</sup>/NADH), and demonstrate the supplement's potential to examine the redox activity of living cells.

### 3.1 Electrochemical Characterization of Nicotinamide Riboside<sup>1</sup>

Nicotinamide adenine dinucleotide (NAD<sup>+</sup>/NADH) is a multifaceted, oxidoreductase cofactor within living cells.<sup>10</sup> Generally, NAD<sup>+</sup> functions as an electron acceptor within catalytic mechanisms of dehydrogenase enzymes, while also functioning as a biomarker within various systems and a regulatory agent for post-translational protein modifications.<sup>11, 12</sup> In particular, NAD<sup>+</sup> determines the activity of enzymes, such as sirtuin enzymes, which are crucial to cellular metabolism, cell survival, and DNA repair.<sup>13, 14</sup> Sirtuin enzymes improve metabolic efficiency by assisting in oxidative metabolism during periods of exercise, calorie restriction, and hypoglycemia.<sup>15</sup> Specifically, sirtuin enzymes use NAD<sup>+</sup> to deacetylate lysine groups of histones and proteins within various subcellular components.<sup>14-16</sup> Humans house seven orthologs of sirtuin enzymes spanning proliferative and non-proliferative tissues; specifically, these enzymes are located within nuclei, cytoplasm, and mitochondria of mammalian cells.<sup>14</sup>

Unfortunately, sirtuin enzyme activity declines as NAD<sup>+</sup> decreases in abundance with respect to age.<sup>11, 12, 17</sup> This has become apparent as the decline of the cofactor has been implicated in the onset of various disease states such as cardiovascular disease, diabetes, and kidney failure as well as neurodegenerative diseases.<sup>18</sup> By 2050, \$1 trillion will be spent yearly on those 65 years of age or older due to neurodegenerative diseases like dementia.<sup>19</sup> These findings justify the widespread interest in the study of sirtuin enzyme activity with respect to NAD<sup>+</sup> levels and NAD<sup>+</sup> supplementation. Research implies that NAD<sup>+</sup> supplementation would promote healthy aging while improving our quality of life.<sup>19-22</sup> Specifically, enabling us to sustain physiological functions that typically decline with age such as vision, hearing, cognitive

---

<sup>1</sup> This section previously appeared as an article in *ChemElectroChem*. It was reproduced with permission from John Wiley and Sons. The original citation is as follows: S. Goines and J. E. Dick, *ChemElectroChem*, 2019, **6**, 5264-5272.

behavior, and motor functions.<sup>23</sup> A current, and rather controversial, question regarding the cofactor is: does an individual's healthspan or lifespan depend heavily on NAD<sup>+</sup> levels? In other words, will NAD<sup>+</sup> supplementation improve the longevity of our health or our lives?

In an attempt to answer this question, NAD<sup>+</sup> levels have been studied qualitatively and quantitatively using single cells, rodent models, and clinical trials.<sup>16, 18, 24</sup> Within clinical trials performed by Martens and co-workers, physiological conditions are noted along with the concentration of the NAD<sup>+</sup> metabolome within blood mononuclear cells in correlation to chronic oral supplementation of NR.<sup>18</sup> The results of the chronic supplementation are also related to particular disease states typically found among middle-aged and older adults, such as heart disease, by noting particular physiological conditions like carotid artery compliance. The general consensus has been that vitamin B3 supplementation improves one's healthspan, rather than one's lifespan.<sup>18</sup> Though many would like to combat ageing, lifespan hangs in the balance due to unavoidable damage to our biological systems, that may also be irreversible if one begins to look at age as a disease.<sup>25</sup>

Regardless, the inevitable decline of NAD<sup>+</sup> is being combated through the use of oral supplements of the vitamin B3 complex such as nicotinamide, nicotinic acid (niacin), nicotinamide mononucleotide (NMN), and NR (**Figure 3.1**), as well as sirtuin activating compounds like resveratrol.<sup>11, 16, 17</sup> As companies battle over rights to sell NR exclusively, scientists are exploring the inherent value of the supplement over the analogs previously listed.<sup>26</sup> Niacin was the general NAD<sup>+</sup> booster until severe flushing and itching caused by the supplement deterred users. Additionally, there is no physiological evidence that niacin increases blood levels of NAD<sup>+</sup>. Alternatively, NR has increased in popularity in recent years and has been shown to increase human blood levels of NAD<sup>+</sup> during clinical trials.<sup>20, 23</sup> NR, as well as NMN (*i.e.*, the

phosphorylated form), may be consumed daily from vegetables, fruits, and meat. In addition, NR and NMN may also be found in micromolar concentrations in milk produced by humans and cows.<sup>20, 27</sup>

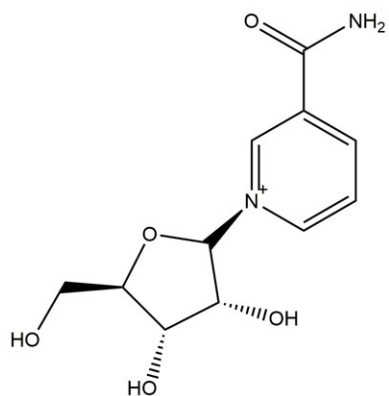


**Figure 3.1. Nicotinamide Riboside**

Chemical structure of nicotinamide riboside (NR, 255.25 g mol<sup>-1</sup>).

In an effort to understand the redox pathway of NR, we electrochemically characterize the supplement using a range of electrochemical techniques. The methods we chose to use allow one to begin to uncover the redox mechanism of the supplement in aqueous systems with minimal background information. More importantly, the workflow developed may be used to characterize electroactive unknowns without the use of calibration curves. For instance, prominent suppliers of NR sell the supplement in capsule form. In principle, we demonstrate that one can purchase a capsule and attain the diffusion coefficient, the number of electrons transferred, and ultimately the concentration of the species of interest without a calibration curve, making the approach user friendly and amenable as a general strategy when approaching new molecules. This methodology may serve as a foundation for the characterization of a number of electroactive molecules that are biologically relevant with the caveat that the reactant and product for the heterogeneous reaction are freely-diffusing molecules. To conclude, we show that the reduction of NR produces a thermodynamically stable dimerization product; in addition, the fate of the kinetic product differs noticeably in whole cell lysate compared to in buffer.

### **3.1.1 Effect of Electrode Material**

As a trending supplement, NR has become a compound of interest among researchers with the question of the compound's effect on healthspan or lifespan leading the discussion. Herein, the electrochemical characterization of NR offers a full view of the compound's redox characteristics without direct use of standards of known concentrations. To prepare the sample solutions, 250 mM KCl was prepared with Milli-Q water to be used as the standard electrolyte. Next, Tru Niagen® capsule contents were dissolved in 10 mL 250 mM KCl. If slightly insoluble, the sample was sonicated for approximately 15 minutes. Following sonication, the sample was filtered using a 1  $\mu$ m PTFE syringe filter. All samples were degassed with N<sub>2</sub> gas for 10 to 15

minutes prior to collecting data unless otherwise noted. In addition, N<sub>2</sub> gas was typically used as a blanket during data collection. **Figure 3.2** is a cyclic voltammogram of NR capsule contents soluble in 10 mL of 250 mM KCl. The voltammogram was captured at a 300 mV/s at a glassy carbon macroelectrode (GC,  $r = 0.0015$  m) versus a Ag/AgCl (1 M KCl) reference electrode using a CH Instruments 601E potentiostat; platinum foil was used as the counter electrode. Additional voltammogram settings are shown in **Figure 2.2**. Electrochemical characterization of the supplement by the means outlined in this article may provide information concerning the mechanisms of NR dependent enzymes using the electrode/electrolyte solution interface as a model.<sup>28</sup>

To investigate the redox mechanisms of NR, cyclic voltammograms of an NR capsule aqueous sample were captured at GC ( $r = 0.0015$  m), platinum (Pt,  $r = 0.001$  m), and gold (Au,  $r = 0.001$  m) macroelectrodes versus a Ag/AgCl (1 M KCl) reference electrode using previous voltammogram settings. Voltammograms were overlaid for comparison (**Figure 3.3**). Initial experiments indicated that electrode material played a role in the mechanism of NR reduction and oxidation. This is shown in **Figure 3.3** as the peak potentials of NR reduction and oxidation shift with respect to electrode material, implying that the electrochemical reaction may depend on the electrode surface. To definitively classify NR reduction and oxidation as inner-sphere or outer-sphere electrode reactions, further voltammetric investigations are completed in section **3.1.3 Determination of Diffusion Coefficient**.



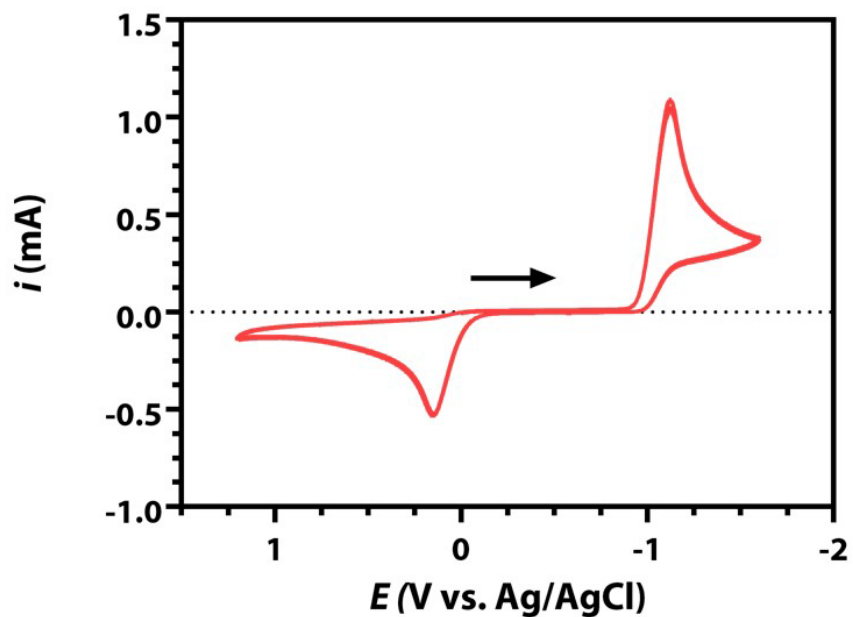


**Figure 3.2. Cyclic Voltammogram of Nicotinamide Riboside**

Cyclic voltammogram of NR capsule contents in 250 mM KCl on a glassy carbon (GC,  $r = 0.0015$  m) macroelectrode vs. Ag/AgCl (1 M KCl), after sparging with N<sub>2</sub> gas, at a scan rate of 300 mV/s.

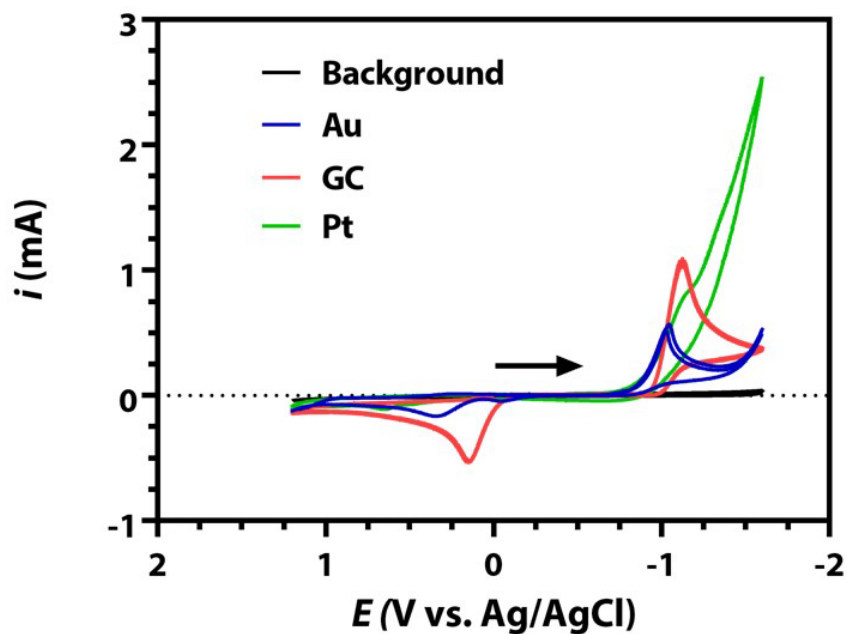


**Figure 3.3. Effect of Electrode Material on Nicotinamide Riboside Cyclic Voltammetry**

Cyclic voltammograms of NR capsule contents in 250 mM KCl on glassy carbon (GC,  $r = 0.0015$  m), gold (Au,  $r = 0.001$  m), and platinum (Pt,  $r = 0.001$  m) macroelectrodes vs. Ag/AgCl (1 M KCl) after sparging with N<sub>2</sub> gas, at a scan rate of 300 mV/s.

Regardless, it is important to note that the rate at which current rose during the reduction of NR varied greatly across different electrode materials, with GC (red curve) having the fastest rate. This finding is important since glassy carbon has a relatively wide potential window. Additionally, the large current associated with Pt (green curve) after NR reduction is assigned to proton reduction in buffer. Thus, future studies on the effects of NR within cells and tissues may use carbon-based materials, which are inert and allow for better electrochemical probing given their large potential windows under biologically relevant pH conditions.

### 3.1.2 Effect of pH

To gain an understanding of the effect of pH on the redox mechanisms of NR, five NR capsule samples of various pH values were prepared in 250 mM KCl. The pH of each solution was measured, then adjusted to five different pH values between 1 and 12 using a 1 M NaOH and a 20% v/v HCl solution. The HCl solution was prepared using a 37% HCl by weight stock solution. More basic solutions turned a deep yellow in comparison to the typical off-white color of typical NR samples. Cyclic voltammograms of each solution were obtained on a GC macroelectrode versus Ag/AgCl (1 M KCl) at a scan rate of 500 mV/s after sparging each solution with N<sub>2</sub> gas. The cyclic voltammograms in **Figure 3.4** do not show variation in peak potential of NR reduction due to pH (generally ~59 mV per pH unit), indicating that the redox mechanism of NR reduction is not proton-coupled.

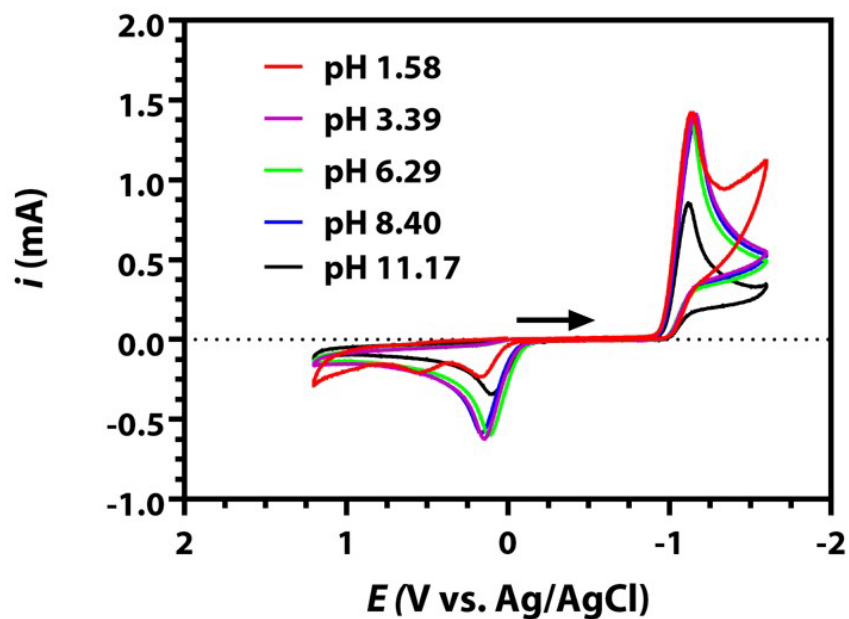


**Figure 3.4. Effect of pH on Nicotinamide Riboside Cyclic Voltammetry**

Cyclic voltammograms of NR capsule contents in 250 mM KCl at pH values ranging from 1.58 to 11.17 obtained at a GC ( $r = 0.0015$  m) macroelectrode vs. Ag/AgCl (1 M KCl), after sparging with N<sub>2</sub> gas, at a scan rate of 500 mV/s.

Interestingly, however, the product of NR reduction, which has an oxidation potential around +0.15 V vs. Ag/AgCl, seems to depend on the pH environment, especially under acidic conditions. This will be the topic of future investigations, as supplement reactivity (and even cofactor reactivity) may change under low pH environments that are sustained during carcinogenesis with enhanced lactic acid generation (*i.e.*, the Warburg Effect<sup>29</sup>).

### 3.1.3 Determination of Diffusion Coefficient

In **Figure 3.3**, we showed the dependence of material on NR reduction, indicating NR may adsorb onto the electrode material. Adsorption was further assessed by comparing the peak current ( $i_p$ ) versus scan rate ( $v$ ) and  $i_p$  vs.  $v^{1/2}$  at a GC macroelectrode. Cyclic voltammograms of NR capsule contents soluble in 10 mL 250 mM KCl were captured at scan rates between 40 mV/s and 1000 mV/s at a GC ( $r = 0.0015$  m) macroelectrode vs. Ag/AgCl (1 M KCl).

Voltammograms obtained to make this comparison are shown in **Figure 3.5a**. A linear regression was performed using an average  $i_p$  vs.  $v$  plot as well as an average  $i_p$  vs.  $v^{1/2}$  plot. The linear relationship derived between  $v^{1/2}$  and  $i_p$  in **Figure 3.5c** indicates that the redox mechanism follows the Randles–Ševčík equation (**Equation 2.1**), suggesting that the mechanism resembles a diffusion-controlled process instead of an adsorption process (*i.e.*, the plot shown in **Figure 3.5c** is more linear than the plot shown in **Figure 3.5b**). In addition to data shown in **Figure 3.3**, discrepancies between the slope of each plot in **Figures 3.5b & 3.5c** are additional indications that weak adsorption does occur. It is important to note that these results indicate that there is a certain error associated with diffusion coefficient calculations.

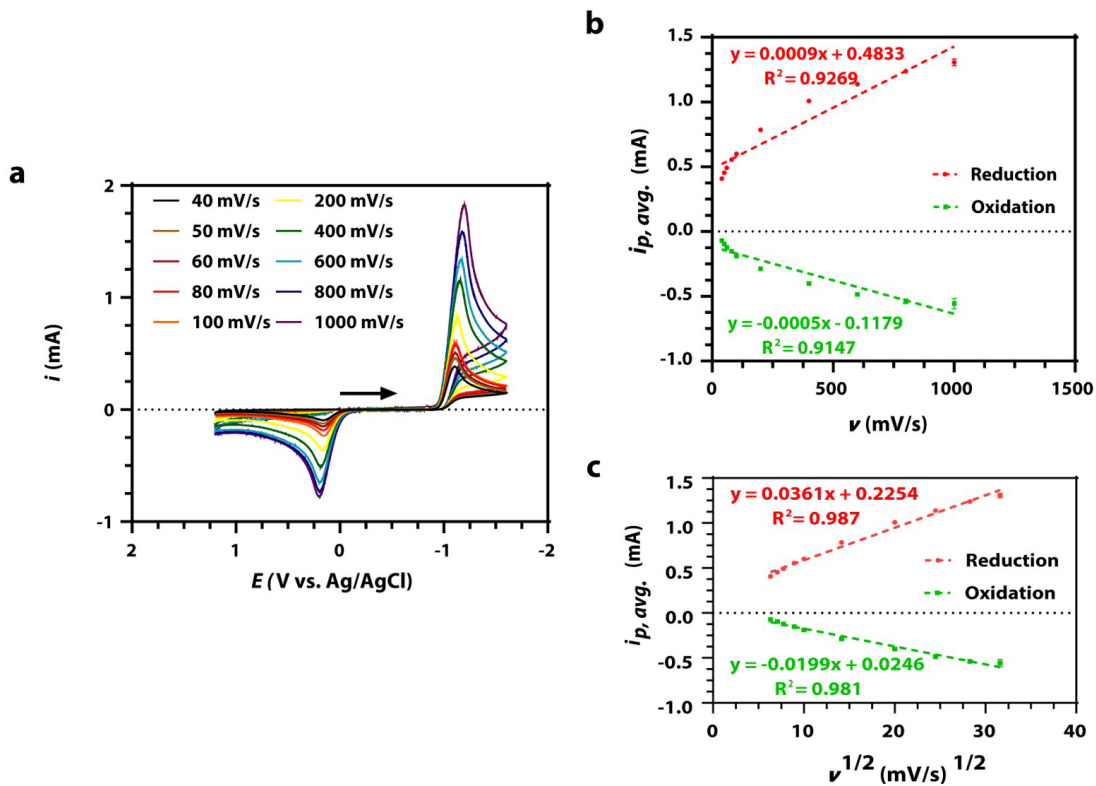


**Figure 3.5. Cyclic Voltammetry of Diffusion-Controlled Nicotinamide Riboside**

a) Cyclic voltammograms of NR capsule contents in 250 mM KCl, after sparging with N<sub>2</sub> gas, at scan rates ranging from 40 mV/s to 1000 mV/s obtained on a GC ( $r = 0.0015$  m) macroelectrode vs. Ag/AgCl (1 M KCl). b) Linear regression trendlines for the average anodic and cathodic peak current versus the scan rate and c) the square root of the scan rate.

Once it was determined that the rate of the redox reaction of NR is largely diffusion-controlled, chronoamperometry was employed to determine the diffusion coefficient. We chose this technique since the concentration of NR within capsule samples and number of electrons transferred during the reduction were still unknown. Chronoamperograms were taken at a Au ultramicroelectrode (Au UME,  $r = 6.25 \mu\text{m}$ ) using a sample interval of 1 ms per point, termed the intermediate time region by Denuault and co-workers in 1991 when the method was developed.<sup>30</sup> Data was collected between 0 and -1.3 V vs. Ag/AgCl (1 M KCl). Within the time region used, the diffusion coefficient may be determined simply by **Equation 2.4** (reprinted below),

$$\frac{i_a(t)}{i_{d,ss}} = (\pi^2/4)a(Dt)^{-1/2} + 1 \quad \text{Equation 2.4}$$

where  $\frac{i_a(t)}{i_{d,ss}}$  is the chronoamperometric current normalized by the steady state current,  $a$  is the radius of the electrode,  $D$  is the diffusion coefficient, and  $t$  is the time in seconds. Results are typically within 1% for  $t_i$  greater than one diffusion time frame.<sup>30</sup> To approximate the diffusion coefficient, normalized current is plotted as a function of  $t^{-1/2}$  (**Figure 3.6d**). A linear regression of this plot was used to determine the slope and the intercept over the intermediate time region. The intercept in this region should be approximately 1 based on the literature.<sup>30</sup> The experimental diffusion coefficient was determined by **Equation 2.5** (reprinted below),

$$D = \pi a^2 / 16S^2 \quad \text{Equation 2.5}$$

where  $a$  is the radius of the electrode and  $S$  is the slope of the linear regression.<sup>30</sup> The experimental data used to create the linear regression is presented in **Figures 3.6b-c**. As previously stated, this technique was done without prior knowledge of the number of electrons transferred ( $n$ ) during NR reduction and the concentration of NR in solution. The average diffusion coefficient of NR was determined to be  $4.6 \times 10^{-6} \pm 0.1 \times 10^{-6} \text{ cm}^2 \text{ s}^{-1}$  ( $N = 3$ ). This diffusion coefficient agrees well with that of NADH ( $D = 2.4 \times 10^{-6} \text{ cm}^2 \text{ s}^{-1}$ ) as the structure of NADH is larger than NR.<sup>31</sup>



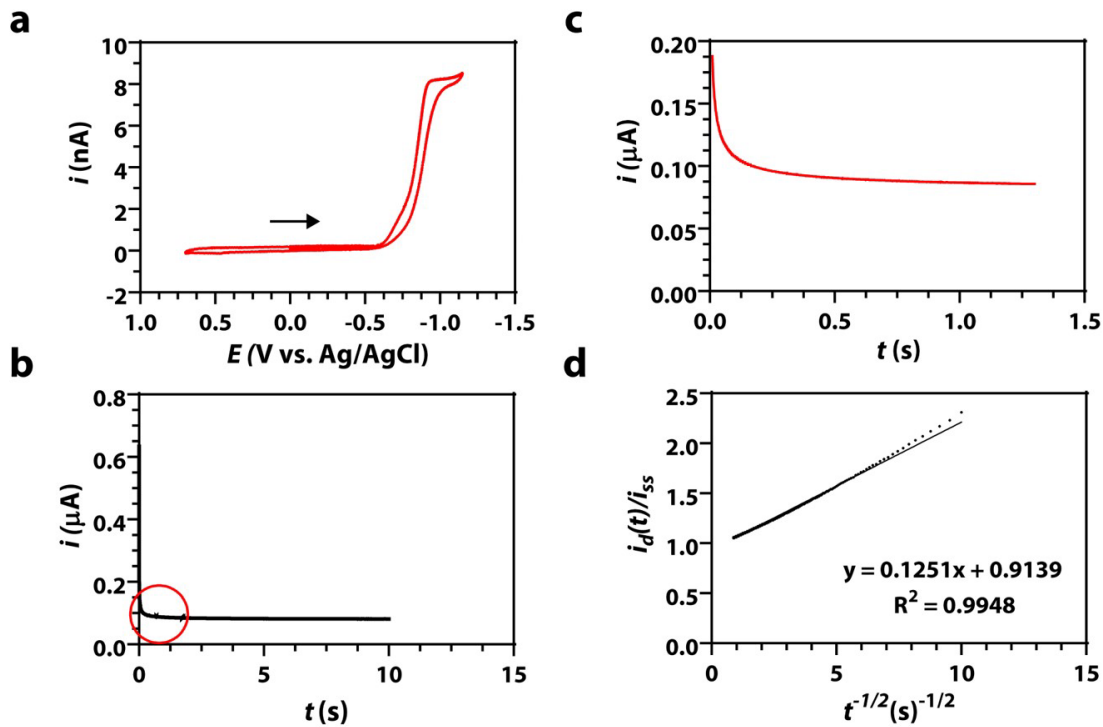


**Figure 3.6. Chronoamperometry of Nicotinamide Riboside**

a) Cyclic voltammogram of NR capsule contents in 250 mM KCl at a Au UME ( $r = 6.25 \mu\text{m}$ ) vs. Ag/AgCl (1 M KCl). b) Initial step of the chronoamperogram of NR capsule contents in 250 mM KCl obtained, after sparging with  $\text{N}_2$  gas, at the Au UME vs. Ag/AgCl (1 M KCl) with the area of interest circled in red. c) The area of interest of the chronoamperogram. d) Linear regression of the normalized current versus the inverse square root of the time based on the raw data shown in Figure 3.6c.

### 3.1.4 Determination of Electrons Transferred

In order to determine the concentration of NR by electrochemical means, the diffusion coefficient and number of electrons transferred ( $n$ ) during the redox mechanism must be known. Square wave voltammetry, a pulse voltammetry technique valued for background suppression and sensitivity, was used to approximate the number of electrons transferred during NR reduction. In cases where the reactant and product are freely diffusing species, the full width at half of the maximum peak (FWHM) can be used as a diagnostic parameter for the number of electrons transferred. A one-electron transfer event is represented by a FWHM of approximately 98 mV.<sup>32</sup>

Square wave voltammograms of NR capsule contents soluble in 10 mL 1 mM ferrocenemethanol in 250 mM KCl were obtained using a GC macroelectrode ( $r = 0.0015$  m). The electrode was pulsed between +0.5 and -1.3 V vs. Ag/AgCl (1 M KCl) for data collection. Pt foil was used as the counter electrode. Oxidation of ferrocenemethanol, a well-known one-electron transfer mediator, produced a FWHM of  $97 \pm 7$  mV ( $N = 6$ ) (**Figure 3.7** inset), validating the use of the electrochemical technique. Reduction of NR is shown at more negative potentials ( $E_{p,c} = -1.05$  V vs. Ag/AgCl) of the voltammogram in **Figure 3.7** with an average FWHM of  $101 \pm 3$  mV ( $N = 5$ ), indicating a one-electron reduction mechanism. A Student's  $t$ -test at 95% confidence indicates that these FWHM values are statistically the same and that the null hypothesis cannot be rejected, providing further evidence that the number of electrons transferred during the reduction of NR is one.

With the number of electrons transferred and the diffusion coefficient, the concentration of NR capsule contents soluble in 10 mL of 250 mM KCl was quantified by cyclic voltammetry of the molecule on a GC macroelectrode ( $r = 0.0015$  m) vs. Ag/AgCl (1 M KCl). The average

concentration determined using 6 TRU Niagen<sup>®</sup> capsules was  $47 \pm 3$  mM NR in 250 mM KCl.

Both values were determined without the use of standards or a calibration curve.

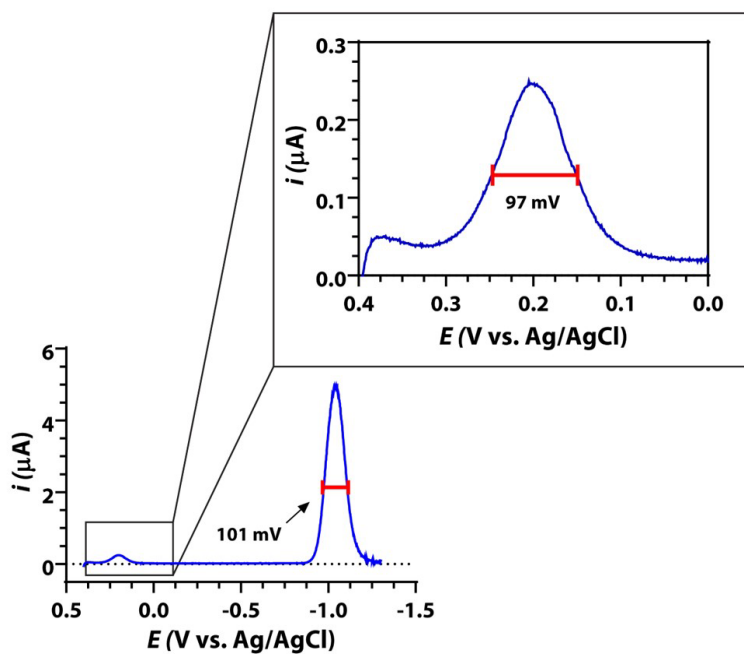


**Figure 3.7. Square Wave Voltammetry of Nicotinamide Riboside**

Square wave voltammograms of 1 mM ferrocenemethanol (control) and NR capsule contents in 250 mM KCl obtained on a GC macroelectrode ( $r = 0.0015$  m) vs. Ag/AgCl (1 M KCl). The red bar represents the FWHM.

### 3.1.5 Mechanistic Insight through Electrolysis

Occasionally throughout the characterization process, two oxidation peaks were observed after the reduction of NR, with the oxidation peak between 0.13 V and 0.25 V vs. Ag/AgCl (1 M KCl) being consistently more dominant. These oxidation peaks were only observed after the reduction of NR, with the dominant peak assumed to be representative of the oxidation of the kinetic product. This characteristic is common amongst  $\text{NAD}^+$  boosters and  $\text{NAD}^+$ .  $\text{NAD}^+$  reduction is a one-electron transfer mechanism that results in the formation of a free radical species. Following the formation of the radical, the radical dimerizes. This dimer was described as the kinetically favorable product by Anne and co-workers in 1992.<sup>33, 34</sup> Studies show that oxidation may result in two peaks due to oxidation of the radical species following cleavage of the dimer and oxidation of the dimer itself; one must note that the redox pathway of  $\text{NAD}^+$  was hypothesized to follow an EC redox mechanism.<sup>31, 33, 34</sup> Nicotinamide follows a similar reduction mechanism, but the reduction product may be oxidized by dissolved oxygen if substituted by an alkyl or hydroxyalkyl group on the nitrogen of the pyridine ring.<sup>35</sup> Furthermore, the chemical mechanisms of NR analogs suggest the formation of a kinetically favorable dimer following reduction of the analogs leading to the oxidation of the dimer and the radical species formed following cleavage of the dimer (**Figure 3.8**).

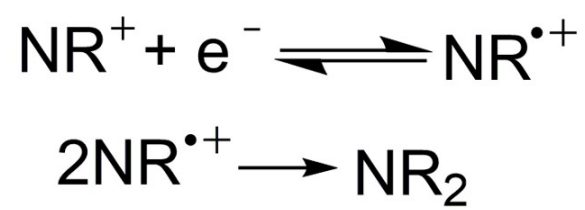


**Figure 3.8. Schematic of Nicotinamide Riboside EC<sub>dim</sub> Mechanism**

EC<sub>dim</sub> mechanism for the reduction of nicotinamide riboside.

Bulk electrolysis of NR was completed to investigate the mechanism with respect to NR and to determine the thermodynamically favorable product of NR reduction, whose oxidation was generally overshadowed by that of the kinetically favorable product in initial cyclic voltammetry experiments. For bulk electrolysis, a NR sample was prepared and filtered as done previously, and the 10 mL sample was placed in the middle component of a bulk electrolysis cell (**Figure 2.7**). On the left and right compartments of the cell, separated from the middle compartment by two frits, 250 mM KCl was added. A Pt wire coil was placed in the left compartment to act as the counter electrode and a Ag/AgCl (1 M KCl) electrode was placed in the right compartment to act as the reference electrode. Prior to bulk electrolysis, a cyclic voltammogram was collected at a GC ( $r = 0.0015$  m) macroelectrode placed in the middle compartment. The macroelectrode was replaced by a GC rod for bulk electrolysis. Bulk electrolysis of NR was performed at  $-1.2$  V vs. Ag/AgCl for approximately 3 hours (**Figure 3.9b**). During the experiment, the NR solution was bubbled with N<sub>2</sub> gas to increase mass transfer by convection to the GC rod. Following bulk electrolysis, an additional cyclic voltammogram was captured on a GC macroelectrode to characterize the product.

The final cyclic voltammogram showed two oxidation peaks of  $\mu$ A peak currents at approximately  $+0.25$  V and  $+0.60$  V vs. Ag/AgCl (**Figure 3.9c**) with the initial oxidation peak in **Figure 3.9a** being orders of magnitude larger.

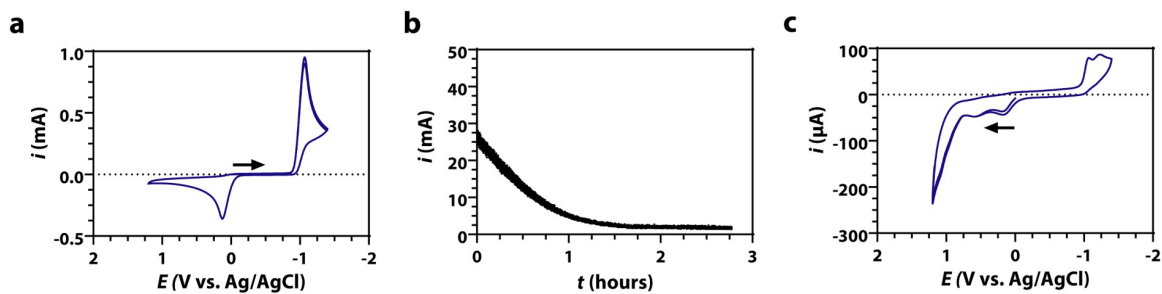


**Figure 3.9. Bulk Electrolysis of Nicotinamide Riboside**

Bulk electrolysis experiment results showing: a) a cyclic voltammogram (CV) of NR in 250 mM KCl at a GC macroelectrode ( $r = 0.0015$  m) vs. Ag/AgCl (1 M KCl), b) an  $i-t$  trace of bulk electrolysis results at a GC rod vs. Ag/AgCl (1 M KCl), and c) a CV of the NR bulk electrolysis product in 250 mM KCl at a GC macroelectrode ( $r = 0.0015$  m) vs. Ag/AgCl (1 M KCl). A Pt coil wire was used as the counter electrode to collect Figures 3.9a-c.



Although the final voltammogram showed the presence of two oxidation peaks at much lower currents, the voltammogram did not show currents near the magnitude of NR reduction pre-electrolysis. This indicates that some follow-up reaction occurs. Importantly, our results indicate that the dimerized species, if formed, may not be the kinetic product (*vide infra*). In addition, bulk electrolysis confirmed the square wave voltammetry results in that one electron is transferred during the reduction.

Following bulk electrolysis of NR, the product and an NR standard were analyzed with a Q Exactive HF-X (ThermoFisher, Bremen, Germany) mass spectrometer. Samples were introduced *via* a heated electrospray source (HESI) at a flow rate of 10  $\mu\text{L}/\text{min}$ . One hundred time domain transients were averaged in the mass spectrum. HESI source conditions were set as: 100  $^{\circ}\text{C}$  nebulizer temperature, sheath gas (nitrogen) 15 arb, auxiliary gas (nitrogen) 5 arb, sweep gas (nitrogen) 0 arb, 250  $^{\circ}\text{C}$  capillary temperature, RF voltage 100 V. The mass range was set to 600-2000  $m/z$ . All measurements were recorded at a resolution setting of 120,000. Solutions were analyzed at 0.1 mg/mL or less based on responsiveness to the ESI mechanism. Xcalibur (ThermoFisher, Bremen, Germany) was used to analyze the data. Molecular formula assignments were determined with Molecular Formula Calculator (v 1.2.3). All observed species were singly charged, as verified by unit  $m/z$  separation between mass spectral peaks corresponding to the  $^{12}\text{C}$  and  $^{13}\text{C}^{12}\text{C}_{-1}$  isotope for each elemental composition. In contrast to the redox mechanisms of NR analogs, LCMS data (**Figure 3.10**) established the dimer as the thermodynamically favorable product. Within the first trial, the  $[\text{M}^+]$  fragment of the dimer was present at an  $m/z$  of  $509.2 \pm 2.3$ . Within the subsequent trial, the  $[2\text{M}^+]$  fragment of the dimer was present at an  $m/z$  of  $511.2 \pm 0.3$ . Reduced or radical forms of NR were also observed in the background of the mass spectra of the product, but could not be differentiated due to limited resolution. Further confirmation of

the thermodynamic product was evident in the absence of the dimer or reduced forms of NR within the standard. From these results, we propose the oxidation peak at +0.15 V vs. Ag/AgCl in initial cyclic voltammograms is due to the kinetic product, likely the radical before dimerization. The oxidation potential of the radical is much more positive than the reduction potential of NR, indicating a significant structural or solvation rearrangement after electron transfer.

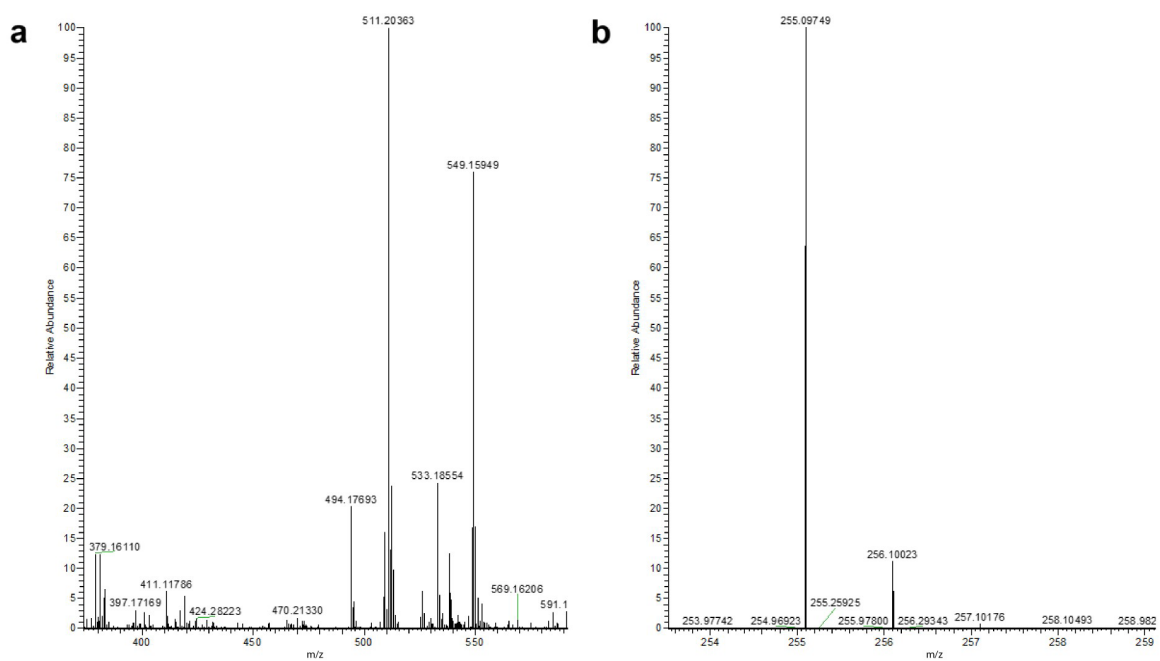


**Figure 3.10. Mass Spectrum of Reduced Nicotinamide Riboside**

Mass spectra of: a) the NR bulk electrolysis product and b) the NR standard.

The metabolism of NR to  $\text{NAD}^+$  within the body is mediated by transferase and kinase enzymes. NR is phosphorylated by an NR kinase to produce NMN. Lastly, an adenylyl-transferase converts NMN to  $\text{NAD}^+$ .<sup>27</sup> To replicate NR reduction in human cells, cyclic voltammetry was completed in whole cell lysate. MRC-5 P19 cells, normal human lung cells, were maintained in a 15 cm-diameter tissue culture dish within a copper-lined incubator at 37 °C, 5%  $\text{CO}_2$ , and 10%  $\text{O}_2$ . Full growth media was composed of DMEM – high glucose, 10% FBS, and 1% penicillin-streptomycin. At > 75% confluence, spent media was removed from the tissue culture dish and cells were washed with 10 mL DPBS (1X, pH 7.4). The tissue culture dish was charged with 45 mL ultrapure Milli-Q water, then placed on a shaker rotating at 30 rpm for approximately 1 hour and 30 minutes. Cell morphology was monitored every 10 minutes until cell lysis was confirmed. The lysate was centrifuged at 1000 rpm at 4 °C for 5 minutes. The supernatant was used to prepare 10 mL of 1 mM nicotinamide riboside chloride (M.W. 290.70 g/mol, 0.00316 g) in whole cell lysate. To fully dissolve nicotinamide riboside chloride, the solution was sonicated for 15 minutes. A background cyclic voltammogram of whole cell lysate was collected at a GC macroelectrode ( $r = 0.0015$  m) vs. Ag/AgCl (1 M KCl) after purging the solution for 5 minutes. Using the same procedure, cyclic voltammograms of 1 mM nicotinamide riboside chloride in whole cell lysate and in DPBS (1X, pH 7.4) were collected. A glassy carbon rod was used as the counter electrode to collect each cyclic voltammogram.

Cyclic voltammograms of NR reduction in whole cell lysate depict a different redox pathway than the reduction of NR in buffer (**Figure 3.11**). This observation may support the suggested active-site dependent model of NR metabolism in the body, indicative of inner-sphere behavior at the electrode surface.<sup>36</sup> While small shifts and kinetic effects may be due to non-specific adsorption of species on the electrode surface, the product peak differs most in whole

cell lysate. Our new insight on the mechanism of NR reduction in aqueous systems provides the community with a better understanding of the potential pathways of NR prior to biosynthesis of NAD<sup>+</sup>, while also providing electrochemical evidence of a salvage pathway within human primary cells. Mechanistic insight into the reduction of NR with respect to biological samples will be a topic of future investigations.

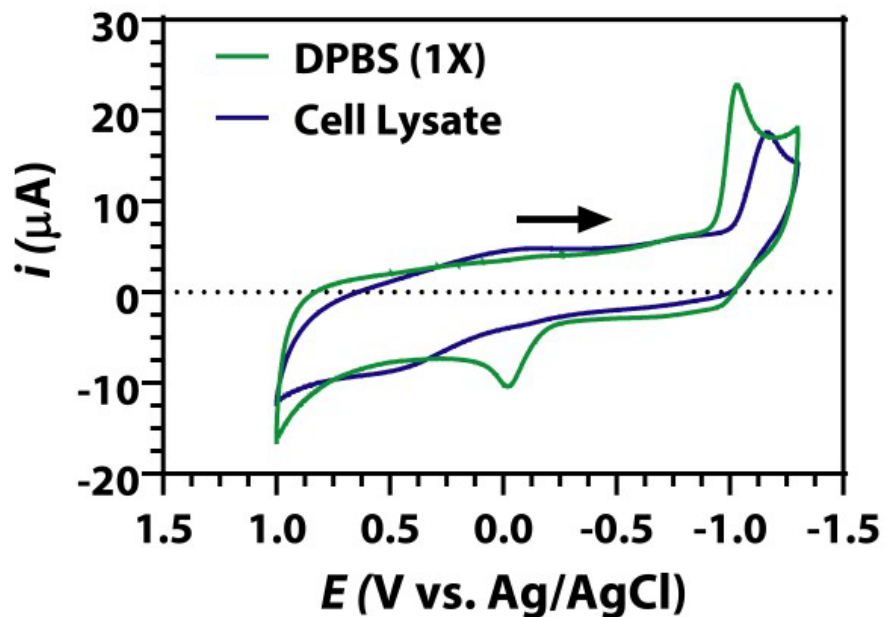


**Figure 3.11. Cyclic Voltammogram of Nicotinamide Riboside in Whole Cell Lysate**

Cyclic voltammograms of 1 mM NR chloride in DPBS (1X, pH 7.4) and in whole cell lysate of MRC-5 P19 cells on a GC macroelectrode ( $r = 0.0015$  m) vs. Ag/AgCl (1 M KCl). A glassy carbon rod was used as the counter electrode.

### 3.2 Scanning Electrochemical Microscopy of Living Cells *via* Nicotinamide Riboside Reduction

While electrochemically imaging pre-cancerous pancreatic cells (*i.e.*, HPNE-KRAS cells) using the procedures outlined in **Chapter 2** section **2.4**, we observed a cell detachment (*i.e.*, a loss in cell viability) prior to completing electrochemical imaging in 1 mM ferrocenemethanol in DPBS (1X, pH 7.4). Subsequently, we used NR as an alternative redox mediator. TRU Niagen<sup>®</sup> capsule contents were added to 10 mL DPBS (1X, pH 7.4), The solution was sonicated for 15 minutes. Following sonication, the solution was filtered using a 1  $\mu\text{m}$  PTFE syringe filter to remove insoluble species. HPNE-KRAS cells were subcultured in a 3.5 cm-diameter tissue culture dish in DMEM-high glucose supplemented with 10% FBS and 1% penicillin-streptomycin. At medium density, full growth media was aspirated from the dish and the cells were rinsed with DPBS (1X, pH 7.4). After aspirating the rinse solution, 2 mL of the NR capsule solution was added. Electrochemical imaging proceeded as described in **Chapter 2** section **2.4**, except the probe potential was set to -1.3 V vs. Ag/AgCl (1 M KCl) at a Au microelectrode tip ( $r = 6.25 \mu\text{m}$ ). The resulting images were normalized by the steady state current (*i.e.*,  $i_{t,\infty}$  where  $d \geq 10a$ , where  $d$  is the tip-to-substrate distance and  $a$  is the radius of the electrode) to interpret feedback unambiguously regardless of tip position. Corresponding optical images were captured using the instrumentation outlined in **Chapter 2**; specifically, the 20 $\times$  objective and a digital CMOS camera were used to capture optical images. Preliminary electrochemical images displayed a positive feedback response with variation in the electrochemical response amongst cells (**Figure 3.12**), implicating electrochemical imaging *via* NR reduction as a method to examine cell metabolism.

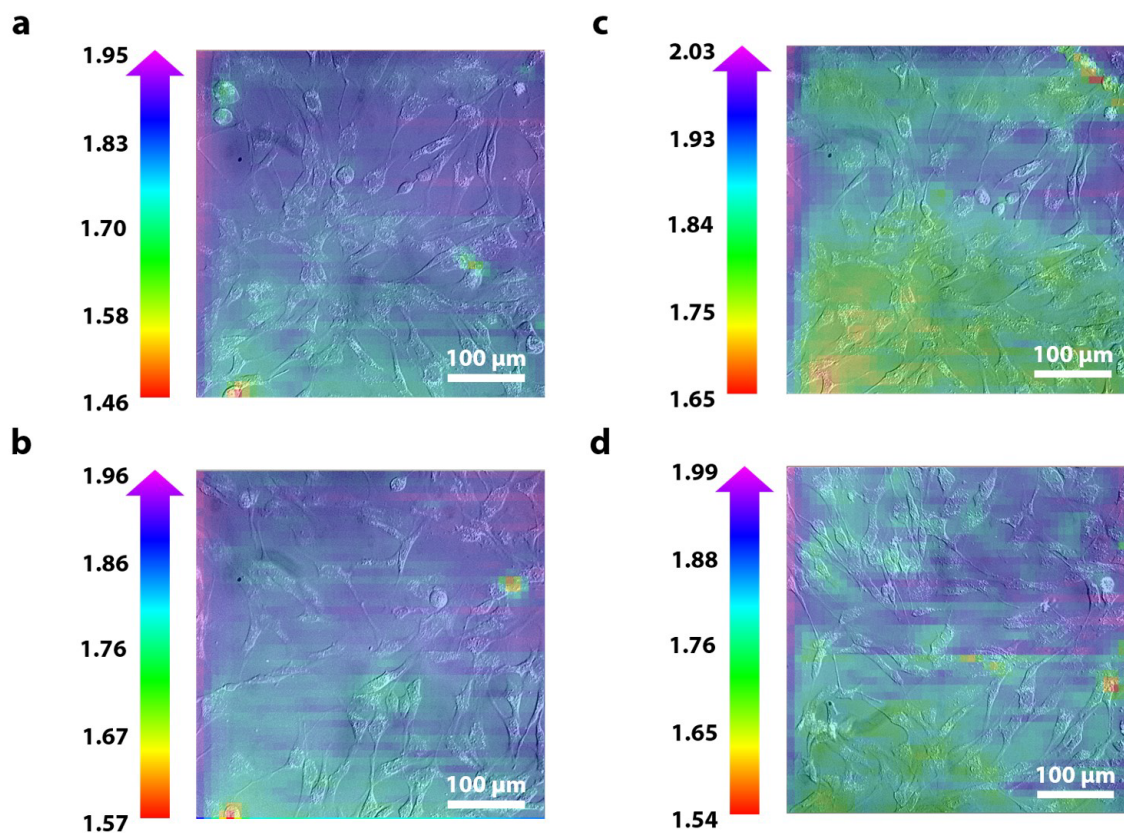


**Figure 3.12. Correlated Optical and Electrochemical Images of HPNE-KRAS Cells in Nicotinamide Riboside**

Sequential optical/electrochemical image overlays of HPNE-KRAS cells in a NR capsule solution in DPBS (1X, pH 7.4). Electrochemical images obtained with a Au microelectrode tip ( $r = 6.25 \mu\text{m}$ ) at  $-1.3 \text{ V}$  vs. Ag/AgCl (1 M KCl) and a GC rod counter electrode.



In addition, preliminary cyclic voltammograms at a Au microelectrode tip ( $r = 6.25 \mu\text{m}$ ) held 2.5 to 5.0  $\mu\text{m}$  above HPNE-KRAS cells in an NR capsule solution displayed an increase in the oxidation of reduced NR (**Figure 3.13**). Further investigations are necessary to distinguish the feedback mechanism responsible for the electrochemical response.

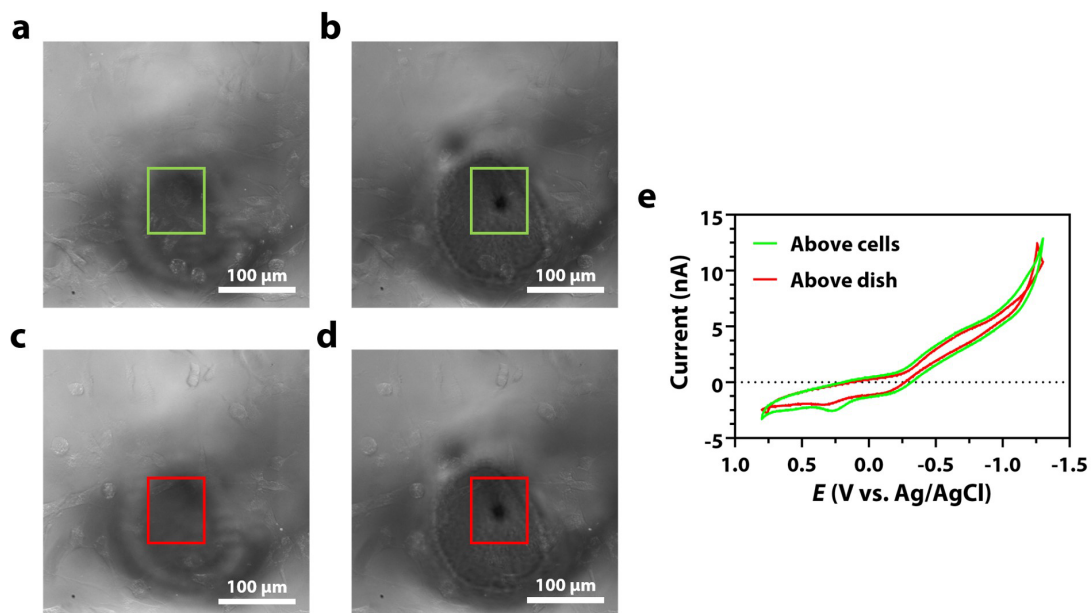


**Figure 3.13. Nicotinamide Riboside Redox Mechanism above HPNE-KRAS Cells**

Optical images of a Au microelectrode tip 100 μm above the dish surface (a & c), then 2.5 to 5 μm above HPNE-KRAS cells (b) or the dish (d). Corresponding cyclic voltammetry of the NR capsule solution 2.5 to 5 μm above cells or the dish is shown to the right (e).

### 3.3 Concluding Remarks<sup>2</sup> & Future Perspectives

Nicotinamide riboside (NR) is a biologically relevant small molecule with potential to improve our quality of life as we get older. Establishing the metabolic pathway of NR in the human body is necessary to better understand the value associated with the use of NR supplements as nicotinamide adenine dinucleotide (NAD<sup>+</sup>/NADH) boosters. In this chapter, we electrochemically characterized NR using a number of techniques using the electrode/electrolyte solution interface as a biological model. Based on our results, the initial one-electron reduction of NR is the result of a weak adsorption event, but the rate of the reaction is determined by mass transfer in the form of diffusion. The diffusion coefficient was determined without prior knowledge of the number of electrons transferred or the concentration of the analyte by chronoamperometry. Though the mechanism is slightly material dependent, preliminary experiments determined that the mechanism does not involve protons as it is not pH dependent. We hypothesized reduction of the supplement is followed by a chemical reaction, in which the radical product of the reduction forms a stable dimer (*i.e.*, an EC<sub>dim</sub> redox mechanism). To determine the kinetically and thermodynamically favorable products of NR reduction, bulk electrolysis was performed to capture the thermodynamic product followed by cyclic voltammetry of the product and LCMS analysis. Results confirmed the dimer as the thermodynamic product, but also showed evidence of a second oxidation product in low abundance indicating an EC<sub>dim</sub> mechanism. We conclude that NR reduction forms a radical species that is oxidized due to kinetic control, but dimerized due to thermodynamic control. The result of two oxidation peaks following reduction depicts the oxidation of the radical and the

---

<sup>2</sup> This section previously appeared as an article in *ChemElectroChem*. It was reproduced with permission from John Wiley and Sons. The original citation is as follows: S. Goines and J. E. Dick, *ChemElectroChem*, 2019, **6**, 5264-5272.

subsequent dimer. Furthermore, this chapter provides a method for the complete electrochemical characterization of an unknown electroactive species.

In addition, we used NR as the redox mediator in scanning electrochemical microscopy (SECM) of pre-cancerous pancreatic (HPNE-KRAS) cells. We observed a variation in feedback above cells, implicating NR reduction as a means of examining cell metabolism. These preliminary results also suggest that the metabolic pathway of NR may be examined electrochemically by SECM. Correlated fluorescence microscopy should be able to elucidate variations in cell cycle and viability, which may be responsible for the variation in feedback above cells. More specifically, NR supplementation has been implicated in increased oxidative metabolism and mitochondria function<sup>20</sup>, which may be monitored by fluorescence microscopy<sup>37</sup>. While typical biological SECM platforms are equipped with fluorescence microscopy, hyperspectral-assisted SECM would enhance our ability to investigate these variations with respect to slight spectral shifts.<sup>38</sup>

## REFERENCES

1. D. Polcari, P. Dauphin-Ducharme and J. Mauzeroll, *Chemical Reviews*, 2016, **116**, 13234-13278.
2. B. Liu, S. A. Rotenberg and M. V. Mirkin, *Proceedings of the National Academy of Sciences of the United States of America*, 2000, **97**, 9855-9860.
3. A. J. Bard, X. Li and W. Zhan, *Biosensors & Bioelectronics*, 2006, **22**, 461-472.
4. B. Liu, S. A. Rogenberg and M. V. Mirkin, *Analytical Chemistry*, 2002, **74**, 6340-6348.
5. Y. Matsumae, Y. Takahashi, K. Ino, H. Shiku and T. Matsue, *Analytica Chimica Acta*, 2014, **842**, 20-26.
6. S. Kuss, R. Cornut, I. Beaulieu, M. A. Mezour, B. Annabi and J. Mauzeroll, *Bioelectrochemistry*, 2011, **82**, 29-37.
7. J. Mauzeroll, A. J. Bard, O. Owhadian and T. J. Monks, *Proceedings of the National Academy of Sciences of the United States of America*, 2004, **101**, 17582-17587.
8. J. Mauzeroll and J. Bard Allen, *Proceedings of the National Academy of Sciences*, 2004, **101**, 7862-7867.
9. Q. Chen and A. I. Cederbaum, *Mol Pharmacol*, 1997, **52**, 648-657.
10. S. Srivastava, *Clinical and Translational Medicine*, 2016, **5**.
11. M. V. Makarov and M. E. Migaud, *Beilstein Journal of Organic Chemistry*, 2019, **15**, 401-430.
12. A. Hikichi, H. Mugaruma, H. Inoue and T. Ohsawa, *Electrochemistry*, 2017, **85**, 13-16.
13. M. B. Schultz, Y. C. Lu, N. Braidy and D. A. Sinclair, *Adp-Ribosylation and Nad+ Utilizing Enzymes: Methods and Protocols*, 2018, **1813**, 77-90.
14. L. Mouchiroud, R. H. Houtkooper and J. Auwerx, *Critical Reviews in Biochemistry and Molecular Biology*, 2013, **48**, 397-408.
15. C. Canto, K. J. Menzies and J. Auwerx, *Cell Metabolism*, 2015, **22**, 31-53.
16. M. S. Bonkowski and D. A. Sinclair, *Nature Reviews Molecular Cell Biology*, 2016, **17**, 679-690.
17. C. O. Schmakel, Santhana.Ks and P. J. Elving, *Journal of the Electrochemical Society*, 1974, **121**, 345-353.
18. C. R. Martens, B. A. Denman, M. R. Mazzo, M. L. Armstrong, N. Reisdorph, M. B. McQueen, M. Chonchol and D. R. Seals, *Nature Communications*, 2018, **9**.

19. W. Giblin, M. E. Skinner and D. B. Lombard, *Trends in Genetics*, 2014, **30**, 271-286.
20. C. Canto, R. H. Houtkooper, E. Pirinen, D. Y. Youn, M. H. Oosterveer, Y. Cen, P. J. Fernandez-Marcos, H. Yamamoto, P. A. Andreux, P. Cettour-Rose, K. Gademann, C. Rinsch, K. Schoonjans, A. A. Sauve and J. Auwerx, *Cell Metabolism*, 2012, **15**, 838-847.
21. E. F. Fang, S. Lautrup, Y. J. Hou, T. G. Demarest, D. L. Croteau, M. P. Mattson and V. A. Bohr, *Trends in Molecular Medicine*, 2017, **23**, 899-916.
22. H. C. Chang and L. Guarente, *Trends in Endocrinology and Metabolism*, 2014, **25**, 138-145.
23. L. Rajman, K. Chwalek and D. A. Sinclair, *Cell Metabolism*, 2018, **27**, 529-547.
24. A. E. Kane and D. A. Sinclair, *Circulation Research*, 2018, **123**, 868-885.
25. J. A. Baur, Z. Ungvari, R. K. Minor, D. G. Le Couteur and R. de Cabo, *Nature Reviews Drug Discovery*, 2012, **11**, 443-461.
26. M. Bomgardner, *Chemical & Engineering News*, 2018, **96**, 26-27.
27. J. Yoshino, J. A. Baur and S. I. Imai, *Cell Metabolism*, 2018, **27**, 513-528.
28. K. Takamura, A. Mori and F. Kusu, *Bioelectrochemistry and Bioenergetics*, 1981, **8**, 229-238.
29. O. Warburg, *Biochem Z*, 1924, **152**, 309-344.
30. G. Denuault, M. V. Mirkin and A. J. Bard, *Journal of Electroanalytical Chemistry*, 1991, **308**, 27-38.
31. J. Moiroux and P. J. Elving, *Journal of the American Chemical Society*, 1980, **102**, 6533-6538.
32. A. J. Bard and L. R. Faulkner, in *Electrochemical Methods: Fundamentals and Applications*, eds. D. Harris, E. Swain, C. Rodney and E. Aiello, John Wiley & Sons, Inc., New York, NY, 2 edn., 2001, ch. Polarography and Pulse Voltammetry, pp. 275-301.
33. A. Anne, P. Hapiot, J. Moiroux and J. M. Saveant, *Journal of Electroanalytical Chemistry*, 1992, **331**, 959-970.
34. J. Moiroux, S. Deycard and T. Malinski, *Journal of Electroanalytical Chemistry*, 1985, **194**, 99-108.
35. M. Miller, B. Czochralska and D. Shugar, *Bioelectrochemistry and Bioenergetics*, 1982, **9**, 287-298.
36. J. A. Khan, S. Xiang and L. Tong, *Structure*, 2007, **15**, 1005-1013.

37. E. B. Gökerküçük, M. Tramier and G. Bertolin, *Genes (Basel)*, 2020, **11**.
38. S. Goines, M. Deng, M. W. Glasscott, J. Leung and J. E. Dick, *Analyst*, 2022, **147**, 2396-2404.

## **Chapter 4    Hyperspectral-Assisted Scanning Electrochemical Microscopy**

Gaining mechanistic insight from scanning electrochemical microscopy (SECM) results may be difficult when considering each component of the experimental design, especially when the sample under investigation is as complex as a living, human cell. When studying two-dimensional cell cultures, one must consider intercellular interactions, such as paracrine (or hormonal) interactions, as well as intracellular interactions, such as electron transfer within a cell. Moreover, heterogeneities among cells of the same type create additional complications when deciphering the mechanisms responsible for the electrochemical signal. To enhance our understanding of the data collected using a scanning electrochemical microscope platform, the electroanalysis is often coupled with other analytical techniques such as optical microscopy, surface plasmon resonance spectroscopy, Raman spectroscopy, infrared spectroscopy, and mass spectrometry.<sup>1</sup>

### **4.1 Correlated Scanning Electrochemical Microscopy**

A scanning electrochemical microscope is often referred to as a “chemical microscope” because it provides topographical information as well as chemical reactivity information related to the substrate under investigation.<sup>2</sup> Scanning electrochemical microscopy is revered among other analytical techniques because it offers high temporal and spatial resolution in addition to molecular selectivity.<sup>1</sup> While the temporal resolution is based on the achievable scan rate of the positioner and the sampling interval of the electrochemical method in use, the spatial resolution is based on the diameter of the probe electrode and the molecular selectivity is based on the



electrochemical reaction used to characterize the substrate. Unfortunately, scanning electrochemical microscopy remains unused in laboratories beyond electroanalytical groups because it lacks the use of standardized reference samples and methods for increased reliability and reproducibility in complex areas such as bioanalytical chemistry.<sup>1</sup>

Today, scanning electrochemical microscopy is often coupled to additional analytical techniques that are more commonly used to validate the electrochemical method. Scanning electrochemical microscopy is generally correlated to spectroscopic techniques (*e.g.*, mass spectroscopy, Raman spectroscopy, and infrared spectroscopy) within materials chemistry research. For example, Etienne and co-workers investigated the corrosion of Zn (Mg, Al) coatings on steel by shear force positioning of the probe electrode (*i.e.*, by positioning the probe at an angle above the substrate surface) to characterize the topography of the surface, and simultaneously defined the chemical bonds using Raman spectroscopy with a confocal Raman micro-spectrometer.<sup>3</sup> Surface characterization was also achieved by Wang and co-workers in 2010 using total reflection Fourier-transformed infrared spectroscopy following polymerization by feedback mode scanning electrochemical microscopy on a substrate; the combination of these techniques allowed investigators to define the polymerization mechanism as well as the percentage of surface modified.<sup>4</sup> Scanning electrochemical microscopy has also shown value in the field of forensics as a means of imaging latent human fingerprints when coupled with matrix-assisted laser desorption/ionization mass spectrometry<sup>5</sup> and optical microscopy<sup>6, 7</sup>. Additionally, mass spectrometry has been coupled with scanning electrochemical microscopy for biological applications such as determining the electrochemical activity of surface spotted enzymes following electrospray ionization mass spectrometry.<sup>5</sup> For most biological applications, scanning electrochemical microscopy is combined with optical microscopy for constant-distance imaging

to improve spatial resolution and one's ability to differentiate between features that may overlap (*e.g.*, diffusional broadening may convolute electrochemical images necessitating optical microscopy, while features smaller than the diffraction limit of an optical system necessitate the high sensitivity of electrochemical microscopy). A specific example of this was presented in 2005 by Yamada and co-workers when imaging neurites; electrochemical images showed areas of decreased current, implying the existence of raised structures undetected in optical micrographs.<sup>2</sup>

The precise determination of cellular boundaries and the complexity of biological pathways make optical microscopy an ideal correlated technique for biological scanning electrochemical microscope experiments involving living cells; optical microscopy provides ease-of-use and optical validation. For example, time-lapse optical and electrochemical imaging has been used simultaneously to monitor the movement and morphology of human bladder cancer cells in real time.<sup>8</sup> In addition to providing ease-of-use and increasing spatial resolution, optical microscopy also provides access to fluorescence detection systems.<sup>9</sup> Generally, biological scanning electrochemical microscope platforms are composed of an inverted microscope, equipped with standard filter cubes for fluorescence microscopy, with a stepper/piezo motorized positioner situated just above the microscope stage for correlated optical and electrochemical imaging.

Fluorescence imaging allows for localization of features within a sample and differentiation between cells within dynamic two-dimensional cell culture systems. Following transfection of cells with DNA- or RNA-specific fluorescence probes, researchers can discern between cell boundaries within co-culture systems.<sup>10</sup> For example, Kuss and co-workers demonstrated the ability to differentiate between HeLa-multidrug resistant and normal HeLa

cells by correlating electrochemical and optical images.<sup>11</sup> In this experiment, each piece of information contributed data that was unique and valuable; fluorescence imaging was used to differentiate between normal and resistant cells, while correlated electrochemical imaging was used to determine the apparent heterogeneous rate constants and tip-to-substrate distance profiles for each cell type.<sup>11</sup> Here, tip-to-substrate distance was determined electrochemically, but others have used super resolution fluorescence imaging to optically discern tip-to-substrate distances on the nanoscale with precision as low as 25 nm.<sup>12</sup> For correlated fluorescence studies of biological samples, transfection is not always necessary; investigators may also make use of fluorescence indicators and redox assays to draw conclusions concerning complex biological samples.

Moreover, fluorescence microscopy is a robust means to studying the biological interactions of living cells within two-dimensional cell culture systems. To uncover dynamic changes with respect to paracrine or intercellular interactions, one must use multiple fluorescence probes or focus on analytes with known spectral properties.<sup>13-15</sup> Fluorescence microscopy allows one to track the activity of fluorescently-tagged cellular organoids or biomolecules at a probe-specific wavelength; furthermore, fluorescent probes have increased the spatial resolution of live cell imaging within biological systems research.<sup>16</sup>

The use of fluorescence microscopy to distinguish between cell boundaries prompted the use of correlated electrochemical techniques such as electrogenerated chemiluminescence (also referred to as electrochemiluminescence or ECL). Here, a luminescent, excited state of an electroactive species is generated by applying a potential sufficient to induce a high-energy electron-transfer mechanism.<sup>17, 18</sup> The signal produced from ECL has a near-zero background making the technique advantageous for sensitive and selective measurements.<sup>17</sup> ECL-active species are often used as labels for biological molecules to perform high throughput

immunoassays.<sup>17</sup> Recently, ECL has been used to image single cells. In 2015, Zhou and co-workers collected negative images of HeLa cells by adsorbing the cells onto an ITO substrate and electro-generating chemiluminescence of a luminophore in solution.<sup>19</sup> Later, Zhang and co-workers imaged microRNA content within limited regions of the cell membrane of tumor cells by interrogating an extracellular ECL mechanism reliant on reactive oxygen species (ROS) released from cells.<sup>20</sup> While ECL is localized to the cell membrane because the charged coreactants generally required for ECL mechanisms are not membrane permeable, this technique serves as a valuable tool for studying membrane transport along the plasma membrane with single cell resolution.<sup>21</sup> Moreover, there is a need for multicolor ECL to elucidate complex modes of transport and improve multiplexed bioassays.<sup>22</sup> By preparing an enhanced ECL luminophore with concomitant multicolor ECL emission, Voci and co-workers widened ECL methodology.<sup>22</sup> Unfortunately, typical microscopy instrumentation is limited to the use of conventional filter cubes, which only allow a user to excite or measure light within a set range of wavelengths.

As the field of live cell microscopy continues to develop, new techniques such as hyperspectral imaging, are necessary to widen the scope of research. The use of tunable filters in hyperspectral imaging has allowed users to increase spectral discrimination in comparison to the use of standard gratings.

## **4.2 Hyperspectral Imaging**

Spectral imaging combines the use of optical microscopy and spectroscopy to obtain spatial and spectral information from each pixel of an image.<sup>14, 15, 23</sup> NASA initially introduced spectral imaging systems to study temperature and weather patterns, but such systems have been broadly developed for bioanalytical research<sup>15</sup>; for example, spectral imaging has been used to

understand pharmacological responses<sup>15</sup>, single-cell viability<sup>24, 25</sup>, and carcinogenesis<sup>25-29</sup>. While most methods depend on labeling the analyte of interest, others have used spectral imaging to characterize analytes with known spectral properties, such as the experimental drug doxorubicin with known fluorescence properties.<sup>15</sup> Hyperspectral imaging may be viewed as monumental to the field of biological imaging as different biochemical complexes are known to display different spectral signatures.<sup>14</sup>

Specifically, hyperspectral imaging allows one to take a series of images over time at various excitation or emission wavelengths that results in a lambda stack of images. This series of images is combined to provide a hyperspectral image in which a spectrum can be obtained at each pixel of the image (see **Figure 4.8** below).<sup>30</sup> The resulting spectral data can be represented as a three-dimensional cube or a stack of multiple two-dimensional images (*i.e.*, a lambda stack of images); here, the depth between each image is a function of the scanned wavelength.<sup>14</sup> Additionally, for simplification, the spectral data is often represented as a typical excitation or emission spectrum. The spectral resolution of these data is dependent on the diffraction gratings, integrated prisms, or filter cubes used by a spectral detector within the optical system.<sup>30, 31</sup>

Hyperspectral imaging is commonly used within nanomaterials research as a means to image single metal nanoparticles based on their surface plasmon resonance (*i.e.*, the energy produced from the production of energetic plasmonic electrons due to the oscillation of conduction band electrons within the metal nanoparticles that are in resonance with the oscillating electric field of the incident light).<sup>32-35</sup> Paired with complementary electrochemical techniques, hyperspectral systems may be used to optically resolve and study electrochemical systems.<sup>32, 35, 36</sup> When applied to biological systems, hyperspectral imaging techniques can be used as a means to track cellular interactions. Though some have developed label-free methods

of hyperspectral imaging, such as hyperspectral imaging based on resonant technology, most rely on fluorescence.<sup>26, 34, 37</sup> By combining hyperspectral imaging with electrochemical techniques, researchers have developed methods to quantitatively study redox reactions of single entities in real time.<sup>32, 35, 38</sup> Development of a cost-efficient system that allows this quantitative analysis is the goal of this work.

Hyperspectral imaging is often achieved when high resolution confocal microscopy is paired with time lapse imaging; within these systems tunable filters are used to discriminate between fluorophores within a sample.<sup>23</sup> Confocal microscopy is favored over conventional optical techniques for fluorescence imaging because it offers sufficient lateral resolution (defined as the shortest distance between two objects to distinguish between them when perpendicular to the light source; 180 nm for confocal systems<sup>39</sup>) to reduce background fluorescence, as well as optical axial resolution (defined as the shortest distance between two objects to distinguish between them when parallel to the light source; 500 nm for confocal systems<sup>39</sup>).<sup>40-42</sup> For spectral imaging, filter cubes within confocal systems are scanned to separate fluorophores based on a lambda stack acquired during a time lapse.<sup>23</sup> Here, a white light laser illumination source would be ideal, as it produces all wavelengths within the visible spectrum (*i.e.*, 380 to 700 nm). The cost of confocal systems often limits researchers to the use of conventional microscopes equipped with white light laser illumination sources. Saha and co-workers used their home-built hyperspectral-assisted scanning electrochemical microscope equipped with a white light laser illumination source to map individual Au nanorods (as small as 40 nm in width) based on their scattering spectra and measured their hydrazine oxidation efficiency using scanning electrochemical cell microscopy.<sup>32</sup> Though white light laser confocal microscopy and bright field microscopy have been used to acquire hyperspectral images of nanoparticles smaller than tens of

nanometers based on their surface plasmon resonance, the high cost of the laser is a deterrent compared to conventional systems.<sup>43,44</sup> The system presented in this dissertation permits the acquisition of hyperspectral images at a marketable cost. For example, Leica Stellaris white light laser confocal systems cost upwards of \$225,000 (without a scanning electrochemical microscope). This dissertation outlines a cost-effective, robust alternative to white light laser hyperspectral imaging: variable fluorescence bandpass hyperspectral imaging paired with scanning electrochemical microscopy for cell biology. The combined system costs roughly \$75,000 less than the aforementioned system.

### **4.3 Variable Fluorescence Bandpass Hyperspectral-Assisted Scanning Electrochemical Microscopy**

Our hyperspectral-assisted biological scanning electrochemical imaging platform widens the scope of biological imaging by allowing the user to capture correlated optical, electrochemical, and spectral data simultaneously. Additionally, our variable fluorescence bandpass source, characterized by a cost-efficient xenon illumination source (*i.e.*, \$5,830 vs. \$22,995 for an Energetiq EQ-99X-FC-S Fiber Coupled Laser-Driven Light Source) coupled to a Sutter Instrument<sup>®</sup> two-stage Lambda VF-5<sup>™</sup> filter changer equipped with VersaChrome<sup>®</sup> tunable filters, allows the user to capture standard fluorescence images as well as hyperspectral images with wavelength resolution ranging between 1 to 16 nm. More specifically, the user may capture emission spectra with 1 nm resolution within a single channel as opposed to collecting a single emission intensity for each conventional filter cube across multiple channels. Our tunable excitation filters have a dynamic range of 380 nm to 620 nm, while our tunable emission filters have a range of 440 nm to 700 nm.

Each independent measurement acts as a member of a set, with each piece contributing varying but useful information. The optical spatial resolution is dependent on the objective lens

in use and the diffraction limit of light; generally, 20× and 40× objective lenses with 959 nm and 559 nm resolution in the *xy* plane, respectively, are used. The wavelength and bandpass resolution are critical to capturing spectral data; a wavelength resolution of 1 nm is feasible if a spectrum is obtained within the bandpass resolution of a single VersaChrome® filter. If a combination of filters must be used to obtain the desired wavelengths within a spectrum, the user is limited by the highest bandpass resolution (*i.e.*, 16 nm) to avoid spectral overlap. Additionally, the spatial resolution of the electrochemical data can be adjusted by varying the size of the electrode tip in use. By using a nanoelectrode, nanometer spatial resolution, below the diffraction limit of light, can be achieved during electrochemical imaging.<sup>45</sup>

To obtain a fluorescence image, an excitation wavelength is directed through an inverted microscope using a VF-5<sup>TM</sup> filter changer, while a second filter changer is used to select wavelength-specific emitted photons to be collected by an adjacent digital camera. By specifying an excitation wavelength while scanning a series of emission wavelengths, we may obtain a set of hyperspectral images in which an emission spectrum can be recorded for each individual pixel within a frame. Alternatively, an excitation spectrum can also be recorded if excitation wavelengths are scanned while an emission wavelength is held constant. The importance of excitation scanning was highlighted by Favreau and co-workers in 2014 when they designed an excitation-scanning hyperspectral imaging system to increase signal-to-noise in biological imaging experiments. The group noted that emission scanning is often victim to reduced light sensitivity due to light attenuation from spectral filtering, making it less than ideal for time-sensitive and photosensitive studies.<sup>37</sup> Here, we constructed this imaging platform to mitigate the challenges associated with imaging two-dimensional cell cultures by combining hyperspectral imaging and scanning electrochemical microscopy (*i.e.*, differentiating cell types, low signal-to-



noise, determining the electrochemical contribution of each cell type, and distinguishing paracrine from intercellular communication effects<sup>46</sup>).

### 4.3.1 Instrumentation<sup>3</sup>

The variable fluorescence bandpass hyperspectral imaging system is composed of a Lambda LS xenon arc lamp (Sutter Instrument Company, Novato, CA), a Leica CTR advanced electronics box (Leica Microsystems, Germany), a Leica SP box LMT200 (Leica Microsystems, Germany), a Leica DMI8 inverted microscope (Leica Microsystems, Germany), a Leica DFC7000 GT digital camera (Leica Microsystems, Germany), a Lambda SC *SmartShutter*<sup>TM</sup> controller (Sutter Instrument Company, Novato, CA), an ORCA-Flash4.0 V3 digital CMOS camera (Hamamatsu Photonics K. K., Hamamatsu City, Japan), two Lambda VF-5<sup>TM</sup> tunable filter changers (Sutter Instrument Company, Novato, CA), and a Lambda 10-3 optical filter changer control system (Sutter Instrument Company, Novato, CA). It is important to note that the xenon arc lamp should remain on for at least 15 minutes to allow the switch board to cool. In addition, the lamp has a lifetime of 1000 hours but is expected to perform longer with proper maintenance (*e.g.*, replacing the xenon bulb). Additionally, the ORCA-Flash4.0 V3 digital CMOS camera on the right camera port was occasionally exchanged for an ORCA-Fusion BT digital CMOS camera (Hamamatsu Photonics K. K., Hamamatsu City, Japan). It is important to note that cameras are interchangeable depending on the camera mount (*i.e.*, the C-mount) in use; the emission Lambda VF-5<sup>TM</sup> tunable filter changer is equipped with a 0.7× C-mount to fit the Leica digital camera. The tunable filter changers were each equipped with a combination of five VersaChrome<sup>®</sup> tunable filters produced by Semrock that allow excitation and emission

---

<sup>3</sup> This section previously appeared as an article in *Analyst*. It was reproduced with permission from the Royal Society of Chemistry. The original citation is as follows: S. Goines, M. Deng, M. W. Glasscott, J. Leung and J. E. Dick, *Analyst*, 2022, **147**, 2396-2404.

wavelengths ranging from 380 nm to 700 nm. One must note that any combination of available filters may be used to amend the ranges permitted by the filter changers. These filters are capable of high transmission, ideal for spectroscopy, and out-of-band blocking. Additionally, Semrock designed these particular VersaChrome<sup>®</sup> tunable thin-film filters with steep edges to increase spectral discrimination compared to standard gratings while also providing more bandwidth control. While the bandpass of our filters range from 13 nm to 16 nm, these filters were incorporated to decrease spectral distortion associated with the angle of incident light. Moreover, a spectrum with 1 nm resolution may be captured if a single tunable filter is used. **Table 4.1** shows the VersaChrome<sup>®</sup> filters available for use in this imaging platform.

**Table 4.1. Available VersaChrome<sup>®</sup> Tunable Filters**

| Location  | Product # | Description                       |
|---|-----------|-----------------------------------|
| VF-5 Tunable Filter Changer<br>(Excitation, SA or S1) | O573380   | OPT, VF,380/16 NM BANDPASS FILTER |
|   | O573440   | OPT, VF,440/16 NM BANDPASS FILTER |
|   | O573490   | OPT, VF,490/15 NM BANDPASS FILTER |
|   | O573550   | OPT, VF,550/15 NM BANDPASS FILTER |
|   | O573620   | OPT, VF,620/14 NM BANDPASS FILTER |
| VF-5 Tunable Filter Changer<br>(Emission, SB or S2)   | O573440   | OPT, VF,440/16 NM BANDPASS FILTER |
|   | O573490   | OPT, VF,490/15 NM BANDPASS FILTER |
|   | O573550   | OPT, VF,550/15 NM BANDPASS FILTER |
|   | O573620   | OPT, VF,620/14 NM BANDPASS FILTER |
|   | O573700   | OPT, VF,700/13 NM BANDPASS FILTER |

The first filter changer is fitted against the xenon arc lamp to select excitation wavelengths, while the second is fitted between the Leica DMI8 inverted microscope and the Leica DFC7000 GT digital camera to capture light emitted from the sample. In addition, the Leica DMI8 inverted microscope is equipped with standard GFP, Y5, TXR, and DAPI filter cubes for standard fluorescence imaging as well as an 80/20 beam splitter for hyperspectral/fluorescence imaging using the tunable filter changers.

For sample analysis, the components of the system must be turned on in the order denoted by the numbering within **Figure 4.1**. Power to the Leica DMI8 inverted microscope and the Leica digital camera are controlled by the Leica CTR advanced electronics box, while the Leica SP box is used to control the motorized microscope stage. To obtain fluorescence and spectral data *via* variable fluorescence bandpass imaging, wavelengths must be specified using the two Lambda VF-5<sup>TM</sup> tunable filter changers and the Lambda 10-3 optical filter changer control system. The majority of programming is maintained within Leica LAS X imaging software and the Lambda 10-3 optical filter changer control system. A detailed description of data acquisition and analysis is presented below.

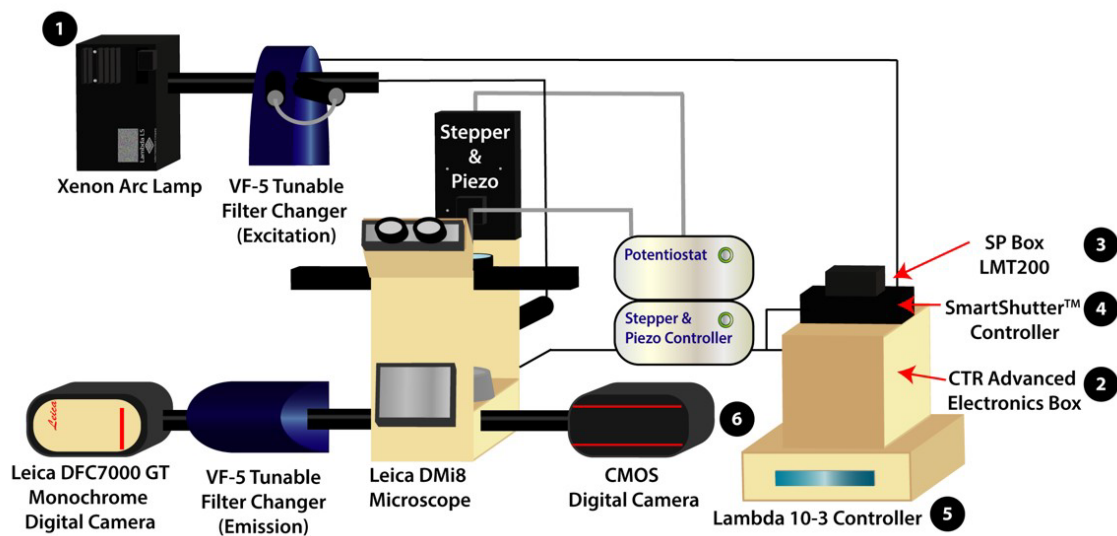


**Figure 4.1. Hyperspectral-Assisted Scanning Electrochemical Microscope Schematic**

Schematic representation of the variable fluorescence bandpass imaging platform with numbered equipment for the power on mechanism.

### 4.3.2 Data Acquisition & Analysis

The hyperspectral imaging system must be turned on in the sequence depicted in **Figure 4.1**. Note that the xenon arc lamp should not be turned on and off within a 15-minute period to protect the switch board of the light source. Additionally, if more than one click is heard during the ignition of the lamp, the bulb may need to be replaced. The bulb should be replaced after approximately 1000 hours of use.

Initially, the home screen of the Lambda 10-3 displays “A” and “B” wavelength values, “C: OFF”, and “L” (**Figure 4.2**). “A” is representative of the emission wavelength and may be programmed using the S1 button, while “B” is representative of the excitation wavelength and may be programmed using the S2 button. “C” and “L” denote functions of the equipment. “L” denotes that local programming of the Lambda 10-3 is enabled and “C: OFF” denotes that the xenon arc lamp shutter is closed. To begin local programming, the Local button may be selected on the keypad.



**Figure 4.2. Lambda 10-3 Home Screen**

Lambda 10-3 optical filter changer control system home screen.

After warming up the xenon arc lamp for 15 minutes, a sample may be placed on the Leica DMI8 inverted microscope stage for analysis. A standard halogen lamp or the room light may be used to focus the sample, since the conventional transmitted light source and condenser have been replaced by the stepper/piezo positioner of the scanning electrochemical microscope. (Note that if an EMCCD camera is in use, a dark room is necessary to reduce background.) Once the sample is in focus, a bright field image may be obtained, then fluorescence microscopy images may be obtained in bypass mode (*i.e.*, white-light output mode) using the conventional filter cubes located in the Leica DMI8 inverted microscope and the Hamamatsu digital camera to the right. Use of this equipment may be specified using the digital pad on the microscope or within the Leica LAS X imaging software, and the software may be used to capture images. To capture images in bypass mode, means to permit unfiltered white light to travel through the VF-5<sup>TM</sup> excitation filter changer to be filtered by conventional filters within the inverted microscope (*e.g.*, GFP, TXR, Y5, and DAPI filters). To enter bypass mode, 430 nm must be entered as the excitation wavelength (*i.e.*, “B” on the Lambda 10-3 optical filter changer control system) and “C: ON” must be shown on the Lambda 10-3 home screen; additionally, the Lambda SmartShutter<sup>TM</sup> must be switched to “OPEN”. Please see the outlined programs below for additional programming instructions, also note that 430 nm is selected as the excitation wavelength because it is unachievable using this in-house system. Additionally, here, the emission wavelength setting is irrelevant as the emission filter changer will be bypassed when imaging with the camera to the right.

#### **4.3.2.1 Programming Specific Excitation & Emission Wavelengths**

To program a specific excitation wavelength: select the S2 button, then key in a three-digit wavelength between 380 and 620 nm, and select Enter. To program a specific emission

wavelength, select the S1 button, then key in a three-digit wavelength between 440 and 700 nm, and select Enter. S2 and S1 do not have to be programmed in this order. If the three-digit wavelength keyed in is not achievable using the given tunable filters, the error message in **Figure 4.3** will appear.

To capture a fluorescence image using the hyperspectral equipment, the 80/20 beam splitter must be selected as the filter within the microscope, the excitation and emission wavelengths must be selected, “C: ON” must be present on the home screen, and the Leica DFC7000 GT digital camera must be used. “C” denotes the function of the Lambda *SmartShutter*<sup>TM</sup>. When “C: OFF” is shown rather than “C: ON”, the Lambda *SmartShutter*<sup>TM</sup> (**Figure 4.4**) will not allow light to travel from the xenon arc lamp through excitation tunable filters; therefore, light will not travel to the Leica DMI8 inverted microscope. To allow light to travel from the light source through the excitation filter changer, “C: ON” must be shown on the Lambda 10-3 (**Figure 4.5**). To change “C: OFF” to “C: ON” on the home screen, simply press Enter when the home screen is being displayed. If light is still not permitted through the selected objective lens of the Leica DMI8 inverted microscope, make sure the FL shutter of the microscope is open by selecting FLURO within the LAS X imaging software or by selecting FL on the microscope digital screen. If light is still not permitted, ensure that the switch of the Lambda *SmartShutter*<sup>TM</sup> is set to “OPEN” or “AUTO”.



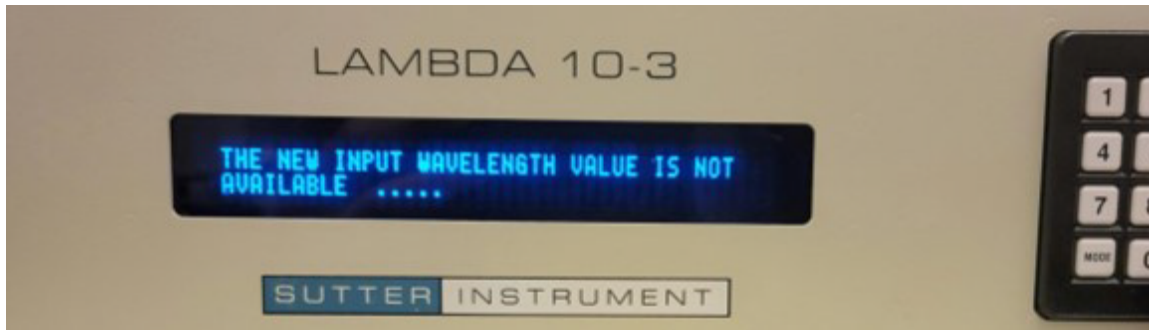


**Figure 4.3. Lambda 10-3 Error After Wavelength Input**

Lambda 10-3 optical filter changer control system error message for a wavelength outside of the existing tunable filter range.



**Figure 4.4. Lambda SmartShutter™**

Shutter control system for the Lambda 10-3 optical filter changer control system.



**Figure 4.5. Open Lambda 10-3 Xenon Arc Lamp Shutter**

Home screen of the Lambda 10-3 optical filter changer control system when "C: ON" is selected.

### 4.3.2.2 Programming to Capture Emission Spectra

To capture an emission spectrum, the “A” filter wheel must be the active. This is denoted by the asterisk in front of the active wheel on the home screen (*e.g.*, **Figure 4.5** shows that the emission filter changer is active). To enable or disable a filter changer select: MODE, then 3. The screen shown in **Figure 4.6** will appear. Here, the shutter intended for time-lapse triggering (TTL) should be enabled and inactive shutters should be disabled. This allows the use of a TTL trigger to capture images as we step through emission wavelengths evenly using the Leica LAS X time lapse imaging software (*i.e.*, an image will be captured based on the exposure time of the camera at each emission wavelength). To enable the emission filter changer, 1 should be selected, then the screen in **Figure 4.7** will be displayed.



**Figure 4.6. Lambda 10-3 TTL Shutter Settings Menu**

Lambda 10-3 optical filter changer control system TTL shutter menu for enabling (EN) and disabling (DS) the excitation filter wheel (SB), the emission filter wheel (SA), and the white-light output shutter (SC).



**Figure 4.7. Lambda 10-3 TTL Shutter Settings Menu #2**

Lambda 10-3 optical filter changer control system shutter menu provided after enabling shutters SA or SB.

Here, the user will select 2 to begin data collection at a low wavelength. To step through emission wavelengths, the following program should be used: Local, Mode, S1, 4, 1, 1, Enter, numerals of the three-digit starting wavelength, Enter, numerals of the three-digit ending wavelength, Enter, one- to two-digit step size, Enter, 1, Enter, 0 (3×), 1, 0, On Line. By selecting 1 for the direction, the scan will proceed from low to high wavelengths (*i.e.*, the direction of the scan can be set to ascend or descend depending on the type of spectrum desired and the program detailed here sets the emission wavelengths to scale up). One must note that the Lambda *SmartShutter*<sup>TM</sup> must be set to “Auto” and “C: ON” must be displayed on the Lambda 10-3 to capture a lambda scan. Within the Leica LAS X imaging software, a lambda scan may be initiated after selecting “t” in the upper left corner of the “Acquisition” tab and inputting parameters specific to the imaging system and the specified emission wavelength range. Within the “Project settings” window in the left-hand tool bar, “use sequencer advanced” and “single image mode” must be selected. In this window under “Z-Movement,” “Z then Lambda” should be selected and the “Shutter control” should be “optimized.” Within the “t” window, the time interval may be adjusted based on the exposure time (for the purpose of imaging microspheres in this manuscript it was set to 10 seconds), the number of pulses (*i.e.*, the number of mechanical spectral shifts) should be set to 1 for a duration (*i.e.*, the amount of time between each mechanical shift limited physically by the filter wheel) of 50 milliseconds, and the cycle number should be based on **Equation 4.1** (for the purpose of imaging the microspheres in section 4.4 it was set to 26).<sup>10</sup>

$$\left(\frac{\lambda_{em}-\lambda_{ex}}{step\ size}\right) + 1$$

**Equation 4.1**

In **Equation 4.1**,  $\lambda_{em}$  is the emission wavelength (nm) and  $\lambda_{ex}$  is the excitation wavelength (nm). Additionally, within the “Triggering” window, “Emission Trig” must be checked as well as “Use in experiment.” The trigger should be linked to the first channel only and occur before the acquisition. To begin the acquisition, “Start” should be selected in the bottom right of the “Acquisition” tab.

### 4.3.2.3 Programming to Capture Excitation Spectra

While additional equipment and algorithms are necessary for background subtraction and spectral differentiation, respectively, the system is capable of collecting excitation spectra.<sup>37</sup>

To capture an excitation spectrum, the “B” filter wheel must be the active. To remove the asterisk in front of the “A” active wheel on the home screen (*e.g.*, **Figure 4.5** shows that the emission filter changer is active) disable the filter changer by selecting: “MODE”, then 3. The screen shown in **Figure 4.6** will appear. Disable the emission filter wheel, referred to as “A” or “SA” within Lambda 10-3 control system menus, by selecting 2. Then enable the excitation filter wheel, referred to as “B” or “SB” within Lambda 10-3 control system menus, by selecting 3. This allows the use of a TTL trigger to capture images as we step through excitation wavelengths evenly using the Leica LAS X time lapse imaging software (*i.e.*, an image will be captured based on the exposure time of the camera at each excitation wavelength). After enabling “SB”, the screen in **Figure 4.7** will be displayed. To capture excitation spectra, one must scan from high to low wavelengths. Furthermore, when the menu shown in **Figure 4.7** appears, the user should select 1.

To step through excitation wavelengths, the following program should be used: Local, Mode, S1, 4, 1, 1, Enter, numerals of the three-digit starting wavelength, Enter, numerals of the three-digit ending wavelength, Enter, one- to two-digit step size, Enter, 2, Enter, 0 (3×), 1, 0, On

Line. By selecting 2 for the direction, the scan will proceed from high to low wavelengths (*i.e.*, the direction of the scan will be set to descend based on the spectrum desired). Ideally, this will increase signal-to-noise as light attenuation is decreased during filtering since the scan is from low to high energy wavelengths. Again, one must note that the Lambda *SmartShutter*<sup>TM</sup> must be set to “Auto” and “C: ON” must be displayed on the Lambda 10-3 to capture a lambda scan. All settings within the Leica LAS X time lapse imaging software are programmed as done in section 4.3.2.2, except within the “Triggering” window, “Excitation Trig” must be checked instead of “Emission Trig.”

#### 4.3.2.4 Data Analysis

Following acquisition of time lapse images using the programming outlined in the sections above, within the “Quantify” tab of the imaging software, a stack profile of the images captured during the time lapse is rendered to produce a spectrum. The raw data is presented as mean intensity (counts per second, *cps*) versus time (seconds, *s*). Since image acquisition is based on a TTL trigger ignited by wavelength steps of the VF-5<sup>TM</sup> tunable filters, the time on the x-axis is directly related to the wavelength at which the image was captured. By right-clicking on the raw data, it can be exported as a Microsoft Excel file; within this file, the time points may be replotted as wavelength values subsequently providing an excitation or emission spectrum.

#### 4.3.3 Hyperspectral Imaging of Invitrogen FluoSpheres<sup>TM</sup> 4

To demonstrate the capabilities and reproducibility of the hyperspectral imaging system, three types of Invitrogen FluoSpheres<sup>TM</sup> were imaged and their corresponding spectra were obtained. For sample preparation, 10  $\mu$ L aliquots of blue-green (430/465), yellow-green

---

<sup>4</sup> This section previously appeared as an article in *Analyst*. It was reproduced with permission from the Royal Society of Chemistry. The original citation is as follows: S. Goines, M. Deng, M. W. Glasscott, J. Leung and J. E. Dick, *Analyst*, 2022, **147**, 2396-2404.

(505/515), and red (580/605) fluorescent polystyrene microspheres were combined in a 3.5 cm-diameter treated tissue culture dish (VWR International LLC, Radnor, PA) with approximately 2 mL Dulbecco's phosphate buffered saline (DPBS, 1X, pH 7.4).

Leica LAS X imaging software was used to image the fluorescent polystyrene microspheres. Beads were focused in bright field using a standard halogen lamp and the 40 $\times$  objective lens equipped with adaptive focus control as well as real-time control for optimum biological imaging. The Lambda 10-3 optical filter changer control system was programmed for the excitation and emission of each bead to set tunable filters to the appropriate wavelengths, and three separate images were obtained using the 80/20 beam splitter and the Leica digital camera. By overlaying each image, the sample was represented as a whole. To obtain the corresponding emission spectra, the Lambda 10-3 optical filter changer control system was programmed to maintain an excitation wavelength of 425 nm while stepping through emission wavelengths from 450 nm to 700 nm with a step size of 10 nm. Leica LAS X time lapse imaging software was used to capture images at each emission wavelength using an emission based TTL trigger. Following image acquisition, a stack profile was rendered to produce emission spectra.

To display the hyperspectral imaging capabilities of the variable fluorescence bandpass platform, lambda scans of the three fluorescent microspheres ( $r = 7.5 \mu\text{m}$ ) shown in **Figure 4.8a** were collected. The use of standard overlap tunable filters while imaging over a wide spectral field resulted in minimal overlap in **Figure 4.8b**. Sufficient variation in emission wavelengths made subsequent imaging of each bead during a lambda scan feasible. Ten successive lambda scans (**Figure 4.8b**) resulted in relative standard deviations of mean emission intensities no greater than 4%. By creating a region of interest within each bead type, we retrieved a lambda scan of an individual bead (**Figure 4.8c**), a feature necessary to capture dynamic correlated data

within a single cell. As a control, this result implies our potential to optically visualize a stained organelle.



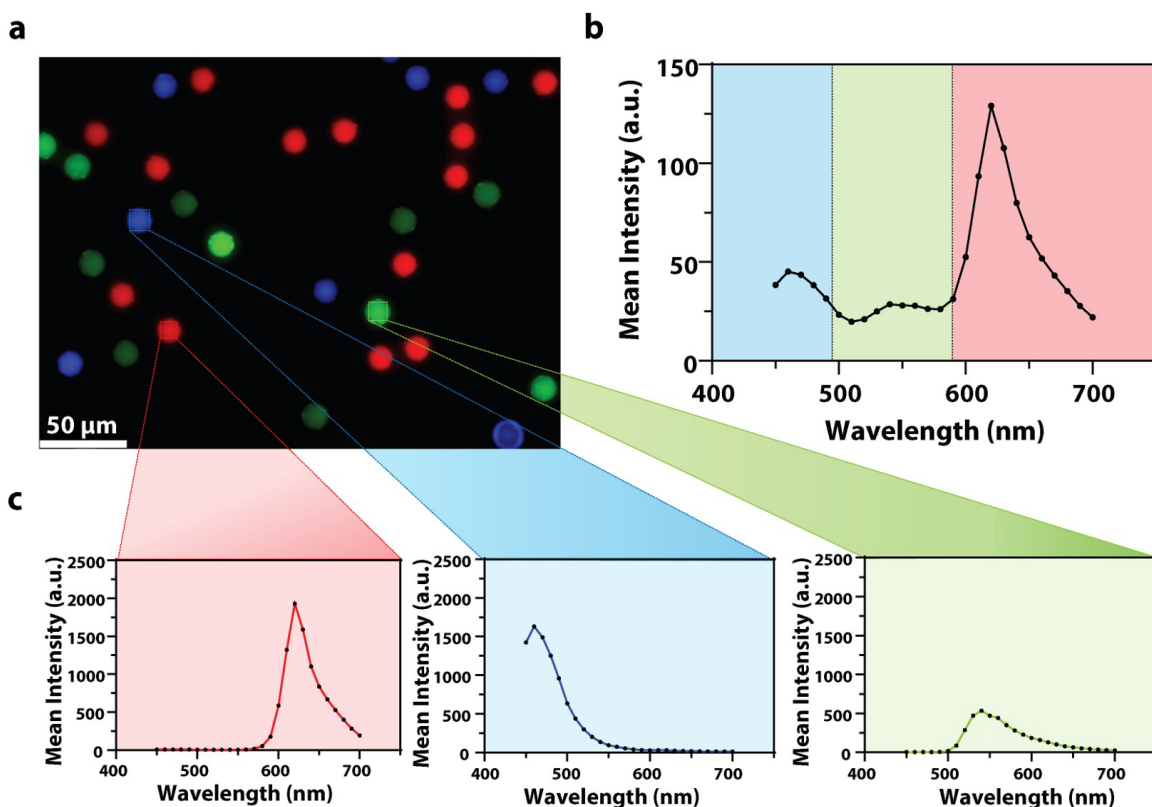


**Figure 4.8. Hyperspectral Image of Invitrogen FluoSpheres™**

(a) An overlay of fluorescence images of blue-green ( $\lambda_{ex}/\lambda_{em}$ , 435/465 nm), yellow-green ( $\lambda_{ex}/\lambda_{em}$ , 505/530 nm), and red ( $\lambda_{ex}/\lambda_{em}$ , 580/605 nm) Invitrogen FluoSpheres™ combined in a 3.5 cm-diameter dish submerged in DPBS (1X, pH 7.4) with (b) an average emission spectrum of the sample ( $N=10$ ). (c) The average spectrum is accompanied by an individual average spectrum of each microsphere type within the sample ( $N=10$ ).

#### 4.3.4 Hyperspectral-Assisted Scanning Electrochemical Microscopy of Hep G2 Cells<sup>5</sup>

To demonstrate the bioanalytical utility of the system, human hepatocarcinoma (Hep G2) cells were imaged with correlated electrochemical and spectral analysis.

Hep G2 cells were cultured in a 3.5 cm-diameter poly-L-lysine treated tissue culture dish using Dulbecco's Modified Eagle's Medium (DMEM) – high glucose supplemented with 10% v/v fetal bovine serum (FBS), 2.5% v/v HEPES buffer, and 1% v/v penicillin-streptomycin (*i.e.*, full growth media). Cells were incubated at 37 °C, 5% CO<sub>2</sub>, and 10% O<sub>2</sub> until they reached 65 to 85% confluence. Hoechst stain solution (10 mg/mL) was thawed and diluted to 10 µg/mL in Dulbecco's phosphate buffered saline (DPBS, 1X, pH 7.4). Spent media in the dish was replaced with 1 mL 10 µg/mL Hoechst stain solution, following a DPBS rinse. The dish was covered in foil and placed on a rotator plate for 10 minutes at 10 rpm at room temperature. Following an additional DPBS rinse, the stain solution was replaced with a 2 mL solution of < 1 mM ferrocenemethanol (FcCH<sub>2</sub>OH) in DPBS for scanning electrochemical microscopy (SECM).

Cells were brought into focus on the microscope stage using a standard halogen lamp, and an initial bright field image was taken. Hep G2 cells were approximately 20 µm in diameter, but cell shape and size varied throughout the sample. A typical fluorescence image was captured using a standard DAPI filter cube and a CMOS digital camera (*i.e.*, in bypass mode). Then, the variable fluorescence bandpass system was used to capture hyperspectral images; these additional fluorescence images were captured using the 80/20 beam splitter and the Leica DFC7000 GT digital camera. To obtain emission spectra, the Lambda 10-3 optical filter changer control system was programmed to maintain an excitation wavelength of 400 nm and step

---

<sup>5</sup> This section previously appeared as an article in *Analyst*. It was reproduced with permission from the Royal Society of Chemistry. The original citation is as follows: S. Goines, M. Deng, M. W. Glasscott, J. Leung and J. E. Dick, *Analyst*, 2022, **147**, 2396-2404.

through emission wavelengths of 440 nm to 700 nm with a step size of 10 nm. A stack profile of the images captured at each emission wavelength was rendered to produce emission spectra of Hep G2 nuclei.

For subsequent SECM, a Pt microelectrode SECM tip with a radius of 5  $\mu\text{m}$  and an  $R_g$  equal to 10 (where  $R_g = r_s/r_{elec}$ ,  $r_s$  is the radius of the insulating sheath, and  $r_{elec}$  is the radius of the metallic tip) was used as the working electrode. The  $R_g$  of the electrode tip is important to consider because a large  $R_g$  may limit radial diffusion to the electrode surface during imaging. A thin glassy carbon rod ( $r = 1.5 \text{ mm}$ ) and a Ag/AgCl (1 M KCl) electrode were used as the counter and reference electrodes, respectively. The counter electrode and a salt bridge to the reference electrode in DPBS were placed in solution using a 3D printed holder connected to the piezo positioner/controller above the dish prior to placing the working electrode in solution. The cells and reference electrode were separated by a salt bridge to prevent interferent effects due to silver leakage. After connecting electrodes to leads of a CH Instruments 920D bipotentiostat, an initial cyclic voltammogram was taken at the surface of the FcCH<sub>2</sub>OH solution (sufficiently far enough from the surface of the Hep G2 cells) to observe the typical faradaic response of FcCH<sub>2</sub>OH in DPBS (**Figure 4.9**).

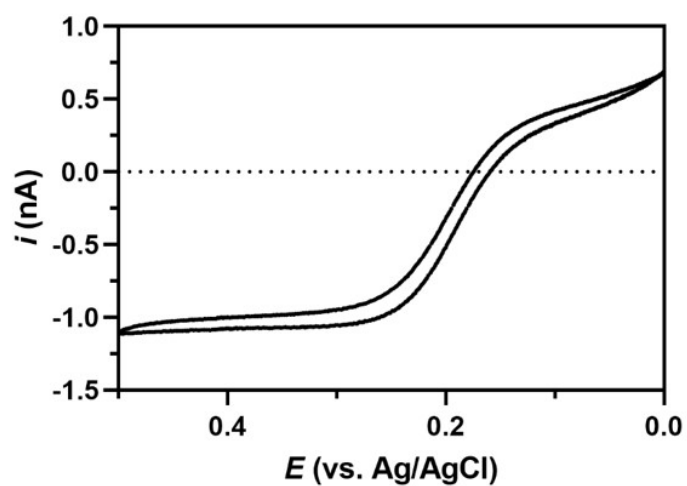


**Figure 4.9. Cyclic Voltammetry of Ferrocenemethanol Above Cells**

Cyclic voltammogram of 0.80 mM FcCH<sub>2</sub>OH in DPBS (1X, pH 7.4) in a 3.5 cm-diameter tissue culture dish > 500  $\mu$ m above Hep G2 cells at a Pt microelectrode SECM tip ( $r = 5 \mu$ m) vs. Ag/AgCl (1 M KCl). A thin glassy carbon rod ( $r = 1.5$  mm) was used as the counter electrode.

For additional electrochemical analysis, the current at +0.5 V vs. Ag/AgCl was used as the limiting current (*i.e.*,  $i_{T,\infty}$ ). The Pt microelectrode SECM tip was then used to approach the surface of cells within the culture dish in the  $z$ -direction while poisoning the electrode sufficiently positive to oxidize FcCH<sub>2</sub>OH (*i.e.*, at +0.5 V vs. Ag/AgCl). The bipotentiostat simultaneously measured current versus the distance travelled by the electrode. The approach was concurrently monitored using bright field microscopy (**Figure 4.10**).

Initially, a decrease in oxidative current in the polarographic convention is observed as a result of hindered diffusion of FcCH<sub>2</sub>OH to the Pt microelectrode SECM tip as the cell membrane is approached. Once an increase in the feedback response was observed near the surface of a Hep G2 cell membrane (**Figure 4.11a**), the Pt microelectrode SECM tip was retracted approximately 5 to 10  $\mu\text{m}$  to avoid potential tip-sample crashes associated with constant-height imaging, while remaining at an appropriate working distance (*i.e.*,  $z \leq 2a$ , where  $z$  is the working distance and  $a$  is the electrode radius). This is often necessary when performing constant-height imaging with large aspect-ratio samples, such as two-dimensional cell cultures, to avoid tip-sample crashes.<sup>47</sup> This method of tip placement in 2D cell cultures has been previously validated.<sup>47-49</sup> Next, the electrode tip was biased at +0.5 V vs. Ag/AgCl and used to scan an area of cells in the  $xy$  plane. Simultaneously measuring current at the electrode tip *via* amperometry resulted in an image of the cells based on their feedback (*i.e.*, current) response (**Figure 4.11c**). Electrochemical images were captured over a period of 5 to 7 minutes. Concurrently, the SECM tip was monitored using a 40 $\times$  objective lens with a resolution of 559 nm in the  $xy$  plane.

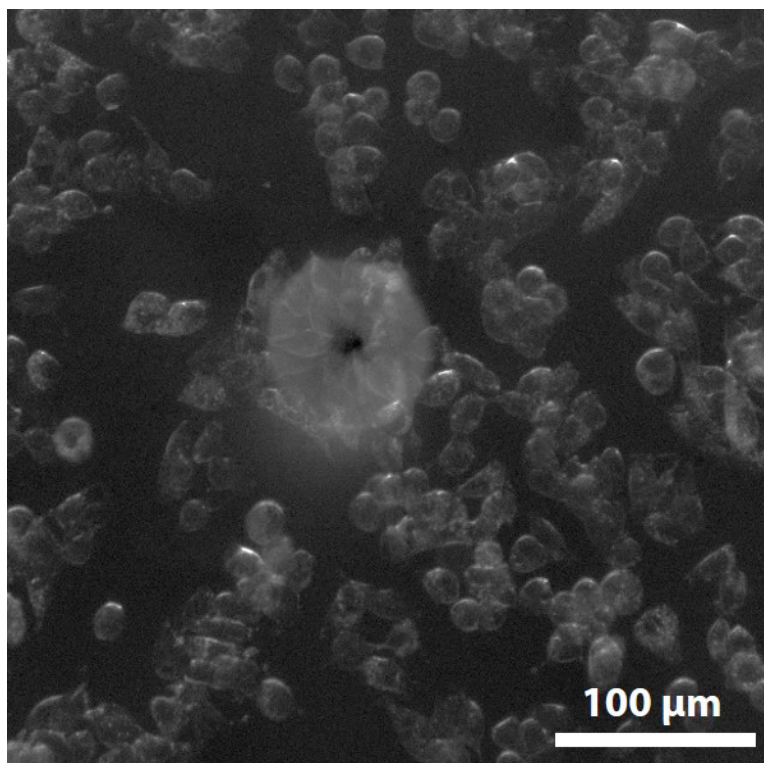


**Figure 4.10. Approach Result with Pt Microelectrode SECM Tip**

Optical image of Pt microelectrode SECM tip ( $r = 5 \mu\text{m}$ ) directly above Hep G2 cells directly after an amperometric approach at  $+0.5 \text{ V}$  vs.  $\text{Ag}/\text{AgCl}$  ( $1 \text{ M KCl}$ ).

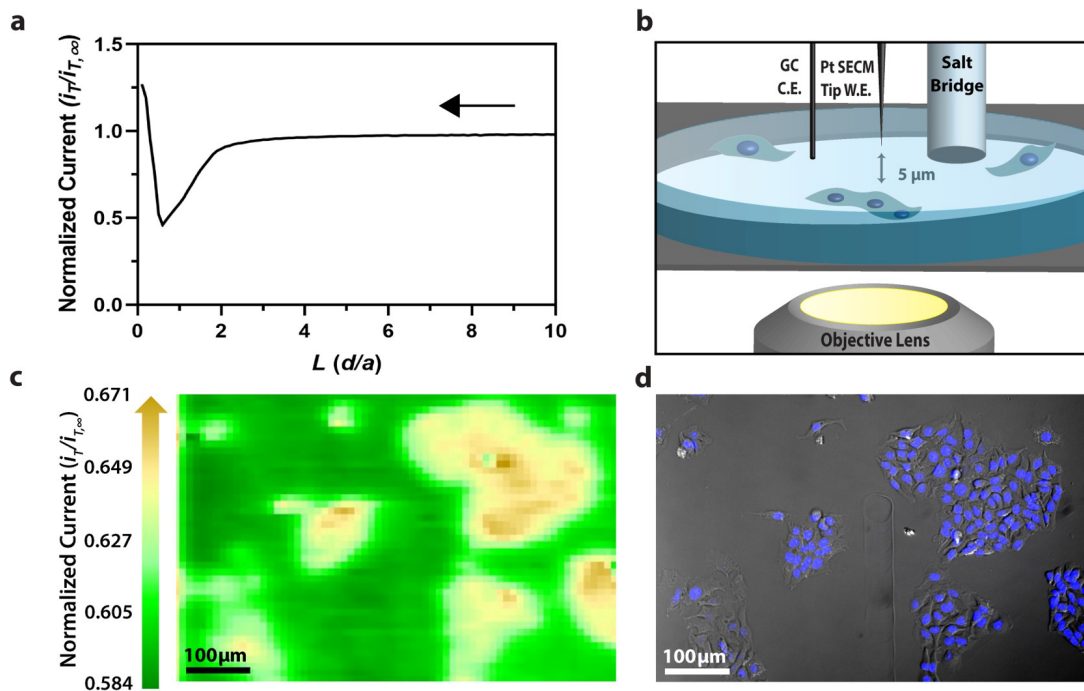


**Figure 4.11. Correlated Electrochemical and Fluorescence Imaging of Hoechst Stained Hep G2 Cells**

(a) Polarographic feedback response of a Pt microelectrode SECM tip ( $r = 5 \mu\text{m}$ ) vs. Ag/AgCl (1 M KCl) scanned in the  $z$ -direction over an insulated tissue culture dish with Hep G2 cells in  $70 \mu\text{M}$  ferrocenemethanol in DPBS (1X, pH 7.4). A thin glassy carbon rod ( $r = 1.5 \text{ mm}$ ) was used as the counter electrode. (b) Schematic of tip-to-cell distance approximation. (c) Correlated polarographic electrochemical image and (d) bright field/fluorescence overlay of Hep G2 cells. The fluorescence image was false colored for visual representation. Cell nuclei stained with Hoechst 33342 ( $\lambda_{\text{ex}}/\lambda_{\text{em}}$ , 400/497 nm).

No visual evidence of the tip contacting the cells or cellular perturbation was observed. Minimal changes in cell morphology indicated minimal changes in cell viability. For time lapse imaging over longer periods, a stage top incubator equipped with a silicon inlet from Tokai Hit<sup>®</sup> may be used for probing cellular reactivity.

In **Figure 4.11c**, cell reactivity provides an increase in feedback relative to the dish surface. Correlated bright field images showed the typical morphology of low density Hep G2 cells. Complementary fluorescence images of the same position were obtained to locate the nuclei of cells that had been previously incubated in a Hoechst nuclear stain solution. When compared, these images (**Figures 4.11c-d**) allowed us to spatially locate and differentiate cells on a single-cell basis. These images are essential for the unambiguous determination of cellular boundaries, which are often difficult to discern when using bright field and electrochemical imaging, alone.

While the fluorescence microscopy detailed above may be achieved using a standard fluorescence microscope, the variable fluorescence bandpass system described here allows multicolor imaging, enabling multi-fluorophore detection within dynamic systems. In addition, the Sutter Instrument<sup>®</sup> Lambda 10-3 optical filter changer control system used to operate our set up allows us to specify wavelengths in increments as low as 1 nm; lambda scans obtained using this novel combination of technology would allow one to discern features within dynamic spectral and optical data otherwise unrecognized by scans obtained with standard filter cubes (*i.e.*, one could observe slight shifts in the excitation of a site-specific fluorophore with nanometer resolution as fluorophore polarization may vary with respect to dynamic interactions<sup>50</sup>). Moreover, being coupled to a scanning electrochemical microscope, this system may be used to observe site-specific electrochemical activity while obtaining spectral and optical



data to locate and differentiate between each cell. **Figure 4.12** serves as a model data set produced by our unique hyperspectral-assisted scanning electrochemical microscope system.

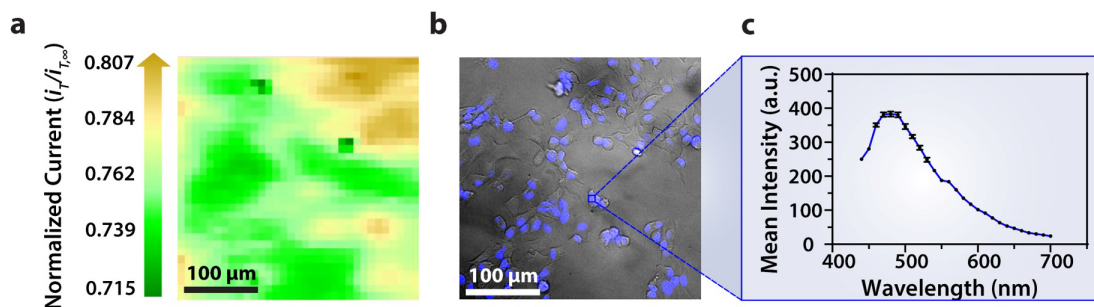


**Figure 4.12. Hyperspectral-Assisted Scanning Electrochemical Microscopy of Hoechst Stained Hep G2 Cells**

(a) Correlated polarographic electrochemical image and (b) bright field/fluorescence overlay of Hep G2 cells with a (c) correlated spectrum of Hoechst 33342 ( $\lambda_{ex}/\lambda_{em}$ , 400/497 nm) for a single nucleus. The electrochemical image was obtained with a Pt microelectrode SECM tip ( $r = 5 \mu\text{m}$ ) vs. Ag/AgCl (1 M KCl) in 0.60 mM ferrocenemethanol in DPBS (1X, pH 7.4). A thin glassy carbon rod ( $r = 1.5 \text{ mm}$ ) was used as the counter electrode. The fluorescence image was false colored for visual representation. Cell nuclei stained with Hoechst 33342 ( $\lambda_{ex}/\lambda_{em}$ , 400/497 nm).

## REFERENCES

1. J. Izquierdo, P. Knittel and C. Kranz, *Analytical and Bioanalytical Chemistry*, 2018, **410**, 307-324.
2. S. Amemiya, J. Guo, H. Xiong and D. A. Gross, *Analytical and Bioanalytical Chemistry*, 2006, **386**, 458-471.
3. M. Etienne, M. Dossot, J. Grausem and G. Herzog, *Analytical Chemistry*, 2014, **86**, 11203-11210.
4. L. Wang, J. Kowalik, B. Mizaikoff and C. Kranz, *Analytical Chemistry*, 2010, **82**, 3139-3145.
5. D. Momotenko, L. Qiao, F. Cortés-Salazar, A. Lesch, G. Wittstock and H. H. Girault, *Analytical Chemistry*, 2012, **84**, 6630-6637.
6. M. Zhang, G. Qin, Y. Zuo, T. Zhang, Y. Zhang, L. Su, H. Qiu and X. Zhang, *Electrochimica Acta*, 2012, **78**, 412-416.
7. M. Zhang, X. Yu, G. Qin, Y. Zhu, M. Wang, Q. Wei, Y. Zhang and X. Zhang, *Science China Chemistry*, 2015, **58**, 1200-1205.
8. M. M. N. Zhang, Y. T. Long and Z. F. Ding, *Chemistry Central Journal*, 2012, **6**.
9. D. Polcari, P. Dauphin-Ducharme and J. Mauzeroll, *Chemical Reviews*, 2016, **116**, 13234-13278.
10. S. Goines, M. Deng, M. W. Glasscott, J. Leung and J. E. Dick, *Analyst*, 2022, **147**, 2396-2404.
11. S. Kuss, D. Polcari, M. Geissler, D. Brassard and J. Mauzeroll, *Proceedings of the National Academy of Sciences*, 2013, **110**, 9249.
12. V. Sundaresan, K. Marchuk, Y. Yu, E. J. Titus, A. J. Wilson, C. M. Armstrong, B. Zhang and K. A. Willets, *Analytical Chemistry*, 2017, **89**, 922-928.
13. E. Lubeck and L. Cai, *Nature Methods*, 2012, **9**, 743-U159.
14. Q. L. Li, X. F. He, Y. T. Wang, H. Y. Liu, D. R. Xu and F. M. Guo, *Journal of Biomedical Optics*, 2013, **18**.
15. Q. A. Alshammari, R. Pala, N. Katzir and S. M. Nauli, *Scientific Reports*, 2021, **11**.
16. M. H. Sung and J. G. McNally, *Wiley Interdisciplinary Reviews-Systems Biology and Medicine*, 2011, **3**, 167-182.
17. H. Ding, W. Guo and B. Su, *ChemPlusChem*, 2020, **85**, 725-733.

18. M. M. Richter, *Chemical Reviews*, 2004, **104**, 3003-3036.
19. J. Zhou, G. Ma, Y. Chen, D. Fang, D. Jiang and H.-y. Chen, *Analytical Chemistry*, 2015, **87**, 8138-8143.
20. H. Zhang, W. Gao, Y. Liu, Y. Sun, Y. Jiang and S. Zhang, *Analytical Chemistry*, 2019, **91**, 12581-12586.
21. S. Voci, B. Goudeau, G. Valenti, A. Lesch, M. Jović, S. Rapino, F. Paolucci, S. Arbault and N. Sojic, *Journal of the American Chemical Society*, 2018, **140**, 14753-14760.
22. S. Voci, R. Duwald, S. Grass, D. J. Hayne, L. Bouffier, P. S. Francis, J. Lacour and N. Sojic, *Chemical Science*, 2020, **11**, 4508-4515.
23. T. Zimmermann, J. Rietdorf and R. Pepperkok, *Febs Letters*, 2003, **546**, 87-92.
24. H. Matsuoka, Y. Kosai, M. Saito, N. Takeyama and H. Suto, *Journal of Biotechnology*, 2002, **94**, 299-308.
25. K. Asai, Y. Sumiyama, M. Watanabe and K. Aizawa, *Surgery Today*, 2006, **36**, 1075-1084.
26. S. J. Leavesley, M. Walters, C. Lopez, T. Baker, P. F. Favreau, T. C. Rich, P. F. Rider and C. W. Boudreaux, *Journal of Biomedical Optics*, 2016, **21**, 10.
27. J. Moreau, P. Bouzy, J. Guillard, V. Untereiner, R. Garnotel, A. Marchal, C. Gobinet, C. Terry, G. D. Sockalingum and G. Thieffin, *Molecules*, 2020, **25**.
28. G. Thomas, J. van Voskuilen, H. Truong, J. Y. Song, H. C. Gerritsen and H. Sterenborg, *Biomedical Optics Express*, 2014, **5**, 4281-4299.
29. A. Travo, O. Piot, R. Wolthuis, C. Gobinet, M. Manfait, J. Bara, M. E. Forgue-Lafitte and P. Jeannesson, *Histopathology*, 2010, **56**, 921-931.
30. A. Dvornikov and E. Gratton, *Biomedical Optics Express*, 2018, **9**.
31. M. Ghaffari, A. L. Chateigner-Boutin, F. Guillon, M. F. Devaux, H. Abdollahi and L. Duponchel, *Analytica Chimica Acta*, 2019, **1062**, 47-59.
32. P. Saha, J. W. Hill, J. D. Walmsley and C. M. Hill, *Analytical Chemistry*, 2018, **90**, 12832-12839.
33. S. R. Kirchner, K. W. Smith, B. S. Hoener, S. S. E. Collins, W. X. Wang, Y. Y. Cai, C. Kinnear, H. Y. Zhang, W. S. Chang, P. Mulvaney, C. F. Landes and S. Link, *Journal of Physical Chemistry C*, 2018, **122**, 6865-6875.
34. J. Juan-Colas, I. S. Hitchcock, M. Coles, S. Johnson and T. F. Krauss, *Proceedings of the National Academy of Sciences of the United States of America*, 2018, **115**, 13204-13209.

35. K. Wonner, M. V. Evers and K. Tschulik, *Journal of the American Chemical Society*, 2018, **140**, 12658-12661.
36. Y. Nomura, K. Yamamoto, T. Hirayama, M. Ohkawa, E. Igaki, N. Hojo and K. Saitoh, *Nano Letters*, 2018, **18**, 5892-5898.
37. P. F. Favreau, C. Hernandez, T. Heaster, D. F. Alvarez, T. C. Rich, P. Prabhat and S. J. Leavesley, *Journal of Biomedical Optics*, 2014, **19**, 10.
38. B. D. B. Aaronson, J. C. Byers, A. W. Colburn, K. McKelvey and P. R. Unwin, *Analytical Chemistry*, 2015, **87**, 4129-4133.
39. C. Fouquet, J.-F. Gilles, N. Heck, M. Dos Santos, R. Schwartzmann, V. Cannaya, M.-P. Morel, R. S. Davidson, A. Trembleau and S. Bolte, *PloS one*, 2015, **10**, e0121096-e0121096.
40. B. R. Masters and P. T. C. So, *Optics Express*, 2001, **8**, 2-10.
41. E. C. Jensen, *Anatomical Record-Advances in Integrative Anatomy and Evolutionary Biology*, 2013, **296**, 1-8.
42. K. Bahlmann, S. Jakobs and S. W. Hell, *Ultramicroscopy*, 2001, **87**, 155-164.
43. C. P. Byers, B. S. Hoener, W. S. Chang, M. Yorulmaz, S. Link and C. F. Landes, *Journal of Physical Chemistry B*, 2014, **118**, 14047-14055.
44. K. Lindfors, T. Kalkbrenner, P. Stoller and V. Sandoghdar, *Physical Review Letters*, 2004, **93**, 4.
45. B. B. Katemann, A. Schulte and W. Schuhmann, *Electroanalysis*, 2004, **16**, 60-65.
46. K. G. Battiston, J. W. C. Cheung, D. Jain and J. P. Santerre, *Biomaterials*, 2014, **35**, 4465-4476.
47. I. Beaulieu, S. Kuss, J. Mauzeroll and M. Geissler, *Analytical Chemistry*, 2011, **83**, 1485-1492.
48. B. Liu, S. A. Rotenberg and M. V. Mirkin, *Proceedings of the National Academy of Sciences of the United States of America*, 2000, **97**, 9855-9860.
49. A. Schulte and W. Schuhmann, *Electrochemical Methods for Neuroscience*, 2007, **1**, 353-372.
50. J. R. Lakowicz, *Principles of Fluorescence Spectroscopy*, Springer Science+Business Media, LLC, 3 edn., 2006.

## Chapter 5 Applications of Hyperspectral-Assisted Scanning Electrochemical Microscopy

During the course of this work, hyperspectral-assisted scanning electrochemical microscopy (SECM) has been used to examine two dimensional co-cultures, the propagation of human cytomegalovirus (HCMV), and the cytotoxic mechanism of perfluorooctane sulfonate (PFOS). In the following chapter, we will summarize these investigations and our findings in detail to demonstrate the versatility of our unique imaging platform.

### 5.1 Probing Dynamic Co-culture Systems<sup>6</sup>

Use of variable fluorescence bandpass hyperspectral imaging in coordination with biological SECM allows for differentiation of cells based on cell location, cell type, and cellular reactivity given use of an appropriate fluorescence label or substance. While fluorescence imaging is often used in biological investigations, there is literature precedent for changes in redox activity (*i.e.*, phototoxic effects) due to incident light<sup>1</sup>, therefore the combination of hyperspectral imaging and electrochemical imaging would allow users to directly probe these effects. This analysis is necessary to resolve the biological systems that give rise to the electrochemical signal.

---

<sup>6</sup> This section previously appeared as an article in *Analyst*. It was reproduced with permission from the Royal Society of Chemistry. The original citation is as follows: S. Goines, M. Deng, M. W. Glasscott, J. Leung and J. E. Dick, *Analyst*, 2022, **147**, 2396-2404.

Here, we demonstrate the efficacy of our system by providing a proof-of-concept analysis where we differentiate between cell types by imaging a two-dimensional co-culture of hepatocarcinoma (Hep G2) and osteosarcoma (U-2 OS) cells using our uniquely designed hyperspectral-assisted scanning electrochemical microscope platform. Cells were maintained using the subculturing procedures outlined in **Chapter 2** section **2.2**, and imaging was completed using the methods outlined in **Chapter 2** section **2.4** and **Chapter 4**.

### **5.1.1 Methods to Distinguish Between Cell Boundaries**

To establish the system's ability to distinguish between cell types *via* multicolor imaging, correlated electrochemical and optical data was obtained using a two-dimensional co-culture of Hep G2 and U-2 OS cells. Hep G2 cells were previously stained with a  $10 \mu\text{g mL}^{-1}$  Hoechst nuclear stain solution, while U-2 OS cells were previously transfected with RFP-LC8; LC8 is a eukaryotic protein localized in the cytoplasm and the nucleus of cells.<sup>2</sup> Hoechst stained Hep G2 cells were cultured in a 3.5 cm-diameter tissue culture dish with U-2 OS cells. Cells were incubated in Hep G2 full growth media (defined in **Chapter 2** section **2.2.4**) at  $37^\circ\text{C}$ , 5%  $\text{CO}_2$ , and 10%  $\text{O}_2$  until they reached 65 to 85% confluence. Prior to imaging, spent media was removed from the dish and cells were washed with Dulbecco's phosphate buffered saline (DPBS, 1X, pH 7.4). Following this wash step, approximately 2 mL of a  $< 1 \text{ mM}$  ferrocenemethanol ( $\text{FcCH}_2\text{OH}$ ) in DPBS was added to the dish for imaging.

Co-cultured cells were brought into focus on the Leica DMI8 inverted microscope stage using a standard halogen lamp, and an initial optical image was taken. To capture RFP emission from U-2 OS cells, a conventional TXR filter cube and a CMOS digital camera were used in bypass mode as described in **Chapter 4** section **4.3**. To capture Hoechst emission from Hep G2 cells, the TXR filter cube was exchanged for a conventional DAPI filter cube. The resulting

fluorescence images were overlaid. Compared to Hep G2 cells, U-2 OS cells were typically elongated with a width between 15 to 20  $\mu\text{m}$ . Spectral imaging was completed using an 80/20 beam splitter and the Leica DFC7000 GT digital camera. To obtain emission spectra of RFP-LC8 modified U-2 OS cells, the Lambda 10-3 optical filter changer control system was programmed to maintain an excitation wavelength of 580 nm and step through emission wavelengths of 610 nm to 700 nm with a step size of 10 nm. A two-dimensional stack profile of the images captured at each emission wavelength was rendered to produce emission spectra of RFP-LC8 in U-2 OS cells. Subsequent hyperspectral imaging of Hep G2 nuclei and electrochemical imaging of the sample was completed as previously described in **Chapter 4** section **4.3**.

Both cell types exhibited an increase in their feedback response relative to the insulating dish (**Figure 5.1a**); variation in the magnitude of the feedback response could indicate variation in cell height, oxidative stress, redox mediator permeability, or cell communication since cells within dynamic co-culture systems often display varying reactivity based on cell type.<sup>3</sup> Please note that the following electrochemical images are normalized based on  $i_{T,\infty}$  (*i.e.*, the steady state current where the tip-to-substrate distance is greater than 10 $\times$  the radius of the electrode) to display the current response relative to the bulk solution and to clarify our interpretation of the feedback response.



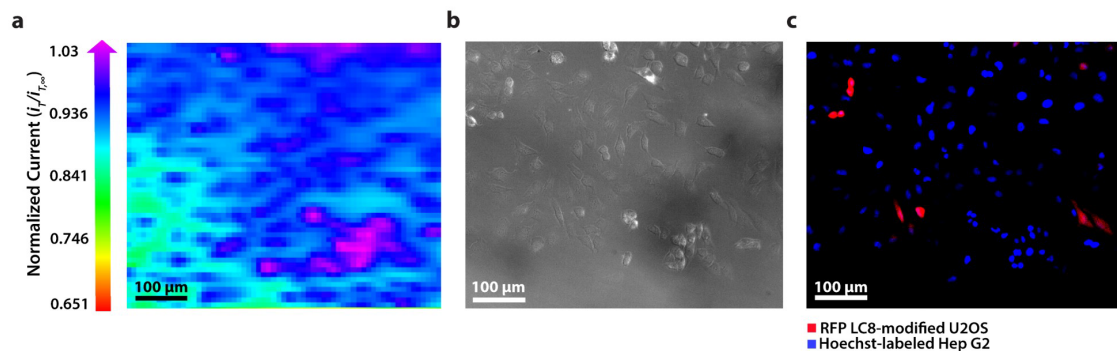


**Figure 5.1. Correlated Optical, Fluorescence, and Scanning Electrochemical Microscopy of a Two-dimensional Co-culture**

(a) Correlated polarographic electrochemical image, (b) bright field image, and (c) fluorescence image of a two-dimensional co-culture of Hep G2 and U-2 OS cells. The electrochemical image was obtained with a Pt microelectrode SECM tip ( $r = 5 \mu\text{m}$ ) vs. Ag/AgCl (1 M KCl) in 0.35 mM ferrocenemethanol in DPBS (1X, pH 7.4). A glassy carbon rod ( $r = 1.5 \text{ mm}$ ) was used as the counter electrode. The fluorescence image was false colored for visual representation. Hep G2 nuclei stained with Hoechst 33342 ( $\lambda_{\text{ex}}/\lambda_{\text{em}}$ , 400/497 nm). U-2 OS cells transfected with RFP-LC8 ( $\lambda_{\text{ex}}/\lambda_{\text{em}}$ , 580/630 nm).

Within this two-dimensional co-culture system, cell type cannot be clearly distinguished based on the electrochemical (**Figure 5.1a**) and bright field (**Figure 5.1b**) images alone. Thus, correlated fluorescence (**Figure 5.1c**) and hyperspectral (**Figure 5.2b-c**) images obtained using our unique variable fluorescence bandpass hyperspectral imaging platform were necessary to discern between cell types as well as cellular boundaries.

By correlating fluorescence images with electrochemical images, we differentiated between the electrochemical feedback of U-2 OS and Hep G2 cells within the co-culture system. In **Figure 5.1a**, a cluster of Hep G2 cells near the bottom right of the image exhibited positive feedback based on the normalized current, while U-2 OS cells typically displayed less feedback relative to the insulating dish in comparison. Although this trend is evident in **Figure 5.1**, we also observed that U-2 OS cells have the potential to exhibit similar feedback to Hep G2 cells with respect to the insulating dish in **Figure 5.2**.

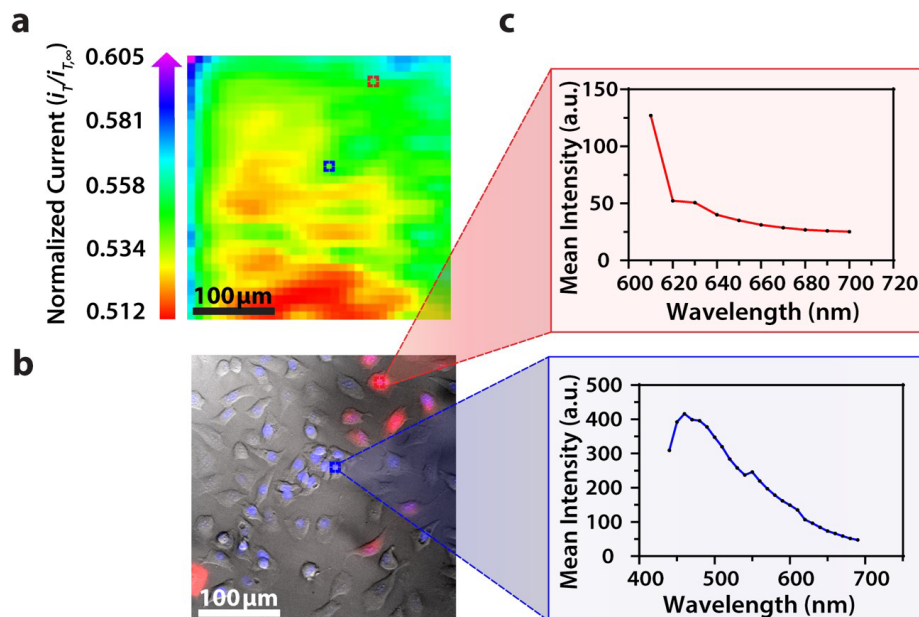


**Figure 5.2. Hyperspectral-Assisted Scanning Electrochemical Microscopy of a Two-dimensional Co-culture**

(a) Correlated polarographic electrochemical image and (b) bright field/fluorescence overlay of a two-dimensional co-culture of Hep G2 and U-2 OS cells. (c) Associated emission spectra for U-2 OS RFP-LC8 and Hoechst 33342 of two individual cells within the co-culture. The electrochemical image was obtained with a Pt microelectrode SECM tip ( $r = 5 \mu\text{m}$ ) vs. Ag/AgCl (1 M KCl) in 0.80 mM ferrocenemethanol in DPBS (1X, pH 7.4). A glassy carbon rod ( $r = 1.5 \text{ mm}$ ) was used as the counter electrode. The fluorescence image was false colored for visual representation. Hep G2 nuclei stained with Hoechst 33342 ( $\lambda_{\text{ex}}/\lambda_{\text{em}}$ , 400/497 nm). U-2 OS cells transfected with RFP-LC8 ( $\lambda_{\text{ex}}/\lambda_{\text{em}}$ , 580/630 nm). Conventional fluorescence images are presented using the bandpass wavelengths provided, while hyperspectral images are presented using the spectra provided.

These are preliminary, qualitative assessments since variation in the feedback response may be due to differences in cellular metabolism based on cell type, cell morphology, and diffusion layer overlap due to cell aggregates. Further hyperspectral analysis, similar to that shown in **Figure 5.2**, may elucidate variations due to cellular metabolism if a redox fluorophore is used.

### **5.1.2 Assessing Redox Activity – Spectral Analysis of Glutathione**

To demonstrate our ability to capture spectral data with 1 nm resolution and assess redox activity by hyperspectral imaging, Hep G2 cells were imaged in the presence of FcCH<sub>2</sub>OH and monochlorobimane (*i.e.*, MBCl, a non-fluorescent probe that fluoresces blue upon conjugation with glutathione, GSH). Hep G2 cells were cultured in a 3.5 cm-diameter tissue culture dish using full growth media. Cells were incubated at 37 °C, 5% CO<sub>2</sub>, and 10% O<sub>2</sub> until they reached 65 to 85% confluence. Full growth media was removed from the dish, and the cells were rinsed with 1 mL DPBS. After aspirating the DPBS rinse, the dish was charged with 2 mL 0.5 mM FcCH<sub>2</sub>OH/20 μM MBCl in DPBS for SECM with complementary hyperspectral imaging of the MBCl-GSH conjugate. GSH production was assessed because there is literature precedent for GSH production at the cell surface induced by oxidative stress due to FcCH<sub>2</sub>OH exposure.<sup>4</sup>

Cells were brought into focus on the Leica DMI8 inverted microscope stage using a standard halogen lamp. A typical fluorescence image was captured using a standard DAPI filter cube and a CMOS digital camera (**Figure 5.3b**). The variable fluorescence bandpass system was used to capture hyperspectral images; these additional fluorescence images were captured using an 80/20 beam splitter and the Leica DFC7000 GT digital camera. To obtain an emission spectrum (**Figure 5.3c**), the Lambda 10-3 optical filter changer control system was programmed to maintain an excitation wavelength of 495 nm and step through emission wavelengths of 535 nm to 550 nm with a step size of 1 nm. A stack profile of the images captured at each emission

wavelength was rendered to produce emission spectra of MBCl-GSH conjugates. An emission peak cannot be fully resolved due to spectral overlap of excitation and emission filters in this range. Subsequent electrochemical imaging (**Figure 5.3a**) was completed as previously described in **Chapter 2** section **2.4**.

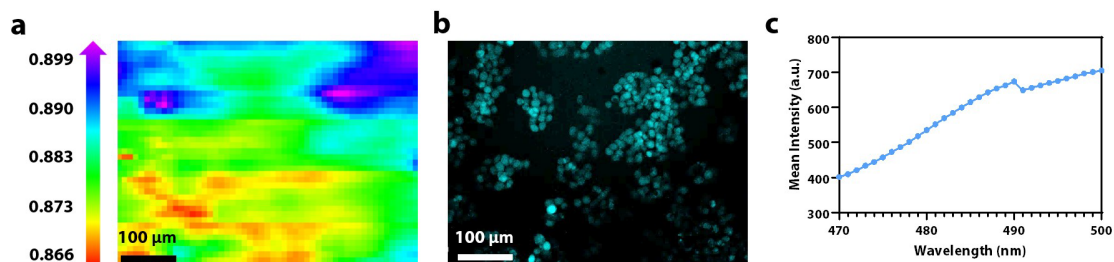


**Figure 5.3. Hyperspectral-Assisted Scanning Electrochemical Microscopy of Hep G2 Cells and Monochlorobimane-Glutathione**

(a) Correlated polarographic electrochemical image and (b) fluorescence image of Hep G2 cells.

The electrochemical image was obtained with a Pt microelectrode SECM tip ( $r = 5 \mu\text{m}$ ) vs.

Ag/AgCl (1 M KCl) in  $\sim 0.50 \text{ mM}$  ferrocenemethanol/ $20 \mu\text{M}$  monochlorobimane in DPBS (1X,

pH 7.4). A glassy carbon rod ( $r = 1.5 \text{ mm}$ ) was used as the counter electrode. The fluorescence

image was false colored for visual representation of the fluorescence of the

monochlorobimane/glutathione conjugate at the cell surface ( $\lambda_{\text{ex}}/\lambda_{\text{em}}$ , 495/535 nm). (c) Correlated

emission spectrum of monochlorobimane/glutathione conjugate with 1 nm resolution ( $\lambda_{\text{ex}}/\lambda_{\text{em}}$ ,

495/535 to 550 nm).

### 5.1.3 Concluding Remarks & Future Perspectives

Here, we recognize that the resolving power of this novel system can be improved through the use of nanoelectrode tips to achieve nanometer resolution during electrochemical imaging and through the use of redox indicative fluorophores to differentiate between the metabolic activity of each cell type. Additionally, the temporal resolution may be improved if an alternative to electrochemical mapping is used to assess redox activity, for example amperometric approaches have been used to determine heterogeneous rate constants above living cells<sup>5</sup> and electrochemiluminescence has been used to image cell membranes<sup>6</sup>. Here, electrochemical mapping was used to correlate cell location between electrochemical and fluorescence responses. Specifically, we demonstrate the use of a cost-effective, hyperspectral-assisted scanning electrochemical microscope system. Future investigations will be geared towards investigating cellular dynamics with nanometer spatial resolution and additional electrochemical techniques to push the resolving power of the system presented here.

## 5.2 Investigating the Propagation of Human Cytomegalovirus

Human cytomegalovirus (HCMV) is one of nine variations of betaherpesvirus.<sup>7-9</sup> HCMV is a global health concern, statistically, effecting more than 70% of the world's population by adulthood<sup>10</sup>, with widespread propagation of the virus by bodily fluids (*e.g.*, tears, milk, saliva, and cervical secretions like placenta) leading to 56% to 94% of asymptomatic cases<sup>9</sup>. Asymptomatic cases among healthy individuals are generally not a concern unless an infected individual is pregnant or a donor of blood, bone marrow, or organs.<sup>7, 11</sup> Unfortunately, there is a 50% probability of congenital infection, which may cause birth defects.<sup>10, 11</sup> Within immunocompromised individuals, severe symptoms such as pneumonia, retinitis, and

encephalitis are more common; in addition, immunocompromised individuals are more likely to be reinfected.<sup>11</sup>

### 5.2.1 Methods to Examine Viral Propagation

While many genomics studies have elucidated means of viral propagation, we employed hyperspectral-assisted scanning electrochemical microscopy. We were provided with normal human lung (MRC-5) cells and a AD169 HCMV strain modified to express GFP upon infection by the lab of Dr. Nathaniel Moorman at the University of North Carolina at Chapel Hill. The titer of the virus sample provided was  $4.7 \times 10^7$  infectious units  $\text{mL}^{-1}$ . MRC-5 P18 cells were cultured in a 3.5 cm-diameter tissue culture dish until  $\sim 100\%$  confluent (*i.e.*, high density) as described in **Chapter 2** section **2.2.5**. To deliver, one infectious unit per cell, assuming  $2.8 \times 10^5$  MRC-5 cells per dish, 6.0  $\mu\text{L}$  of AD169-GFP HCMV was diluted with 2 mL MRC-5 full growth media. After aspirating spent full growth media, cells were rinsed with 1 mL DPBS and the virus-media solution was added to the dish. The dish was placed in the incubator set to 37 °C, 5%  $\text{CO}_2$ , and 10%  $\text{O}_2$ . The plate was swirled every ten minutes for even propagation of the virus. After one hour, the virus-media solution was aspirated from the dish, and the cells were rinsed with 1 mL DPBS two times. Next, 2 mL full growth media was added to the dish and the dish was placed in the incubator for later use.

Propagation of HCMV is slow; specifically, replication does not reach peak level in fibroblast cells until after 48 to 72 hours.<sup>7</sup> Furthermore, infected cells were imaged using the hyperspectral system in bypass mode with a Lecia DMI8 inverted microscope, a conventional GFP filter cube, and a CMOS digital camera at 48 hours and 96 hours after primary infection (**Figure 5.4**).



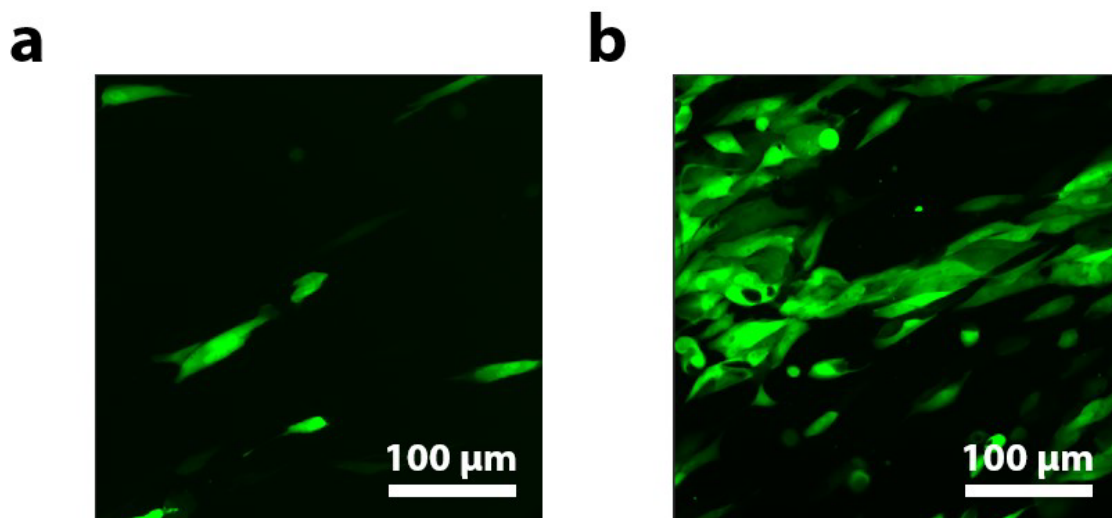


**Figure 5.4. AD169-GFP Human Cytomegalovirus Infected MRC-5 Cells**

Fluorescence images of MRC-5 P18 cells infected with AD169-GFP human cytomegalovirus after (a) 48 hours and (b) 96 hours of primary infection. Images false colored for visual representation.

Additionally, these cells were electrochemically imaged after 48 hours in 1 mM potassium hexacyanoferrate (II) trihydrate (*i.e.*, potassium ferrocyanide) in DPBS using a Pt microelectrode SECM tip ( $r = 5 \mu\text{m}$ ), biased at +0.5 V vs. Ag/AgCl (1 M KCl), and a glassy carbon rod ( $r = 1.5 \text{ mm}$ ) counter electrode. Imaging (**Figure 5.5a**) was completed as previously described in **Chapter 2** section **2.4**. Complementary optical and fluorescence images were obtained with the hyperspectral system using an excitation of 450 nm and an emission of 520 nm (**Figure 5.5b**). Emission spectra were obtained at an excitation of 450 nm and between emission wavelengths of 500 nm to 700 nm with a step size of 20 nm using the 80/20 beam splitter and the Leica DFC7000 GT digital camera (**Figure 5.5c**).

Within **Figure 5.5a**, a decrease in the electrochemical signal is observed above HCMV infected cells. We suspect that this change in redox activity is directly related to changes in cell morphology since negatively charged, ferrocyanide is not a membrane permeable redox mediator. In addition, HCMV infections are characterized by an increase in cell volume due to the formation of intra-nuclear and intra-cytoplasmic inclusion bodies as new virus particles and lysosomes form (*i.e.*, cytomegaly).<sup>9</sup> Furthermore, as the cell membranes of newly infected cells expand, these membranes limit radial diffusion to the electrode surface, decreasing the electrochemical signal. A decrease in the electrochemical signal and lack for fluorescence signal near the bottom left of **Figure 5.5a** and **Figure 5.5b**, respectively, implicates electrochemistry's ability to predict viral spread prior to fluorescence detection by changes in cell morphology.

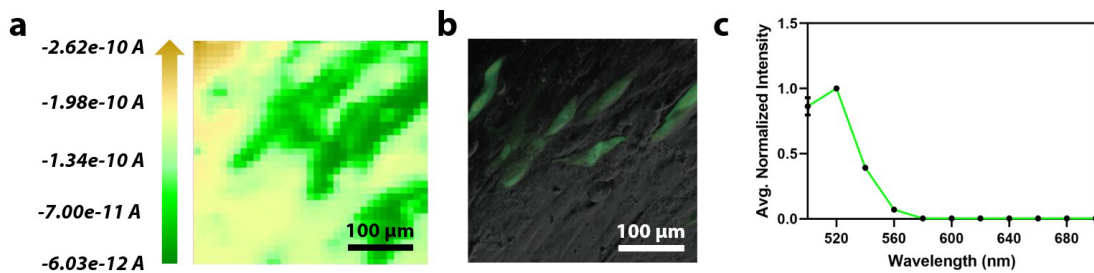


**Figure 5.5. Hyperspectral-Assisted Scanning Electrochemical Microscopy of AD169-GFP Human Cytomegalovirus Infected MRC-5 Cells**

(a) Correlated polarographic electrochemical image, (b) optical/fluorescence overlay, and (c) spectrum of AD169-GFP human cytomegalovirus infected MRC-5 P18 cells. The electrochemical image was obtained with a Pt microelectrode SECM tip ( $r = 5 \mu\text{m}$ ) vs. Ag/AgCl (1 M KCl) in 1 mM potassium ferrocyanide in DPBS (1X, pH 7.4). A glassy carbon rod ( $r = 1.5 \text{ mm}$ ) was used as the counter electrode. The fluorescence image was false colored for visual representation of the fluorescence of GFP at the onset of viral infection ( $\lambda_{\text{ex}}/\lambda_{\text{em}}$ , 450/520 nm). Correlated emission spectrum of AD169-GFP human cytomegalovirus was obtained with 20 nm resolution ( $\lambda_{\text{ex}}/\lambda_{\text{em}}$ , 450/500 to 700 nm).

### 5.2.2 Concluding Remarks & Future Perspectives

In this section, we demonstrated the use of hyperspectral-assisted scanning electrochemical microscopy (SECM) to study the viral propagation of GFP labeled-human cytomegalovirus (HCMV) in normal human lung (MRC-5) cells. Specifically, we used a non-permeable redox mediator to electrochemically map the topography of MRC-5 cells while visualizing viral propagation by fluorescence microscopy. By correlating electrochemical, optical, and spectral data, we elucidated a change in topography prior to GFP emission. Moreover, these results implicate hyperspectral-assisted SECM as an early diagnostic tool for studying viral propagation among single cells.

### 5.3 Examining Perfluorooctane Sulfonate Exposure Effects on Living Cells<sup>7</sup>

Labeled ‘forever chemicals’ based on characteristic networks of strong C – F bonds, manufactured per- and poly-fluoroalkyl substances (PFAS) are used in the production of a variety of daily-use consumer goods.<sup>12</sup> Global production and use of PFAS since the 1940s has resulted in the contamination of food, beverages, and waterways worldwide.<sup>13</sup> Unfortunately, PFAS display strong binding capacities for serum albumin, phospholipids, and fatty acid binding proteins inevitably causing health risks.<sup>14, 15</sup> For example, perfluorooctanoic acid (PFOA) and perfluorooctane sulfonate (PFOS) may establish two and three hydrogen bonds, respectively, with human liver-fatty acid binding protein between the carboxyl head of the PFAS and amino acid residues of the protein.<sup>15</sup> Moreover, the properties that make PFAS useful – such as high thermal stability, chemical stability, and surfactant activity – are the culprits responsible for

---

<sup>7</sup> This section previously appeared as an article in *Analyst*. It was reproduced with permission from the Royal Society of Chemistry. The original citation is as follows: S. Goines and J. E. Dick, *Analyst*, 2022, DOI: 10.1039/d2an00904h.

various health concerns associated with exposure (*i.e.*, infertility<sup>16</sup>, kidney and testicular cancers<sup>17</sup>, and liver and kidney disease<sup>18</sup>).<sup>13</sup>

Prior to 2002, PFOS was one of the most widely used PFAS in the United States until the polymer's adverse health effects became evident. Case-controlled and cohort studies near regions of high contamination presented exposure as an occupational hazard as well as a public health concern.<sup>13, 19-22</sup> Quantifiable concentrations of PFOS were reported in bodily fluids (*i.e.*, blood, milk, and urine), hair, and nails.<sup>13</sup> With a half-life greater than five years, PFOS may be retained in human tissue for prolonged periods of time. Bioaccumulation studies report PFOS in the brain, lungs, kidneys, and liver with the micropollutant being dominant in the liver, making hepatotoxicity studies a relevant area of focus.

Recent studies have investigated cytotoxicity, cell proliferation, and bioaccumulation of PFOS through colorimetric and fluorescence viability assays, flow cytometry, qPCR, and mass spectrometry.<sup>14-16, 23-28</sup> Unfortunately, these studies generally rely on cell lysis or fixation limiting our ability to probe metabolism as a function of time. Very few techniques are readily accessible to probe the mechanism of cytotoxicity in living cells *in vitro*, while accounting for cell-to-cell heterogeneity and the heterogeneity of intracellular material.<sup>29, 30</sup> While fluorescence microscopy is minimally destructive, this method may have phototoxic effects on cellular respiration.<sup>1</sup> However, electrochemical techniques that use nano- and micro-electrodes have been used to examine living cells in real time with minimal perturbation to cellular homeostasis.<sup>31-33</sup> Additionally, electrochemistry has become more appealing to those constructing diagnostic technologies since decreasing electrode size enables one to detect a single entity (*i.e.*, a single cell, organelle, or biomolecule) within seconds.<sup>34</sup>

Here, we use electrochemical imaging to investigate the mechanism of PFOS cytotoxicity with respect to living cells *in vitro*. Scanning electrochemical microscopy (SECM) – a scanning probe technique used to characterize local topography and reactivity – has been used in a variety of bioanalytical investigations because it is inherently non-invasive and provides high spatial and temporal resolution.<sup>31</sup> With the use of membrane permeable, hydrophobic redox mediators, SECM has been used to examine variations in the cellular redox state. For example, neutral, ferrocene derivatives<sup>35, 36</sup> and menadione<sup>37</sup> are often used to examine the cellular redox state as a function of glutathione. In particular, SECM is useful when examining cellular response to stimuli. Previously, SECM has been used to image changes in cellular respiration<sup>38-40</sup>, the secretion of proteins<sup>41, 42</sup>, and transmembrane protein activity<sup>3</sup>. Biological SECM platforms are typically composed of a traditional SECM piezoelectric positioner mounted on an inverted, fluorescence microscope. These platforms allow users to differentiate between cells and investigate redox activity *via* fluorescence and electrochemical microscopy.

Hyperspectral-assisted SECM has the potential to elucidate redox mechanisms responsible for an electrochemical response by offering validation through three forms of data: electrochemical, optical, and spectral data.<sup>43</sup> Previously, we demonstrated the use of variable fluorescence bandpass hyperspectral imaging in combination with SECM by showing the technique's ability to discern between extra- and intra-cellular boundaries within a two-dimensional co-culture system.<sup>43</sup> This previous investigation did not make use of redox indicative-fluorophores, limiting our insight into the redox mechanism responsible for the observed electrochemical response. Here, we use hyperspectral-assisted SECM to investigate the redox mechanism associated with PFOS cytotoxicity using hepatocarcinoma (Hep G2) cells. Hep G2 cells are often used as a model within pharmaceutical, cytotoxicity studies based on

comparable phase II enzyme activity between Hep G2 and normal hepatocytes. Phase II enzymes, such as glutathione-*S*-transferase, are responsible for catalyzing conjugation reactions involved in regulatory processes following oxidative stress.<sup>44</sup> Additionally, PFOS exposure has been implicated in hepatotoxicity *via* lipid accumulation.<sup>28, 45</sup> Specifically, hyperspectral-assisted SECM is used to distinguish between PFOS exposure effects and mediator induced stress in real time. This section aims to build a framework for the electrochemical characterization of cytotoxic redox mechanisms with minimal perturbation to cellular homeostasis. While this investigation is specific to exposure to PFOS, it presents a generalizable method of study for toxicology research.

### 5.3.1 Cell Viability Following Exposure

The experiments performed in this section were completed following exposure to PFOS, therefore we confirmed Hep G2 cell viability following exposure prior to investigating exposure effects *via* hyperspectral-assisted SECM.

Hep G2 P22 cells were cultured in Dulbecco's Modified Eagle's Medium (DMEM) – high glucose (with 4500 mg L<sup>-1</sup> glucose, L-glutamine, sodium pyruvate, and sodium bicarbonate) supplemented with 10% v/v fetal bovine serum (FBS), 2.5% v/v 1 M HEPES buffer (sterile, pH 7.3), and 1% v/v penicillin-streptomycin (*i.e.*, full growth media) in a 10 cm-diameter tissue culture dish. At > 65% confluence, spent media was removed from the dish and cells were rinsed with 5 mL Dulbecco's phosphate buffered saline (DPBS, 1X, pH 7.4). After rinsing the cells, a mixture of 2:1 DPBS to TrypLE Express was added to the dish (*i.e.*, 4 mL DPBS to 2 mL TrypLE Express). The dish was placed in the incubator set to 37 °C and 5% CO<sub>2</sub> to facilitate suspension of cells. After 6 minutes, 9 mL of full growth media was added to the dish to halt trypsinization and the suspension was centrifuged at 1000 rpm at room temperature for 5

minutes. After removing the supernatant from the cell pellet, cells were resuspended in 1 mL full growth media and counted using the automated Corning Cell Counter. With  $5.73 \times 10^6$  cells mL<sup>-1</sup>, aliquots of 109  $\mu$ L (*i.e.*,  $6.25 \times 10^5$  cells per aliquot) were delivered to nine 3.5 cm-diameter tissue culture dishes. The following day, 2 mL solutions of 0, 50, and 100  $\mu$ M PFOS-supplemented full growth media were added to three of the dishes to prepare three samples per PFOS concentration. Hu and co-workers reported significantly higher reactive oxygen species (ROS) content in Hep G2 cells *via* dichlorofluorescein (DCF) fluorescence imaging following 15 hours of PFOS exposure.<sup>28</sup> To ensure significant exposure effects and to initialize the cytotoxic mechanism, Hep G2 cells were exposed to PFOS for 16 hours.

To analyze cell viability after the incubation, spent PFOS-supplemented full growth media was removed from each sample. The cells were rinsed with 1 mL DPBS, then a 1.5 mL solution of 2:1 DPBS to TrypLE Express was added to each dish to suspend cells. After incubating the dishes for 5 minutes, 1 mL full growth media was added to each suspension to halt trypsinization. The suspensions were centrifuged as done previously. After removing the supernatant, cell pellets were resuspended in 1 mL full growth media. Prior to using the automated cell counter to analyze the viability of a suspension, 1 mL Trypan Blue was added to the suspension to stain dead/membrane damaged cells. The results of this experiment shown in **Figure 5.6** demonstrate that Hep G2 cells exposed to up to 100  $\mu$ M PFOS for up to 16 hours remain intact and viable, with viability above 95%.

In addition, the following experiments use Hep G2 cells at various passage numbers. We did not observe significant variation in experimental results based on passage number, but did suspect variation based on cell density due to diffusion layer overlap among neighboring cells.



To minimize variation due to cell density, cells were counted prior to passaging and grown to reach medium to high density prior to imaging.

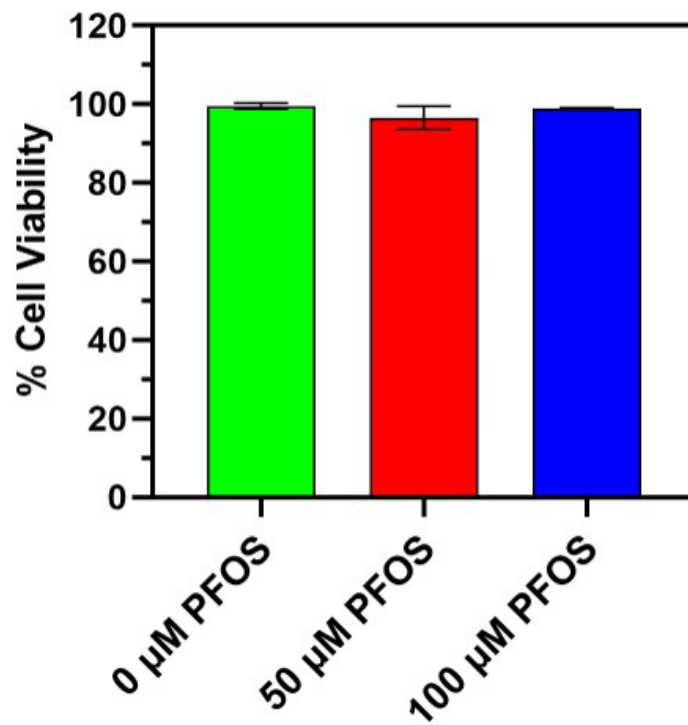


**Figure 5.6. Cell Viability Following PFOS Exposure**

Cell viability of Hep G2 P23 cells exposed to 0, 50, and 100  $\mu\text{M}$  PFOS-supplemented full growth media for 16 hours at 37  $^{\circ}\text{C}$  and 5%  $\text{CO}_2$  ( $N = 3$ ).

### 5.3.2 Hyperspectral-Assisted Scanning Electrochemical Microscopy of Hep G2 Following PFOS Exposure: Reactive Oxygen Species Content Analysis

Previously, PFOS exposure effects on intracellular reactive oxygen species (ROS) was investigated by 2',7'-dichlorofluorescein diacetate (DCF-DA) loading<sup>28</sup>; DCF-DA is a membrane permeable substance that reacts with intracellular esterases to release esterified acids and react with intracellular ROS to fluoresce as dichlorofluorescein (DCF).<sup>46</sup> In this section, we correlate DCF fluorescence with the electrochemical response of ferrocenemethanol (FcCH<sub>2</sub>OH) oxidation *via* correlated microscopy.

Hep G2 P20 cells were cultured in full growth media within 3.5 cm-diameter tissue culture dishes. At 75% to 80% confluence (*i.e.*, medium to high density), spent media was removed from the dishes and the cells were rinsed with 1 mL DPBS. Next, 2 mL solutions of 0, 50, and 100  $\mu$ M PFOS-supplemented full growth media were added to the dishes to prepare a sample for each concentration of PFOS. Each dish was labeled based on the concentration of PFOS added, then placed in the incubator.

After incubating the cells for 16 hours overnight, spent PFOS-supplemented full growth media was removed from the dishes. To analyze the intracellular ROS content, the cells were rinsed with 1 mL DPBS and loaded with 1 mL 10  $\mu$ M DCF-DA in DPBS for 10 minutes in the dark at room temperature. Next, the cells were rinsed with 1 mL DPBS, then 2 mL of full growth media was added to each dish before placing them in the incubator for later use.

Prior to imaging, tilt correction was performed as described in **Chapter 2** section **2.4**. Next, spent media was removed from the 100  $\mu$ M PFOS sample and the cells were rinsed with DPBS before adding 0.5 mM FcCH<sub>2</sub>OH in DPBS to the sample dish. After placing the dish on the microscope stage, three electrodes were placed in solution: a salt bridge to an external Ag/AgCl (1 M KCl) reference electrode in DPBS, a glassy carbon rod counter electrode ( $r = 1.5$

mm), and a Pt microelectrode SECM tip ( $r = 5 \mu\text{m}$ ) using a 3D printed holder attached to the piezoelectric positioner of the 920D bipotentiostat. Next, cells were brought into focus in bright field using a  $20\times$  objective lens, then the Pt microelectrode SECM tip was used to approach cells at  $+0.5 \text{ V vs. Ag/AgCl}$  (**Figure 5.7**). After obtaining a feedback response and observing cell movement, the Pt microelectrode SECM tip was moved upward  $10 \mu\text{m}$  until no cell movement was observed.

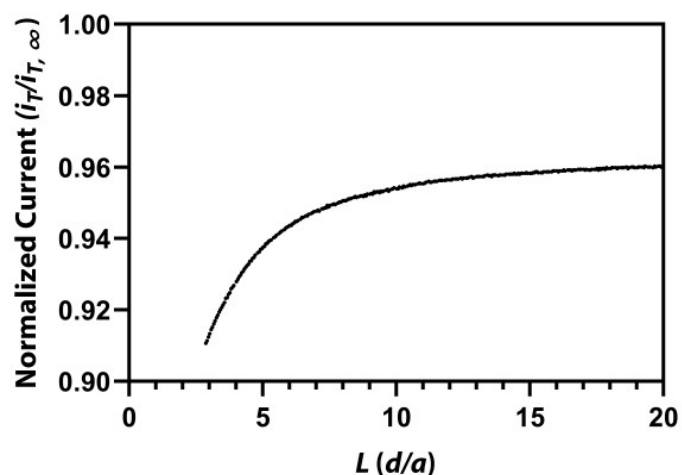


**Figure 5.7. Approach Curve to Hep G2 Cells**

Approach curve to 100  $\mu$ M PFOS treated Hep G2 P20 cells in 0.5 mM FcCH<sub>2</sub>OH in DPBS (1X, pH 7.4) obtained using a Pt microelectrode SECM tip ( $r = 5 \mu$ m) biased at +0.5 V vs. Ag/AgCl (1 M KCl) in a 3.5 cm-diameter tissue culture dish treated for optimal attachment. A glassy carbon rod counter electrode ( $r = 1.5$  mm) was used.

Next, a fluorescence image of 2',7'-dichlorofluorescein (DCF), indicative of ROS content, was captured at  $\lambda_{\text{ex}}/\lambda_{\text{em}}$  495/535 nm using the hyperspectral system. The system was then used to collect a two-dimensional stack of images obtained at multiple emission wavelengths with a single excitation wavelength from the emission of 535 nm to 550 nm with a step size of 1 nm at an excitation of 495 nm (**Figure 5.8i**). A corresponding electrochemical image was obtained with the Pt microelectrode SECM tip at +0.5 V vs. Ag/AgCl approximately one hour after adding the redox mediator solution to the cell culture dish. This incubation period allowed passive diffusion of FcCH<sub>2</sub>OH into the cells<sup>3</sup>; this is critical since transmembrane charge transfer and cell potential may influence the feedback observed. Electrochemical imaging was completed at a working distance  $\leq 10 \mu\text{m}$  to maintain an appropriate working distance (*i.e.*,  $d \leq 2a$ , where  $d$  is the working distance from the substrate and  $a$  is the radius of the electrode tip) while avoiding tip-to-sample crashes that may be observed when imaging large aspect ratio samples; this technique has been used previously when imaging cell samples<sup>47</sup>. This series of imaging steps was repeated with samples exposed to 50  $\mu\text{M}$  and 0  $\mu\text{M}$  PFOS. All electrochemical, optical, and spectral data are shown in **Figure 5.8**.

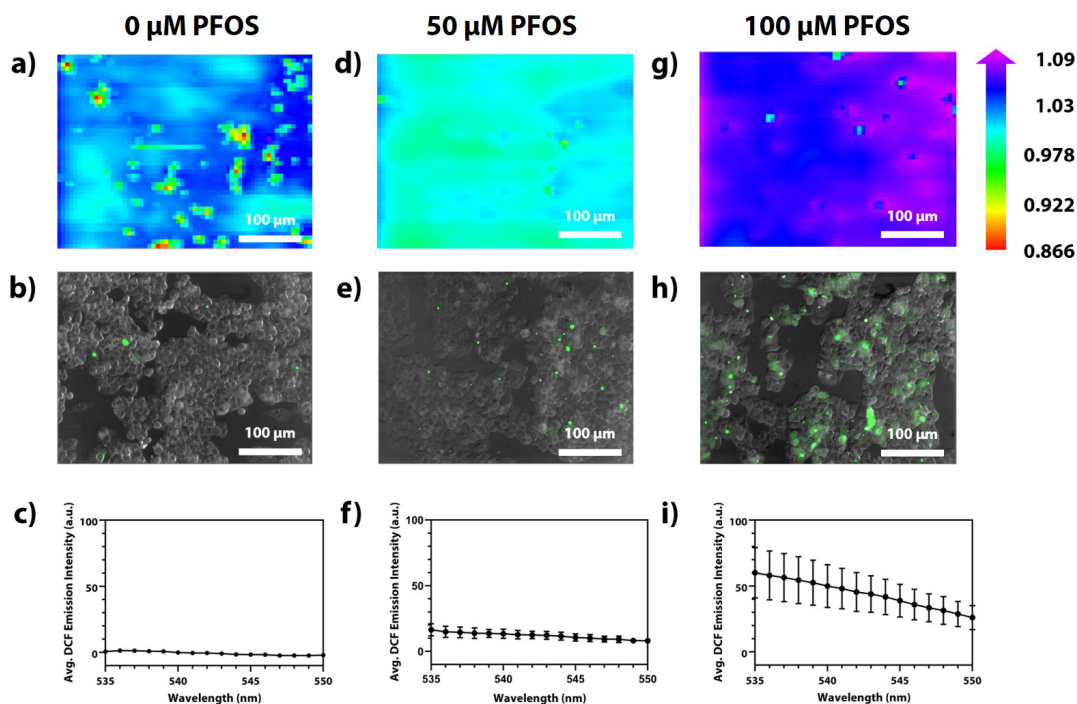


**Figure 5.8. Hyperspectral-Assisted Scanning Electrochemical Microscopy of Hep G2 Following PFOS Exposure & 2',7'-Dichlorofluorescein Diacetate Loading**

Correlated electrochemical, optical, and spectral data for Hep G2 P20 cells exposed to 0 (a-c), 50 (d-f), and 100 (g-i)  $\mu\text{M}$  PFOS-supplemented media for 16 hours at 37 °C and 5%  $\text{CO}_2$ . Images obtained in 0.5 mM  $\text{FcCH}_2\text{OH}$  in DPBS (1X, pH 7.4). Electrochemical images (a, d, and g) obtained using a Pt microelectrode SECM tip ( $r = 5 \mu\text{m}$ ) at +0.5 V vs.  $\text{Ag}/\text{AgCl}$  (1 M  $\text{KCl}$ ) and a glassy carbon rod counter electrode ( $r = 1.5 \text{ mm}$ ); images normalized by  $i_{T,\infty}$  when  $d \geq 100 \mu\text{m}$ . Fluorescence images (b, e, and h) of ROS indicator, DCF, obtained at  $\lambda_{\text{ex}}/\lambda_{\text{em}}$  495/535 nm. Hyperspectral images used to produce (c, f, and i) obtained at  $\lambda_{\text{ex}}$  495 nm. The fluorescence images were false colored for visual representation.

After electrochemically imaging Hep G2 cells – previously exposed to PFOS and loaded with DCF-DA – in the presence of FcCH<sub>2</sub>OH, an increase in the electrochemical response was observed as a function of PFOS concentration (**Figure 5.8**). Here, it is important to note that the electrochemical response is normalized by the limiting current (*i.e.*,  $i_{T,\infty}$  when  $d \gg 10a$ , where  $d$  is the electrode tip distance from the substrate and  $a$  is the electrode radius) for direct comparison of electrochemical images regardless of variations in tip-to-substrate distance. In addition, fluorescence images validated literature precedent as the emission intensity of DCF increased as a function of PFOS concentration.<sup>28</sup> These data demonstrate an increase in cellular redox activity as a function of PFOS exposure, with this increase being seemingly related to intracellular ROS content.

### **5.3.3 Scanning Electrochemical Microscopy of Hep G2 Following PFOS Exposure: Variation in Cellular Reactivity Over Time**

Additionally, Hu and co-workers reported a statistically significant decrease in mitochondrial membrane potential as well as variations in antioxidative enzyme activity within Hep G2 cells following a 48-hour exposure to  $\geq 100 \mu\text{M}$  PFOS.<sup>28</sup> To examine related changes in the cellular redox state over time, Hep G2 cells were exposed to PFOS-supplemented full growth media for 48 hours then electrochemically imaged for 2 hours.

Specifically, Hep G2 P23 cells were cultured in full growth media within 3.5 cm-diameter tissue culture dishes. At 75% to 80% confluence, spent media was removed from the dishes and the cells were rinsed with 1 mL DPBS. Next, 2 mL solutions of 0 and 100  $\mu\text{M}$  PFOS-supplemented full growth media were added to dishes to prepare samples for each concentration. Each dish was labeled based on the concentration of PFOS added, then placed in the incubator. After incubating the cells for 48 hours, spent PFOS-supplemented full growth media was



removed from the dishes. Next, the cells were rinsed with 1 mL DPBS, then 2 mL of full growth media was added to each dish before placing them in the incubator for later use.

For electrochemical imaging, spent media was removed from a 100  $\mu\text{M}$  PFOS sample and the cells were rinsed with DPBS before adding 0.5 mM FcCH<sub>2</sub>OH in DPBS to the sample dish. Cells were brought into focus in bright field using a 20 $\times$  objective lens, then electrochemically imaged as done previously. After the initial image, a second image was captured every hour for two additional hours at the same  $xy$  and  $z$  positions. Lastly, an optical image of the imaged region was captured. This imaging procedure was repeated for a 0  $\mu\text{M}$  PFOS sample.

Cells exposed to PFOS exhibited a higher electrochemical response directly following exposure (**Figure 5.9f-h**) as well as a relatively higher change in the overall electrochemical response over time compared to the control featured in **Figures 5.9b-d**. As the electrochemical response increased with respect to time, we inferred an increase in oxidative stress due to bioaccumulation of PFOS and exposure to FcCH<sub>2</sub>OH. To probe this further, we investigated the mechanism associated with the electrochemical response.

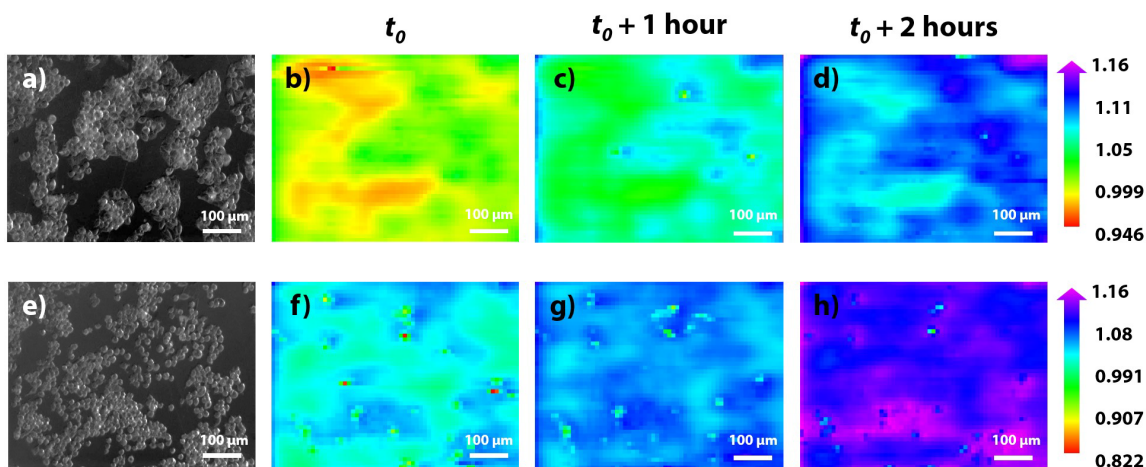


**Figure 5.9. Time Lapse Scanning Electrochemical Microscopy of Hep G2 Following PFOS Exposure**

Correlated optical images and electrochemical images of Hep G2 cells previously exposed to 0  $\mu\text{M}$  (a-d) and 100  $\mu\text{M}$  (e-h) PFOS-supplemented full growth media for 48 hours at 37  $^{\circ}\text{C}$  and 5%  $\text{CO}_2$ . Images obtained in 0.5 mM  $\text{FcCH}_2\text{OH}$  in DPBS with a Pt microelectrode SECM tip ( $r = 5 \mu\text{m}$ ) at +0.5 V vs. Ag/AgCl (1 M KCl); a glassy carbon rod was used as the counter electrode ( $r = 1.5 \text{ mm}$ ).

### 5.3.4 Ferrocenium Methanol Reduction *via* Glutathione

Here, it is important to note that PFOS bioaccumulation, local changes in topography<sup>3</sup>, and cellular redox activity based on the permeability of FcCH<sub>2</sub>OH<sup>3</sup> may contribute to the electrochemical response. While electrochemical imaging of cancer cells by oxidation of FcCH<sub>2</sub>OH to ferrocenium methanol (Fc<sup>+</sup>CH<sub>2</sub>OH) has literature precedence<sup>3,4,31,48</sup>, the use of FcCH<sub>2</sub>OH should not be approached without reservations. FcCH<sub>2</sub>OH has been implicated in the upregulation of glutathione (GSH) due to oxidative stress (*i.e.*, an imbalance in ROS production and accumulation in the cell versus antioxidant activity<sup>49</sup>) induced upon entrance into the cell.<sup>4</sup> This upregulation to maintain cellular homeostasis of ROS is followed by transport of GSH from the cell *via* multi-drug resistant protein 1, which Kuss and co-workers hypothesize to chemically regenerate FcCH<sub>2</sub>OH from Fc<sup>+</sup>CH<sub>2</sub>OH produced at the electrode surface.<sup>4</sup> This mechanism of regeneration is referred to as an E<sub>r</sub>C<sub>i</sub>' mechanism – a special type of EC mechanism – where an electrochemically reversible redox reaction (E<sub>r</sub>) is followed by a chemically irreversible reaction (C<sub>i</sub>) that regenerates the initial redox reactant, denoted by the prime symbol (“’”). Here, we initially hypothesized that a similar feedback mechanism (**Figure 5.10. GSH Facilitated ET**) is feasible since we electrochemically image Hep G2 cells *via* FcCH<sub>2</sub>OH oxidation in feedback mode.

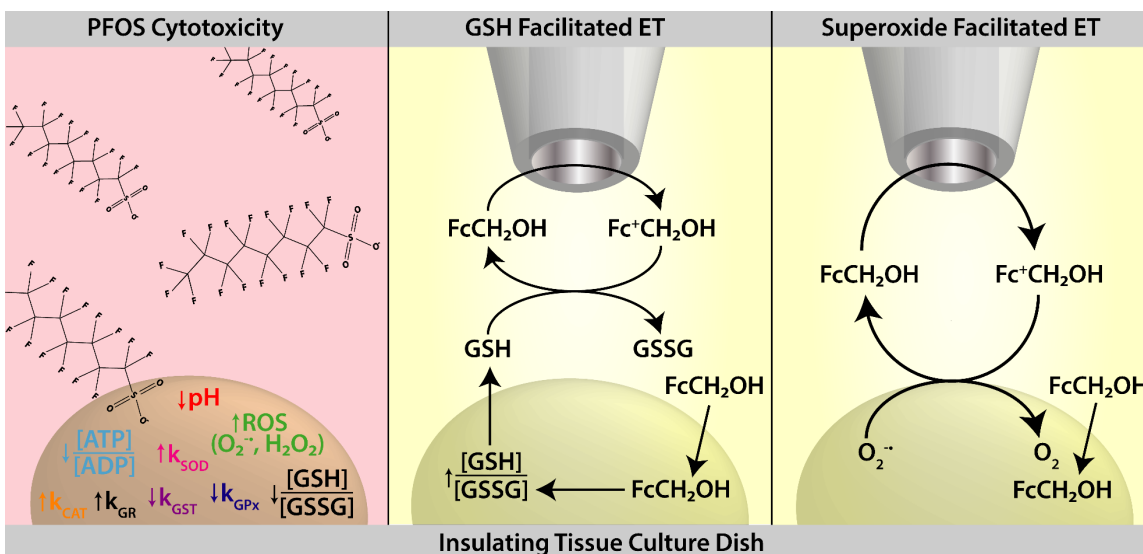


**Figure 5.10. Schematic Representation of PFOS Cytotoxic Mechanism**

Schematic representation the mechanism for PFOS cytotoxicity in Hep G2 cells and subsequent possible feedback mechanisms *via* GSH or superoxide anion radical during electrochemical imaging of PFOS-incubated Hep G2 cells by FcCH<sub>2</sub>OH oxidation.

To confirm if the  $E_rC_i'$  reaction mechanism is feasible, cyclic voltammetry of  $FcCH_2OH$  oxidation was performed in the presence of GSH in bulk solution. Solutions of 0.5 mM GSH and  $FcCH_2OH$  were prepared in DPBS. After purging each solution with argon gas for 5 minutes, initial voltammograms were obtained with a three-electrode system similar to that used in the microscopy experiments: a Pt macroelectrode ( $r = 1$  mm), a Ag/AgCl (1 M KCl) reference electrode, and a glassy carbon rod counter electrode ( $r = 1.5$  mm). To obtain the voltammograms, the Pt macroelectrode was scanned between 0 V and +0.5 V vs. Ag/AgCl at 0.2 V s<sup>-1</sup>, based on the potential range for the reversible oxidation of  $FcCH_2OH$ . Controls are shown in the polarographic convention in **Figure 5.11**.

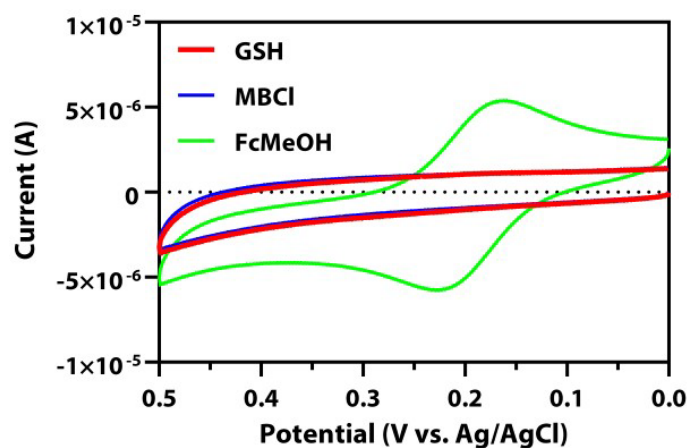
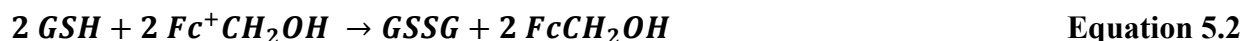


**Figure 5.11. Ferrocenium Methanol Reduction *via* Glutathione Voltammetric Controls**

Overlay of cyclic voltammograms of 0.5 mM FcCH<sub>2</sub>OH (abbreviated FcMeOH above, green), 0.5 mM GSH (red), and 0.5 mM MBCl (blue) in DPBS (1X, pH 7.4) at a Pt macroelectrode ( $r = 1$  mm) vs. Ag/AgCl (1 M KCl) after purging each solution for 5 minutes with argon gas. A glassy carbon rod ( $r = 1.5$  mm) was used as the counter electrode.

Next, five solutions of 0.5 mM FcCH<sub>2</sub>OH were prepared containing 0 mM, 0.5 mM, 1.0 mM, 2.0 mM, and 4.0 mM GSH in DPBS. After purging each solution with argon gas for 5 minutes, a voltammogram was captured in each solution. Between each voltammogram, the Pt macroelectrode was polished using 1.0 mm, 0.3 mm, and 0.05 mm alumina powder, in subsequent order, then rinsed with ultrapure water.

Similar to the E<sub>r</sub>C<sub>i</sub>' reaction mechanism corresponding to ferroceniumdimethanol oxidation in the presence of GSH<sup>50</sup>, we elucidated an E<sub>r</sub>C<sub>i</sub>' reaction mechanism in bulk solution using a Pt macroelectrode with FcCH<sub>2</sub>OH oxidation to Fc<sup>+</sup>CH<sub>2</sub>OH followed by the catalytic regeneration of FcCH<sub>2</sub>OH in the presence of GSH (**Equation 5.1 & 5.2**).



This is evident in **Figure 5.12** as the peak current indicative of FcCH<sub>2</sub>OH oxidation between +0.20 and +0.30 V vs. Ag/AgCl increases as the GSH concentration in solution increases, while the peak current indicative of Fc<sup>+</sup>CH<sub>2</sub>OH reduction near +0.18 V vs. Ag/AgCl decreases in magnitude at high concentrations of GSH. We must note that when the concentration of GSH is virtually constant in solution (*i.e.*, when GSH is in excess), the catalytic reaction with ferroceniumdimethanol may be characterized by pseudo-first order kinetics rather than second order kinetics; thus, when GSH is in excess (*i.e.*, 4 mM GSH) in the system presented here, a significant increase in oxidative current is observed (**Figure 5.12**).<sup>50</sup>

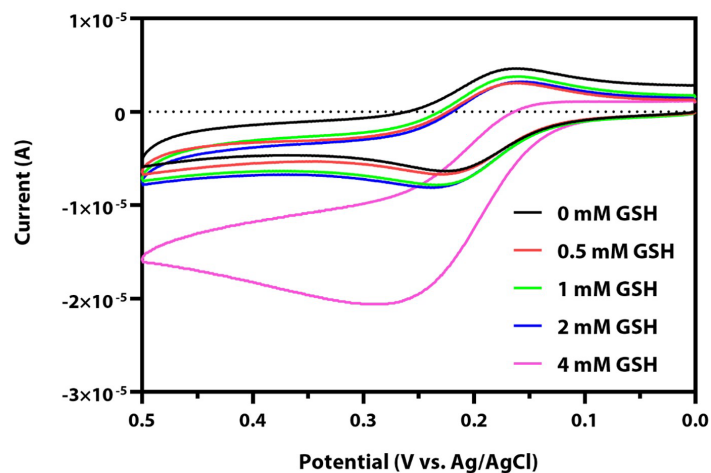


**Figure 5.12.  $E_r C_i'$  Mechanism Following Ferrocenemethanol Oxidation in Glutathione**

Cyclic voltammograms of 0.5 mM FcCH<sub>2</sub>OH combined with 0 mM (black), 0.5 mM (red), 1 mM (green), 2 mM (blue), and 4 mM (pink) GSH in DPBS at a Pt macroelectrode ( $r = 1$  mm) vs. Ag/AgCl (1 M KCl) after purging each solution for approximately 5 minutes with argon gas. A glassy carbon rod was used as the counter electrode ( $r = 1.5$  mm).



With cancer cells being equipped with GSH transporters, such as multi-drug resistance proteins, it is more probable for metastatic cells like Hep G2 cells to produce a positive feedback response during electrochemical imaging in the presence of FcCH<sub>2</sub>OH. Additionally, this feedback mechanism is only feasible due to FcCH<sub>2</sub>OH induced oxidative stress. Here, PFOS exposure creates an additional source of oxidative stress. Furthermore, we took additional steps to distinguish between redox mediator induced stress and effects due to PFOS exposure using variable fluorescence bandpass hyperspectral imaging.

### 5.3.5 Hyperspectral Imaging of Hep G2 Following PFOS Exposure: Glutathione Contribution Analysis

We hypothesized that if the feedback mechanism depicted in **Figure 5.10. GSH Facilitated ET** were responsible for the positive feedback observed during electrochemical imaging, that extracellular GSH content would increase with respect to PFOS concentration. Therefore, Hep G2 P19 cells were cultured in full growth media within 3.5 cm-diameter tissue culture dishes. At  $\leq 50\%$  confluence (*i.e.*, medium density), spent media was removed from the dishes and the cells were rinsed with 1 mL DPBS. Next, 2 mL solutions of 0, 50, and 100  $\mu\text{M}$  PFOS-supplemented full growth media were added to the dishes to prepare one sample for each PFOS concentration.

After incubating the cells for 16 hours overnight, spent PFOS-supplemented full growth media was removed from the dishes. The cells were loaded with 10  $\mu\text{M}$  DCF-DA as done previously. Next, 2 mL of 0.5 mM FcCH<sub>2</sub>OH/20  $\mu\text{M}$  monochlorobimane (MBCl) in DPBS was added to each dish. These steps were followed to image under similar conditions as used previously to observe the electrochemical response. MBCl was added to solution to conjugate with GSH in solution, then fluoresce to analyze GSH content (*i.e.*, MBCl is a fluorescence reporter for GSH); this allowed us to determine if extracellular GSH was responsible for the

positive feedback response (*i.e.*, to confirm or deny the proposed hypothesis). To analyze GSH content, fluorescence images were obtained at an excitation of 390 nm and an emission of 490 nm (*i.e.*, an emission indicative of the MBCl-GSH conjugate) using the hyperspectral imaging platform. Additional spectral data was captured using the hyperspectral imaging platform. An example spectrum is provided in **Figure 5.13**. Mean emission intensities at 490 nm were averaged over three distinct regions of interest ( $N = 3$ ) to produce data presented in **Figure 5.14**.

Contrary to the proposed hypothesis, an increase in GSH content was not a function of PFOS concentration (**Figure 5.14**), but rather GSH content decreases as PFOS concentration increases. Based on an ordinary one-way ANOVA followed by an unpaired *t*-test, the MBCl-GSH emission intensity decreases significantly from the control using a 95% confidence interval. This significant decrease in GSH content based on MBCl-GSH emission is supported by data collected by Hu and co-workers that reports a decrease in GSH content of lysed Hep G2 cells as function of PFOS exposure.<sup>28</sup> Here, it is important to note that the technique presented allows users to investigate the cellular redox state of living cells *in vitro* opposed to that of lysed cells.

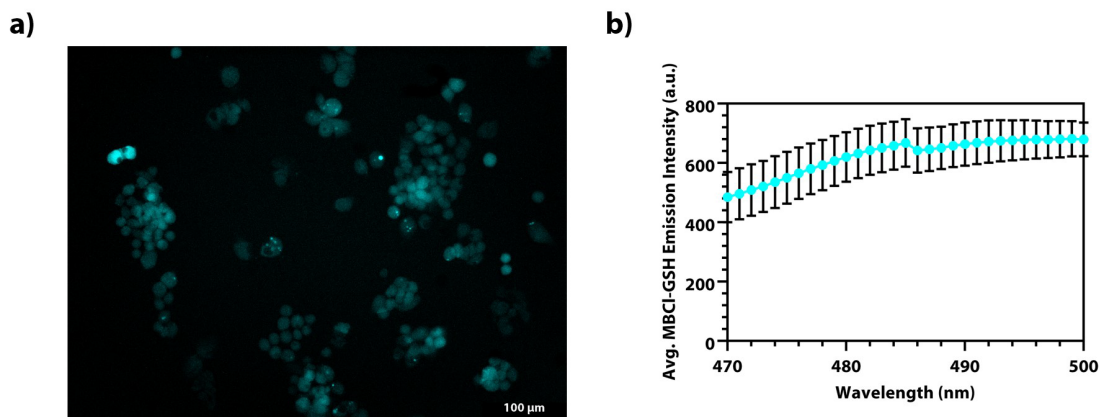


**Figure 5.13. Hyperspectral Imaging of Glutathione Following PFOS Exposure**

(a) Fluorescence image of Hep G2 P19 cells exposed to 100 μM PFOS-supplemented media for 16 hours at 37 °C and 5% CO<sub>2</sub>, then loaded with 10 μM DCF-DA. Cells imaged in the presence of 0.5 mM FcCH<sub>2</sub>OH/20 μM MBCl in DPBS (1X, pH 7.4). Image of MBCl-GSH conjugate fluorescence at  $\lambda_{\text{ex}}/\lambda_{\text{em}}$  390 nm/490 nm. Image false colored for visual representation. (b) Corresponding emission spectrum at  $\lambda_{\text{ex}}$  390 nm. Technical average of three spectra of the same area of cells ( $n = 3$ ).

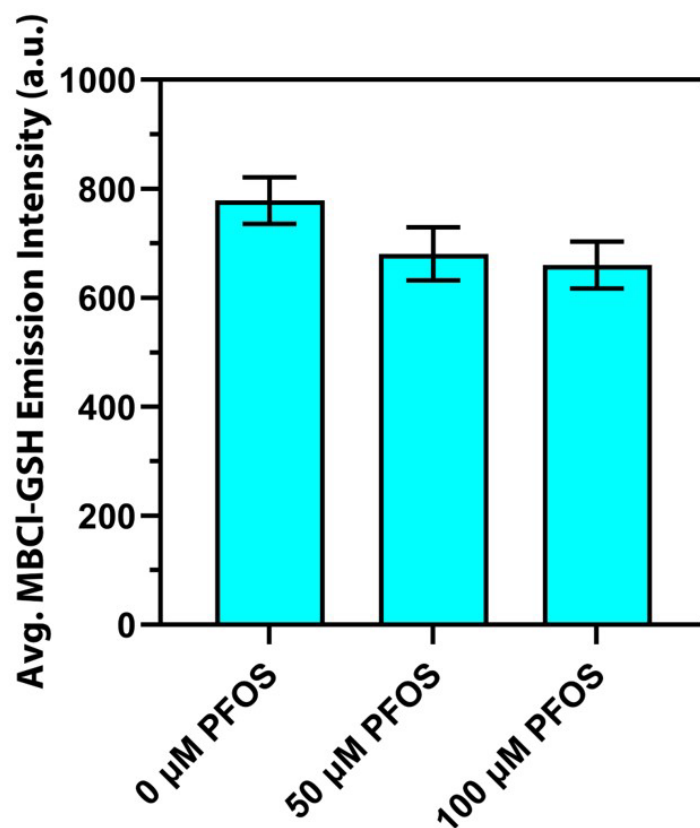


**Figure 5.14. Glutathione Contribution Analysis Following PFOS Exposure**

GSH content analysis of Hep G2 cells exposed to PFOS for 16 hours at 37 °C and 5% CO<sub>2</sub>. Hep G2 cells were loaded with DCF-DA, then imaged in the presence of 0.5 mM FcCH<sub>2</sub>OH/20 μM MBCl in DPBS. Average MBCl-GSH conjugate emission intensity at  $\lambda_{ex}/\lambda_{em}$  390/490 nm is provided as a function of PFOS concentration ( $N = 3$ ). \*Significantly different from the control,  $*p < 0.05$ .

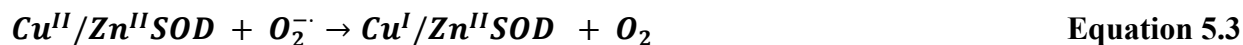
### 5.3.6 Hyperspectral-Assisted Scanning Electrochemical Microscopy of Hep G2 Following PFOS Exposure: Superoxide Dismutase 1 Contribution Analysis

After using hyperspectral-assisted imaging to rule out GSH facilitated electron transfer, reported trends in antioxidative species and enzymes following Hep G2 exposure to PFOS were considered to determine the redox mechanism responsible for the redox state observed *via* electrochemical imaging. Following PFOS exposure, antioxidative enzymes such as superoxide dismutase (SOD), catalase (CAT), and glutathione reductase (GR) increase in activity, while glutathione-*S*-transferase (GST) and glutathione peroxidase (GPx) decrease in activity (**Figure 5.10. PFOS Cytotoxicity**); it is important to note, literature precedent for antioxidative enzyme activity is based on manufactured assay kits using lysed cells.<sup>28</sup> With SOD enzyme activity increasing most significantly<sup>28</sup>, we hypothesized that electrons lost during the dismutation of superoxide to oxygen by cytoplasmic superoxide dismutase 1 (SOD 1) facilitate the regeneration of FcCH<sub>2</sub>OH *via* bimolecular electron transfer.

To investigate the role of SOD 1 and superoxide anion radical, Hep G2 P28 cells were cultured in 3.5 cm-diameter tissue culture dishes using full growth media. At 60 to 65% confluence, spent media was removed from the dishes and the cells were rinsed with 1 mL DPBS. To inhibit superoxide dismutase 1 (SOD 1), cells were incubated in 5  $\mu$ M SOD 1 inhibitor (*i.e.*, LCS-1, which is a 2-phenylpyridazin-3(2H)-one based non-copper chelater that selectively inhibits SOD 1 (Cu/Zn-SOD) with an IC<sub>50</sub> of 1.07  $\mu$ M) in DPBS in the dark at room temperature for 15 minutes. After inhibition of SOD 1, the cells were rinsed with 1 mL DPBS. Next, 2 mL of 0 and 100  $\mu$ M PFOS-supplemented full growth media was added to the dishes to prepare multiple samples for each concentration. After incubating cells for 16 hours overnight, spent media was removed from the dishes. Next, the cells were loaded with 10  $\mu$ M DCF-DA as done previously. Finally, the dishes were electrochemically imaged in 0.5 mM FcCH<sub>2</sub>OH in

DPBS as done previously. Fluorescence images obtained using the hyperspectral system used an excitation of 495 nm and an emission of 535 nm.

Following treatment with LCS-1, the activity of SOD 1 in the Hep G2 cells was suspended to prohibit the following mechanism for the dismutation of superoxide (**Equations 5.3-5.5**)<sup>51</sup>:



Upon recognition of a Cu<sup>II</sup>-redox species, the first reaction mechanism (**Equation 5.3**) executed by SOD 1 is an outer-sphere electron transfer<sup>51</sup>, making it feasible for electrons lost *via* superoxide dismutation to be gained by Fc<sup>+</sup>CH<sub>2</sub>OH to facilitate the regeneration of FcCH<sub>2</sub>OH. Alternatively, superoxide anion radicals have been implicated in the regeneration of ferrocene analogs.<sup>52</sup> By suspending SOD 1 activity, we differentiated between these two possible mechanisms.

After inhibiting SOD 1, an increase in the electrochemical response more significant than that of **Figures 5.8 & 5.9** was observed in **Figure 5.15** – where SOD 1 was inhibited by LCS-1 prior to PFOS exposure and imaging – providing evidence for a mechanism in which superoxide anion radicals directly facilitate the bimolecular electron transfer mechanism associated with the positive feedback response as shown in **Figure 5.10. Superoxide Facilitated ET**. This

mechanism is supported by literature precedent for one-electron reduction of ferrocenium ions *via* superoxide anion radicals.<sup>52, 53</sup>

Moreover, hydrogen peroxide (H<sub>2</sub>O<sub>2</sub>) was omitted as a mediator within this bimolecular electron transfer mechanism based on the role of SOD 1 in H<sub>2</sub>O<sub>2</sub> production (**Equations 5.3-5.5**) and the activity of other antioxidative enzymes. While CAT decomposes H<sub>2</sub>O<sub>2</sub>, CAT enzyme activity does not increase as significantly as SOD 1 (*i.e.*, < 3.2 units per mg compared to SOD 1 when Hep G2 are exposed to 100 μM PFOS and < 21.9 units per mg compared to SOD 1 when Hep G2 are exposed to 200 μM PFOS<sup>28</sup>) signifying low dependence on H<sub>2</sub>O<sub>2</sub> oxidative stress. Additionally, enzymes responsible for producing additional H<sub>2</sub>O<sub>2</sub> like GST and GPx reportedly exhibit decreased enzyme activity due to lack of GSH. Furthermore, superoxide anion radicals are responsible for the increase in cellular reactivity observed following PFOS exposure.

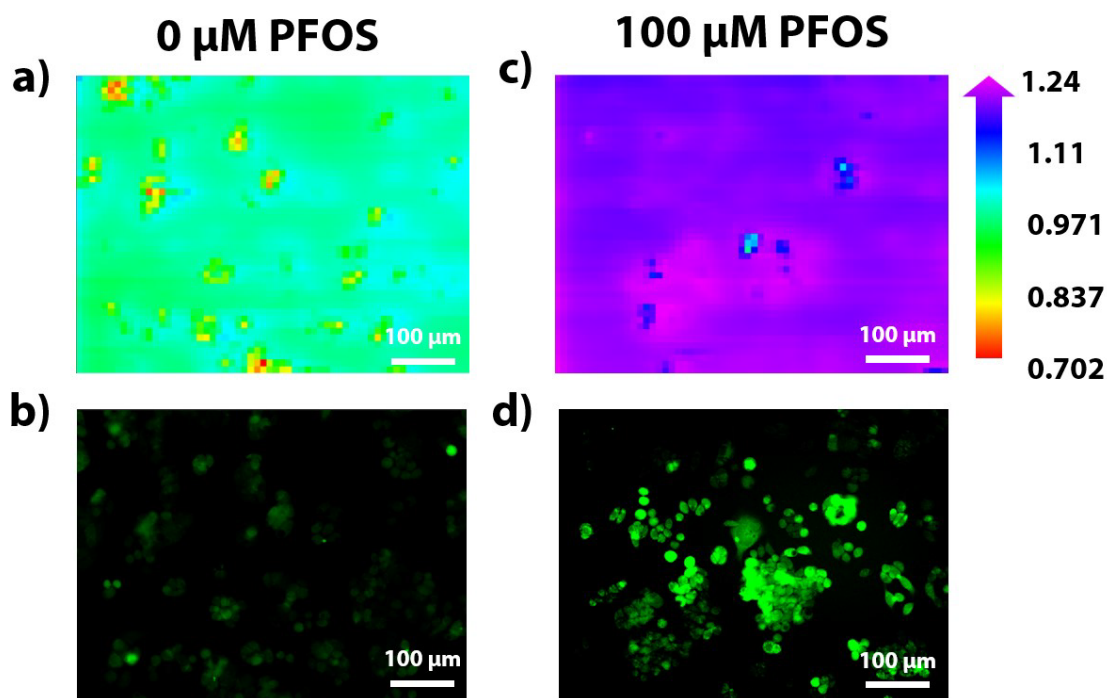


**Figure 5.15. Superoxide Dismutase 1 Contribution Analysis Following PFOS Exposure**

Correlated electrochemical images (a & c) and bright field/fluorescence image overlays (b & d) of SOD 1 inhibited Hep G2 P28 cells previously exposed to 0  $\mu\text{M}$  (a – b) and 100  $\mu\text{M}$  (c – d) PFOS-supplemented full growth media for 16 hours at 37  $^{\circ}\text{C}$  and 5%  $\text{CO}_2$ . Hep G2 cells loaded with DCF-DA prior to imaging. Cells imaged in 0.5 mM  $\text{FcCH}_2\text{OH}$  in DPBS. Electrochemical images obtained using a Pt microelectrode SECM tip ( $r = 5 \mu\text{m}$ ) at +0.5 V vs.  $\text{Ag}/\text{AgCl}$  (1 M  $\text{KCl}$ ) and a glassy carbon rod as a counter electrode ( $r = 1.5 \text{ mm}$ ); images normalized by  $i_{T,\infty}$  when  $d \geq 100 \mu\text{m}$ . Fluorescence images of ROS indicator, DCF, were obtained at  $\lambda_{\text{ex}}/\lambda_{\text{em}}$  495/535 nm. The fluorescence images were false colored for visual representation.



### 5.3.7 Concluding Remarks & Future Perspectives

In sum, per- and poly-fluoroalkyl substances (PFAS) are an emerging class of toxic environmental micropollutant. New measurement tools are necessary not only to sense PFAS in the environment<sup>54-58</sup> but to quantify the toxic effect PFAS have on cells. In particular, perfluorooctane sulfonate (PFOS) is one of the most toxic PFAS, and the US Environmental Protection Agency recently lowered the advisory limit down to 10 ppt. In this section, we used hyperspectral-assisted scanning electrochemical microscopy to investigate the redox mechanism responsible for the electrochemical response of hepatocarcinoma (Hep G2) cells during ferrocenemethanol (FcCH<sub>2</sub>OH) oxidation following PFOS exposure. The power of using hyperspectral imaging is that spectra can be collected at each pixel, allowing one to precisely investigate spectral intensities and shifts. Specifically, we distinguished between cytotoxic redox mechanisms using redox active-fluorophores and a typical one-electron transfer redox mediator. Following PFOS exposure, a dramatic increase in oxidative current from FcCH<sub>2</sub>OH-regeneration was accompanied by an increase in dichlorofluorescein fluorescence and a decrease in monochlorobimane-glutathione fluorescence. These results indicate FcCH<sub>2</sub>OH-regeneration is accompanied by an increase in reactive oxygen species and a decrease in glutathione content, respectively. By inhibiting the antioxidative enzyme responsible for the dismutation of superoxide to hydrogen peroxide, we implicated a bimolecular electron transfer mechanism for superoxide facilitated FcCH<sub>2</sub>OH-regeneration.

As countries continue to establish environmental advisory limits for PFAS, understanding which PFAS have the most deleterious effects on cellular metabolism is imperative. In addition, it would be beneficial to differentiate between the effects of PFAS and similar hydrocarbons going forward. For instance, PFOS displays higher hydrophobicity and potential to alter the cell membrane compared to octanesulfonate.<sup>59</sup> The ability to make such a diagnosis at the single cell

level allows one to account for heterogeneities in complex tissues. The method presented in this article for electrochemically monitoring cell metabolism and oxidative stress following PFAS exposure can be used for rapid toxicological screening of different PFAS on different cell lines. Such measurements will begin to inform technological innovations for sensing<sup>54-58</sup>, extracting<sup>60, 61</sup>, and destroying<sup>62-65</sup> PFAS in the environment.

## REFERENCES

1. J. B. Robertson, C. R. Davis and C. H. Johnson, *Proceedings of the National Academy of Sciences of the United States of America*, 2013, **110**, 21130-21135.
2. K. L. West, J. L. Kelliher, Z. Z. Xu, L. W. An, M. R. Reed, R. L. Eoff, J. D. Wang, M. S. Y. Huen and J. W. C. Leung, *Nucleic Acids Research*, 2019, **47**, 6236-6249.
3. S. Kuss, D. Polcari, M. Geissler, D. Brassard and J. Mauzeroll, *Proceedings of the National Academy of Sciences*, 2013, **110**, 9249.
4. S. Kuss, R. Cornut, I. Beaulieu, M. A. Mezour, B. Annabi and J. Mauzeroll, *Bioelectrochemistry*, 2011, **82**, 29-37.
5. B. Liu, S. A. Rogenberg and M. V. Mirkin, *Analytical Chemistry*, 2002, **74**, 6340-6348.
6. S. Voci, B. Goudeau, G. Valenti, A. Lesch, M. Jović, S. Rapino, F. Paolucci, S. Arbault and N. Sojic, *Journal of the American Chemical Society*, 2018, **140**, 14753-14760.
7. S. Terhune, E. Torigoi, N. Moorman, M. Silva, Z. Qian, T. Shenk and D. Yu, *Journal of Virology*, 2007, **81**, 3109-3123.
8. A. L. McCormick, L. Smith Vanessa, D. Chow and S. Mocarski Edward, *Journal of Virology*, 2003, **77**, 631-641.
9. F. Gugliesi, A. Coscia, G. Griffante, G. Galitska, S. Pasquero, C. Albano and M. Biolatti, *Microorganisms*, 2020, **8**.
10. A. E. Hale and N. J. Moorman, *Annual Review of Virology*, 2021, **8**, 201-218.
11. G. Gerna, F. Baldanti and M. G. Revello, *Human Immunology*, 2004, **65**, 381-386.
12. Y. Pan, H. Zhang, Q. Cui, N. Sheng, L. W. Y. Yeung, Y. Sun, Y. Guo and J. Dai, *Environ Sci Technol*, 2018, **52**, 7621-7629.
13. Z. Zeng, B. Song, R. Xiao, G. Zeng, J. Gong, M. Chen, P. Xu, P. Zhang, M. Shen and H. Yi, *Environment International*, 2019, **126**, 598-610.
14. D. S. Garcia, M. Sjodin, M. Hellstrandh, U. Norinder, V. Nikiforova, J. Lindberg, E. Wincent, A. Bergman, I. Cotgreave and V. M. Kos, *Chemico-Biological Interactions*, 2018, **281**, 1-10.
15. N. Sheng, R. N. Cui, J. H. Wang, Y. Guo, J. S. Wang and J. Y. Dai, *Archives of Toxicology*, 2018, **92**, 359-369.
16. A. Di Nisio, M. S. Rocca, I. Sabovic, M. D. Ponce, C. Corsini, D. Guidolin, C. Zanon, L. Acquasaliente, A. R. Carosso, L. De Toni and C. Foresta, *Chemosphere*, 2020, **242**, 9.

17. E. M. Sunderland, X. D. C. Hu, C. Dassuncao, A. K. Tokranov, C. C. Wagner and J. G. Allen, *Journal of Exposure Science and Environmental Epidemiology*, 2019, **29**, 131-147.
18. B. N. Conway, A. N. Badders, T. Costacou, J. M. Arthur and K. E. Innes, *Diabetes Metabolic Syndrome and Obesity-Targets and Therapy*, 2018, **11**, 707-716.
19. D. Herzke, E. Olsson and S. Posner, *Chemosphere*, 2012, **88**, 980-987.
20. E. C. Bonefeld-Jorgensen, M. H. Long, S. O. Fredslund, R. Bossi and J. Olsen, *Cancer Causes & Control*, 2014, **25**, 1439-1448.
21. R. R. Worley, S. M. Moore, B. C. Tierney, X. Y. Ye, A. M. Calafat, S. Campbell, M. B. Woudneh and J. Fisher, *Environment International*, 2017, **106**, 135-143.
22. S. Hurley, D. Goldberg, M. M. Wang, J. S. Park, M. Petreas, L. Bernstein, H. Anton-Culver, D. O. Nelson and P. Reynolds, *Environmental Health*, 2018, **17**.
23. K. Kleszczynski and A. C. Skladanowski, *Toxicology and Applied Pharmacology*, 2011, **251**, 163-168.
24. A. F. Ojo, C. Peng and J. C. Ng, *Environmental Pollution*, 2020, **263**, 12.
25. C. E. Rockwell, A. E. Turley, X. G. Cheng, P. E. Fields and C. D. Klaassen, *Food and Chemical Toxicology*, 2017, **100**, 24-33.
26. J. A. Gimenez-Bastida, M. Surma and H. Zielinski, *Toxicology in Vitro*, 2015, **29**, 1683-1691.
27. A. Peropadre, M. J. Hazen, J. M. P. Martin and P. F. Freire, *Environmental Pollution*, 2020, **260**, 9.
28. X. Z. Hu and D. C. Hu, *Archives of Toxicology*, 2009, **83**, 851-861.
29. F. R. Niu, D. C. Wang, J. P. Lu, W. Wu and X. D. Wang, *Journal of Cellular and Molecular Medicine*, 2016, **20**, 1789-1795.
30. C. J. Tape, *Trends in Biotechnology*, 2016, **34**, 627-637.
31. D. Polcari, P. Dauphin-Ducharme and J. Mauzeroll, *Chemical Reviews*, 2016, **116**, 13234-13278.
32. H. K. McCormick and J. E. Dick, *Analytical and Bioanalytical Chemistry*, 2021, **413**, 17-24.
33. F. P. Filice and Z. F. Ding, *Analyst*, 2019, **144**, 738-752.
34. S. Goines and J. E. Dick, *Journal of the Electrochemical Society*, 2019, **167**.

35. Y. Li, J. Lang, Z. Ye, M. Wang, Y. Yang, X. Guo, J. Zhuang, J. Zhang, F. Xu and F. Li, *Analytical Chemistry*, 2020, **92**, 4771-4779.
36. J. Lang, Y. Li, Z. Ye, Y. Yang, F. Xu, G. Huang, J. Zhang and F. Li, *Analytical Chemistry*, 2021, **93**, 5797-5804.
37. J. Mauzeroll and J. Bard Allen, *Proceedings of the National Academy of Sciences*, 2004, **101**, 7862-7867.
38. C. S. Santos, A. J. Kowaltowski and M. Bertotti, *Scientific Reports*, 2017, **7**, 11428.
39. M. Nebel, S. Grützeke, N. Diab, A. Schulte and W. Schuhmann, *Angewandte Chemie International Edition*, 2013, **52**, 6335-6338.
40. H. Kikuchi, A. Prasad, R. Matsuoka, S. Aoyagi, T. Matsue and S. Kasai, *Frontiers in Physiology*, 2016, **7**.
41. J. P. Wilburn, M. Ciobanu and D. E. Cliffel, *Journal of The Electrochemical Society*, 2015, **163**, H3077-H3082.
42. Y. Takahashi, I. Shevchuk Andrew, P. Novak, B. Babakinejad, J. Macpherson, R. Unwin Patrick, H. Shiku, J. Gorelik, D. Klenerman, E. Korchev Yuri and T. Matsue, *Proceedings of the National Academy of Sciences*, 2012, **109**, 11540-11545.
43. S. Goines, M. Deng, M. W. Glasscott, J. Leung and J. E. Dick, *Analyst*, 2022, **147**, 2396-2404.
44. W. M. A. Westerink and W. G. E. J. Schoonen, *Toxicology in Vitro*, 2007, **21**, 1592-1602.
45. D. Li, L. Jiang, Y. Hong and Z. Cai, *Environmental Pollution*, 2021, **268**, 115774.
46. Z. Nova, H. Skovierova, J. Strnadel, E. Halasova and A. Calkovska, *International Journal of Molecular Sciences*, 2020, **21**, 1148.
47. I. Beaulieu, S. Kuss, J. Mauzeroll and M. Geissler, *Analytical Chemistry*, 2011, **83**, 1485-1492.
48. P. Sun, F. O. Laforge, T. P. Abeyweera, S. A. Rotenberg, J. Carpino and M. V. Mirkin, *Proceedings of the National Academy of Sciences of the United States of America*, 2008, **105**, 443-448.
49. D. J. Betteridge, *Metabolism*, 2000, **49**, 3-8.
50. M. Davceva, V. Mirceski and S. Komorsky-Lovric, *International Journal of Electrochemical Science*, 2011, **6**, 2718-2729.
51. R. C. Maji, P. P. Das, S. Mishra, A. Bhandari, M. Maji and A. K. Patra, *Dalton Transactions*, 2016, **45**, 11898-11910.

52. B. A. Aderibigbe and H. E. Mukaya, in *Nano- and Microscale Drug Delivery Systems*, ed. A. M. Grumezescu, Elsevier, 2017, pp. 33-48.
53. M. Hayyan, M. A. Hashim and I. M. AlNashef, *Chemical Reviews*, 2016, **116**, 3029-3085.
54. P. J. Kauffmann, N. A. Park, R. B. Clark, G. L. Glish and J. E. Dick, *ACS Measurement Science Au*, 2022, **2**, 106-112.
55. R. B. Clark and J. E. Dick, *ACS Sensors*, 2020, **5**, 3591-3598.
56. R. Kazemi, E. I. Potts and J. E. Dick, *Analytical Chemistry*, 2020, **92**, 10597-10605.
57. R. B. Clark and J. E. Dick, *Chemical Communications*, 2021, **57**, 8121-8130.
58. M. W. Glasscott, K. J. Vannoy, R. Kazemi, M. D. Verber and J. E. Dick, *Environmental Science & Technology Letters*, 2020, **7**, 489-495.
59. W. Xie, I. Kania-Korwel, P. M. Bummer and H. J. Lehmler, *Biochimica et Biophysica Acta (BBA) - Biomembranes*, 2007, **1768**, 1299-1308.
60. E. Kumarasamy, I. M. Manning, L. B. Collins, O. Coronell and F. A. Leibfarth, *ACS Central Science*, 2020, **6**, 487-492.
61. R. Ranaweera, C. Ghafari and L. Luo, *Analytical Chemistry*, 2019, **91**, 7744-7748.
62. Z. Sun, C. Zhang, L. Xing, Q. Zhou, W. Dong and M. R. Hoffmann, *Environmental Science & Technology*, 2018, **52**, 2953-2962.
63. S. Hao, Y.-J. Choi, B. Wu, C. P. Higgins, R. Deeb and T. J. Strathmann, *Environmental Science & Technology*, 2021, **55**, 3283-3295.
64. G. K. Longendyke, S. Katel and Y. Wang, *Environmental Science: Processes & Impacts*, 2022, **24**, 196-208.
65. J. Cui, P. Gao and Y. Deng, *Environmental Science & Technology*, 2020, **54**, 3752-3766.

## Chapter 6 Nanoelectrode Fabrication for Single Cell Analysis

Disease progression at the single cell level is generally characterized by local abundance of disease-associated metabolites. Usually, metabolite concentration is directly related to the stage of a disease (*e.g.*, pre-cancerous cells may be distinguished from normal cells based on a buildup of lactate<sup>1,2</sup>). In addition, single cell analysis may elucidate the signaling pathways responsible for disease progression. Furthermore, examination of disease progression at the single cell level may provide a basis for preventative care. For example, Chakraborty and co-workers informed preventative care to mitigate DNA damage following exposure to an alkylating carcinogen using single cell gel electrophoresis to demonstrate the potential use of four natural products as anticancer therapeutics within hamster lung fibroblast cells.<sup>3</sup> In addition, in 2019 a basis for evaluating the onset of congenital heart defects was determined following single cell transcriptome analysis of embryonic transcriptional determinates of cardiac progenitor cells.<sup>4</sup> The use of single cell analysis to inform preventative care extends to electrochemistry and imaging. Electrochemical biosensors were equipped with antibodies for DNA recognition of circulating tumor cancer cells with rolling circle amplification for ultrasensitive detection of these cells in peripheral blood; this strategy is advantageous to diagnostics and informing preventative measures.<sup>5</sup> An example of advantageous multicolor imaging was demonstrated in 2020; Stepula and co-workers used multicolor imaging *via* target immune-SERS microscopy to evaluate biomarkers predicative for breast cancer in single cells to inform preventative care.<sup>6</sup> Thus, the methods described in this dissertation are useful for single cells analysis with the use of nanoelectrodes.

## 6.1 Nanoelectrode Fabrication<sup>8</sup>

With heightened interest in higher sensitivity measurement science, electrochemists have geared up to discover new truths of nature within complex systems *via* nanoelectrochemistry. Characterized by increased signal-to-noise and decreased double-layer capacitance<sup>7</sup>, nanoelectrodes are designed to probe the limits of electron-transfer kinetics<sup>8,9</sup> and study the redox chemistry of single entities. In particular, nanoelectrodes have been used to study single metal crystals<sup>10</sup>, single nanoparticles<sup>11</sup>, and single molecules (*e.g.*, single enzymes<sup>12</sup>) as well as to elucidate dynamic changes in mass transport at the nanoscale level within materials chemistry and biochemistry<sup>13</sup>. Additionally, nanoelectrodes are invaluable tools for studying intracellular redox chemistry, especially those that have been functionalized to be metabolite specific<sup>14,15</sup>. Numerous procedures detail the fabrication of submicron-electrodes *via* lithography<sup>16</sup>, electrochemical deposition<sup>17-19</sup>, electrochemical etching<sup>20,21</sup>, laser pullers<sup>22-24</sup>, focused ion beam (FIB) milling<sup>25</sup>, and chemical vapor deposition<sup>26</sup>. Some fabrication methods even use a combination of techniques<sup>27,28</sup> or unique techniques, such as interfacial reactions<sup>29</sup>, to obtain the desired electrode material and size. Laser-assisted fabrication using laser-based micropipette pullers (*i.e.*, laser pullers) is most popular due to its ease-of-use and safety. However, despite the number of publications outlining fabrication procedures, the reproduction of such protocols is often a challenge. Not only are electrodes with nanometer radii fragile, leading to significant random errors when used, but systematic differences between laser pullers also further limit the precise reproduction of fabrication procedures between labs through written parameters.

---

<sup>8</sup> Section 6.1 was reproduced from a manuscript in preparation: “A Troubleshooting Guide for Laser Pulling Nanoelectrodes” by Koun Lim<sup>†</sup>, Sondrica Goines<sup>†</sup>, Mingchu Deng, Hadley McCormick, and Jeffrey E. Dick with permission from the authors listed here. (<sup>†</sup>Authors contributed equally to this work.)



Thus, in this section, we varied each parameter involved in laser-assisted submicron- and nano-electrode fabrication to guide a user in finding a parameter setting specific to the laser puller available to them. In this section, our goal is to outline troubleshooting guidelines in each step of the laser pulling process. We note that we focus on the fabrication of nanoelectrodes and not nanoelectrode polishing, a complex step that is necessary to reproducibly fabricate useful nanosensors.

Typically, nanoelectrode fabrication using a laser puller has two parts: 1) the sealing process where a quartz capillary is heated under vacuum to encase a Pt wire (**Figure 6.1a**), and 2) the pulling process where the Pt-sealed quartz capillary is pulled into two separate pieces with a fine tip (**Figure 6.1b**). Ultimately, there are six parameters involved in the fabrication process: 1) vacuum, 2) heat, 3) filament, 4) velocity, 5) delay, and 6) pull. Here, we varied each parameter to show the optimization of a laser-assisted fabrication procedure. The procedure outlined specifically works with 0.025 mm Pt wires and quartz capillaries (ID:0.3 mm, OD: 0.1 mm). In all experiments, a Sutter P-2000 laser puller was used.

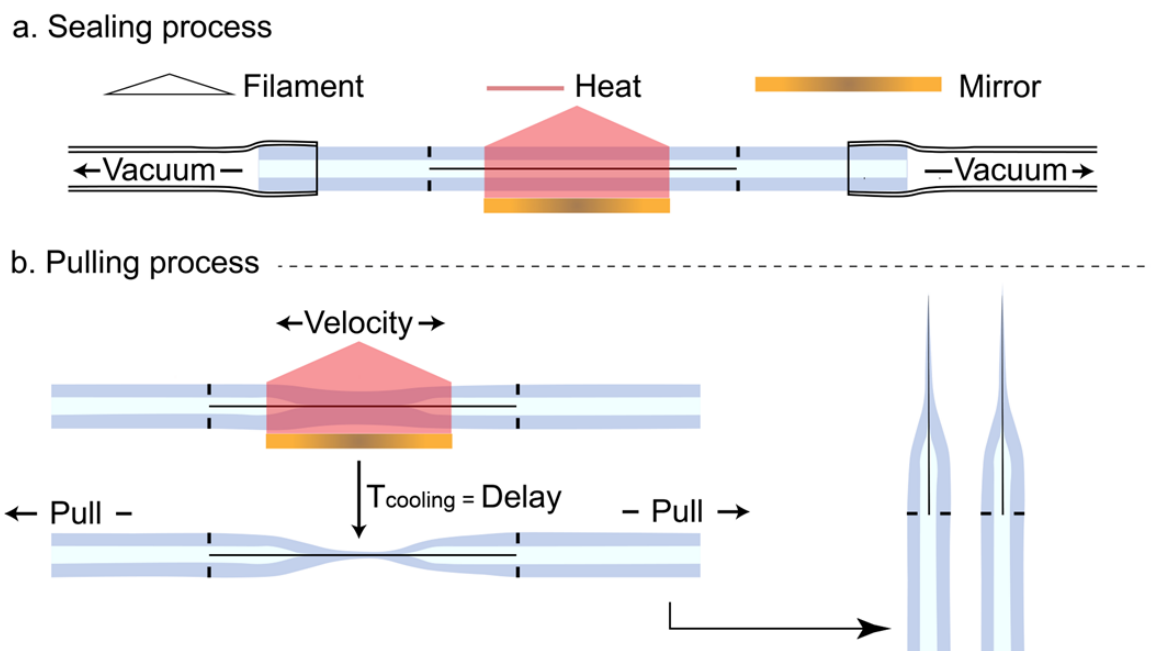


**Figure 6.1. Schematic Representation of Laser Pulling Pt Nanoelectrodes**

A schematic illustration of submicron-electrode fabrication using a Sutter P-2000 laser puller.

The first step in the fabrication is to seal a Pt wire in a quartz capillary (a) using a program involving heat, filament, and vacuum. The second step in the fabrication is to pull the Pt-sealed quartz capillary (b) using a program involving heat, filament, velocity, delay, and pull.

### 6.1.1 Materials & Methods

Laser-based micropipette puller systems (Model P-2000) and quartz capillaries (ID:0.30 mm, OD: 1.0 mm, Item#: Q100-30-15) were purchased from Sutter Instrument Company and Pt wire with a diameter of 0.025 mm (Purity: 99.99%, PT005114) was purchased from Goodfellow. A BV-10 microelectrode beveler and its corresponding diamond abrasive plates (*i.e.*, 104C – coarse, 104D – fine, 104E – very fine, and 104F – extra fine) were purchased from Sutter Instrument Company. Nichrome wire (0.25 mm, product# 13082) was purchased from Ted Pella and tungsten wires (W559504) were purchased from Advent. Tinned copper wire (30 AWG) was purchased from Treedix. A rotary vacuum pump (RZ 6) was purchased from Vacuubrand. Vacuum tubes were purchased from Fisher Scientifics (60985-540, 14-469-1A) and New Age Industries (1400154). All other chemicals were purchased from Sigma-Aldrich.

From the vacuum pump to the laser puller, a series of vacuum tubes were connected. Lastly, a Y-adaptor was used to part a single vacuum line into two using smaller vacuum tubes that tightly wrap around each end of the quartz capillary. A small hole was drilled on each side of the laser puller cover to bring the vacuum tubes in (**Figure 6.2**). A single Pt wire (approximately 4 cm long) was loaded into a clean quartz capillary, then pushed into the center of the capillary with a nichrome wire (Ted Pella, 0.25 mm, product #13082). The location of the ends of the Pt wire was marked on the quartz capillary using a Sharpie marker to indicate the location of the Pt wire. At least five quartz capillaries were loaded with Pt wire before the sealing process. Before placing the Pt wire-loaded capillary into the laser puller, the Sharpie marks were removed with acetone or isopropyl alcohol prevent debris from coating the gold-plated retro mirror of the puller during heating.

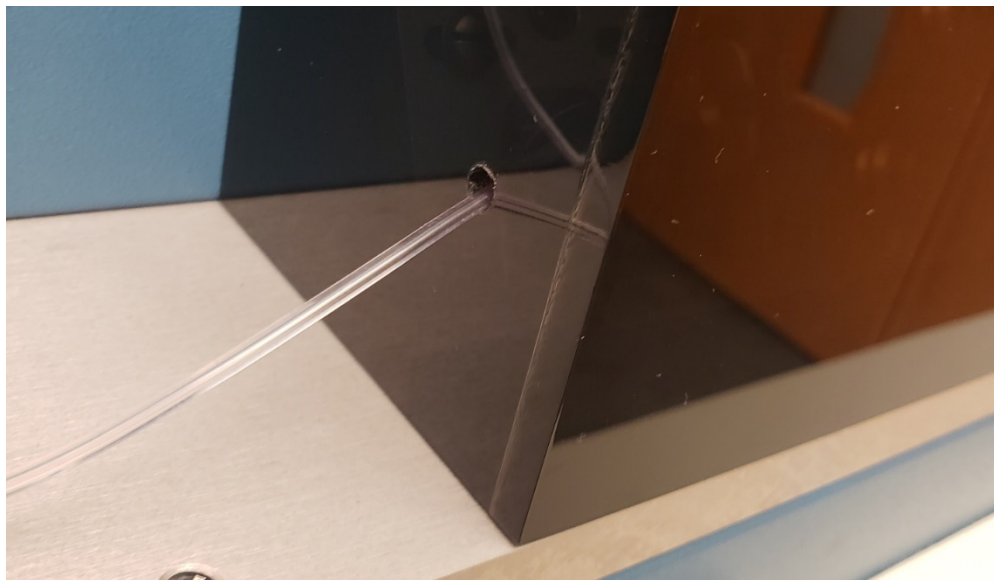


**Figure 6.2. P-2000 Laser Puller Modification**

A small hole slightly bigger than the diameter of the vacuum tube was drilled on the side of the laser puller cover to bring the vacuum tubes in. This vacuum tube is later connected to the Pt wire-loaded quartz capillary for the sealing process.

Next, the puller bars of the instrument were held in place with horizontal metal bars placed between the center bearings and the puller bars (**Figure 6.3a**). The Pt wire-loaded capillary was centered in the laser puller using the clamping knobs (**Figure 6.3b**). Once the Pt wire-loaded quartz capillary was centered and secured in the laser puller, a vacuum line was connected on each end of the quartz capillary (**Figure 6.3c**). The vacuum was turned on for at least 2 minutes prior to the sealing process and stayed on until the end of the sealing process. The placement of each clamp within the laser puller was marked on the quartz capillary using a marker to approximate the placement of the quartz capillary within the puller throughout the entire process. A bench-top upright microscope was used to examine the sealing process between cycles to determine the status. All images used in this section were taken with a personal smartphone, Galaxy S9+, by aligning the phone with an eyepiece of the microscope. The TEM image used in the graphical abstract was taken using a Talos F200X in the Chapel Hill Analytical and Nanofabrication Laboratory.

One cycle of the sealing process means turning the laser on and off once. For a complete seal, the laser was turned on for 30 seconds and off for 30 seconds. Generally, this cycle was repeated 4 times. While the on and off time for the laser can be arbitrarily picked, it is advised for the safety of the laser to turn off the laser as long as the laser was turned on. It is also possible to reduce the number of cycles and increase the laser exposure time to complete the seal. Experimentally, the laser puller was automatically turned off after approximately a minute of constant exposure. Therefore, it is possible to heat the Pt wire-loaded capillary for longer but, in order to keep the laser safe and maintain constant control over the variables within the fabrication procedure, the laser was turned on for 30-second intervals.

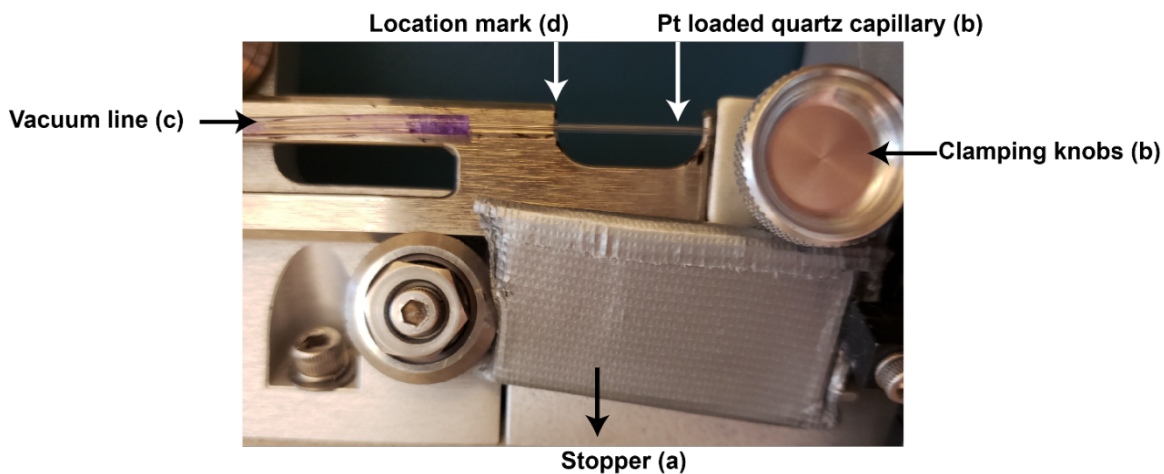


**Figure 6.3. Laser Puller Set Up During Seal**

The puller bar was pulled forward towards the retro mirror assembly and was held in place with self-made stoppers (a). The Pt loaded-quartz capillary was placed into the groove of the puller bar, then clamped down with the clamping knobs (b). Next, the vacuum line (c) connected to a vacuum was carefully connected to the loaded quartz capillary. Finally, a mark was made with a Sharpie marker on the quartz capillary (d) to mark the placement of the capillary for reloading in the same position every time.

Here, two Sutter P-2000 laser pullers were used to prepare submicron-electrodes. Therefore, parameter values featured in figure captions may vary based on the puller in use, however the troubleshooting steps outlined here may be used consistently to optimize fabrication procedures across laboratories. For an optimal seal using laser puller #1 (used in **Figures 6.4-6.11 & 6.15**), the puller was programmed: Heat: 840, Filament: 5, Velocity: 120, Delay: 129, Pull: 0. However, the only important parameters were heat, filament, and pull settings. The other parameters (velocity and delay) could be arbitrarily set. For the subsequent pulling process, the puller was programmed: Heat: 817, Filament: 2, Velocity: 120, Delay: 128, Pull: 250. The voltammograms featured in **Figures 6.13 & 6.16** were prepared using a second Sutter P-2000 laser puller. To seal the Pt wire featured in **Figure 6.13**, puller #2 was programmed: Heat: 700, Filament: 4, Velocity: 60, Delay: 140, Pull: 1. To pull the final electrode, the puller was programmed: Heat: 695, Filament: 2, Velocity: 60, Delay: 100, Pull: 200. To seal the Pt wire featured in **Figure 6.16**, puller #2 was programmed: Heat: 775, Filament: 5, Velocity: 120, Delay: 129, Pull: 1. For the subsequent pulling process, the puller was programmed: Heat: 800, Filament: 3, Velocity: 120, Delay: 128, Pull: 200. The pullers are labeled #1 and #2 based on the order in which they were purchased. The associated parameter values are provided as an initial reference and may be subject to optimization using the steps outlined in this manuscript.

### **6.1.2 The Seal Process**

Sealing a Pt wire in a quartz capillary requires reforming the quartz capillary to encase the Pt wire. A complete seal shows a smooth and tight encasing of the quartz around the Pt wire without degradation (**Figure 6.4a**). A simple microscopic examination of the seal is important when ensuring a complete seal from all angles and higher magnitudes (**Figure 6.4b**).

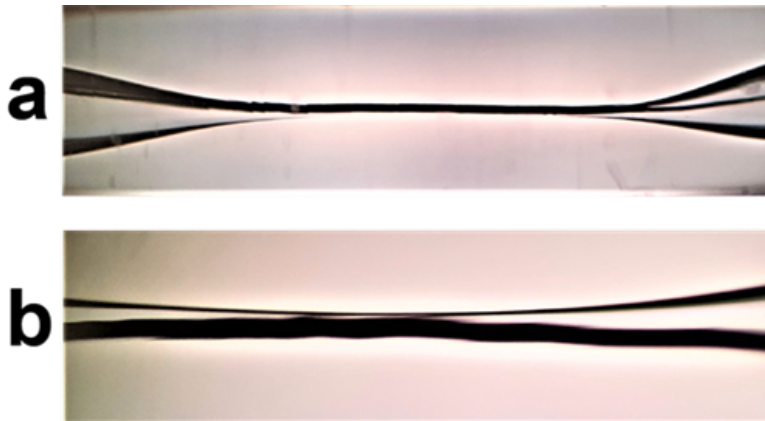


**Figure 6.4. Incomplete vs. Complete Seal**

Representative microscopic images of a complete seal (a) using a 10× objective and an incomplete seal (b) observed using a 20× objective of a bench-top upright microscope. All images were taken using a cellphone by aligning it with an eyepiece of the microscope.



A successful sealing process is governed by 3 parameters: 1) vacuum, 2) heat, and 3) filament. Specifically, finding a combination of heat and filament under a sufficient vacuum is key to the sealing process.

#### **6.1.2.1 Vacuum & Heat**

For vacuum, it is either strong enough or not. Typically, if the vacuum strength was not sufficient, the seal did not occur or did not complete despite the number of sealing cycles. As a result of increasing the sealing cycles, the capillaries show uneven and elongated deformation of capillaries without a complete seal (**Figure 6.5**). A sudden inability to seal is typically related to a loss of vacuum strength due to clogged vacuum tubes, cracked quartz capillaries, or defective machines. On the other hand, a sufficient or strong vacuum may result in drawing the Pt wire out of the quartz capillary. Thus, both ends of the quartz capillary should be connected to the vacuum lines before turning on the vacuum. Similar to vacuum, the heat parameter is either high enough or not. Usually, the heat was applied at 30-second intervals (30 seconds on/30 seconds off) over the course of 3-4 cycles to ensure that the outer and inner diameters would shrink to make a proper seal. The cycle number was often adjusted to complete a seal if a seal was almost complete (**Figure 6.4b**). Otherwise, after finding an optimal heat parameter, a constant 4 cycles with 30-second intervals were used as the standard procedure. Moreover, even with an appropriate heat setting, there were occasions where the Pt wire lost its integrity because the wire itself was damaged prior to the sealing process (**Figure 6.6**). Thus, in order to find the heat setting most suitable for the sealing process, it was crucial to always insert clean and unused Pt wires with care to ensure the conservation of the Pt wire integrity.

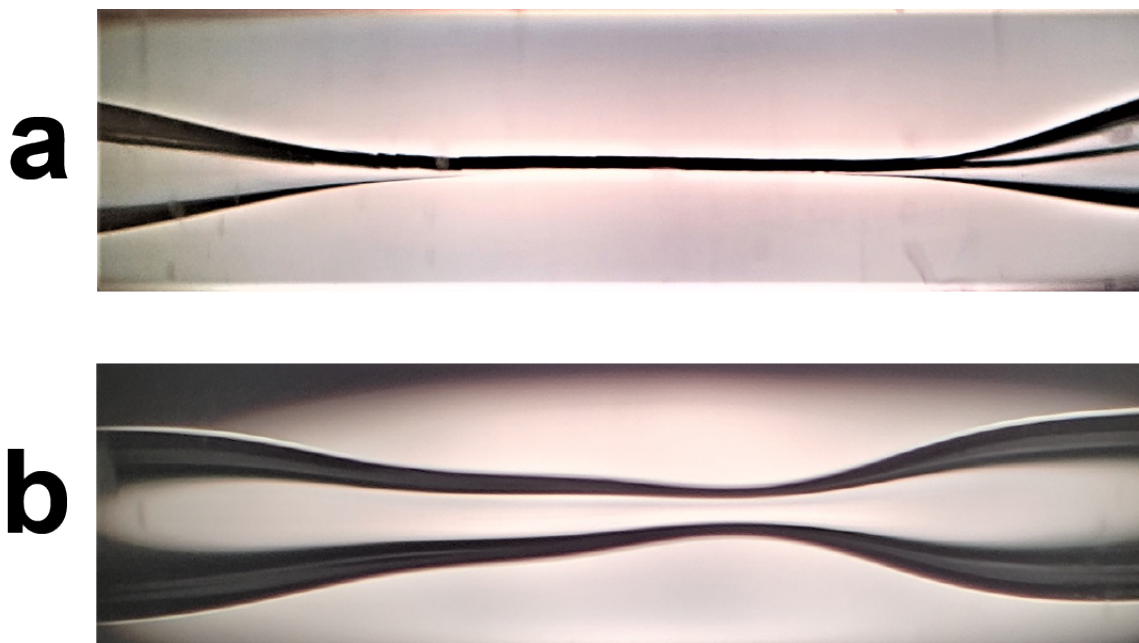


**Figure 6.5. Effect of Vacuum on the Seal Process**

A complete seal of the Pt wire inserted in a quartz capillary (a) was obtained when the vacuum was sufficient with a standard protocol (Heat: 840, Filament: 5, 30 on/off, 4 cycles). However, with insufficient vacuum, the quartz capillary did not completely seal (b). In addition, repeating the standard protocol for numerous rounds to force the seal resulted in uneven condensing of the quartz capillary.

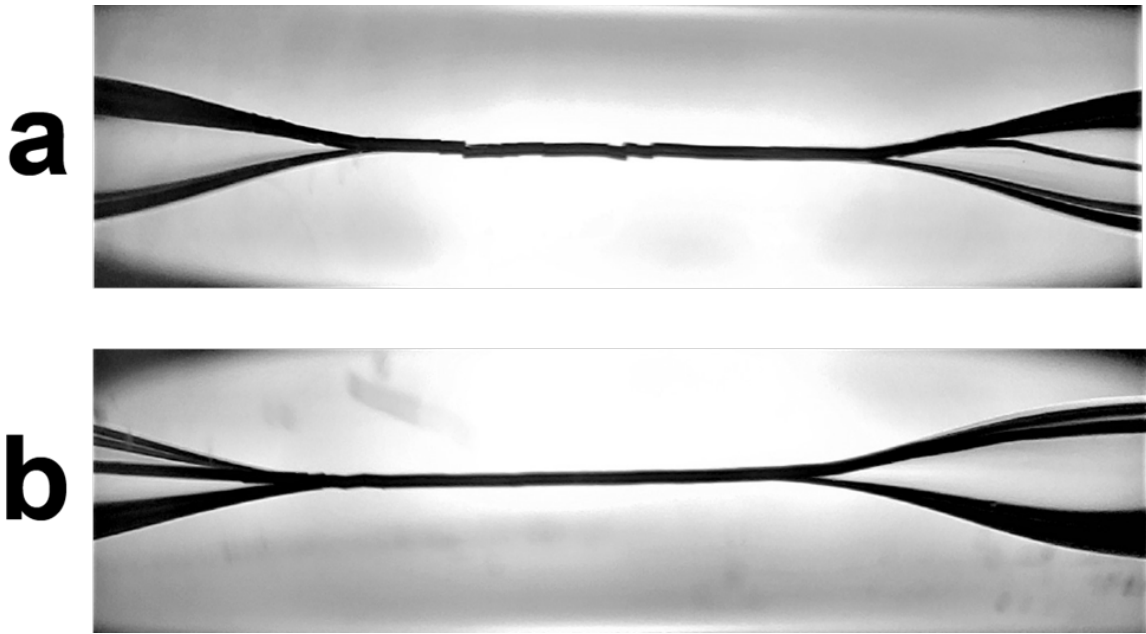


**Figure 6.6. Loss of Pt Wire Integrity Upon Complete Seal**

The integrity of the encased Pt wire was compromised (a), even when the sealing protocol remained the same (Heat: 840, Filament: 5, 30 on/off, 4 cycles). Numerous factors such as bending during the insertion of Pt wires and dirty Pt wires can contribute to the loss of Pt wire integrity upon a complete seal.

To elucidate the correlation between the heat value and the seal status, the protocol was set to vary heat while other parameters remained constant: Filament:5, Velocity: 120, Delay: 128, Pull: 0, 30-second interval, 4 cycles. If the heat setting was too high, the inner diameter began to completely seal, resulting in a complete blockage with a line of melted Pt tracing where the inner capillary once was (**Figure 6.7a**). Here, the inner quartz reached the melting temperature of the Pt wire and the Pt wire started to melt forming spheres prior to seal completion. As the heat started to approach the proper heat value, the Pt wire was partially sealed but still disconnected in the middle where the heat was applied (**Figure 6.7b**). When the vacuum and heat were sufficient, a complete seal was achieved (**Figure 6.7c**). On the contrary, if the heat was insufficient, the seal was incomplete (**Figure 6.7d**), compromising the Pt wire integrity at times (**Figure 6.7d**) even if a clean and uncompromised wire was used in the beginning. The heat values were typically adjusted in units of 10, 5, or 1 depending on the seal status. However, when changing the heat parameter by a unit of 1 either resulted in melting of the Pt wire or an incomplete seal (**Figure 6.7d**), the filament was often changed as an easier and faster option for obtaining a complete seal.

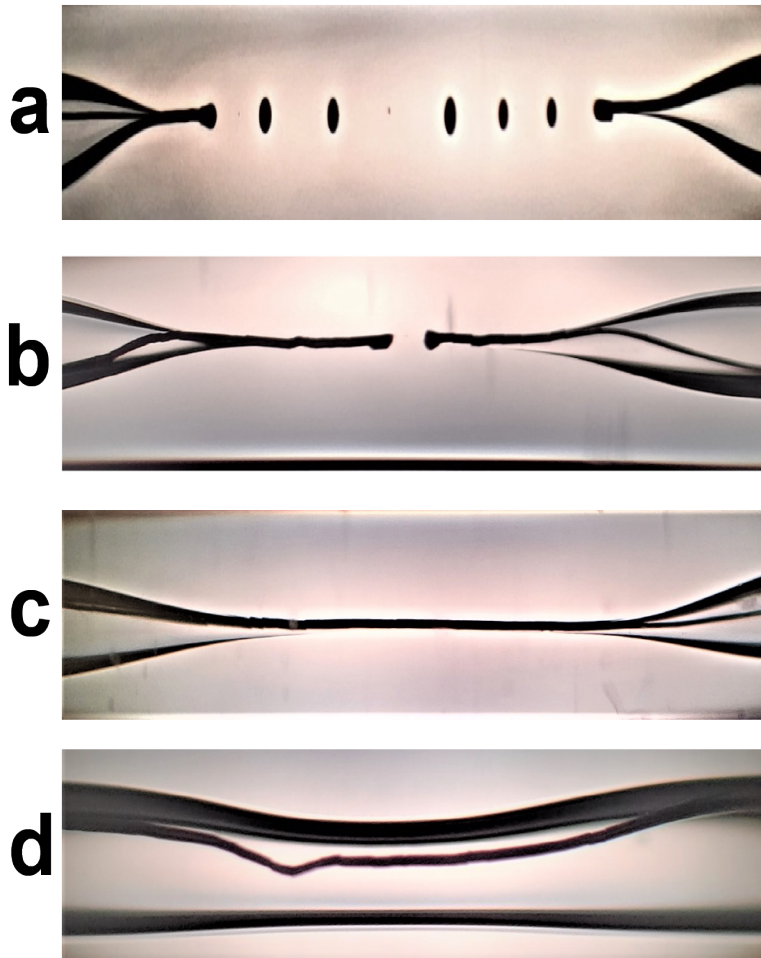


**Figure 6.7. Effect of Heat on the Sealing Process**

The effect of heat on the sealing process while keeping the other parameters constant (Filament: 5, Velocity: 120, Delay: 128, 30 seconds on/off, 4 cycles). A melted and discontinued Pt wire (a) was due to the heat setting being too high (Heat: 880). A melted and discontinued Pt wire with a seal (b) was due to the heat setting approaching the appropriate heat value (Heat: 865). (c) A smooth and complete seal was observed when the heat value was optimal (Heat: 840). Lastly, an incomplete seal was observed when the heat setting was too low (Heat:800) and, at times, the integrity of the Pt wire was compromised (d). All images were taken using a cellphone by aligning it with an eyepiece of the microscope with a 10× objective.

### 6.1.2.2 Filament

The filament is defined as a distribution of heat (**Figure 6.1a**). Higher values of filament indicate a wider distribution of heat. Here, it is essential to know that there is a total of 16 values (0-15) available for the filament parameter, but the P-2000 laser-based micropipette puller only supports values up to 5. As the manual states (page 19), any value above 5 repeats the previous heat distribution pattern. The experimentally varied filaments confirmed a distribution pattern (**Figure 6.8**). However, laser puller #1 showed a change of heat distribution among filaments from 0-6 (**Figure 6.8**). Therefore, we highly recommend testing this systematic difference in filament distribution between each laser puller, while holding the heat value constant. Once the first distribution pattern is observed, we advise only to use a number from this first set.

Intuitively, a higher heat value is used with a higher filament resulting in a wider seal. Generally, when the filament was increased by 1, the heat value was also increased by approximately 60-100 for a complete sealing process (**Figure 6.9**). Filament values lower than 3 harshly degraded Pt wires before a complete seal was obtained, while filament values above 5 were avoided due to the repeating heat distribution. Thus, the filament value was varied from 3 to 5 to elucidate the effect of filament on the sealing process.

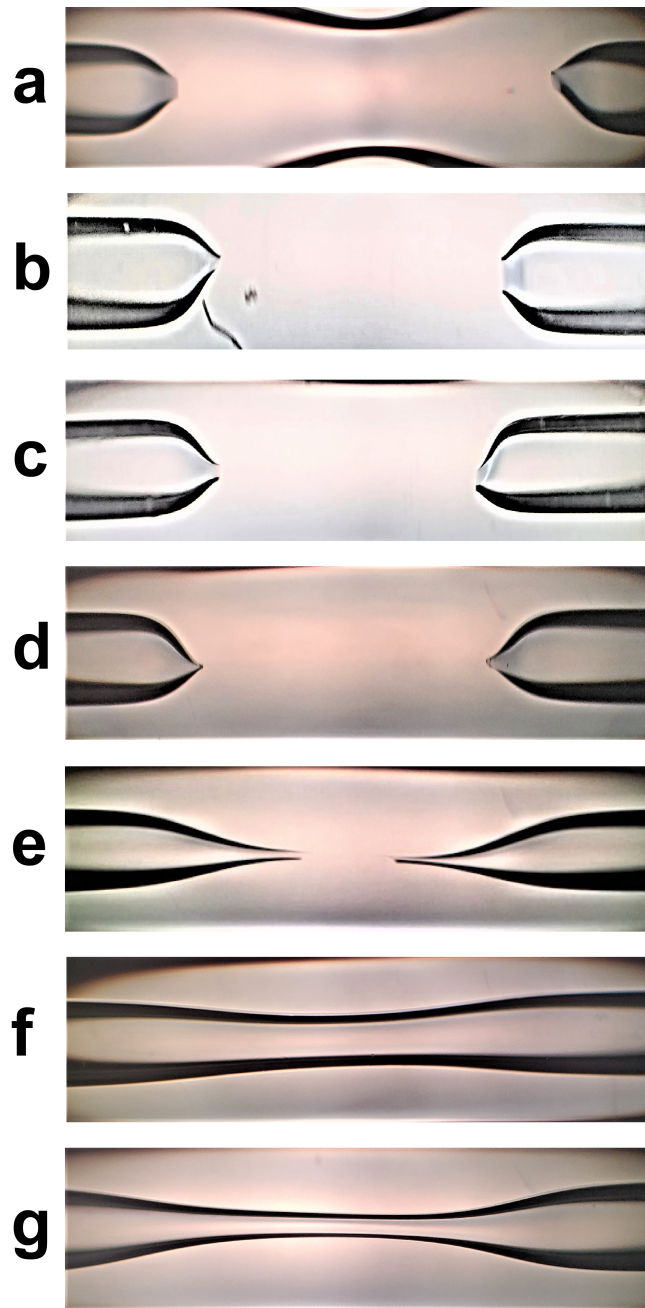


**Figure 6.8. Variation in Heat Distribution Length Based on Filament**

The difference in heat distribution length according to the filament value. Using a constant temperature of 740, the filament was varied from 0 (a) to 6 (g), revealing the first distribution pattern. All images were taken using a cellphone by aligning it with an eyepiece of the microscope with a 10× objective.

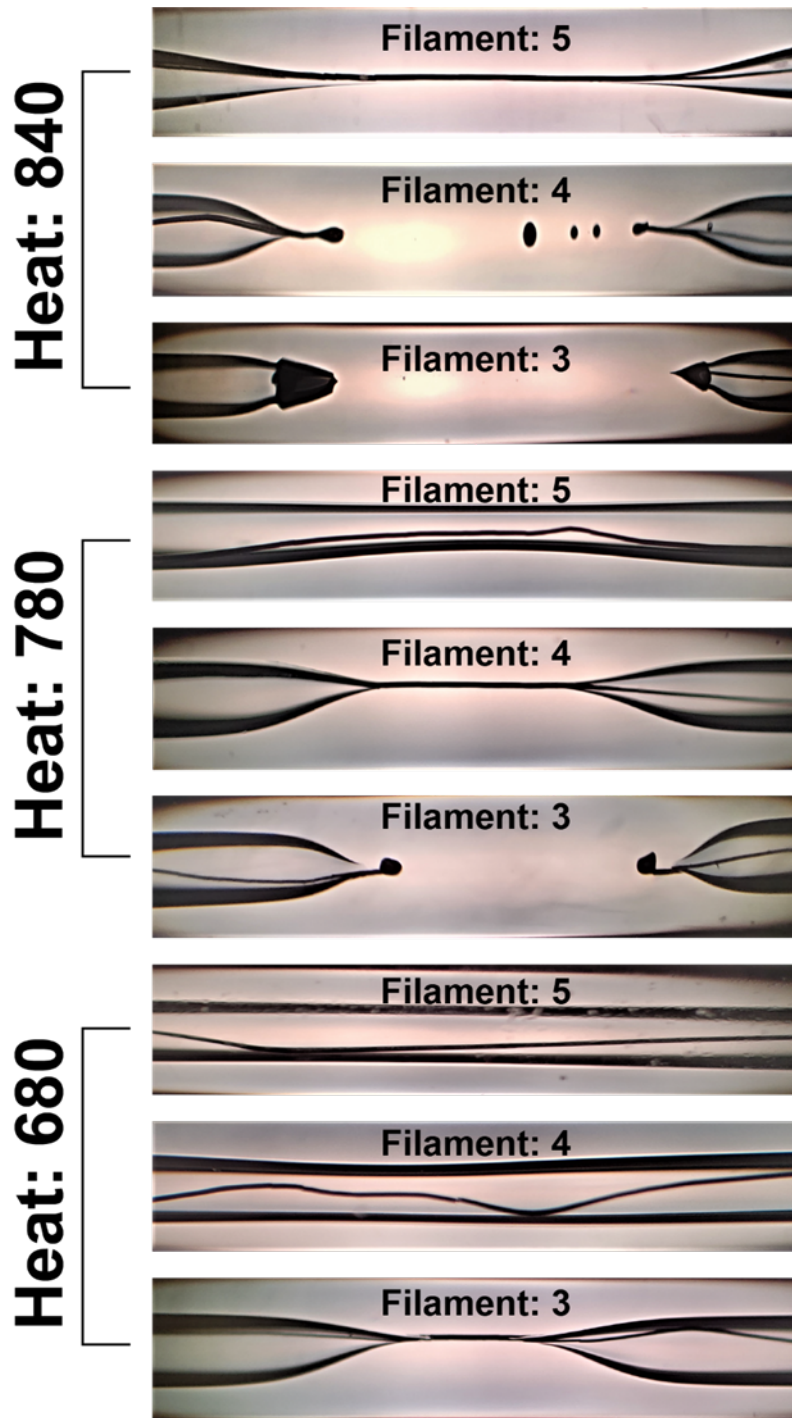


**Figure 6.9. Interdependent Relationship Between Heat and Filament**

Each heat and filament setting were applied for 4 cycles of 30 seconds on/off. As the filament value increased, a higher value of heat was needed to complete the seal.



Comparing 3 completely sealed quartz capillaries under three different filaments, a filament of 3 completed a seal with the shortest seal area (**Figure 6.10a**). Next, a higher heat setting was used for a filament of 4 to complete a seal (**Figure 6.10b**). Despite the higher heat setting, the integrity of the Pt wire was maintained. Lastly, a filament of 5 needed the highest heat setting to seal the Pt wire without damage (**Figure 6.10c**), and the seal area was the longest among the varied filament values. Therefore, when it came to sealing a Pt wire in a quartz capillary, using a higher filament such as 4 or 5 was more forgiving in terms of the fluctuation of heat values or the duration of heat application.

In summary, for a complete and efficient sealing process, ensuring that the vacuum is sufficient, try a starting heat value of 680-740 for a filament of 4 or a starting heat value of 750-860 for a filament of 5. However, it is important to note that these values of heat and filament are dependent on the current status of the laser puller. Therefore, it is advised to compare the filament effects first and then, set the heat. Other researchers have reported the pre-thinning of the glass before threading a Pt wire into the quartz capillary<sup>30</sup>. While this is feasible, the heat set for the seal after the pre-thinning would be different, leading to another optimization step. Therefore, in this section, the pre-thinning of the quartz capillary is not discussed.

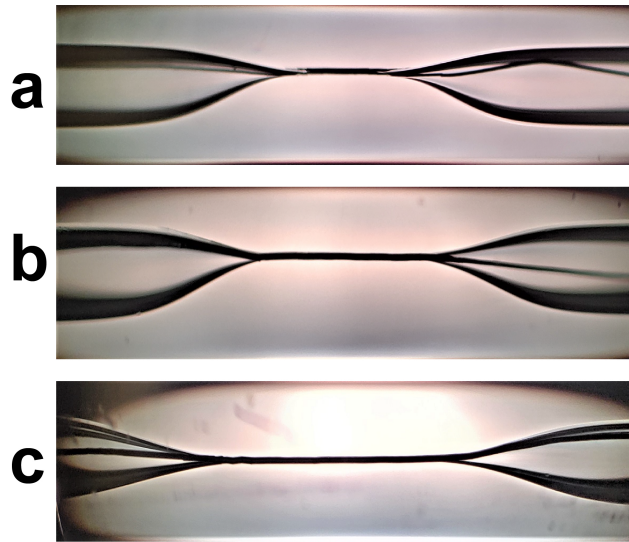


**Figure 6.10. Effect of Filament on the Seal Process**

The effect of filament values on the sealing process. While all filament values from 3(a) to 5(c) made a complete and smooth seal, a higher filament value resulted in a longer seal area. All images were taken using a cellphone by aligning it with an eyepiece of the microscope with a 10× objective.

### 6.1.3 The Pull Process

Under the assumption that the seal was complete and smooth, pulling submicron- or nano-electrodes is governed by 5 parameters: 1) heat, 2) filament, 3) velocity, 4) delay and 5) pull. According to the laser puller manual, the resulting electrode radius is smaller when all the parameters except delay are higher. Thus, the pull value was typically set at a value  $\geq 200$  to give a smaller radius. For nanoelectrode fabrication (*i.e.*, radii  $< 500$  nm), we suggest a pull setting of 250, the highest number possible for the pull value. The other parameters were varied systematically to elucidate their effects on laser-assisted fabrication.

#### 6.1.3.1 Filament

When deciding on a filament value, a good rule of thumb is to use a higher filament value for sturdier and longer tips with a bigger radius or a smaller filament value for flexible and shorter tips with a smaller radius. When a filament of 5 or 4 was used, the resulting electrodes were longer and physically harder at the tip with more quartz surrounding the Pt wire (**Figure 6.11a**). On the other hand, when a filament of 2 or 3 was used, the resulting electrodes were shorter and more flexible (**Figure 6.11b**). While a filament of 4 or 5 can be used to pull sturdy submicron-electrodes (radii  $< 1$   $\mu\text{m}$ ), those electrodes typically provide a larger capacitive current due to the uneven elongation of the Pt wire during the pulling process resulting in a pinched Pt wire (**Figure 6.12**). Thus, using a filament of 2 or 3 is recommended for nanoelectrode fabrication.

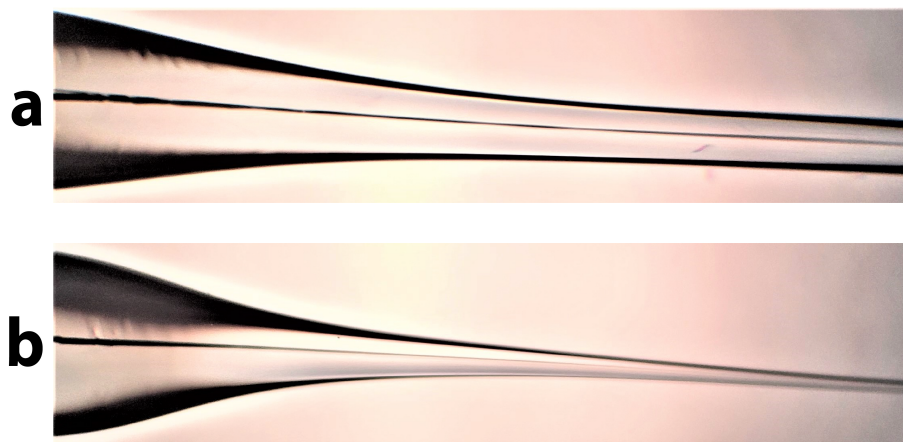


**Figure 6.11. Variation in Outer Diameter of Tip Based on Filament**

The difference between outer diameters of quartz capillaries based on the filament setting during the pull process. Using a higher filament such as 5 (a), the electrode is pulled with more quartz surrounding the Pt wire, resulting in a physically sturdy electrode with a bigger radius. Using a lower filament such as 2 or 3 (b), the electrode is pulled with a thinner quartz layer, resulting in a more fragile electrode with a smaller radius. All images were taken using a cellphone by aligning it with an eyepiece of the microscope with a 10 $\times$  objective.

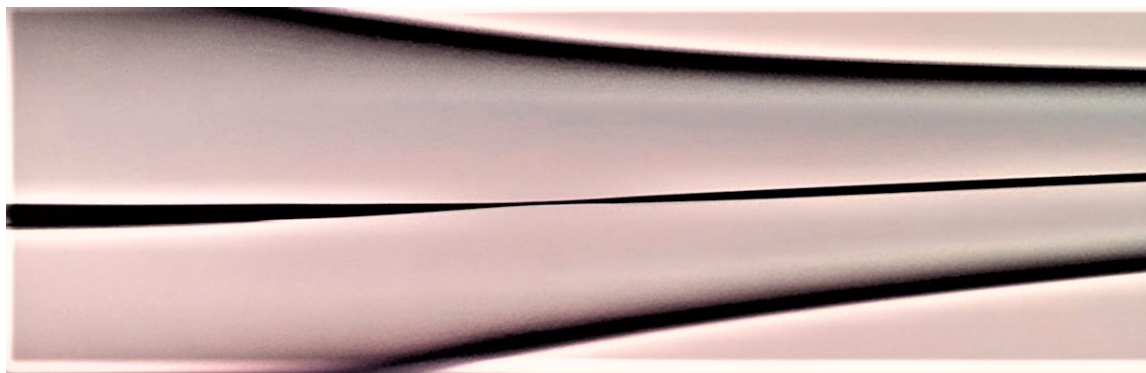


**Figure 6.12. Pinched Pt Wire Result**

When using a higher filament such as 4 or 5, a pinched Pt wire was observed which provided a resistive and capacitive electrode.

### 6.1.3.2 Heat, Velocity, & Delay

The delay value indicates the cooling time between the heat off and the hard pull setting. Any value above 128 means there is a  $(128 - \text{delay})$  millisecond between the laser turning off and the start of the hard pull. A delay of 128 means the hard pull follows immediately after the laser is turned off. Lastly, any delay value below 128 means the hard pull is activated while the laser is on, and then, the laser is turned off after a  $(128 - \text{delay})$  millisecond (ms). Thus, if the delay was set to 130, it resulted in a 2 ms delay between the laser off and the hard pull. If the delay was set to 126, it resulted in a hard pull and then, the laser was turned off after a 1 ms delay. As previously mentioned, smaller delay values result in smaller radii (**Figure 6.13**). However, when the delay parameter is set below 128, the resulting electrodes may show electrical noise (**Figure 6.14**). Thus, the smallest value of delay generally used was 128.

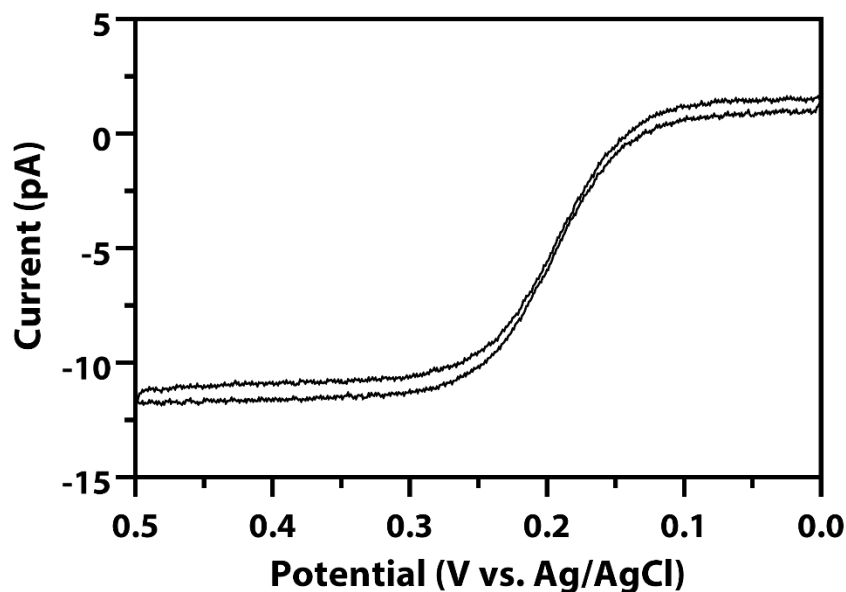


**Figure 6.13. Cyclic Voltammetry of Nanoelectrode Fabricated with a Delay of 100**

Representative cyclic voltammogram of nanoelectrode fabricated with a delay of 100.

Nanoelectrode ( $r = 88$  nm) fabricated with laser puller #2 [Seal (30 seconds on/30 seconds off, 4 $\times$ ) – Heat: 700, Filament: 4, Velocity: 60, Delay: 140, Pull: 1; Pull – Heat: 695, Filament: 2, Velocity: 60, Delay: 100, Pull: 200]. Voltammogram captured in 0.5 mM ferrocenemethanol in DPBS (1X, pH 7.4) vs. Ag/AgCl (1 M KCl) at 50 mV s $^{-1}$ .

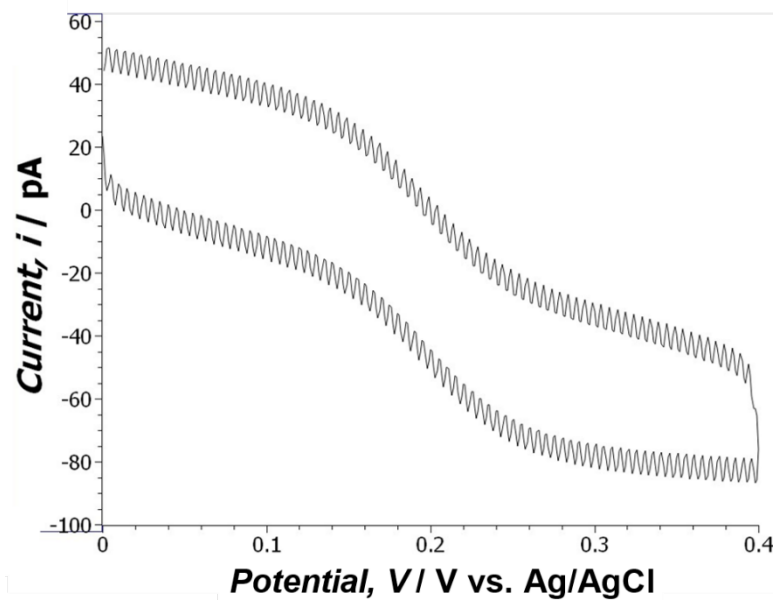


**Figure 6.14. Cyclic Voltammetry of Electrode Fabricated with a Delay < 128**

When delay was set below 128 (*i.e.*, the laser was turned off after the pull occurred), the resulting electrode showed electrical noise despite cleaning procedures. The voltammogram was taken from 0 V to +0.4 V vs. Ag/AgCl (1 M KCl) at  $50 \text{ mV s}^{-1}$  using 1 mM ferrocenemethanol in pH 7.5 100 mM MOPS.



Next, velocity indicates the velocity that the pull force is moving before the hard pull is executed. Previously, it has been reported that nanoelectrodes with exceptionally small radii (*i.e.*, radii  $\leq 50$  nm) can be pulled when the ratio of the diameter of the Pt wire to the outer diameter of the quartz capillary is between 0.2 to 0.4<sup>31</sup>. Thus, if Pt wires of 25  $\mu\text{m}$  diameter were used, the outer diameter should be between 62.5 and 125  $\mu\text{m}$ . However, the exact variance of the outer diameter during the pulling process is a challenge due to the brittleness of quartz capillaries. Thus, the velocity was varied instead of the outer diameter (*i.e.*, higher the velocity, thinner the outer glass).

Interconnected to velocity is the heat value. Typically, a higher heat could allow a higher velocity with even taper lengths. Technically, the heat value can be varied to pull electrodes from 4 – 8 seconds for reproducible pulling, but as higher heat values result in a smaller radius, the initial heat and velocity were adjusted to pull electrodes evenly around 4 seconds. Overall, under a given filament of 2 or 3 and a delay setting of 128, the starting values of heat and velocity were determined first using blank quartz capillaries.

#### **6.1.4 How to Interpret Failure**

Largely, there were two different types of failures with nanoelectrode fabrication: 1) melted Pt wires (**Figure 6.15a**) and 2) small discontinuities throughout pulled Pt wires (**Figure 6.15b**). Typically, these melted Pt wires indicated that the hard pull occurred when the Pt wire was too hot, whereas the discontinuity in Pt wires indicated that the electrodes were moved or pulled when the Pt was not hot enough. While troubleshooting, it is important to note the strong interconnection between heat, velocity, and delay. Changing one parameter influences the other parameters and certain steps need to be retaken. As a general rule, it is preferred to decrease the delay to a minimum of 128, and increase heat and velocity when feasible to ensure the resulting electrode has as small a radius as possible.

When melted Pt wires are observed (**Figure 6.15a**), the first effort can be made with increasing delay by a factor of 3 or less to cool down the heated Pt wire. If adjusting the delay

does not help, then, the second effort should involve decreasing the heat by a factor of 1. When discontinuity of the Pt wire is observed (**Figure 6.15b**) as the first failure or the sequential failure from a melted Pt wire, the first effort should be to decrease the delay until it reaches 128. Next, the heat was increased by an increment of 1. If none of those two efforts fixed the discontinuity of the Pt wire, then, the velocity was decreased by an increment of 1. The heat was increased before decreasing the velocity to avoid losing a smaller electrode radius. Through the navigations of failures, it is also important to understand that temporary malfunctions of laser pullers can change parameters within minutes or between each pull attempt. Thus, it is important to understand the status of each laser-based micropipette puller in use and interpret each failure encountered, instead of relying on one absolute procedure to pull. Parameter values may be adjusted according to results, variation in heat and filament, and systematic differences between the puller and the researcher.

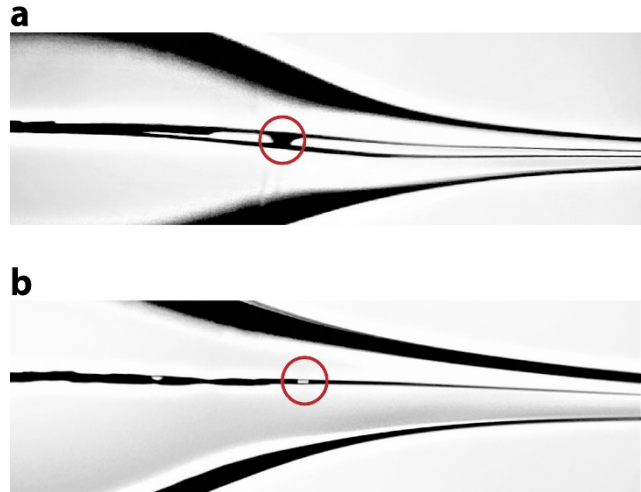


**Figure 6.15. Nanoelectrode Fabrication Failures**

Representative microscopic images of nanoelectrode fabrication failures. The first image shows a characteristic deformation of the Pt wire (a) indicative of melting. The melted wire is highlighted with a red circle. The second image shows a Pt wire pulled using a longer delay (b). There are cleaner cuts at the disconnected sites highlighted with a red circle. All images were taken using a cellphone by aligning it with an eyepiece of the microscope with a 10 $\times$  objective.

### 6.1.5 Making Connections & Maintenance

When handling the Pt-sealed quartz capillaries, it is advised to ensure the handler is grounded to avoid unnecessary displacement of static charge to the electrode surface. Once the Pt-sealed quartz capillary was pulled, a conductive wire was dipped into liquid gallium and inserted into the backend of the capillary to make electrical contact with the sealed Pt wire and conclude the electrode fabrication procedure. Electrical contact can be made with various conductive wires (*e.g.*, tungsten, copper wire, tinned-copper wire, etc.), paints (*e.g.*, silver paint), or powders (*e.g.*, graphite powder), but it is advised to use the least resistive materials available. Finally, the radius of the working electrode may be calculated *via* cyclic voltammetry using the following equation:

$$i_{limiting} = 4nFDC^*r$$

$i_{limiting}$  is the limiting current value indicated with the red box (**Figure 6.16**),  $n$  is the number of electrons involved in the redox reaction,  $F$  is Faraday's constant,  $96485 \text{ C mol}^{-1}$ ,  $D$  is the diffusion coefficient of the redox species used in the system,  $C^*$  is the bulk concentration of the redox species, and  $r$  is the radius of the electrode (*i.e.*, the unknown to solve for). **Figure 6.16** shows a voltammogram of a laser pulled and beveled nanoelectrode. The calculated radius of the electrode from the limiting current is 250 nm. Nanoelectrodes should not be polished on a polishing pad with alumina. We would like to make the important point that polishing a nanoelectrode with alumina or a polishing pad with  $\sim 1 \mu\text{m}$  grit size is like polishing a macroelectrode with bowling balls.

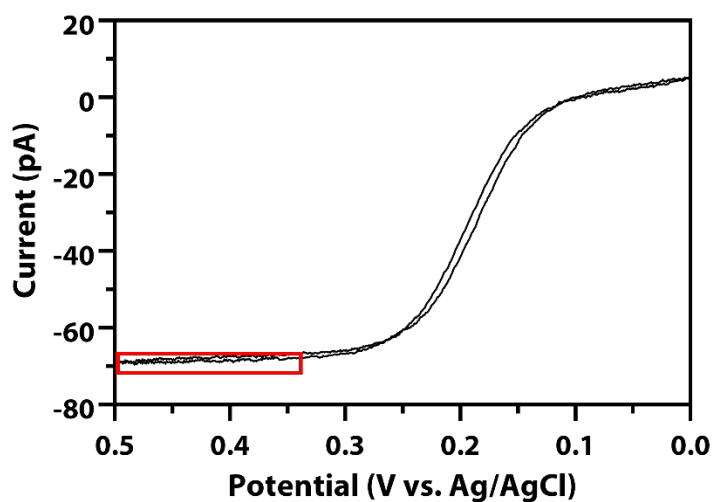


**Figure 6.16. Nanoelectrode Characterization by Cyclic Voltammetry**

Representative cyclic voltammogram of nanoelectrode characterization using cyclic voltammetry. Voltammogram captured in 1.02 mM ferrocenemethanol in 250 mM KCl vs. Ag/AgCl (1 M KCl) at  $50 \text{ mV s}^{-1}$ . The region marked with red box is where the limiting current is observed indicating  $r = 250 \text{ nm}$ .

We suggest chemical or electrochemical methods to polish. Dipping the nanoelectrode in a piranha solution for 10 – 20 seconds is one method to rid the surface of organics. Cyclic voltammetry cycling in strong acid can also be used, but we would like to alert the reader to emerging investigations indicating platinum dissolution under such conditions.<sup>32,33</sup>

Another common problem is electronic noise observed from sensitive nanoelectrodes, which is generally a result of having a poor Faraday cage or poor electrical connection to the potentiostat in use. Thus, always maintaining a clean and stable work environment is key in nanoelectrode characterization.

If no faradaic current was observed, it typically means the electrode surface was not exposed but there was a proper electrical connection (**Figure 6.17**). In this case, beveling the electrode tip was required to expose the conductive Pt surface. The act of beveling was also beneficial to reduce the recessed electrode area (*i.e.*, seemingly small radii and large capacitive current), dirty electrode surfaces (*i.e.*, resistive cyclic voltammograms), and exposed Pt wire (*i.e.*, seeming large radii) to make reliable nanoelectrodes. To bevel, we used a BV-10 microelectrode beveler and its corresponding diamond abrasive plates (*i.e.*, 104C – coarse, 104D – fine, 104E – very fine, and 104F – extra fine). However, beveling is a double-edged sword. The improper cleaning of the beveling pads between each use could result in a pile-up of small broken shreds from previous bevels (**Figure 6.18**) or a complete mask of the metallic electrode surface. While a thorough water wash of electrodes could significantly remove the pile-ups, it may not thoroughly rinse a masked electrode surface. Therefore, those masked electrodes must be beveled again using a clean beveling pad or scored to reveal the electrode surface once more. One of the best ways to polish nanoelectrodes is by focused ion beam milling.<sup>34,35</sup> We recognized that not all

laboratories are equipped with such equipment. Furthermore, if beveling, one should not expect to attain sub-100 nm nanoelectrodes.

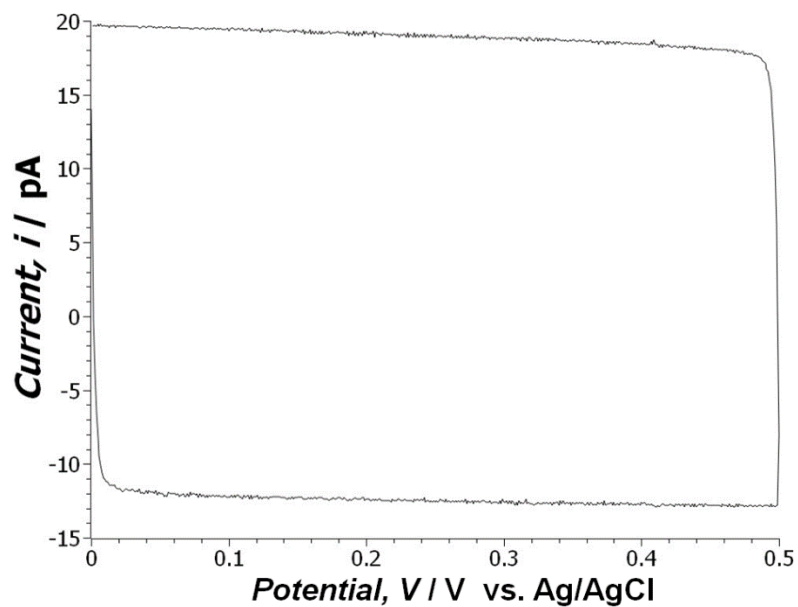


**Figure 6.17. Cyclic Voltammogram of Electrode Without Exposed Platinum Tip**

When the fabricated electrode has liable electric communication with the potentiostat, but its tip is not exposed to the surrounding environment and the voltammogram results in big capacitive current without redox peaks. The cyclic voltammogram was taken from 0 V to +0.4 V vs. Ag/AgCl (1 M KCl) at 50 mV s<sup>-1</sup> using 1 mM ferrocenemethanol in pH 7.5 100 mM MOPS.



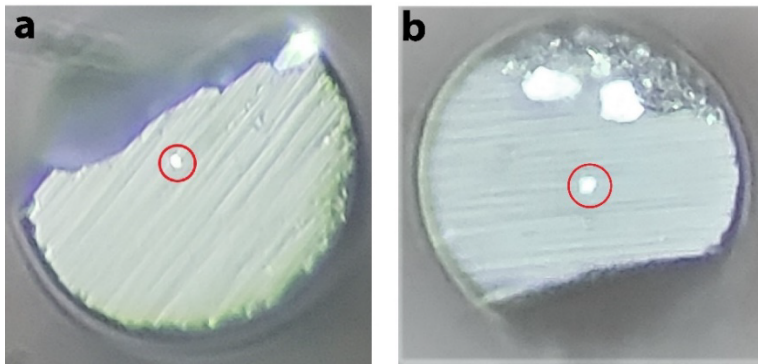


**Figure 6.18. Electrode Surface Following Subsequent Beveling**

Chipped quartz of a pulled electrode. The chip that does not physically damage the electrode surface (a) indicated with a red circle, which still functions well as an electrode. A dirty pad was used for subsequent beveling, which led to a compilation of glass fragments (b) on the electrode surface from the previous beveling.

Additionally, proper care and maintenance of laser pullers as instructed in the manual is required to obtain reproducible results between sealing and pulling procedures. If an incomplete seal is obtained using the tested optimal parameters for vacuum, heat, and filament, we suggest cleaning the gold-plated retro mirror prior to adjusting parameters. This mirror may become covered in debris and materials discharged from the quartz surface during previous heating steps. To minimize transfer, the quartz should be cleaned with acetone or isopropyl alcohol prior to loading into the instrument; in addition, the quartz should always be handled with clean gloves. To clean this mirror, the shroud covering the laser beam path must be removed, then the mirror can be wiped with a Kimwipe dampened with acetone or isopropyl alcohol. If a seal is obtained, but it is an uneven seal under sufficient vacuum, the scanning mirror tilt may be misaligned. First, check the scanning mirror tilt micrometer towards the back of the puller. If the puller is no longer in the manufacturer default setting listed on the label in the back of the instrument, the tilt may be inspected using thermal paper. Specifically, the shroud must be removed, an empty capillary must be inserted between puller bars, and the thermal paper must be inserted between the capillary and the retro mirror (shiny side toward the glass). Next, the following pull program should be used: Heat: 200, Filament: 5, Velocity: 0, Delay: 40, Pull: 0. If the resulting marks are asymmetric, the micrometer behind the should be adjusted as directed in the manual. In addition, if electrode tips are uneven after the pulling process, the puller bars should be dusted with a clean dry Kimwipe (or dry cotton swab as instructed in the manual). Specifically, the top edges of the puller bars and puller bar grooves should be dusted to maintain a reproducible pulling process. If the pulley system is a concern, contact the instrument company prior to adjusting. Lastly, the exterior should be dusted periodically with a dry cloth or Kimwipe.

### 6.1.6 Concluding Remarks

In section 6.1, 6 parameters are discussed to succeed in the nanoelectrode fabrication: 1) vacuum, 2) heat, 3) filament, 4) velocity, 5) delay and 6) pull. The first part of the fabrication is to seal the Pt wire without any damages. Here, it is important to adjust three parameters: vacuum, heat, and filament. Once the vacuum and heat are sufficient (*i.e.*, the quartz capillary encases an intact Pt wire), the filament may be adjusted to optimize the width of the seal. Single-digit filament values should be used to establish the correlation between the numeric value of the filament and the microscopic images of the effect on the quartz capillary to minimize the systematic variation between laser-based micropipette pullers. The second part of the fabrication is to pull the Pt-sealed quartz capillary into two separate electrode tips. As there is no one-size-fits-all procedure for submicron-electrode fabrication, this section provides examples on how to interpret each failure and vary each parameter to troubleshoot through each individual laboratory's fabrication procedure.

## 6.2 Correlated Scanning Electrochemical Microscopy of Single Living Cells

Hyperspectral assisted-scanning electrochemical microscopy (SECM) is a valuable tool for multicolor analysis of single live cells. Previously, we demonstrated single cell and single organelle resolution when using our variable fluorescence bandpass hyperspectral imaging platform. Here, we demonstrate that correlated high resolution electrochemical mapping is also feasible with the use of nanoelectrode tips ( $r < 1 \mu\text{m}$ ) (**Figure 6.19**). SECM with nanoelectrode tips has been used to image cellular redox activity and topography with single cell resolution.<sup>36</sup> Specifically, SECM allows one to examine extra- and intra-cellular redox mechanisms with the use of hydrophilic and hydrophobic redox mediators, respectively.

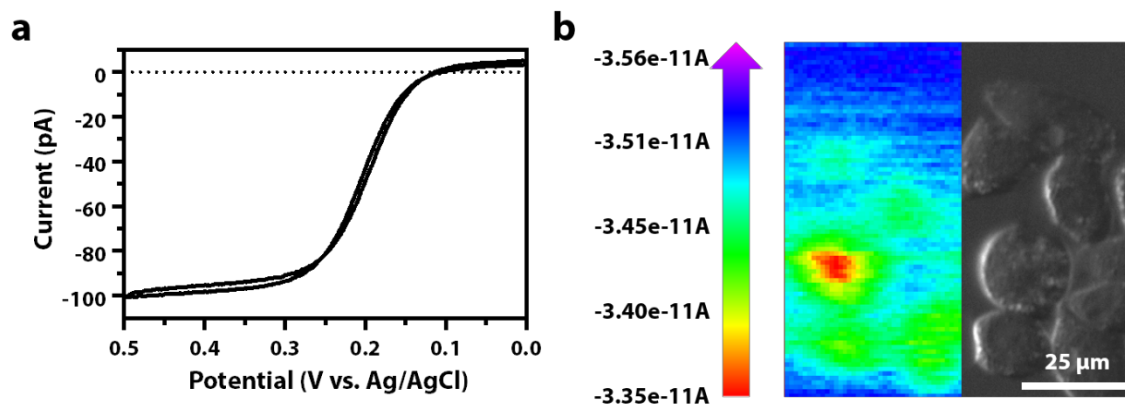


**Figure 6.19. Scanning Electrochemical Microscopy of Single Living Cells**

(a) Cyclic voltammogram at a laser pulled platinum nanoelectrode ( $r = 756 \text{ nm}$ ) vs. Ag/AgCl (1 M KCl) in 1 mM ferrocenemethanol in 250 mM KCl obtained at a scan rate of  $50 \text{ mV s}^{-1}$ . (b) Correlated optical and electrochemical image of Hep G2 cells in 0.5 mM ferrocenemethanol in DPBS (1X, pH 7.4). The electrochemical image was obtained with the electrode biased at +0.5 V vs. Ag/AgCl (1 M KCl) and 1 micrometer resolution. A glassy carbon rod was used as the counter electrode ( $r = 1.5 \text{ mm}$ )

For example, ferrocenemethanol (FcCH<sub>2</sub>OH) – the primary hydrophobic, neutral, permeable mediator used here – has been used to examine membrane permeability based on the mediator’s ability to passively diffuse through the cell membrane.<sup>37</sup> The mediator has also been used to examine cell activity and viability.<sup>38</sup> In addition, hydrophilic, charged, nonpermeable redox mediators, such as ferrocene dicarboxylate, are used to examine cell viability based on damage to the cell membrane. SECM is not limited to the use of extrinsic redox mediators. The cellular redox state of single cells is often characterized by redox species intrinsic to the cell such as membrane transport of reactive oxygen species (ROS)<sup>39-41</sup>, reactive nitrogen species (RNS)<sup>39-41</sup>, and antioxidant species like thiodione<sup>42</sup>. Moreover, these studies are generally completed concomitantly with fluorescence assays, such as 3-(4,5-dimethylthiazol-2-yl)-2,5-diphenyl-2H-tetrazolium bromide (or MTT) viability assays, to support evidence provided by SECM.<sup>43</sup> Moreover, the use of nanoelectrode tips enables the direct examination of intracellular redox species with minimal perturbation to cellular homeostasis.<sup>44, 45</sup> Mirkin and co-workers detected ROS and RNA species within breast cancer cells using Pt Black nanoelectrodes with radii  $\leq 300$  nm.<sup>39</sup> Similarly, we detected oxygen in a single cell using a nanoelectrode tip (**Figure 6.20**). Initially, an approach to the cell surface based on the methods described in **Chapter 2** resulted in an increase in normalized current upon penetrating the cell membrane following literature precedent.<sup>46</sup> Following the approach, a cyclic voltammogram within the cell showing a peak at -0.4 V vs. Ag/AgCl (1 M KCl), indicative of oxygen reduction on platinum in polarographic convention.<sup>47</sup>

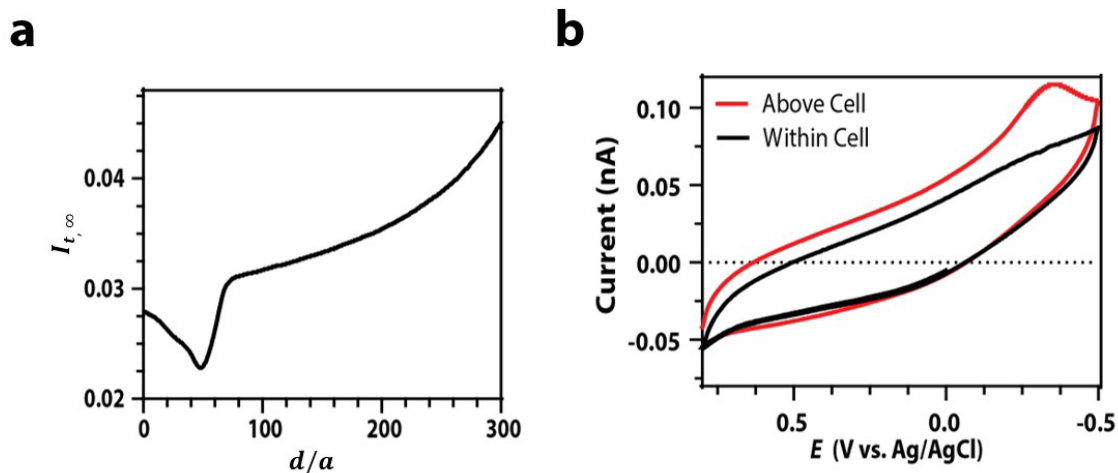


**Figure 6.20. Intracellular Measurement with a Laser Pulled Pt Nanoelectrode**

(a) Amperometric approach to normal human lung (MRC-5) cells in 0.06 mM 1,2-naphthoquinone in DPBS (1X, pH 7.4) using a laser pulled platinum nanoelectrode tip ( $r = 483$  nm) biased at -0.4 V vs. Ag/AgCl (1 M KCl). (b) Cyclic voltammetry at the laser pulled platinum nanoelectrode tip above the cell and within the cell obtained using a scan rate of  $50 \text{ mV s}^{-1}$ .

### 6.2.1 Concluding Remarks & Future Perspectives

Hyperspectral assisted-scanning electrochemical microscopy (SECM) of single cells may elucidate cell-to-cell heterogeneity with respect to cell morphology, membrane transport, cell viability, and the overall cellular redox state. By examining individual cells with this technology, one may reveal the dynamic mechanisms involved in cell response to stimuli and disease progression. Our understanding of these mechanisms is generally based on amperometric SECM involving the indirect or direct detection of relevant redox species. Unfortunately, many biologically relevant small molecules are not electroactive. Potentiometric SECM combined with the use of potentiometric biosensors for the indirect detection of these species would expand our imaging and detection capabilities. Recently, we demonstrated potentiometric biosensors may be miniaturized from macroelectrodes to microelectrodes with minimal interferent effects and electrode fouling due to potentiometry's insensitivity to electrode size.<sup>48, 49</sup> The miniaturization of these sensors to nanoelectrode tips would offer a less destructive means for intracellular detection based on the size of the electrode<sup>45</sup> and potentiometry's use of a high input impedance to deliver negligible current from the electrode tip<sup>49</sup>. The use of nanosized potentiometric biosensors in combination with hyperspectral assisted-SECM will be the topic of future investigations.

## REFERENCES

1. F. Alam, S. RoyChoudhury, A. H. Jalal, Y. Umasankar, S. Forouzanfar, N. Akter, S. Bhansali and N. Pala, *Biosensors & Bioelectronics*, 2018, **117**, 818-829.
2. L. Rassaei, W. Olthuis, S. Tsujimura, E. J. R. Sudholter and A. van den Berg, *Analytical and Bioanalytical Chemistry*, 2014, **406**, 123-137.
3. S. Chakraborty, M. Roy and R. K. Bhattacharya, 2004, **23**, 12.
4. T. Y. de Soysa, S. S. Ranade, S. Okawa, S. Ravichandran, Y. Huang, H. T. Salunga, A. Schricker, A. del Sol, C. A. Gifford and D. Srivastava, *Nature*, 2019, **572**, 120-124.
5. C. Shen, S. Liu, X. Li and M. Yang, *Analytical Chemistry*, 2019, **91**, 11614-11619.
6. E. Stepula, X.-P. Wang, S. Srivastav, M. König, J. Levermann, S. Kasimir-Bauer and S. Schlücker, *ACS Applied Materials & Interfaces*, 2020, **12**, 32321-32327.
7. B. K. Jena, S. J. Percival and B. Zhang, *Anal Chem*, 2010, **82**, 6737-6743.
8. J. Velmurugan, P. Sun and M. V. Mirkin, *J Phys Chem C*, 2009, **113**, 459-464.
9. Y. Yu, T. Sun and M. V. Mirkin, *Anal Chem*, 2016, **88**, 11758-11766.
10. J. Velmurugan, J. M. Noel, W. Nogala and M. V. Mirkin, *Chemical Science*, 2012, **3**, 3307-3314.
11. Y. Li, J. T. Cox and B. Zhang, *J Am Chem Soc*, 2010, **132**, 3047-3054.
12. A. J. Bard, *ACS Nano*, 2008, **2**, 2437-2440.
13. Y. Liu, M. Li, F. Zhang, A. Zhu and G. Shi, *Anal Chem*, 2015, **87**, 5531-5538.
14. H. K. McCormick and J. E. Dick, *Anal Bioanal Chem*, 2021, **413**, 17-24.
15. P. Sun, F. O. Laforge, T. P. Abeyweera, S. A. Rotenberg, J. Carpino and M. V. Mirkin, *Proc Natl Acad Sci U S A*, 2008, **105**, 443-448.
16. C. Wang and X. Hu, *Talanta*, 2006, **68**, 1322-1328.
17. B. K. Jena, S. J. Percival and B. Zhang, *Analytical Chemistry*, 2010, **82**, 6737-6743.
18. C. Y. Wang and X. Y. Hu, *Talanta*, 2006, **68**, 1322-1328.
19. S. L. Chen and A. Kucernak, *Journal of Physical Chemistry B*, 2003, **107**, 8392-8402.
20. R. M. Penner, M. J. Heben, T. L. Longin and N. S. Lewis, *Science*, 1990, **250**, 1118-1121.

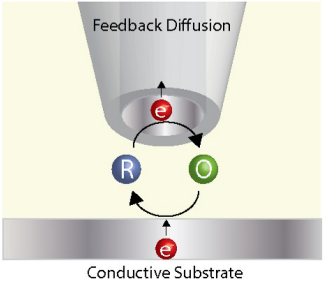
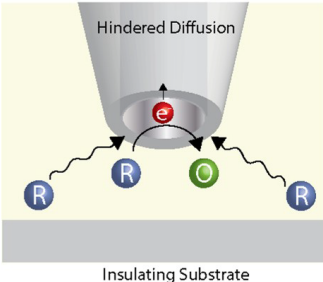
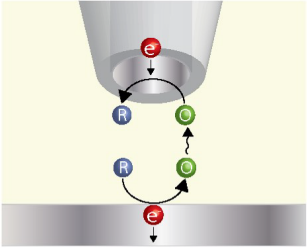
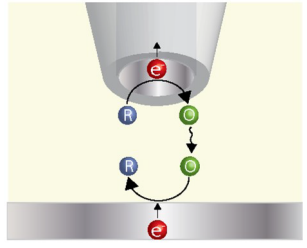


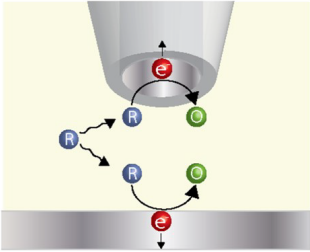
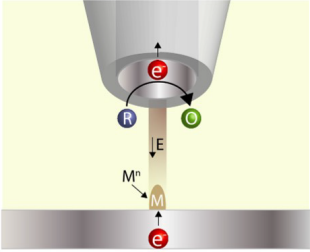
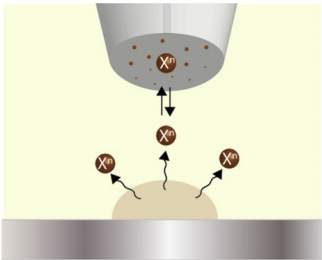
21. P. Sun, Z. Q. Zhang, J. D. Guo and Y. H. Shao, *Analytical Chemistry*, 2001, **73**, 5346-5351.
22. B. B. Katemann and W. Schuhmann, *Electroanalysis*, 2002, **14**, 22-28.
23. M. A. Mezour, M. Morin and J. Mauzeroll, *Analytical Chemistry*, 2011, **83**, 2378-2382.
24. Y. X. Li, D. Bergman and B. Zhang, *Analytical Chemistry*, 2009, **81**, 5496-5502.
25. Y. H. Lanyon, G. De Marzi, Y. E. Watson, A. J. Quinn, J. P. Gleeson, G. Redmond and D. W. M. Arrigan, *Analytical Chemistry*, 2007, **79**, 3048-3055.
26. D. J. Guo, X. Y. Wu, J. G. Lei, B. Xu, R. Kometani and F. Luo, *18th Cirp Conference on Electro Physical and Chemical Machining (Isem Xviii)*, 2016, **42**, 733-736.
27. B. Zhang, J. Galusha, P. G. Shiozawa, G. L. Wang, A. J. Bergren, R. M. Jones, R. J. White, E. N. Ervin, C. C. Cauley and H. S. White, *Analytical Chemistry*, 2007, **79**, 4778-4787.
28. D. W. M. Arrigan, *Analyst*, 2004, **129**, 1157-1165.
29. X. Y. Zhu, Y. H. Qiao, X. Zhang, S. S. Zhang, X. H. Yin, J. Gu, Y. Chen, Z. W. Zhu, M. X. Li and Y. H. Shao, *Analytical Chemistry*, 2014, **86**, 7001-7008.
30. M. A. Mezour, M. Morin and J. Mauzeroll, *Anal Chem*, 2011, **83**, 2378-2382.
31. G. Fish, O. Bouevitch, S. Kokotov, K. Lieberman, D. Palanker, I. Turovets and A. Lewis, *Review of Scientific Instruments*, 1995, **66**, 3300-3306.
32. S. J. Percival, J. E. Dick and A. J. Bard, *Analytical Chemistry*, 2017, **89**, 3087-3092.
33. X. Deng, F. Galli and M. T. M. Koper, *Journal of the American Chemical Society*, 2018, **140**, 13285-13291.
34. R. Chen, K. K. Hu, Y. Yu, M. V. Mirkin and S. Amemiya, *Journal of the Electrochemical Society*, 2016, **163**, H3032-H3037.
35. T. H. Kai, C. G. Zoski and A. J. Bard, *Chemical Communications*, 2018, **54**, 1934-1947.
36. F. P. Filice and Z. F. Ding, *Analyst*, 2019, **144**, 738-752.
37. J. D. Henderson, F. P. Filice, M. S. M. Li and Z. F. Ding, *Journal of Inorganic Biochemistry*, 2016, **158**, 92-98.
38. A. J. Bard, X. Li and W. Zhan, *Biosensors & Bioelectronics*, 2006, **22**, 461-472.
39. Y. Li, K. K. Hu, Y. Yu, S. A. Rotenberg, C. Amatore and M. V. Mirkin, *Journal of the American Chemical Society*, 2017, **139**, 13055-13062.

40. K. K. Hu, Y. Li, S. A. Rotenberg, C. Amatore and M. V. Mirkin, *Journal of the American Chemical Society*, 2019, **141**, 4564-4568.
41. Y. X. Wang, J. M. Noel, J. Velmurugan, W. Nogala, M. V. Mirkin, C. Lu, M. G. Collignon, F. Lemaitre and C. Amatore, *Proceedings of the National Academy of Sciences of the United States of America*, 2012, **109**, 11534-11539.
42. J. Mauzeroll, A. J. Bard, O. Owhadian and T. J. Monks, *Proceedings of the National Academy of Sciences of the United States of America*, 2004, **101**, 17582-17587.
43. F. P. Filice, J. D. Henderson, M. S. M. Li and Z. Ding, *ACS Omega*, 2019, **4**, 2142-2151.
44. K. Hu, Y.-L. Liu, A. Oleinick, M. V. Mirkin, W.-H. Huang and C. Amatore, *Current Opinion in Electrochemistry*, 2020, **22**, 44-50.
45. H. K. McCormick and J. E. Dick, *Analytical and Bioanalytical Chemistry*, 2021, **413**, 17-24.
46. P. Sun, F. O. Laforge, T. P. Abeyweera, S. A. Rotenberg, J. Carpino and M. V. Mirkin, *Proceedings of the National Academy of Sciences of the United States of America*, 2008, **105**, 443-448.
47. C. C. Liang and A. L. Juliard, *Nature*, 1965, **207**, 629-630.
48. N. L. Walker and J. E. Dick, *Biosensors and Bioelectronics*, 2021, 112997.
49. L. A. Smith, M. W. Glasscott, K. J. Vannoy and J. E. Dick, *Analytical Chemistry*, 2020, **92**, 2266-2273.

## APPENDIX A

**Table A1. Operational Modes of Scanning Electrochemical Microscopy**

| Operational Modes & Schematics  | Applications   | Advantages  | Disadvantages  |
|---|--|---|--|
| <p style="text-align: center;"><b>Positive Feedback</b></p>  <p style="text-align: center;"><b>Negative Feedback</b></p>   | <ul style="list-style-type: none"> <li>• Kinetics</li> <li>• Surface Modifications</li> <li>• Enzymatic measurements</li> <li>• Biological imaging</li> <li>• Corrosion studies</li> <li>• Catalysis</li> <li>• Energy</li> <li>• ITIES</li> </ul>                                     | <ul style="list-style-type: none"> <li>• Versatile</li> </ul>                           | <ul style="list-style-type: none"> <li>• Smallest tip-to-substrate distance preferred for high sensitivity</li> </ul>  |
| <p style="text-align: center;"><b>Substrate Generation/Tip Collection</b></p>  <p style="text-align: center;"><b>Tip Generation/Substrate Collection</b></p>  | <ul style="list-style-type: none"> <li>• Kinetics</li> <li>• Substrate modifications</li> <li>• Enzymatic measurements</li> <li>• Biological imaging</li> <li>• Corrosion studies</li> <li>• Catalysis</li> <li>• Energy</li> <li>• Concentration profile/flux measurements</li> </ul> | <ul style="list-style-type: none"> <li>• Amperometric or potentiometric mode</li> </ul> | <ul style="list-style-type: none"> <li>• Low collection efficiency</li> <li>• Inference between tip &amp; substrate reactions</li> <li>• Lateral diffusion at the substrate</li> </ul> |

|   |  |   |  |
|---|--|---|--|
| <p style="text-align: center;"><b>Redox Competition</b></p>  | <ul style="list-style-type: none"> <li>• Kinetics</li> <li>• Enzymatic measurements</li> <li>• Biological imaging</li> <li>• Corrosion studies</li> <li>• Catalysis</li> <li>• Energy</li> </ul> | <ul style="list-style-type: none"> <li>• Increased sensitivity vs TG/SC mode</li> </ul>   | <ul style="list-style-type: none"> <li>• Limited applications</li> </ul> |
| <p style="text-align: center;"><b>Direct</b></p>             | <ul style="list-style-type: none"> <li>• Surface modifications</li> </ul>  | <ul style="list-style-type: none"> <li>• High patterning resolution</li> </ul>  | <ul style="list-style-type: none"> <li>• Limited applications</li> </ul> |
| <p style="text-align: center;"><b>Potentiometric</b></p>   | <ul style="list-style-type: none"> <li>• Ion-selective measurements</li> </ul>   | <ul style="list-style-type: none"> <li>• High selectivity of electroactive and non-electroactive species</li> <li>• Faradaic reaction not required</li> </ul> | <ul style="list-style-type: none"> <li>• Limited applications</li> </ul> |

**Table A1** provides a brief overview of operational modes of scanning electrochemical microscopy based on the information provided by Polcari and co-workers in 2016.<sup>1</sup>

## Reference

1. D. Polcari, P. Dauphin-Ducharme and J. Mauzeroll, *Chemical Reviews*, 2016, **116**, 13234-13278.